Combining optics and RIXS on 4d and 5d transition-metal halides with strong spin-orbit coupling

Dissertation
zur
Erlangung des Doktorgrades
der Mathematisch-Naturwissenschaftlichen Fakultät
der Universität zu Köln

vorgelegt von
Philipp Warzanowski

angenommen im Jahr 2025

Abstract

Transition-metal compounds with $4d$ and $5d$ electrons have become a central focus over the past two decades, as the interplay of strong spin-orbit coupling, electronic correlations, and crystal-field effects can generate local spin-orbit entangled states. These form the basis for novel phenomena such as bond-directional Kitaev interaction, which can ideally generate a possible quantum spin liquid ground state, or excitonic magnetism manifested by the exchange-driven condensation of local triplet excitations. Deviations from ideal symmetry or the competition between various parameters, however, might affect the local states and suppress such phases, making a detailed understanding of the local states essential.
In this thesis, we investigate the role of spin-orbit coupling in Mott-insulating transition-metal compounds with different d^N electron configurations, namely d^3, d^4, and d^5, since the effect of spin-orbit coupling can manifest differently in each of these configurations.
In the first project, we analyze the low-energy excitations of the $4d^5$ compound α-$RuCl_3$, one of the most studied candidates for realizing the Kitaev model. Using optical spectroscopy and Raman scattering in conjunction, we identify the spin-orbit exciton, the characteristic excitation from the $j_{\text{eff}} = 1/2$ ground state to $j_{\text{eff}} = 3/2$, and establish that the two additional higher-lying features have to be understood as the double and triple spin-orbit excitons, refuting previous interpretations that severely challenged the local $j_{\text{eff}} = 1/2$ picture. From the excitation energy and splitting of the spin-orbit exciton, we calculate that the ground state wavefunction in α-$RuCl_3$ exhibits more than 98% of $j_{\text{eff}} = 1/2$ character, agreeing with theoretical predictions and the notion that this compound is a proximate Kitaev material. The unusually large spectral weight of the multiple spin-orbit excitons reflects the underlying hopping processes that yield Kitaev interaction.
The second, third, and fourth projects of this thesis focus on the K_2PtCl_6-type antifluorite halides A_2MX_6 with $A = \{K^+, Rb^+\}$, $X = \{Cl^-, Br^-\}$ and $M = \{Re^{4+}, Os^{4+}, Ir^{4+}\}$. Choosing the Re-, Os-, or Ir-based version of these compounds allows us to examine the $5d^3$, $5d^4$, or $5d^5$ electron configurations, respectively. The isolated MX_6 octahedra in these crystals result in large Mott gaps and narrow excitation peaks, which makes these materials ideal to study with optical spectroscopy and resonant inelastic x-ray scattering at the transition-metal L_3 edge. Putting these methods together yields a very comprehensive picture of the electronic structure and allows us, e.g., to uncover the origin of the splitting in the spin-orbit exciton in K_2IrCl_6.
For the $5d^4$ systems A_2OsX_6, our data confirm a robust local $J = 0$ scenario. The spectra display well-defined onsite multiplets, which are described best within the intermediate coupling regime, where spin-orbit coupling and Hunds coupling must be considered on equal footing. Determining the cubic crystal-field splitting using RIXS, we compare the

electronic parameters in two different approaches: the t_{2g}-only Kanamori model and the single-site model of the entire d shell. Both models describe the energies of the intra-t_{2g} RIXS energies equally well, which allows us to establish these compounds as solid reference systems for other Os^{4+} $J = 0$ systems.
For the $5d^3$ case in K_2ReCl_6, we probe the competition of spin-orbit coupling and Hund's exchange in the quest of finding a spin-orbit-induced Jahn-Teller effect. While the value of spin-orbit coupling is sizable, it is not strong enough to turn fully around the $S = 3/2$ scenario. However, we find that spin-orbit coupling enhances the coupling to the lattice in multiplets that acquire a non-vanishing orbital moment, which alters the observed lineshapes slightly.
For the $5d^5$ system K_2IrCl_6, we investigate the nature of the spin-orbit exciton. The RIXS spectra display a characteristic splitting of this excitation, which had been explained by static distortions of the octahedra in previous works. However, based on a careful analysis using a vibronic Franck-Condon picture, we can assign the observed RIXS feature to a vibronic excitation with a well-resolved phonon sideband. The strong temperature sensitivity of the lineshape agrees with a recent theoretical prediction that goes beyond the simple Franck-Condon picture and attributes the splitting to a dynamic Jahn-Teller effect involving coupling to E_g phonon modes. The ground state itself retains cubic $j_{\text{eff}} = 1/2$ character, while the lattice couples only to the excited $j_{\text{eff}} = 3/2$ state. This demonstrates that ideal $j_{\text{eff}} = 1/2$ moments with cubic symmetry can indeed be realized in $5d^5$ Mott systems. It also shows direct RIXS at the L_3 edge of $5d$ metals is capable of resolving vibronic phonon sidebands, which can be described with a single Franck-Condon factor.

Kurzzusammenfassung

Übergangsmetallverbindungen mit $4d$- und $5d$-Elektronen sind innerhalb der letzten zwei Jahrzehnte in den Fokus gerückt, da sie durch das Wechselspiel von Spin-Bahn-Kopplung, elektronischen Korrelationen und Kristallfeldeffekten lokale Spin-Bahn-verschränkte Zustände hervorbringen können. Diese bilden die Grundlage für neuartige Phänomene wie zum Beispiel die richtungsabhängige Kitaev-Wechselwirkung, die im Idealfall eine Quantenspinflüssigkeit im Grundzustand hervorbringt, oder den exzitonischen Magnetismus, der sich manifestiert, wenn Austauschwechselwirkungen eine Kondensation von angeregten lokalen Triplettzuständen bewirken. Abweichungen von idealer Symmetrie oder die Wechselwirkung konkurrierender Parameter können die lokalen Zustände beeinflussen und die entstehenden Phasen unterdrücken. Dies macht ein detailliertes Verständnis der lokalen Zustände essenziell.
In dieser Arbeit untersuchen wir die Rolle von Spin-Bahn-Kopplung in Mott-isolierenden Übergangsmetallverbindungen mit unterschiedlichen d^N-Elektronenkonfigurationen, insbesondere d^3, d^4 und d^5, in denen die Spin-Bahn-Kopplung unterschiedliche Ausprägungen zeigt.
Im ersten Projekt dieser Arbeit untersuchen wir die niederenergetischen Anregungen von α-$RuCl_3$, einem der meistuntersuchten Kandidaten, um das Kitaev-Modell im Kristall zu realisieren. Mittels optischer Spektroskopie und Ramanstreuung bestimmen wir das Spin-Bahn-Exziton, die charakteristische Anregung eines $j_{\text{eff}} = 1/2$-Grundzustandes in den $j_{\text{eff}} = 3/2$-Zustand, und weisen nach, dass die beobachteten höherliegenden Anregungen als doppelte und dreifache Spin-Bahn-Exzitonen verstanden werden müssen, womit wir frühere Interpretationen ausräumen, die die Anwendbarkeit des $j_{\text{eff}} = 1/2$-Szenarios infrage stellten. Aus der Anregungsenergie und der Aufspaltung des Spin-Bahn-Exzitons berechnen wir, dass die Grundzustandswellenfunktion von α-$RuCl_3$ zu über 98% $j_{\text{eff}} = 1/2$-Charakter trägt, was durch theoretische Vorhersagen gestützt wird und mit dem Bild übereinstimmt, dass diese Verbindung als ein fast ideales Kitaevmaterial angesehen werden kann.
Die weiteren Projekte befassen sich mit den K_2PtCl_6-artigen Antifluorit-Halogeniden A_2MX_6 mit $A = \{K^+, Rb^+\}$, $X = \{Cl^-, Br^-\}$ und $M = \{Re^{4+}, Os^{4+}, Ir^{4+}\}$. Durch Auswahl der Re-, Os-, oder Ir-Ionen lassen sich in diesen Verbindungen jeweils die $5d^3$-, $5d^4$- und $5d^5$-Elektronenkonfigurationen untersuchen. Die isolierten MX_6-Oktaeder in diesen Kristallen führen zu einer Mott-Lücke mit hoher Anregungsenergie und schmalen Anregungspeaks, was sie ideal für eine Untersuchung mittels optischer Spektroskopie und resonanter inelastischer Röntgenstreuung (RIXS) an der L_3-Kante des Übergangsmetallions macht. Die

Kombination beider Methoden ergibt ein sehr umfassendes Bild der elektronischen Struktur und erlaubt es uns, zum Beispiel im Falle von K_2IrCl_6, den Ursprung der Aufspaltung des Spin-Bahn-Exzitons aufzudecken.
Für die $5d^4$-Systeme A_2OsX_6 bestätigen unsere Messungen ein stabiles lokales $J = 0$ Szenario. Die Spektren zeigen klare Onsite-Multipletts, die sich am besten durch ein intermediäres Kopplungsregime beschreiben lassen, in dem die Spin-Bahn-Kopplung und die Hundsche Kopplung gleichermaßen relevant sind. Durch die Bestimmung der Kristallfeldaufspaltung mittels RIXS können wir die elektronischen Parameter über zwei Zugänge beschreiben: einmal über ein reines t_{2g}-Kanamori-Modell und einmal über ein lokales Modell der gesamten d-Schale. Beide Modelle beschreiben die intra-t_{2g}-Energien aus den RIXS-Daten gleichermaßen gut, was uns erlaubt, diese Os^{4+}-basierten $J = 0$ Systeme als zuverlässige Referenzsysteme zu betrachten.
Für den $5d^3$-Fall in K_2ReCl_6 untersuchen wir den Wettstreit zwischen Spin-Bahn-Kopplung und Hundscher Wechselwirkung im Hinblick auf einen spin-bahn-induzierten Jahn-Teller-Effekt. Obwohl die Stärke der Spin-Bahn-Kopplung beachtlich ist, ist sie nicht ausreichend, um das $S = 3/2$-Szenario umzudrehen. Dennoch zeigt sich, dass die Spin-Bahn-Wechselwirkung die Kopplung an das Gitter für die Multipletts verstärkt, die ein endliches Bahndrehmoment erlangen, was die Linienform dieser Anregungen beeinflusst.
Für das $5d^5$-System K_2IrCl_6 untersuchen wir den Charakter des Spin-Bahn-Exzitons. Die RIXS-Spektren zeigen eine charakteristische Aufspaltung, die in der Vergangenheit einer statischen Verzerrung der Oktaeder zugeschrieben worden ist. Unsere sorgfältige Analyse mit einem vibronischen Franck-Condon-Modell zeigt jedoch, dass das beobachtete Feature im RIXS-Spektrum als vibronische Anregung mit einem energieaufgelösten Phonon-Seitenband interpretiert werden muss. Die starke Temperaturabhängigkeit der Linienform stützt eine aktuelle theoretische Vorhersage, die über das vereinfachte Franck-Condon-Bild hinausgeht und die Aufspaltung auf einen dynamischen Jahn-Teller-Effekt zurückführt, der durch die Kopplung an E_g-Phononen ausgelöst wird. Der Grundzustand zeigt dabei weiterhin einen ungestörten kubischen $j_{\text{eff}} = 1/2$ Charakter, während das Gitter nur an den angeregten $j_{\text{eff}} = 3/2$ Zustand koppelt. Dies veranschaulicht zwei Aspekte: Ideale $j_{\text{eff}} = 1/2$ Momente mit kubischer Symmetrie können tatsächlich in $5d$-Mott-Isolatoren verwirklicht werden, und darüber hinaus kann direktes RIXS an der L_3-Kante der $5d$-Metallionen tatsächlich vibronische Phonon-Seitenbänder auflösen, die durch einen einzelnen Franck-Condon-Faktor beschrieben werden.

Contents

1 Introduction

Since the rise of quantum mechanics in the last century opened the door to a quantitative description of solid-state physics, scientists have sought to understand, predict, and control a plethora of phenomena of solids. Particularly in crystalline matter, the macroscopic behavior cannot be understood from the properties of the constituent electrons and ions alone. It is the aggregation of the vast number of electrons and ions, their interactions, and the symmetry of the crystal lattice that gives rise to a wide range of emergent phenomena such as magnetism or superconductivity [1, 2]. In a sense, a crystal resembles a pointillist painting, where the whole is more than the sum of its parts. An effective description to account for the dynamical properties of crystalline matter is governed by the notion of quasiparticles and collective excitations [3, 4]. This notion is particularly important when the electronic properties exhibit highly unusual behavior. Notable examples are heavy-fermion compounds, where the dispersion of electrons suggests an increase in their effective mass by up to a factor of a thousand [5], or conversely, topological insulators and graphene, which harbor electronic states in which the electrons behave as relativistic particles [6, 7]. Other flavors of quasiparticles appear even more exotic as they imply a separation of the fundamental properties of the electron. Intriguing examples are the separation of spin and charge in materials with strongly confined one-dimensional magnetic chains [8, 9], or the apparent fractionalization of electronic charge in fractional quantum Hall systems [10, 11].

Early progress in the description of electrons in solids can be attributed to Bloch [12], who provided a quantitative description of the itinerant character of electrons in a crystal. This laid the foundation for band theory, which has been a powerful tool to predict electronic behavior for a wide range of materials. One fundamental result is its capability to distinguish between metals and insulators, based solely on the filling of the electronic states. The impact of band theory can be witnessed every day, given the realization of transistors and their miniaturization, forming them into a cornerstone of modern communication and information technology.
The predictions of band theory fall short whenever the electronic properties are not captured adequately using an effective single-particle picture. A paradigmatic example and the center of this thesis is the case of strongly correlated electron systems. Here, the electronic behavior emerges from a strong competition between itinerancy and Coulomb repulsion. If the energy gain from delocalization exceeds Coulomb repulsion, the electrons remain itinerant and the system exhibits metallic behavior. However, in case Coulomb repulsion is the larger factor, electrons respond via localization on the atomic site. In consequence,

even materials with half filling display insulating behavior in this case. These materials are known as Mott insulators, after the pioneering works of Mott and Peierls [13, 14]. Typically, such behavior is found in transition-metal compounds with partially filled d shells. In the past, the physics of Mott insulators has been explored most intensely in $3d$ systems, particularly oxides [15–19]. The tendency for the Mott-insulating behavior results from the small radial extension of the $3d$ orbitals and their narrow bandwidths, which yield strong Coulomb repulsion and low kinetic energies, respectively.
One consequence of the electronic localization is the preservation of orbital and spin degrees of freedom [20]. Thus, Mott insulators exhibit well-defined local moments. It is the role of virtual electron hopping between neighboring sites that induces spin and orbital correlations and leads to magnetic exchange interactions. It is therefore no surprise that Mott insulators exhibit very often a magnetic ground state at low temperatures [19]. The local properties of the moments are dictated by the electronic configuration d^N of the transition-metal ion and by the local interplay of crystal-field effects, intra-atomic Coulomb interaction, and spin-orbit coupling, as well as hybridization with the ligands. The crystal field reduces the symmetry of the electronic states compared to that of a free ion, which lifts the degeneracy of the states and partially quenches the orbital moment. Intra-atomic Coulomb interaction establishes Hund's rules, which set the spin and orbital occupation in the crystal. The role of spin-orbit interaction is to couple the spin and orbital degrees of freedom, which can lead to distinct magnetic behavior.
For $3d$ electrons, the strength of spin-orbit coupling is usually weak, on the order of tens of meV, and can often be treated perturbatively [19, 21]. In this case, spin-orbit coupling anchors the spin degrees of freedom relative to the orbital degrees and hence to the crystal lattice. This results in magnetic anisotropy, which can give rise to complex magnetic structures. Presumably, the most prominent are non-collinear magnets in crystals without a center of inversion. Notable examples include spin spirals, found for example in type-II multiferroic $TbMnO_3$ [22–24], or skyrmion lattices in compounds such as metallic MnSi or the Mott-insulating cluster magnet Cu_2OSeO_3 [25–28].

For $4d$ and $5d$ transition metals, the balance between Coulomb repulsion and delocalization shifts. The larger radial extent promotes a larger bandwidth and reduces electronic correlations. Under these considerations, especially $5d$ transition-metal compounds are suspected to show metallic behaviour. At the same time, however, the strength of spin-orbit coupling increases from $3d$ to $5d$ elements by roughly an order of magnitude [21], sufficient to locally entangle the spin and orbital degrees of freedom into an effective spin-orbital moment j_{eff}. This induces an additional splitting based on the total angular momentum of the states and renormalizes their bandwidths. As a consequence, such a system can recover a Mott insulating state again, as shown, for example, for Sr_2IrO_4 [29], $Sr_3Ir_2O_7$ [30], or the honeycomb iridate Na_2IrO_3 [31], which has coined the term spin-orbit-assisted Mott insulators for these compounds.
These discoveries have sparked significant interest in further exploring the interplay between strong spin-orbit coupling and electronic correlations. A generic phase diagram

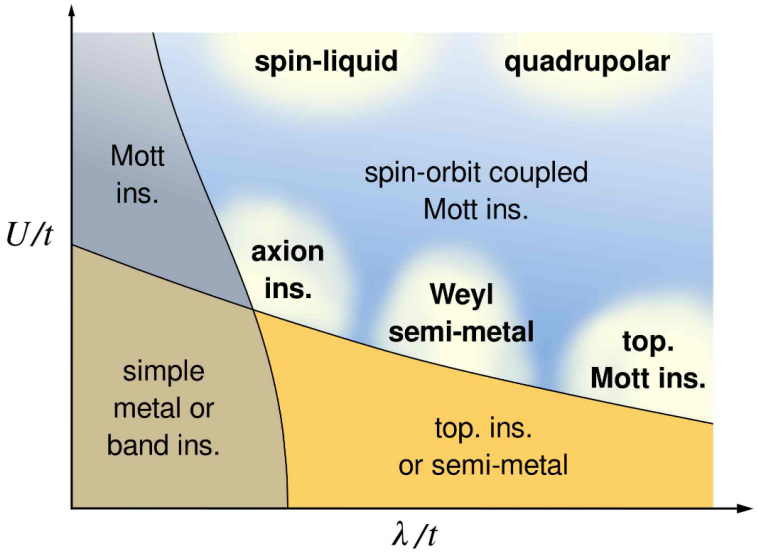

Figure 1.1 Sketch of a phase diagram for electronic ground states comparing the strength of electronic correlations U/t and the relative strength of spin-orbit coupling λ/t. The phase space shaded in blue indicates phases with Mott-insulating behavior. Used with permission of Annual Reviews, Inc., from [32]; permission conveyed through Copyright Clearance Center, Inc..

that emerges from this interplay is shown in Fig. 1.1. Within this thesis, we focus our attention on studying the electronic structure of Mott insulators with both strong electronic correlations and strong spin-orbit coupling.

Spin-orbit entangled $j_{\text{eff}} = 1/2$ moments and the low-energy electronic structure of α-$RuCl_3$

Most attention in the family of spin-orbit coupled Mott insulators has been garnered by d^5 systems, such as materials with Ir^{4+} or Ru^{3+} ions, which yield effective $j_{\text{eff}} = 1/2$ moments. These draw parallels with quantum $S = 1/2$ systems, but where the $j_z = \pm 1/2$ configurations, i.e., the "up" and "down" states, occupy a complex mixture of different orbitals [33], see Fig. 1.2(b). This has attracted considerable interest in studying exchange interactions on different geometries. For example, the layered perovskite Sr_2IrO_4 [34] shows signatures of 2D Heisenberg antiferromagnetism, where the dispersion of magnetic excitations bears a strong resemblance to that in the $S = 1/2$ cuprate La_2CuO_4 [35, 36]. Accordingly, this has sparked interest in finding cuprate-like superconductivity in iridates [37], but this has not been observed. A striking feature of the $j_{\text{eff}} = 1/2$ moments is the possibility to exhibit strong Kitaev exchange [38–40]. This bond-directional Ising-type exchange interaction is highly anisotropic and offers a pathway to explore a quantum spin-liquid state [41, 42]. The original Kitaev model [43] describes Kitaev exchange on a tricoordinated honeycomb lattice and features a quantum spin-liquid ground state. The bond-directional character of

the Kitaev exchange couples only one specific component of the spin operator along one particular bond. Unable to fulfill the exchange for all three spin components simultaneously, this yields strong exchange frustration and restricts spin-spin correlations to nearest neighbors. Intriguingly, the excitation spectrum of the Kitaev model can be solved exactly and reveals fractionalized spin excitations in the form of Majorana fermions and spinless $\mathbb{Z}_2$ gauge fluxes.
Jackeli and Khaliullin proposed a route to realize dominant Kitaev interactions in $j_{\text{eff}} = 1/2$ compounds that show octahedral coordination on a honeycomb lattice with an edge-sharing geometry [38]. The edge-sharing geometry is a key ingredient to suppress Heisenberg exchange for an ideal 90° ligand-metal-ligand bonding angle, assuming that the leading-order contribution to exchange interactions originates from ligand-mediated superexchange. Under these considerations, the $5d^5$ honeycomb iridates Na_2IrO_3 and α-Li_2IrO_3 [44–53], as well as the $4d^5$ ruthenium compound α-$RuCl_3$ [54–62], have entered the spotlight as prime candidates for the realization of a Kitaev quantum spin liquid. The crystal strcucture of α-$RuCl_3$ and the concept of bond-directional Kitaev exchange on the honeycomb layer are shown in Fig. 1.3. Eventually, each of these compounds develops magnetic order below their respective transition temperatures, around 14 K for the iridates and 7 K for α-$RuCl_3$, due to additional exchange paths and deviations from the ideal 90° bonding angle. The magnetic properties of these compounds are typically captured by an extended magnetic model, which includes a combination of Kitaev and Heisenberg exchanges plus additional off-diagonal exchange interactions [63, 64]. Nonetheless, these compounds have shown clear signatures of Kitaev interaction [50, 60, 61, 65–67]. The most compelling result is the observation of a quantized half-integer thermal Hall effect in the magnetically disordered phase of α-$RuCl_3$ found at around 7 T with an applied field perpendicular to the honeycomb planes [68, 69]. This result is considered the strongest experimental indication for the presence of fractionalized Majorana fermions [68–70] and continues to motivate both theorists and experimentalists alike to increase their efforts to explore the properties of α-$RuCl_3$ in the presence of strong magnetic fields and possibly identify a field-induced quantum spin liquid in α-$RuCl_3$ [71–78].

Taking a step back, the formation of the $j_{\text{eff}} = 1/2$ moments from $4d$ and $5d$ orbitals follows from a balance of local energy scales. As mentioned above, these are predominantly crystal-field effects, electron-electron interaction, and spin-orbit coupling. These are reflected by the cubic crystal-field splitting $10Dq$, Hund's coupling J_{H}, and by the strength of the spin-orbit coupling ζ. Alternatively, one can introduce an effective spin-orbit coupling $\lambda = \pm\zeta/2S$ for a given electron configuration [19]. For $4d$ and $5d$ systems, the cubic crystal-field splitting $10Dq$ typically dominates over J_{H} and λ [79]. As such, the ground state of an octahedrally coordinated transition-metal ion will always adopt a low-spin configuration, occupying the t_{2g} orbitals first. The role of spin-orbit coupling is to further lift the degeneracy of the t_{2g} orbitals that show an effective orbital momentum $l_{\text{eff}} = -1$ [80] (hence the subscript, which we will omit onward). As a result, this yields a lower-lying $j = 3/2$ quartet and a $j = 1/2$ doublet. For Ir^{4+} or Ru^{3+} ions with an t_{2g}^5 configuration, this

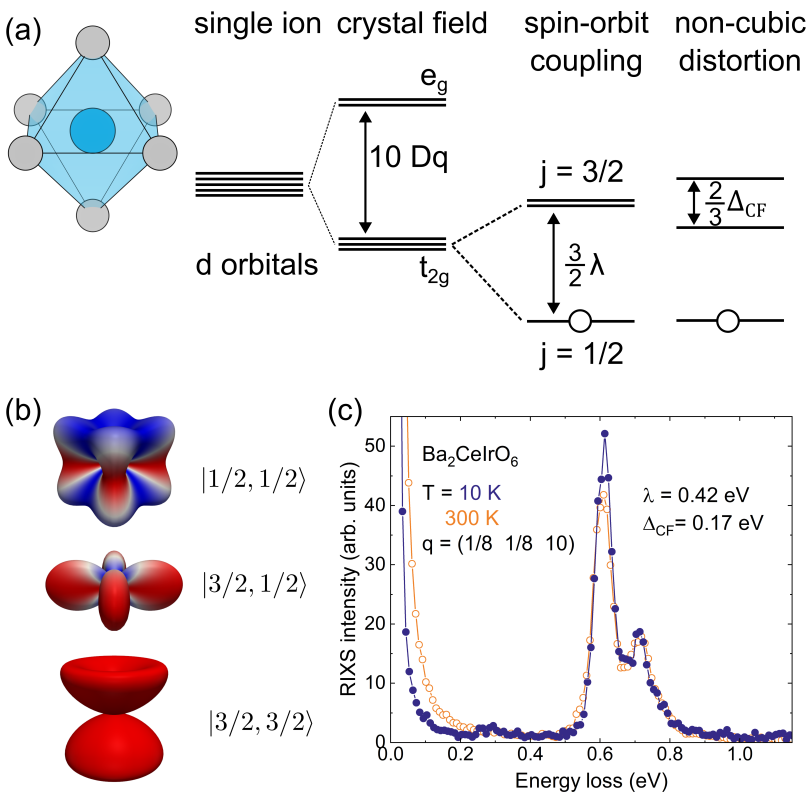

Figure 1.2 Energy-level scheme of local $j_{\text{eff}} = 1/2$ moments in d^5 systems. (a) A transition-metal ion surrounded by an octahedral ligand cage with a d^5 electron configuration serves as the base structural unit to realize a $j = 1/2$ moment. Crystal-field effects and spin-orbit coupling split the fivefold degenerate d orbitals into a $j_{\text{eff}} = 1/2$ doublet and a $j_{\text{eff}} = 3/2$ quartet. The energy levels of the spin-orbital states are shown in the hole picture. The presence of non-cubic distortions further lifts the degeneracy of the $j = 3/2$ quartet and admixes $j = 3/2$ character to the ground state. (b) Density plot of the $|j, j_z\rangle$ states. The color indicates the spin character. Red denotes $S_z = |\uparrow\rangle$, and blue $S_z = |\downarrow\rangle$. (c) Exemplary RIXS spectrum of the Ir^{4+} double perovskite Ba_2CeIrO_6, adopted from [65]. The spectrum shows the spin-orbit exciton at around 0.6 eV and resolves an experimental splitting of around 0.1 eV. From the energy and the splitting of the feature, one can extract the strength of λ and Δ_{CF}.

is equivalent to a single hole occupying the $j = 1/2$ state, see Fig. 1.2(a).
The ideal $j = 1/2$ scenario requires a perfect cubic crystal field. In the presence of non-cubic distortions Δ_{CF}, the ground state acquires a mixed character of the $j = 1/2$ and $j = 3/2$ wavefunctions [38, 65, 81]. A sensitive way to determine the ground state is to probe its excitations. Similar to playing a musical instrument, we gain valuable knowledge about a system by observing its resonances and transitions. For the $j = 1/2$ ground state, the most direct way is to measure the splitting of the spin-orbit exciton, i.e., the on-site excitation $|j = 1/2\rangle \rightarrow |j = 3/2\rangle$ at energy $\frac{3}{2}\lambda$. Non-cubic distortions lift the degeneracy

of the $j = 3/2$ quartet, which manifests as a splitting of this excitation feature, see Fig. 1.2(a). For iridates with $\lambda \approx 0.4\,\mathrm{eV}$, resonant inelastic x-ray scattering (RIXS) at the Ir L_3-edge has proven instrumental in studying the local electronic structure and resolving such splittings. Targeting the x-ray absorption edges of the transition-metal ions, RIXS boosts specifically the scattering cross section of electronic transitions of that ion, turning it into a highly sensitive probe for the electronic sturcture. An example of the splitting of the spin-orbit exciton is shown for the $j = 1/2$ compound Ba_2CeIrO_6 in Fig. 1.2(c).
For the honeycomb iridates Na_2IrO_3 and α-Li_2IrO_3, a ratio of $\lambda/\Delta_{CF} \approx 3$ has been found [49], but interestingly, experimental results on the local electronic structure of α-$RuCl_3$ have been discussed controversially in this regard. This follows from the rich excitation spectrum of α-$RuCl_3$ below the Mott gap at around 1 eV and is based on different assignments and interpretations of the excitation features observed by Raman scattering, RIXS, infrared spectroscopy, and neutron scattering [54, 60, 82, 83]. As a result, λ and Δ_{CF} have not been determined unequivocally. For instance, the broad features observed at around 0.53 and 0.75 eV by infrared spectroscopy have been interpreted as crystal-field excitations $|t_{2g}^5\rangle \rightarrow |t_{2g}^4 e_g\rangle$ [82, 84], which in turn challenge the applicability of the $j = 1/2$ scenario that requires $10Dq \gg \lambda$. This sets the stage for the first study of this thesis, which examines the low-energy electronic excitation spectrum of α-$RuCl_3$ using a combination of optical spectroscopy and Raman scattering. The combination of both methods is pivotal for tackling this problem. Raman scattering and optical spectroscopy obey different selection rules and therefore probe electronic excitations via different mechanisms. In Raman scattering as well as RIXS, onsite *dd* excitations, i.e., local excitations within the *d* shell, are directly allowed. In contrast, optical spectroscopy can detect such excitations only if inversion symmetry is broken, for instance via the simultaneous excitation of an odd-parity phonon [85]. By comparing the excitation energies between Raman scattering and optical spectroscopy and by analyzing the temperature dependence of the spectral weight, we identify the phonon-assisted character and thus determine the energy of the spin-orbit exciton at 248 and 290 meV. This yields the effective parameters of $\lambda_{\mathrm{eff}} = 0.18\,\mathrm{eV}$ and $\Delta_{CF} = 0.05 - 0.07\,\mathrm{eV}$ and a ratio of $\lambda_{\mathrm{eff}}/\Delta_{CF} \approx 3$, translating into a ground state with approximately 98% $j = 1/2$ character. Coincidentally, the ratio is similar to the values found for the honeycomb iridates where both λ_{eff} and Δ_{CF} are more than a factor of 2 larger [49]. Furthermore, we employ the same approach to identify the two other prominent features at 0.53 and 0.75 eV in the optical data as double and triple spin-orbit excitons. These multiple spin-orbit excitons result from the exchange of holes between adjacent Ru sites and can be viewed as pairwise intersite excitations, as also observed in YVO_3 [86] or in the $5d$ antifluorite halides studied in this thesis. Remarkable for α-$RuCl_3$ is the comparable strength between the single, double, and triple spin-orbit excitons. This is a consequence of the same hopping mechanism that promotes Kitaev interaction and suppresses Heisenberg exchange in this compound. In this sense, the large spectral weight of the multiple spin-orbit excitons reflects the relevance of the prominent Kitaev exchange in α-$RuCl_3$.

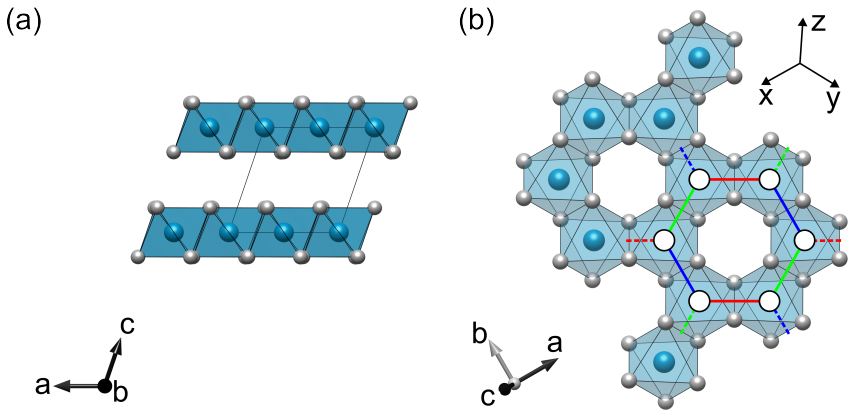

Figure 1.3 Crystal structure of α-$RuCl_3$. (a) View along the *ac* plane showing the layered structure of the crystal. Ru ions are shown in blue, Cl ions in gray. (b) View on the *ab* plane showing the formation of the honeycomb lattice with edge-sharing geometry. The main idea of Kitaev exchange in α-$RuCl_3$ is shown as an overlay. The colored bonds indicate which spin component couples along which direction. Choosing a local frame of reference, the corresponding spin component is selected by the bond that lies perpendicular to the edge-sharing plane. For instance, S_x components couple along blue bonds, S_y along green bonds, and S_z components along red bonds. The structural data to create the figure are taken from [59].

The effect of strong spin-orbit coupling on the electronic configuration d^N and their realizations in the antifluorite halides A_2MX_6

As motivated by, e.g., Takayama *et al.* [33], the effect of strong spin-orbit coupling can take different forms depending on the electronic configuration d^N. Apart from anisotropic exchange between $j = 1/2$ moments, unusual magnetism is also predicted for seemingly non-magnetic d^4 systems with $J = 0$, where strong dispersion can manifest a condensation of $J = 1$ triplons, which is labeled excitonic magnetism [87]. The case of d^3 acts as an outlier. At first glance, the half-filled t_{2g}^3 manifold shows a fully quenched orbital moment $L = 0$, which suppresses the effect of spin-orbit coupling in the ground state. But, for very strong spin-orbit coupling stabilizing the complex-valued $|j, j_z\rangle$ basis, a d^3 system is predicted to develop a spin-orbit-induced Jahn-Teller distortion, as suggested by Streltsov and Khomskii [88]. The spin-orbit entangled moments of crystals with d^1 and d^2 configurations cannot be described by dipoles. Instead, these states exhibit quadrupolar or octupolar moments. The interaction of these moments can form ordered states with hidden order parameters [89, 90].
Within this thesis, we study the $5d^3$, $5d^4$, and $5d^5$. For this purpose, we choose a platform to realize different d^N within the same structural framework. We find K_2PtCl_6-type antifluorite halides A_2MX_6 as a well-suited model system for this endeavor.
Typically, A is an alkali ion or monovalent molecule, such as K^+, Rb^+, or NH_4^+, X is a

halide ion, usually Cl^-, Br^-, or I^-, and M is the tetravalent transition-metal ion yielding the respective configuration $5d^N$, e.g., Re^{4+} for $5d^3$, Os^{4+} for $5d^4$, and Ir^{4+} for $5d^5$. The main structural motif of these halide systems is the fcc arrangement of well-isolated MX_6 octahedra without nearest-neighbor bonds, see Fig. 1.4(a). This family of materials is closely related to the double perovskites $A_2BB'O_6$, which also provide a versatile platform to realize various scenarios of (mixed) d^N configurations on an fcc lattice [91]. Their central structural theme is the alternating arrangement of corner-sharing BO_6 and $B'O_6$ octahedra. In comparison to that, the antifluorites exhibit an empty B site, labeling them as vacancy-ordered double perovskites. Within this thesis, we study K_2ReCl_6, K_2OsX_6 with $X = \{Cl, Br\}$, Rb_2OsBr_6, and K_2IrCl_6 as cases for $5d^5$, $5d^4$, and $5d^5$, respectively.

Many $5d$ antifluorite halides were studied actively from the late 1950s through the 1980s [92]. These compounds served as early model systems for materials with magnetic $5d$ ions, allowing a systematic investigation of their paramagnetic properties and the interactions on the fcc lattice in the ordered phases [93–96]. At the same time, structural studies highlighted the role of the rotational modes of the octahedra to drive structural phase transitions in these compounds [97–100]. As such, many members of the A_2MX_6 family can exhibit a common series of up to three structural phase transitions [101–103]. At room temperature, most of these compounds show cubic symmetry and crystallize in the cubic space group $Fm\bar{3}m$. The symmetry of these compounds can change consecutively from cubic to tetragonal ($P4/mnc$) to monoclinic ($C2/c$) and again to monoclinic ($P2_1/n$). Often, the monoclinic angle is close to 90° [102–105], and non-cubic effects are expected to be small.

With the current interest in correlated electron systems with strong spin-orbit coupling, these compounds have resurfaced recently. Among others, newer works include the reinvestigation of $5d^5$ A_2IrX_6 in view of the electronic and magnetic properties of the spin-orbit entangled $j = 1/2$ moments [102, 106–110], but also studies on the pronounced ferroelastic coupling in K_2ReCl_6 [105] and the violation of polarization selection rules of the phonon modes induced by octahedral rotations observed by Raman scattering [111]. The role of multipolar moments has been investigated for $5d^1$ and $5d^2$ antifluorites [112–117], but especially more experimental studies of tungsten-based $5d^2$ antifluorites are needed.

The antifluorite halides exhibit several properties that facilitate probing their local electronic structure. First, the combination of isolated MX_6 units and large nearest-neighbor distances results in very narrow bandwidths of the $5d$ states, which shifts the Mott gap considerably higher than in most other $5d$ Mott insulators. For example, many of the d^5 iridates show a Mott gap of less than 0.7 eV [21, 29, 31, 65, 118, 119], but in K_2IrCl_6 the Mott gap lies above 1.5 eV. For L-edge RIXS with its strong sensitivity for local excitations, this is not an issue. But for optical spectroscopy, the spin-orbit exciton is located around 0.6 eV and therefore overshadowed by excitations across the Mott gap. The larger gap in K_2IrCl_6 solves this problem. A second beneficial point of the isolated octahedra is the narrow lineshape of the onsite excitations. This yields a clear separation between excitation peaks and allows for a precise determination of the energies. In particular, the high resolution of optical spectroscopy can reveal small splittings and features that are typically

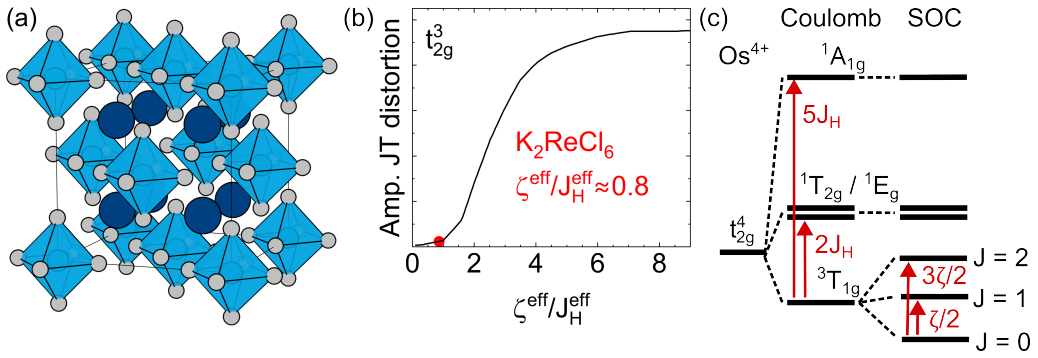

Figure 1.4 (a) Crystal structure of the A_2MX_6 antifluorite halides. The isolated MX_6 octahedra form an fcc lattice (blue octahedra and grey spheres). The alkali ions A are shown as dark spheres. (b) Evolution of the spin-orbit-induced Jahn-Teller distortion for the t_{2g}^3 configuration. The red dot marks the result of our analysis on K_2ReCl_6. (c) Energy-level diagram of the t_{2g}^4 multiplets in LS coupling when we choose $M = Os^{4+}$.

smeared out in other compounds. The third advantage is the negligible dispersion of the excited states. This is particularly useful when comparing spectra taken with RIXS and optics. The typical photon energies for the L_3 edges of the $5d$ ions lie at around 10 keV [120]. This is sufficient to probe the dispersion of excited states with RIXS across the entire Brillouin zone. Optical spectroscopy, however, is usually restricted to excitations around the Γ point due to the comparatively small wave vectors of infrared and visible light. The phonon-assisted character and the emergence of phonon sidebands might redistribute the wave vector among the excited particles, but the lack of a sizable dispersion facilitates the comparison of excitation energies.
Employing both, optical spectroscopy and RIXS enables us to exploit the unique strengths and sensitivities of each method, which are pointed out further when discussing the projects individually.

As a $5d^5$ compound, K_2IrCl_6 forms the bridge between the first study of this thesis on $4d^5$ α-$RuCl_3$ and the other antifluorite halides. From a magnetic perspective, $j = 1/2$ moments on an fcc lattice offer the opportunity to study the interplay of geometric frustration and Kitaev exchange [39, 121]. Nearest-neighbor antiferromagnetic Heisenberg exchange on the fcc lattice yields a three-dimensional version of the geometrical frustration on the triangular lattice [122], which had been proposed by Anderson as a model platform to realize a quantum spin liquid in 2D [123]. In the case of the fcc lattice, Kitaev exchange actually reduces the degree of frustration, but next-nearest-neighbor Heisenberg exchange counteracts this, opening the window for a spin-liquid phase [65]. The first experimental candidates for this scenario have been Ir^{4+} A_2BIrO_6 double perovskites [65, 124, 125] and the A_2IrX_6 antifluorites [102, 106–108]. At low temperatures, these compounds do develop antiferromagnetic order, e.g., Ba_2CeIrO_6 below $T_N = 14$ K and K_2IrCl_6 below $T_N = 3$ K,

but the analysis of the magnetic susceptibility reveals a large degree of frustration $f \approx 10$ in these systems [65, 106]. A recent neutron scattering study of K_2IrCl_6 reports on a novel type of magnetic ground state, labeled a nodal spin liquid [110]. This type of ground state follows from the interplay of nearest-neighbor Heisenberg exchange and Kitaev exchange, together with a strong disposition towards fluctuations in this compound due to the weak strengths of the interaction terms.

The cubic symmetry paired with strong frustration turns the double perovskites and antifluorite halides into interesting testing grounds for the robustness of the $j = 1/2$ scenario. As already mentioned, non-cubic distortions yield a mixed ground-state character, but such distortions are, strictly speaking, not expected for cubic symmetry. Nonetheless, all d^5 iridate compounds studied with RIXS thus far have shown signatures of non-cubic distortions, irrespective of their symmetry [35, 65, 102, 107, 126–136]. As seen in Fig. 1.2(c), RIXS at the L_3 edge finds $\Delta_{CF} = 0.17\,\text{eV}$ for the globally cubic double perovskite Ba_2CeIrO_6[65]. A scenario based on magnetoelastic coupling yields an explanation for this seeming contradiction. In order to lift the degree of frustration in this compound, the lattice can develop local distortions with very short correlation lengths that do not extend across the lattice. X-ray diffraction measurements, however, cannot rule out a few percent of antisite defects between the alternatingly arranged IrO_6 and CeO_6 octahedra that can break local symmetries and evoke non-cubic distortions as well.

As mentioned above, the vacancy of the B site in K_2IrX_6 (X = Cl, Br) eliminates this type of defect, but it also renders the IrX_6 octahedra susceptible to rotational instabilities, which can induce phase transition. The compound K_2IrBr_6 undergoes two phase transitions, first to tetragonal and then to monoclinic symmetry below 170 K and 133 K, respectively [102]. But thanks to the almost ideal tolerance factor and the stronger ionicity of the Cl^- ion compared to the Br^- ion, K_2IrCl_6 remains cubic even below liquid helium temperatures [101, 103, 106, 107]. RIXS and Raman studies on the spin-orbit exciton, however, show a very similar picture for both compounds, reporting a splitting of $\Delta_{exp} \approx 0.04\,\text{eV}$ for K_2IrBr_6 and 0.05 eV for K_2IrCl_6 [102, 107, 109]. This contrasts the cubic $j = 1/2$ picture and casts doubt over a scenario in which the splitting is caused primarily by static distortions, especially for the cubic K_2IrCl_6. A recent theoretical study attributes the apparent splitting of the spin-orbit exciton in K_2IrCl_6 to a dynamic Jahn-Teller effect [137]. In the static case, the Jahn-Teller effect describes the distortion of the crystal to lift degeneracies for a net gain of energy. Since the $j = 1/2$ ground state shows no orbital degeneracy, it is not Jahn-Teller active [88]. Electron-phonon coupling between the t_{2g} electrons and E_g phonon modes can, however, hybridize the $j = 3/2$ state with E_g phonon modes, which manifests as a level splitting in the excited $j = 3/2$ state, i.e., the dynamic Jahn-Teller effect [137, 138]. This implies the entanglement of spin, orbital, and lattice degrees of freedom and calls for further experiments to unveil this exotic character.

The observation of vibronic excitations, i.e., excitations with a vibrational and electronic character, via L-edge RIXS is non-trivial, and the splitting of the spin-orbit exciton alone can not discriminate between a statically distorted scenario and a dynamic Jahn-Teller effect. But it is the combined approach of optical spectroscopy and RIXS that solves this

problem.
The large Mott gap in K_2IrCl_6 allows us to probe the spin-orbit exciton with optics in isolation, similarly as in α-$RuCl_3$. However, for K_2IrCl_6, the lineshape is more complex, as the phonon-assisted character is governed by three odd-parity phonons with similar strengths. The vibronic character of the spin-orbit exciton can be identified in optics from the pattern of phonon sidebands that accompany the phonon-assisted electronic excitation as a result of the Franck-Condon principle [85]. The lineshape and the intensity distribution of the sidebands are characterized by the Franck-Condon factors, which evaluate the overlap between the vibrational wavefunctions in the electronic ground state and excited state. In fact, any onsite *dd* excitation is expected to show such sidebands with optics, but practically these are smeared out in crystals with a more rigid structure. The presence of pronounced vibronic sidebands has been demonstrated on IrX_6 impurities in host crystals [139–141], but also in single crystals of other members of the antifluorite family, e.g., K_2ReCl_6 and K_2OsCl_6 in literature [142–145] as well as in this thesis. Note that the spin-orbit exciton in α-$RuCl_3$ also reveals a vibronic pattern, however, way less pronounced.
A comparison with the multiplet of $\Gamma_7(^2T_2)$ character, which is insensitive to non-cubic distortion, of $5d^3$ K_2ReCl_6, we identify that the spin-orbit exciton can be described *without* the need of a static distortion. A crucial indication of considerable electron-phonon coupling is the temperature dependence of the lineshape. The Γ_7 multiplet of K_2ReCl_6 has no orbital degree of freedom and thus shows a negligible coupling to the lattice. The temperature dependence of the excitation reflects mainly the thermal population of the symmetry-breaking phonon modes. In contrast, the lineshape of the spin-orbit exciton is much more sensitive to the temperature and broadens significantly. This makes the evaluation of the three Franck-Condon factors from the three odd-parity phonon modes in optics challenging. However, in RIXS we apply the same vibronic model and find excellent agreement with the data using a single Franck-Condon factor. The temperature dependence shows a significant increase in the energy of the sideband and of the Huang-Rhys factor. Both effects can be reconciled with a scenario of coupling to the E_g phonons and the role of electron-phonon coupling going beyond the simple Franck-Condon picture. The observation of vibronic excitations with RIXS at the L_3 edge is striking. Typically, L-edge RIXS on iridates is insensitive to phonon excitations. Previous RIXS studies of vibronic excitations discuss indirect contributions that have to be described using two Franck-Condon factors, one for the initial absorption process and a second one for the emission process [146–149]. Describing the lineshape with a single Franck-Condon factor, we can understand that electron-phonon coupling has to be applied only to the final state, which is exactly the case of the dynamic Jahn-Teller effect in K_2IrCl_6.
In addition, our data show vibronic sidebands also for the double spin-orbit exciton, highlighting the quasimolecular character of the A_2MX_6 halides. Compared to α-$RuCl_3$, this excitation is significantly weaker but directly infrared-active, suggesting that fluctuations of octahedral rotations might break inversion symmetry on the bond between two sites.

The interest in d^4 systems arises, among others, from the exotic nature of excitonic mag-

netism. In its ground state, the t_{2g}^4 configuration yields a non-magnetic $J = 0$ singlet on a single site, which exhibits Van Vleck paramagnetism. In the presence of strong intersite interactions, the local excitation into the $J = 1$ state can acquire significant dispersion. If this interaction is comparable to or exceeds the energy gap set by spin-orbit coupling, a magnetic ground state can form through the condensation of excited $J = 1$ triplons [87]. A characteristic feature to identify this type of magnetic response is the dispersion of longitudinal magnetic modes, which resembles the amplitude mode (Higgs mode) of superconductors [33].

Mott-insulating $4d^4$ ruthenates are considered suitable model candidates. An inelastic neutron scattering experiment on orthorhombic Ca_2RuO_4 reports a longitudinal magnetic mode with the predicted dispersion [150]. However, these findings remain subject to debate, with alternative interpretations based on an anisotropic $S = 1$ ground state with strong exchange interaction [151, 152]. The key parameter determining the ground state is the ratio Δ_{CF}/ζ. For example, the cubic system K_2RuCl_6, with $\Delta_{CF} \approx 0$, yields a $J = 0$ ground state [153], whereas the distorted and orbitally ordered dimer compound $La_4Ru_2O_{10}$ shows $S = 1$ [154]. The analysis of the energy and spectral weight of Mott-Hubbard excitations in Ca_2RuO_4 yields $2.4 \leq \Delta_{CF}/\zeta \leq 4$ [155], pointing to a regime where both parameters must be treated on equal footing.

For $5d$ compounds, the stronger spin-orbit coupling can stabilize the $J = 0$ scenario [156], but interaction effects are typically considered too weak to induce the condensation of $J = 1$ triplons [157]. In $5d^4$ Ir^{5+} double perovskites, RIXS experiments have established the $J = 0$ ground state character [158–162]. The magnetism of these compounds, however, has been the subject of a controversial debate. Especially the magnetically ordered compound Ba_2YIrO_6 has been claimed to exhibit unconventional magnetism [163, 164], but further studies have suggested extrinsic effects, such as non-stoichiometric Ir^{4+} and Ir^{6+} impurities in these compounds [165–167]. Similar concern of magnetic impurities has also appeared in other $5d^4$ double perovskites [162]. Apart from iridates, compounds based on $5d^4$ Os^{4+} ions have also been investigated. The pyrochlores $Y_2Os_2O_7$ and $Ho_2Os_2O_7$ are candidate $J = 0$ systems [168–170], but the $J = 0$ ground state is more fragile due to trigonal distortions in these materials. The magnetic properties of $Y_2Os_2O_7$ are also affected by non-stoichiometric defects, and $Ho_2Os_2O_7$ develops magnetic order below $T = 36\,\mathrm{K}$ given the presence of $4f$ moments of the Ho^{3+} ion. These results illustrate that a well-characterized $5d^4$ reference compound that displays a clean $J = 0$ ground state is needed. This motivates the study of the antifluorite-type halides A_2OsX_6, which is presented in this thesis.

Magnetic susceptibility measurements confirm a robust $J = 0$ ground state. Utilizing the advantages of RIXS and optical spectroscopy allows for a comprehensive investigation of the rich excitation spectrum of the $5d^4$ configuration. RIXS at the Os L_3 edge reveals intra-t_{2g} and t_{2g}-to-e_g excitations, as well as charge-transfer excitations, which promote an electron from the ligand to the transition-metal site. Making use of the resonant enhancement of the RIXS process, we can clearly distinguish the intra-t_{2g} from the t_{2g}-to-e_g excitations by tuning the incident energy. This allows us to assign the character of the *dd*

excitations over a wide energy range. Using optical spectroscopy, we observe the intra-t_{2g} excitations via the phonon-assisted mechanism as well. The sensitivity of intersite processes shows Mott-Hubbard and charge-transfer excitations, and additionally, weak overtones and multiples of the intra-t_{2g} transitions (analogous to the double spin-orbit excitons in t_{2g}^5). We also observe a nearest-neighbor charge exciton located below the onset of the Mott gap. The transitions to the e_g shell are undetectable by optics due to the overlap with Mott-Hubbard excitations. Besides the richness of excitation features displayed by the combination of both methods, we can also make use of the high energy resolution of less than 1 meV of the optical experiments compared to the resolution $\delta E = 0.06\,\text{eV}$ for RIXS at the Os L_3 edge to calibrate the energy loss of the RIXS spectra to further enhance experimental accuracy. Additionally, our optical data reveal a splitting of the excitation to the $J = 1$ state below the cubic to tetragonal phase transition of K_2OsCl_6 below 45 K [99] of as little as $\Delta_{\text{exp}} \approx 4\,\text{meV}$ at 5 K.

Under these circumstances, we can determine the local parameters $10Dq$, J_{H}, and ζ from the excitation energies with great accuracy via numerical cluster calculations using Quanty [171]. In particular, we can compare two scenarios using either the full d shell or the often chosen t_{2g}-only Kanamori model, which neglects the presence of the e_g states entirely. An energy-level diagram of the latter is shown in Fig. 1.4(c). In consequence, this yields two different sets of parameters. For K_2OsCl_6, we find $10Dq = 3.27\,\text{eV}$, $J_{\text{H}} = 0.43\,\text{eV}$, and $\zeta = 0.34\,\text{eV}$ for the full d shell, and $J_{\text{H}}^{\text{eff}} = 0.28\,\text{eV}$ and $\zeta^{\text{eff}} = 0.41\,\text{eV}$ for the Kanamori t_{2g} model. This is particularly striking because the ratio between Hund's coupling and spin-orbit coupling changes from $J_{\text{H}}/\zeta \approx 1.3$ to $J_{\text{H}}^{\text{eff}}/\zeta^{\text{eff}} \approx 0.7$, suggesting a different hierarchy of the energy scales. Neither of the values is more significant or more accurate. Instead, these results show that values extracted from the experiment reflect the choice of the underlying model.

The effect of the ligand on the electronic structure is illustrated by the shift of the excitation energies comparing the chlorine and bromine compounds. The largest differences include the lowering of the charge-transfer peaks from $\Delta_{\text{CT}}^{\text{Cl}} = 4.6\,\text{eV}$ to roughly $\Delta_{\text{CT}}^{\text{Br}} = 4.0\,\text{eV}$, as well as a reduction of the cubic crystal-field splitting from $10Dq^{\text{Cl}} = 3.27\,\text{eV}$ to $10Dq^{\text{Br}} = 2.9\,\text{eV}$. The onset of the Mott gap lowers from $\Delta^{\text{Cl}} = 2.2\,\text{eV}$ to $\Delta^{\text{Br}} = 1.8\,\text{eV}$. These effects are a result of the different ionic sizes of Cl and Br, but also the stronger covalent character of the Os-Br binding, which induces a larger admixture of the Br $4p$ character compared to the Cl $3p$ case. As a consequence, this also renormalizes the values for $J_{\text{H}}^{\text{Br}} = 0.42\,\text{eV}$ and $\zeta^{\text{Br}} = 0.33\,\text{eV}$ for the full d shell. A brief comparison between K_2OsBr_6 and Rb_2OsBr_6 with room temperature RIXS shows no significant influence of the alkali ion on the electronic parameters.

The case of d^3 offers an interesting perspective on the effects of spin-orbit coupling. In the LS coupling regime, the ground state exhibits $S = 3/2$ with a fully quenched orbital moment. As a result, spin-orbit coupling can be neglected for the description of the ground state. This changes in the jj-coupling regime: placing three electrons in the $j = 3/2$ quartet renders the configuration Jahn-Teller active, contrary to the behavior of other t_{2g}^n configu-

rations. Typically Jahn-Teller distortions are reduced for t_{2g}^1 and become fully suppressed for t_{2g}^2, t_{2g}^4, and t_{2g}^5 by spin-orbit coupling above a certain threshold λ_c [88].
The key aspect governing the Jahn-Teller activity in the d^3 configuration is the orbital occupation. Hund's coupling favors an equal occupation of the real-valued cubic t_{2g} orbitals $|xy\rangle$, $|yz\rangle$, and $|zx\rangle$. The spherical symmetry of the t_{2g}^3 manifold renders this configuration insensitive to non-cubic distortions. Spin-orbit coupling favors occupation in the j basis, which consists of a complex linear combination of these cubic orbitals. The relevant energy scale is the ratio ζ/J_H. For $\zeta^\mathrm{eff}/J_\mathrm{H}^\mathrm{eff} \geq 9$, the electronic states of the d^3 configuration are stabilized within the $|j, j_z\rangle$ basis, resulting in a fully developed Jahn-Teller distortion [88]. However, such a large ratio is not realized for any stable transition-metal ion. The closest candidates are $5d^3$ systems, in which ζ and J_H are of comparable size. In this intermediate regime, Streltsov and Khomskii [88] have proposed a crossover between the orbitally quenched LS limit and the Jahn-Teller-distorted jj scenario, see Fig. 1.4(b). In particular, the antifluorite compound K_2ReCl_6 has been suggested as a sensitive candidate to observe signatures of this behavior [88] given the three structural phase transitions at 111, 103, and 76 K [105]. Following the approach taken for the $5d^4$ osmates, we investigate K_2ReCl_6 using RIXS and optical spectroscopy to extract local energy scales from the electronic excitation spectra. Given the case of the half-filled t_{2g} shell, all intra-t_{2g}^3 transitions are characterized by a transition from $S = 3/2$ to $S = 1/2$, i.e., they carry a spin flip. Hence, these transitions are not only parity forbidden in optics but also forbidden by the spin-selection rules. This yields even weaker excitations than, e.g., the d^5 spin-orbit exciton (comparing the peak values of the real part of the optical conductivity $\sigma_1(\omega)$ for the spin-orbit exciton in K_2IrCl_6 and the intra-t_{2g} transitions in K_2ReCl_6, the latter are an order of magnitude lower), but it also yields very narrow linewidths. As such, we can resolve vibronic features more easily, which we use to corroborate the vibronic scenario in K_2IrCl_6, and we can trace the temperature dependence of the excitation energies very carefully. Our results do not reveal a resolvable splitting due to a Jahn-Teller distortion, but we find broader peaks for the multiplets that show a non-vanishing orbital component and that couple stronger to the lattice. In addition, we find an increase of the excitation energies of the individual and pairwise intra-t_{2g} excitations in the monoclinic phases, which we attribute to the lowering of the ground state energy by up to 3 meV at 18 K.
Similar to the case of the osmates, we determine the electronic parameters by comparing the full d shell and the t_{2g}-only Kanamori model and find $10Dq = 3.25$ eV, $J_\mathrm{H} = 0.46$ eV, and $\zeta = 0.29$ eV for the full d shell, and $J_\mathrm{H}^\mathrm{eff} = 0.34$ eV and $\zeta^\mathrm{eff} = 0.28$ eV for the t_{2g} only case. The opposite trend that ζ^eff is lower than ζ in the d^3 compared to the case of d^4 reflects that the admixture of e_g character opens the door for a stronger effect of ζ or d^3. The comparison of the parameters shows that K_2ReCl_6 yields $\zeta^\mathrm{eff}/J_\mathrm{H}^\mathrm{eff} \approx 0.8$, which is too small for the formation of a spin-orbit induced Jahn-Teller effect, see Fig. 1.4(b). A careful analysis from these parameters reveals that the weight of the $S = 3/2$ state takes 97% of the ground state in the t_{2g}-only model, which is slightly lowered to 93% when we include e_g orbitals. Our calculations of the ground state properties find that sizeable effects

of spin-orbit coupling set in above $\zeta^{\text{eff}}/J_{\text{H}}^{\text{eff}} > 2$, in agreement with a recent DFT study that finds a Jahn-Teller distortion only when ζ is more than doubled by its original value for K_2ReX_6 compounds [172].

1.1 Structure of the thesis

The questions and challenges outlined above have led to four publications, which are presented in this thesis in chronological order of their appearance. In chapter 4, we present the analysis of the spin-orbit exciton and low-energy electronic structure of α-$RuCl_3$. Chapter 5 discusses the characterization of the $5d^4$ Os-based antifluorites A_2OsX_6. The case of $5d^3$ K_2ReCl_6 with respect to the LS and jj coupling scenarios is shown in chapter 6. And finally, chapter 7 presents the study of the spin-orbit exciton in K_2IrCl_6, highlighting the importance of spin orbital lattice entanglement in this compound.
A central theme throughout this thesis is the analysis of excitation spectra in order to understand the local electronic structure. To provide the necessary background, basic aspects of Mott insulators and the single-site Hamiltonian are recalled in chapter 2. As pointed out repeatedly, the main experimental effort of this work is the combined use of optical spectroscopy and RIXS. For optical spectroscopy, we employ particularly Fourier-transform infrared spectroscopy (FTIR) in transmission geometry for the excitations below the Mott gap and complement it for the antifluorites by ellipsometry at higher energies. The basic principles of both techniques, as well as RIXS, are discussed in chapter 3. The conclusion and summary of the results are presented in chapter 8.

2 Orbital occupation in the d shell

At the heart of this thesis, we are curious how spin-orbit coupling affects the occupation of d orbitals and its consequences on the properties of the compounds presented in the introduction. Given the localized nature of the electronic states in Mott insulators, we predominantly focus on the onsite properties that lift the orbital degeneracies within a single site. For a great part, these can be approximated by considering the local Hamiltonian of a single transition-metal ion M surrounded by charged ligands X that form the MX_6 octahedron [173]. In the following chapter, we briefly discuss the single-site model and its main terms, including the crystal field, electron-electron Coulomb interaction, and spin-orbit coupling. This lays out the groundwork to interpret and understand the excitation spectra of the studied compounds.
We also include a brief discussion of intersite excitations and exchange interactions. We discuss electron-hole excitations across the Mott gap that carry large dipole moments but also very weak multiples and overtones of the onsite intra-t_{2g} excitations. For the considerably large strength of the double- and triple spin-orbit exciton in α-$RuCl_3$, we recapitulate the main idea behind the Jackeli-Khaliullin mechanism that describes the relevant hopping paths between edge-sharing octahedra on a honeycomb lattice.

2.1 The Hubbard model

The Hubbard model serves as an effective model to capture the competition between electron delocalization and Coulomb repulsion of a Mott insulator. In its simplest case for a system with a single orbital per site, the Mott-Hubbard Hamiltonian is expressed using electron creation and annihilation operators $a^\dagger_{i,\sigma}$, $a_{i,\sigma}$ and the number operator $n_{i,\sigma} = a^\dagger_{i,\sigma} a_{i,\sigma}$ [16], reading as

$$H_{MH} = \sum_{i,j} -t_{ij} \left(a^\dagger_{i,\sigma} a_{j,\sigma} \right) + U \sum_i n_{i,\uparrow} n_{i,\downarrow}. \tag{2.1}$$

The first term denotes the energy gain via delocalization, characterized by the hopping of an electron from site i to site j, set by the overlap integral t_{ij} between the orbitals on both sites. The second term associates double occupancy on a single site with the energy cost U. The fundamental properties of this model are set by the balance between U and t [16, 19]. For half-filling, the scenario of a Mott insulator is reflected by the case $U \gg t$, when double occupancy becomes unfavorable and a ground state of localized electrons forms. An illustrative way to depict the insulating character is to use a band-like picture, splitting

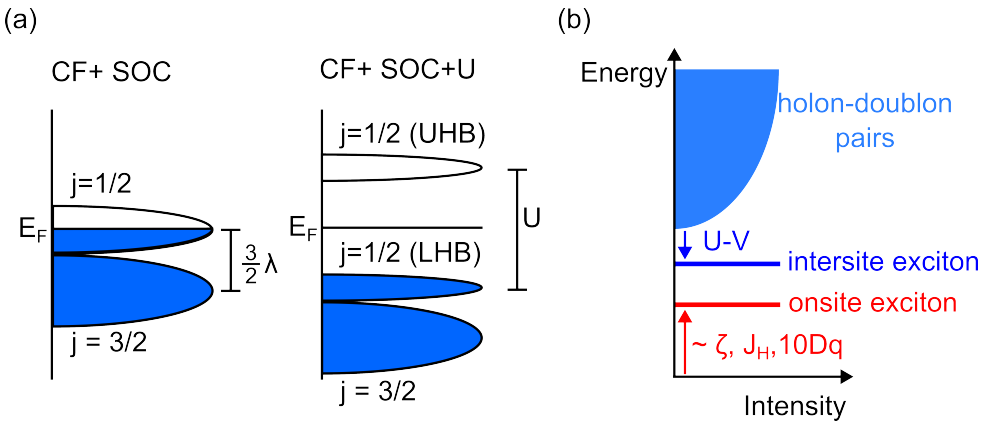

Figure 2.1 Depiction of the level splitting in a Mott insulator. (a) For a metallic spin-orbit coupled $j = 1/2$ system, the valence states exhibit a completely filled $j = 3/2$ shell and a half-filled $j = 1/2$ shell. Strong Coulomb interaction U turns this system into a Mott insulator with a completely "filled" $j = 1/2$ lower Hubbard band and a completely "empty" $j = 1/2$ upper Hubbard band. Note that the band picture fails in Mott insulators and that the sketch has to be interpreted rather as the (inverse) photoemission spectrum. (b) Excitation spectrum of a Mott insulator depicting the onset of excitations across the Mott gap. In addition, it shows the conceptual difference of the excitation energies between intersite and onsite excitons. Note that onsite excitons are not limited to energies below the Mott gap. Onsite excitations lying within the continuum of electron-hole pairs usually decay rapidly or hybridize with the continuum, showing broadened excitation peaks.

the valence states into an "occupied" lower Hubbard band (LHB) and an "unoccupied" upper Hubbard band (UHB). An example is shown for a spin-orbit-assisted Mott insulator, like Sr_2IrO_4, see Fig. 2.1(a). Note, however, that the LHB and UHB are not conventional single-particle bands. Instead, they result from electron-electron interactions and the local electron occupation. Adding or removing an electron in this picture changes the LHB and UHB themselves [19].

The fundamental electronic excitation of the Hubbard model takes one electron from one site and adds it to another site. This is equivalent to creating an electron and a hole (holon-doublon pair) in the crystal. Both particles can, in principle, hop along the lattice and acquire dispersion. As such, these Mott-Hubbard excitations form a continuum of excited states. For one electron per site, the onset of the Mott gap is found at the energy $E = U - W$. The bandwidth $W \sim 2zt$ is set by the hopping parameter and the number of nearest neighbors z.

Onsite excitons in Mott insulators

A Mott insulator hosts local spin and orbital degrees of freedom, and the corresponding excitations (such as magnons, orbitons, crystal-field excitations, and spin-orbit excitons,

among others) can be understood as onsite excitons. In the band picture, an exciton in a semiconductor can be understood as a charge-neutral quasiparticle formed by a bound electron-hole pair. In the case of the onsite exciton, the electron-hole pair is created on the same site. An important example is the spin-orbit exciton, which is the onsite excitation from $|j = 1/2\rangle$ to $|j = 3/2\rangle$. This excitation depends only on local parameters, i.e., λ and Δ, but not on U. The excitonic flavor of these excitations follows from the composite character, where the electron and hole are bound on the same sites. These excitons can hop between lattice sites, but only as composite quasiparticles, before they decay [35, 174]. To clarify, we distinguish these excitations from intersite excitons, see Fig. 2.1(b). Similar to the band exciton, an intersite exciton is stabilized by the excitonic binding energy. Typically, these excitons are found below the onset of the charge gap. In a Mott insulator, the minimum energy is found at $E = U - V$, where V is the attractive binding potential between the electron and hole, analogous to $E = E_{\text{gap}} - E_b$ in a semiconductor. An example of such a Coulomb-type of exciton can be seen in the optical conductivity of the osmium halides, see chapter 5. The identifying characteristic of these features is their energy dependence with respect to the Mott gap. K_2OsCl_6 and K_2OsBr_6 show the onset of the Mott gap at around 2.2 and 1.8 eV, respectively. For both crystals, we observe a feature located at around 2 and 1.7 eV, roughly 10% below the Mott gap. In contrast, the intra-t_{2g} onsite excitations in the same energy range are found, to first order, for both compounds at the same energies.
The correspondence between onsite excitons in a Mott insulator and local excitations of a single MX_6 octahedron allows us to determine the local electronic properties of the crystal by a simplified single-site Hamiltonian, reducing the complexity significantly.

2.2 The single-site Hamiltonian

The main idea of the single-site model is to approximate the onsite electronic properties by a small cluster. In our case, this is the transition-metal ion surrounded by its charged ligand octahedron. There is an extensive body of literature that deals with the electronic structure of local clusters. Our discussion of the single-site Hamiltonian follows the lines of [19, 80, 175, 176].
From the discussion of chapter 1, we recollect that the main effects that we consider are crystal-field effects, intra-atomic Coulomb interaction, and spin-orbit coupling. This Hamiltonian can be written as

$$H_{\text{single}} = H_{\text{CF}} + H_{e-e} + H_{\text{SOC}} \tag{2.2}$$

and forms the central body of the single-site model. The structure of this Hamiltonian inherits many properties from atomic multiplet theory [177]. This means Eq. (2.2) can be treated as a perturbation to the spherically symmetric Hamiltonian of the free transition-metal ion. Thus, the orbital structure of the d orbitals can be constructed on the basis of

single-electron hydrogen wavefunctions

$$\psi_{n,l,m}(\mathbf{r}) = R_{n,l}(r)Y_l^m(\theta,\phi), \tag{2.3}$$

where $R_{n,l}(r)$ and $Y_l^m(\theta,\phi)$ depict the separable radial and angular parts of the wavefunction, respectively. In the hydrogen model, the wavefunctions are characterized by their principal quantum number n, the orbital quantum number l, and its projections along the quantization axis m.
One key issue of the eigenstates is that there is no analytical expression to determine the radial part of the wavefunction in a cluster or crystal [178]. However, the symmetry properties of the wavefunction can be used to gain information about the radial part indirectly from effective model parameters, which are obtained from a fit of the excitation energies.
Before we discuss the individual terms in Eq. (2.2), we need to address the many-body character for general electron configurations d^N. In the case of N electrons, a Slater determinant presents a simplified expression of a many-body wavefunction that comprises the fermionic anti-commutation rules [176]. It can be expressed as

$$\Psi(\mathbf{r}_1,\mathbf{r}_2...,\mathbf{r}_N) = \frac{1}{\sqrt{N!}}\begin{vmatrix} \psi_1(\mathbf{r}_1) & \psi_2(\mathbf{r}_1) & \dots & \psi_N(\mathbf{r}_1) \\ \psi_1(\mathbf{r}_2) & \psi_2(\mathbf{r}_2) & \dots & \psi_N(\mathbf{r}_2) \\ \vdots & \vdots & \ddots & \vdots \\ \psi_1(\mathbf{r}_N) & \psi_2(\mathbf{r}_N) & \dots & \psi_N(\mathbf{r}_N), \end{vmatrix}, \tag{2.4}$$

or more concisely, as $|\Psi\rangle = a_1^\dagger a_2^\dagger ... a_N^\dagger |0\rangle$, using creation operators in second quantization. The physical eigenstates that constitute the local electronic structure are the multiplets based on a linear superposition of Slater determinants. Typically, multiplets are labeled by their spin and orbital symmetries using a term symbol of the form ${}^{2S+1}X$. Here, $2S+1$ denotes the spin multiplicity, and X specifies the orbital symmetry. For atoms, this is conventionally given by letters that reflect the total orbital moment $L = S, P, D, ...$ In environments with lower symmetry, e.g., in a crystal field, it is expressed by Mulliken symbols such as $A_{1g}, E_g, T_{2g}, ...$, which denote the orbital degeneracy and correspond to the irreducible representations of the particular point group of the system [80]. For example, the ground state of a t_{2g}^3 configuration, as seen in K_2ReCl_6, shows $S = 3/2$ and $L = 0$ within a cubic environment in the absence of spin-orbit coupling. As such, the ground state has a spin multiplicity $2S + 1 = 4$ and no orbital degeneracy. The corresponding ground state is the ${}^4A_2$ multiplet that can be written as a superposition of four Slater determinants

$$\begin{aligned}
|{}^4A_2\rangle_1 =& a^\dagger_{xy,\uparrow}a^\dagger_{yz,\uparrow}a^\dagger_{zx,\uparrow}|0\rangle \\
|{}^4A_3\rangle_2 =& a^\dagger_{xy,\downarrow}a^\dagger_{yz,\downarrow}a^\dagger_{zx,\downarrow}|0\rangle \\
|{}^4A_2\rangle_3 =& \frac{1}{\sqrt{3}}\left(a^\dagger_{xy,\downarrow}a^\dagger_{yz,\uparrow}a^\dagger_{zx,\uparrow} + a^\dagger_{xy,\uparrow}a^\dagger_{yz,\downarrow}a^\dagger_{zx,\uparrow} + a^\dagger_{xy,\uparrow}a^\dagger_{yz,\uparrow}a^\dagger_{zx,\downarrow}\right)|0\rangle \\
|{}^4A_2\rangle_4 =& \frac{1}{\sqrt{3}}\left(a^\dagger_{xy,\uparrow}a^\dagger_{yz,\downarrow}a^\dagger_{zx,\downarrow} + a^\dagger_{xy,\downarrow}a^\dagger_{yz,\uparrow}a^\dagger_{zx,\downarrow} + a^\dagger_{xy,\downarrow}a^\dagger_{yz,\downarrow}a^\dagger_{zx,\uparrow}\right)|0\rangle \\
\Rightarrow |{}^4A_2\rangle =& \alpha|{}^4A_2\rangle_1 + \beta|{}^4A_3\rangle_2 + \gamma|{}^4A_3\rangle_3 + \delta|{}^4A_3\rangle_4.
\end{aligned} \tag{2.5}$$

Crystal-field splitting

The first term in Eq. (2.2), H_{CF}, captures the effective electrostatic potential between the charged surrounding and the single ion. In a Mott insulator, the main effect of this potential is to lift the degeneracy of the d orbitals and to reduce the orbital symmetry of the electronic states from fully symmetric to the local site symmetry. For a cluster with octahedral coordination, this splits the d orbitals into the lower-lying triply degenerate t_{2g} states and the doubly degenerate e_g states.
Generally, there are two effects that comprise the crystal-field splitting. First, there is the electrostatic contribution, which is determined from the Madelung potential of the charges in the crystal [4]. Second, covalency and the hybridization between the transition-metal d states and the ligand p states lead to the formation of molecular orbitals that show bonding and antibonding character, which manifests as a splitting. In principle, both effects can yield the same experimental level splitting. For simplicity, we focus on the electrostatic effect now and omit the discussion of covalency effects to a later point.
As a consequence of the single-site approximation, the strength of the nearest-neighbor potential of the ligands is typically renormalized to simulate the Madelung potential of the crystal. This potential is then referred to as the crystal-field potential V_{CF}. In this version, the ligands act as point charges. The electrostatic potential resulting from the Coulomb interaction between the transition-metal ion at position $\mathbf{r}$ and the surrounding N point charges located at $\mathbf{R}_i$ reads as

$$V_{\mathrm{CF}} = \sum_{i}^{N} \frac{Ze^2}{|\mathbf{R}_i - \mathbf{r}|}. \tag{2.6}$$

To apply the crystal-field potential to the spherical harmonics $\psi_{n,l,m}$ it is a common approach to use a multipole expansion,

$$\begin{aligned} V_{\mathrm{CF}} &= \sum_{k=0}^{\infty} \sum_{m=-k}^{k} r^k A_{k,m} C_k^m(\theta,\phi), \\ A_{k,m} = \frac{Ze^2}{R^{k+1}} \sum_{i}^{N} Y_k^{*m}(\theta_i,\phi_i), &\quad C_k^m(\theta,\phi) = \sqrt{\frac{4\pi}{2k+1}} Y_k^m(\theta,\phi), \end{aligned} \tag{2.7}$$

where $A_{k,m}$ are the components of the multipole moment and $C_k^m(\theta,\phi)$ are the renormalized spherical harmonics [80]. For d orbitals with $l = 2$ and an ideal octahedron with cubic symmetry, the crystal-field potential reduces to [80]

$$V_{\mathrm{CF},O_h} = \frac{7}{2}\frac{Ze^2 r^4}{R^5}\left(C_4^0(\theta,\phi) + \sqrt{\frac{5}{14}}C_4^4(\theta,\phi) + \sqrt{\frac{5}{14}}C_4^{-4}(\theta,\phi)\right) + V_0. \tag{2.8}$$

The two remaining terms are the zeroth-order monopole contribution V_0 with $k = 0$, which only shifts the energy of the entire d shell, and the fourth-order contribution that scales

with r^4. Acting on the $\psi_{n,2,m}$ states, this means the crystal field can be described by a single effective parameter $Dq = \frac{1}{6}\frac{Ze^2}{R^5}\langle R_{n,2}|r^4|R_{n,2}\rangle$ [80]. On the basis of the spherical harmonics $\mathbf{Y} = \left[|Y_2^{-2}\rangle, |Y_2^{-1}\rangle, |Y_2^0\rangle, |Y_2^1\rangle, |Y_2^2\rangle\right]$, the matrix elements can be written as

$$V_{\mathrm{CF}} = \begin{pmatrix} V_0 + Dq & 0 & 0 & 0 & 5Dq \\ 0 & V_0 - 4Dq & 0 & 0 & 0 \\ 0 & 0 & V_0 + 6Dq & 0 & 0 \\ 0 & 0 & 0 & V_0 - 4Dq & 0 \\ 5Dq & 0 & 0 & 0 & V_0 + Dq, \end{pmatrix}, \tag{2.9}$$

which show two eigenenergies and yield the crystal-field splitting

$$\begin{aligned} E_1 &= V_0 - 4Dq \\ E_2 &= V_0 + 6Dq \\ \Rightarrow \Delta E &= 10Dq. \end{aligned} \tag{2.10}$$

The orbitals at E_1 correspond to the t_{2g} manifold, while the ones at E_2 belong to the e_g manifold. The former lie lower in energy since their lobes point in between two ligands, minimizing Coulomb repulsion, whereas the latter point directly towards them, see Fig. 2.2. In the cubic basis, the real-valued states read as

$$\begin{aligned} t_{2g} &: \begin{cases} |xy\rangle = \frac{\mathrm{i}}{\sqrt{2}}\left(|Y_2^{-2}\rangle - |Y_2^2\rangle\right) \\ |yz\rangle = \frac{\mathrm{i}}{\sqrt{2}}\left(|Y_2^{-1}\rangle + |Y_2^1\rangle\right) \\ |zx\rangle = \frac{1}{\sqrt{2}}\left(|Y_2^{-1}\rangle - |Y_2^1\rangle\right) \end{cases} \\ e_g &: \begin{cases} |z^2\rangle = |Y_2^0\rangle \\ |x^2 - y^2\rangle = \frac{1}{\sqrt{2}}\left(|Y_2^{-2}\rangle + |Y_2^2\rangle\right) \end{cases} . \end{aligned} \tag{2.11}$$

As mentioned in the introduction, the crystal-field splitting has a profound impact on the orbital structure of the d states. Instead of an orbital moment $l = 2$ of the free ion, the t_{2g} states behave effectively as $l_{\mathrm{eff}} = -1$, whereas the e_g states show a quenched orbital moment $l_{e_g} = 0$ [80]. This is, for instance, a crucial prerequisite for the formation of the $j = 1/2$ and $j = 3/2$ states when spin-orbit coupling is applied.

In $4d$ and $5d$ oxides, the crystal-field splitting is typically on the order of $10Dq \approx 2 - 4\,\mathrm{eV}$ [179–182] and marks the largest parameter in Eq. (2.2) within the point-charge picture. This has the consequence that $4d^N$ and $5d^N$ configurations for $N > 3$ typically adopt a low-spin state, i.e., fully occupying the t_{2g} orbitals first, before the e_g states are filled. Many low-spin models, hence, neglect the e_g states. An often used example is the t_{2g}-only Kanamori model that is discussed in the next section.

We briefly touch upon non-cubic distortions. There are various sources for these, such

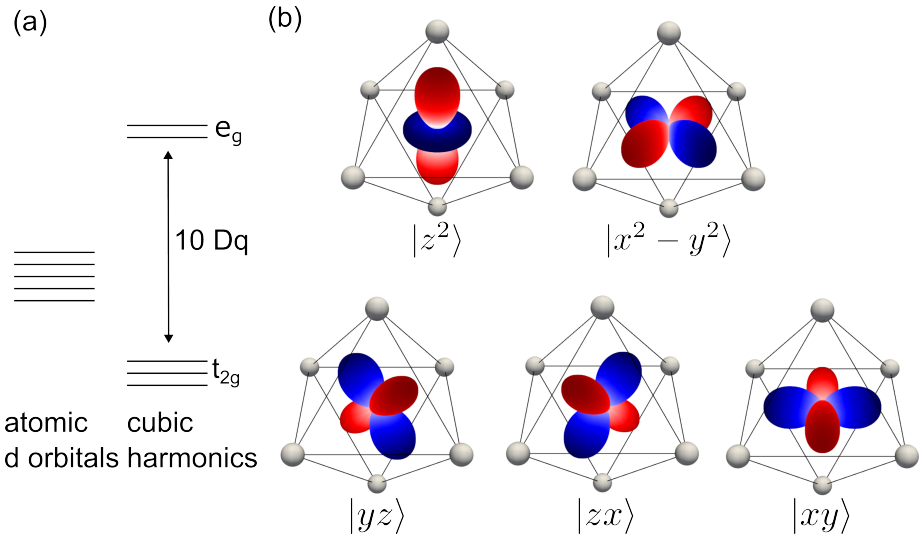

Figure 2.2 Left: Splitting of the d orbitals under the cubic crystal-field. The initially degenerate d orbitals are split into a t_{2g} and an e_g manifold. Right: Density plot of the real-valued cubic harmonics within the octahedral cage. The color denotes the phase of the wavefunction.

as a non-cubic crystal structure, Jahn-Teller distortions, or structural defects. Irrespective of their origins, static distortions manifest as additional splittings of the t_{2g} and e_g states. For an intuitive picture, we restrict the discussion to t_{2g} orbitals, which we use to calculate the non-cubic distortion in the case of α-$RuCl_3$, see chapter 4. For example, an octahedron that is either elongated or compressed along one of the cubic axes yields a tetragonal distortion, which lifts the degeneracy of t_{2g} orbitals. In the t_{2g} basis $\hat{\mathbf{k}} = [|xy\rangle, |yz\rangle, |zx\rangle]$, one can write for an octahedron elongated along the z axis [19]

$$V_{tet} = \frac{2}{3}\begin{pmatrix} \Delta & 0 & 0 \\ 0 & -\frac{\Delta}{2} & 0 \\ 0 & 0 & -\frac{\Delta}{2} \end{pmatrix}, \tag{2.12}$$

which yields a splitting of Δ between the higher-lying $|xy\rangle$ orbital and the lower-lying $|yz\rangle$ and $|zx\rangle$. The elongation or compression along the body diagonal of the octahedron yields a trigonal distortion that can be written analogously [183]

$$V_{trig} = \frac{1}{3}\begin{pmatrix} 0 & \Delta & \Delta \\ \Delta & 0 & \Delta \\ \Delta & \Delta & 0 \end{pmatrix}, \tag{2.13}$$

The corresponding eigenstates form a singlet and a doublet

$$\begin{aligned} |a_{1g}\rangle &= \frac{1}{\sqrt{3}}\left(|xy\rangle + |yz\rangle + |zx\rangle\right) \\ |e^{\pi}_{g,1}\rangle &= \pm\frac{1}{\sqrt{2}}\left(|yz\rangle + |zx\rangle\right) \\ |e^{\pi}_{g,2}\rangle &= \pm\frac{1}{\sqrt{6}}\left(2|xy\rangle - |yz\rangle - |zx\rangle\right), \end{aligned} \tag{2.14}$$

located at the energy $\frac{2}{3}\Delta$ and $-\frac{1}{3}\Delta$, respectively [19]. For α-$RuCl_3$, we combine spin-orbit coupling and trigonal distortion to analyze the spin-orbit exciton to determine the ground state character. Including the cubic e_g orbitals, the effect of the tetragonal and trigonal distortions can be calculated by adding more crystal-field parameters in Eq. (2.7) [80]. Following [175], the case of a tetragonal crystal field yields

$$V_{\mathrm{CF},D_{4h}} = V_{\mathrm{CF},O_h} - 7Ds\, C_2^0(\theta,\phi) - 21Dt\, C_4^0(\theta,\phi), \tag{2.15}$$

while for a trigonal crystal field

$$\begin{aligned} V_{\mathrm{CF},D_{3d}} =& -7D\sigma\, C_2^0(\theta,\phi) - 14\left(Dq + \frac{3}{2}D\tau\right)C_4^0(\theta,\phi) \\ & - 14\sqrt{\frac{10}{7}}Dq\left(C_4^3(\theta,\phi) + C_4^{-3}(\theta,\phi)\right). \end{aligned} \tag{2.16}$$

Here, $Ds, Dt, D\sigma$, and $D\tau$ are the additional crystal-field parameters included to describe the lower symmetry of the environment [175, 178]. We used these, for instance, to check the sensitivity of the t_{2g}^3 multiplets in the presence of distortions, see chapter 6.

Electron-electron interaction

In a Mott insulator, we have identified the role of Coulomb repulsion as a means to localize electrons on their atomic sites. At the same time, it is also crucial for the orbital occupation and formation of the multiplet structure.
Similar to the crystal-field potential V_{CF}, we can express the Coulomb potential between two electrons at positions $\mathbf{r}_i$ and $\mathbf{r}_j$ as

$$V_{e-e} = \sum_{i\neq j}\frac{1}{2}\frac{e^2}{|\mathbf{r}_i - \mathbf{r}_j|}. \tag{2.17}$$

Using a multipole expansion [176], this becomes

$$V_{e-e} = \sum_{i\neq j}\sum_{k=0}^{\infty}\sum_{m=-k}^{k}\frac{e^2}{2}\frac{r_<^k}{r_>^{k+1}}(-1)^m C_k^{-m}(\theta_i,\phi_i)C_k^m(\theta_j,\psi_j), \tag{2.18}$$

where $r_< = \min[r_i, r_j]$ and $r_> = \max[r_i, r_j]$ refer to the smaller and larger radius of the two electrons, respectively. V_{e-e} is a two-particle potential. For the relevant multipole components, this means that k has to be even and to satisfy orbital conservation, set by the triangular inequality $|l_1 - l_2| \leq k \leq |l_1 + l_2|$ [176]. As such, this gives $k = 0, 2$, and 4 for d orbitals. The Slater-Condon parameters F^k yield the strength of the Coulomb interaction expressed via the radial integrals [176]

$$F^k = \langle R_{n,2}(r_1) R_{n,2}(r_2) | e^2 \frac{r_<^k}{r_>^{k+1}} | R_{n,2}(r_1) R_{n,2}(r_2) \rangle. \tag{2.19}$$

The monopole contribution F^0 determines the overall Coulomb energy for a given electron configuration d^N. It shifts the energy by a constant offset if an electron is added or removed from the shell. This factor is analogous to Hubbard U in Eq. (2.1). Within the single-site model, the number of electrons is fixed. Hence, F^0 is typically not determined. The dipole and quadrupole terms F^2 and F^4, however, govern the energies of multiplets within the shell. Their effect is most clearly seen in Hund's second rule, which states that the ground state favors a configuration with maximum spin, since parallel spins reduce Coulomb repulsion.
A convenient way to express the Slater-Condon parameters for atomic multiplets is given by the Racah parameters A, B, and C [176, 184]:

$$A = F^0 - \frac{49}{441} F^4, \quad B = \frac{1}{49} F^2 - \frac{5}{441} F^4, \quad C = \frac{35}{441} F^4. \tag{2.20}$$

These simplify the expression for different term energies. For example, the energy of the three lowest multiplets of the free ion d^2 configuration read as $E(^3F) = A - 8B$, $E(^3P) = A + 7B$, and $E(^1G) = A + 4B + 2C$ [176].

In a crystal, the situation becomes more subtle when two or more effects have to be considered simultaneously. Early success in determining the multiplet structure and obtaining the effective parameters for $3d$ compounds can be attributed to Tanabe and Sugano [80]. Their energy-level diagrams offer an intuitive tool to estimate $10Dq$ and the Racah parameters from experimental data, assuming an ideal cubic crystal field and no spin-orbit coupling. These diagrams allow us to predict, for example, if a metal-ligand complex exhibits a low-spin or high-spin configuration based on the ratio $10Dq/B$. For the d^4 configuration, the $J = 0$ low-spin state is favored if $10Dq/B \gtrsim 27$ [80]. This statement holds for a ratio of $C/B \approx 4$. For $3d$ ions, this condition can be inferred from Hartree-Fock calculations that yield $F^4/F^2 \approx \frac{5}{8} = 0.625$ [185, 186]. The often chosen ratio $C/B = 4$ corresponds to $F^4/F^2 = \frac{36}{55} = 0.655$. Our results on K_2OsCl_6 yield $10Dq = 3.27\,\text{eV}$ and $B = 0.05\,\text{eV}$, corroborating that the $J = 0$ state is well justified.

As mentioned in the previous section, electronic interaction can often be modeled without the full multiplet treatment. One example is the Kanamori model, which is an extension of

the Hubbard model adding multiple degenerate orbitals on each site. Electron-electron interactions are accounted for by distinguishing whether two electrons occupy the same site or occupy the same orbitals or different ones. This yields the effective parameters U (from Eq. (2.1)) and $J_{\mathrm{H}}^{\mathrm{eff}}$ as Hund's coupling in the crystal environment. The electron-electron interactions in the t_{2g}-only Kanamori model can be written as [187]

$$H_{\mathrm{Ka}} = U \sum_{m} n_{m,\uparrow} n_{m,\downarrow} + (U - 2J_{\mathrm{H}}^{\mathrm{eff}}) \sum_{m \neq m'} n_{m,\uparrow} n_{m',\downarrow} + (U - 3J_{\mathrm{H}}^{\mathrm{eff}}) \sum_{m<m',\,\sigma} n_{m,\sigma} n_{m',\sigma} - J_{\mathrm{H}}^{\mathrm{eff}} \sum_{m \neq m'} a_{m,\uparrow}^{\dagger} a_{m,\downarrow} a_{m',\downarrow}^{\dagger} a_{m',\uparrow} + J_{\mathrm{H}}^{\mathrm{eff}} \sum_{m \neq m'} a_{m,\uparrow}^{\dagger} a_{m,\downarrow}^{\dagger} a_{m',\uparrow} a_{m',\downarrow}. \quad (2.21)$$

The first three terms reflect the effective Coulomb interaction for double occupancy in the same orbital, in different orbitals with opposite spins, and in different orbitals with parallel spins, respectively. The last two terms reflect the mixing of different Slater determinants to obtain the multiplet structure. Under the assumption that the Hamiltonian is rotationally invariant, Eq. (2.21) can be transformed to

$$H_{\mathrm{Ka}} = (U - 3J_{\mathrm{H}}^{\mathrm{eff}}) \frac{\hat{N}(\hat{N}-1)}{2} - 2J_{\mathrm{H}}^{\mathrm{eff}} \mathbf{S}^2 - \frac{J_{\mathrm{H}}^{\mathrm{eff}}}{2} \mathbf{L}^2 + \frac{5J_{\mathrm{H}}^{\mathrm{eff}}}{2} \hat{N}, \quad (2.22)$$

where $\hat{N}$, $\mathbf{S}$, and $\mathbf{L}$ denote the total electron number, total spin, and total orbital moment operators, respectively [187]. This Hamiltonian can be solved for different electron counts and different configurations to yield the t_{2g} multiplets. We summarize the results in Tab. 2.1. If we restrict the full electron-electron interaction to the t_{2g} manifold, it yields the same results as the Kanamori model. However, a t_{2g}-only model does not resolve all intra-t_{2g} multiplets. For t_{2g}^4, the $^1T_2$ and the ^1E multiplets are accidentally degenerate. This is only repaired in the full multiplet model. By symmetry, the same applies for the t_{2g}^2 case, but also for the $^2T_1$ and the ^2E states in $5d^3$ K_2ReCl_6. In addition, spin-orbit coupling splits the $^3T_1$ ground state of the t_{2g}^4 into a $J = 0$ singlet, a $J = 1$ triplet, and a $J = 2$ quintet. In the full multiplet theory, the $J = 2$ quintet is further split into a doublet and a triplet, which is not captured in the t_{2g}-only case.
Another important consequence is the strength of the effective parameters. For the t_{2g}-only model, U and $J_{\mathrm{H}}^{\mathrm{eff}}$ can be calculated from the Slater-Condon parameters as

$$\begin{aligned} U &= F^0 + \frac{4}{49} F^2 + \frac{36}{441} F^4 \\ J_{\mathrm{H}}^{\mathrm{eff}} &= \frac{3}{49} F^2 + \frac{20}{441} F^4. \end{aligned} \quad (2.23)$$

But, if we consider the full d shell, we find

$$\begin{aligned} U &= F^0 \\ J_{\mathrm{H}} &= \frac{1}{14} \left(F^2 + F^4 \right). \end{aligned} \quad (2.24)$$

N	Multiplet	S	L	Energy
0	$^1A_1$	0	0	0
1	$^2T_2$	1/2	1	0
2	$^3T_1$	1	1	$U - 3J_\mathrm{H}^\mathrm{eff}$
	$^1T_2$, ^1E	0	2	$U - J_\mathrm{H}^\mathrm{eff}$
	$^1A_1$	0	0	$U + 2J_\mathrm{H}^\mathrm{eff}$
3	$^4A_2$	3/2	0	$3U - 9J_\mathrm{H}^\mathrm{eff}$
	$^2T_1$, ^2E	1/2	2	$3U - 6J_\mathrm{H}^\mathrm{eff}$
	$^2T_2$	1/2	1	$3U - 4J_\mathrm{H}^\mathrm{eff}$
4	$^3T_1$	1	1	$6U - 13J_\mathrm{H}^\mathrm{eff}$
	$^1T_2$, ^1E	0	2	$6U - 11J_\mathrm{H}^\mathrm{eff}$
	$^1A_1$	0	0	$6U - 8J_\mathrm{H}^\mathrm{eff}$
5	$^2T_2$	1/2	1	$10U - 20\,J_\mathrm{H}^\mathrm{eff}$
6	$^1A_1$	0	0	$15U - 30\,J_\mathrm{H}^\mathrm{eff}$

Table 2.1 Summary of the multiplet states of the t_{2g} orbitals for partial filling. The energy is calculated according to (2.22). Note that the cases of N=2 and N=4 yield the same energies apart from a constant offset. This follows electron-hole symmetry, which is lost when spin-orbit coupling is applied.

We illustrate the difference for $5d^4$ K_2OsCl_6. The Slater-Condon parameters we obtain from the t_{2g}-only model are $F^2 = 2.9\,\mathrm{eV}$ and $F^4 = 2.1\,\mathrm{eV}$, which yield $J_\mathrm{H}^\mathrm{eff} = 0.28\,\mathrm{eV}$. For the full d shell, the fit yields $F^2 = 3.7\,\mathrm{eV}$ and $F^4 = 2.2\,\mathrm{eV}$, which gives $J_\mathrm{H} = 0.43\,\mathrm{eV}$. The resulting Hund's coupling in the t_{2g} manifold yields $J_{\mathrm{H},t_{2g}} = 0.33\,\mathrm{eV}$.

Spin-orbit coupling

The spin emerges as an additional degree of freedom in the relativistic treatment of the electron wavefunction in the Dirac equation. Spin-orbit coupling arises as a relativistic correction term to the hydrogen Hamiltonian when the Dirac equation is expanded in the non-relativistic limit. It couples the spin and orbital degrees of freedom, which can be understood in a classical picture as the interaction of the electron's spin with the magnetic field induced by the loop current due to the orbital motion around the nucleus. The Hamiltonian reads

$$H_\mathrm{SOC} = \sum_i \zeta_i \, \mathbf{l}_i \cdot \mathbf{s}_i, \tag{2.25}$$

with the strength of the spin-orbit interaction ζ_i and the spin and orbital momentum operators $\mathbf{s}_i$ and $\mathbf{l}_i$ of the ith electron [80]. Typically, the strength of spin-orbit coupling can be

treated as a constant for a given shell $\zeta_i = \zeta_{n,l} = \zeta$ [19] and can be calculated [21] via

$$\zeta = \langle R_{n,l}(r)|\frac{\hbar^2}{2m^2c^2}\frac{1}{r}\frac{\mathrm{d}V}{\mathrm{d}r}|R_{n,l}(r)\rangle. \tag{2.26}$$

Here m and c are the electron's mass and the speed of light, respectively, and V denotes the radial potential between the electron and the nucleus. The strength of spin-orbit coupling increases for heavier elements. The main reason is the scaling of spin-orbit coupling with the atomic number $\zeta \sim Z^x$, but the exact scaling is difficult to estimate, and the precise values for ζ have to be determined from the experiment [19]. The most direct consequence of spin-orbit coupling is the additional splitting of the multiplet structure based on the total spin-orbital moment $\mathbf{J}$. We show this in the single-electron basis, but the same general structure can also be applied for multiple electrons. The expectation values of Eq. (2.25) yield

$$\langle\psi_{n,l,s}|\zeta\,\mathbf{l}\cdot\mathbf{s}|\psi_{n,l,s}\rangle = \frac{\zeta}{2}\left(j(j+1) - l(l+1) - s(s+1)\right). \tag{2.27}$$

For a single electron with $s = 1/2$, the possible total angular momenta are $j = l - s$ and $j = l + s$, and the energies of these states yield [188]

$$\frac{\zeta}{2}\left(j(j+1) - l(l+1) - s(s+1)\right) = \begin{cases} -\frac{\zeta}{2}(l+1), & \text{for } j = l - s \\ \frac{\zeta}{2}l, & \text{for } j = l + s. \end{cases} \tag{2.28}$$

Note that one has to be cautious with the case of the t_{2g} electrons with $l_{\mathrm{eff}} = -1$. Here, the angular momentum in Eqs. (2.27) and (2.28) is treated as a positive integer, but the sign of the energies flips, i.e., $+\zeta$ for the doublet $j = 1/2$ and $-\frac{\zeta}{2}$ for the quartet $j = 3/2$. This yields the $j = 3/2$ ground state and an excited $j = 1/2$ state with a splitting of $\frac{3}{2}\zeta$ for t_{2g}^1.
Spin-orbit coupling breaks electron-hole symmetry, which is manifested as an effective sign change of spin-orbit coupling changing from the electron to the hole picture. This is often expressed as an effective spin-orbit coupling parameter $\lambda = \pm\zeta/2S$ with a positive sign for half filling or less and a negative sign for more than half filling. This means the t_{2g}^5 configuration can be treated as a single hole, and the energies of the hole read $-\lambda$ for the $j = 1/2$ ground state and $+\frac{1}{2}\lambda$ for the excited $j = 3/2$.
Recalling the matrices for the components of the orbital momentum operator $\mathbf{l}$ in the t_{2g} basis ($|yz\rangle, |zx\rangle, |xy\rangle$) from [80]

$$\mathbf{l}_x = \begin{pmatrix} 0 & 0 & 0 \\ 0 & 0 & i \\ 0 & -i & 0 \end{pmatrix}, \quad \mathbf{l}_y = \begin{pmatrix} 0 & 0 & -i \\ 0 & 0 & 0 \\ i & 0 & 0 \end{pmatrix}, \quad \mathbf{l}_z = \begin{pmatrix} 0 & i & 0 \\ -i & 0 & 0 \\ 0 & 0 & 0 \end{pmatrix}, \tag{2.29}$$

and the Pauli matrices for the components of the spin operator $\mathbf{s}$

$$\mathbf{s}_x = \frac{1}{2}\begin{pmatrix} 0 & 1 \\ 1 & 0 \end{pmatrix}, \quad \mathbf{s}_y = \frac{1}{2}\begin{pmatrix} 0 & -i \\ i & 0 \end{pmatrix}, \quad \mathbf{s}_z = \frac{1}{2}\begin{pmatrix} 1 & 0 \\ 0 & -1 \end{pmatrix}, \tag{2.30}$$

we can write Eq. (2.25) in the spinful t_{2g} basis $\hat{\mathbf{K}} = [|yz,\uparrow\rangle, |yz,\downarrow\rangle, |zx,\uparrow\rangle, |zx,\downarrow\rangle, |xy,\uparrow\rangle, |xy,\downarrow\rangle]$ as

$$H_{\mathrm{SOC}} = \frac{\zeta}{2}\begin{pmatrix} 0 & 0 & i & 0 & 0 & -1 \\ 0 & 0 & 0 & -i & 1 & 0 \\ -i & 0 & 0 & 0 & 0 & i \\ 0 & i & 0 & 0 & i & 0 \\ 0 & 1 & 0 & -i & 0 & 0 \\ -1 & 0 & -i & 0 & 0 & 0 \end{pmatrix}. \tag{2.31}$$

This yields the eigenenergies $-\frac{\zeta}{2}$ and ζ discussed above and the eigenstates, which can be written in the $|j, j_z\rangle$ basis as a complex superposition of the t_{2g} orbitals [79]:

$$\begin{aligned} |1/2,+1/2\rangle &= \frac{1}{\sqrt{3}}\left(|yz,\downarrow\rangle + \mathrm{i}|zx,\downarrow\rangle + xy,\uparrow\rangle\right) \\ |1/2,-1/2\rangle &= \frac{1}{\sqrt{3}}\left(|yz,\uparrow\rangle - \mathrm{i}|zx,\uparrow\rangle + xy,\downarrow\rangle\right) \end{aligned} \tag{2.32}$$

and

$$\begin{aligned} |3/2,+3/2\rangle &= \frac{1}{\sqrt{2}}\left(-|yz,\uparrow\rangle - \mathrm{i}|zx,\uparrow\rangle\right) \\ |3/2,-3/2\rangle &= \frac{1}{\sqrt{2}}\left(|yz,\downarrow\rangle - \mathrm{i}|zx,\downarrow\rangle\right) \\ |3/2,+1/2\rangle &= \frac{1}{\sqrt{6}}\left(-|yz,\downarrow\rangle - \mathrm{i}|zx,\downarrow\rangle + 2|xy,\uparrow\rangle\right) \\ |3/2,-1/2\rangle &= \frac{1}{\sqrt{6}}\left(|yz,\uparrow\rangle - \mathrm{i}|zx,\uparrow\rangle + 2|xy,\downarrow\rangle\right). \end{aligned} \tag{2.33}$$

These are the eigenstates shown in Fig. 1.2(b).
At first glance, spin-orbit coupling does not affect the e_g states due to $l_{e_g} = 0$. Applied on the full d shell, spin-orbit coupling introduces a mixing between $j = 3/2$ and e_g states and shifts the energies $\sim \zeta^2/10Dq$ as a higher-order correction [79]. This effect is, for instance, revealed by the additional splitting of the t_{2g}^4 $J = 2$ multiplet, as mentioned in the last section.

Dealing with more than one electron (or hole), one has to account for both Hund's rules and spin-orbit coupling. Conceptually, there are two schemes on how to combine these effects. The *LS* scheme constructs the eigenbasis based on total spin $\mathbf{S}$ and total angular momentum $\mathbf{L}$. These couple to the total angular momentum $\mathbf{J} = \mathbf{L} + \mathbf{S}$ and yield the multiplets listed in Tab. 2.1. The Hamiltonian to apply spin-orbit coupling in this scheme reads

$$H_{\mathrm{SOC}} = \lambda \mathbf{L} \cdot \mathbf{S} \tag{2.34}$$

and the corresponding eigenenergies are determined analogously to Eq. (2.27), noting that the total moment can take several values from $J = |L - S|, ..., |L + S|$. In the opposite jj-coupling scheme, one begins from the single-particle $|j, j_z\rangle$ states with $\mathbf{j}_i = \mathbf{l}_i + \mathbf{s}_i$. The many-body basis builds on Slater determinants of these orbitals, and the total angular moment is calculated from $\mathbf{J} = \sum_i \mathbf{j}_i$, characterizing the multiplet structure. Coulomb interaction acts as a splitting of different J multiplets here. In each case the total $\mathbf{J}$ is the same, but the physical properties of the multiplets can differ significantly. For example, the t_{2g}^3 configuration displays $L = 0$ and $S = 3/2$ in LS coupling, but not in jj coupling. Instead, three electrons occupy the $j = 3/2$ quartet. This state retains a finite orbital character, which makes it prone to a Jahn-Teller effect. Thus, the choice of the coupling scheme affects the predicted properties in direct consequence. To clarify, the $L = 0$, $S = 3/2$ ground state can be expressed in the $|j, j_z\rangle$ basis, and the three electrons in the $j = 3/2$ state can be written in the LS basis equally well, but these will not be the eigenstates that contribute to the electronic properties.
The ratio J_H/ζ can be used as a helpful gauge to estimate the appropriate coupling scheme. The limit of $J_H/\zeta \to \infty$ indicates coupling in the LS scheme, while $J_H/\zeta \to 0$ suggests coupling in the jj-scheme. In $5d$ systems, where both parameters are almost equal, this requires a careful approach. On the one hand, we apply full numerical treatment of the single-site Hamiltonian in Eq. (2.2) performed via Quanty. On the other hand, we will also make use of the simplified t_{2g}-only model for clearer physical insight. For the $5d^4$ Os^{4+} halides, we utilize the expressions of the excitation energies of [189], and for the $5d^3$ K_2ReCl_6, we use the matrix elements of [190] to account for spin-orbit coupling and Coulomb interaction equally.

Ligand-field theory

Ligand-field theory extends the single-site picture by incorporating covalency between the transition-metal ion and its ligands. Compared to the purely electrostatic crystal-field splitting, this has two major consequences. First, it introduces the atomic character of the ligands, explicitly including a completely filled p^6 shell. This opens the possibility of charge-transfer excitations, where an electron is promoted from the ligand to the transition-metal ion, $|p_X^6 d_M^N\rangle \to |p_X^5 d_M^{N+1}\rangle$. This has a direct consequence on the classification of strongly correlated electron systems via the Zaanen-Sawatzky-Allen scheme [191]. For correlated insulators, Hubbard U has to be compared to the charge-transfer gap Δ_{CT}, the minimum energy required to create a charge-transfer process. For $U < \Delta_{CT}$, the system is a Mott insulator, for $U > \Delta_{CT}$, it is a charge-transfer insulator. This distinction is typically more relevant for $3d$ systems, where both energy scales are similar [19]. For $5d$ systems, $U \approx 2\,\text{eV}$ [19], whereas charge-transfer peaks of bromides, chlorides, or oxides lie typically around $\Delta_{CT} \gtrsim 4\,\text{eV}$ and above. In both cases, incorporating the ligand p shell gives rise to superexchange, allowing electrons to hop virtually between two metal sites through the ligand orbitals [192, 193]. This type of exchange is often a dominant contribution to magnetic exchange in correlated electron systems.

The second consequence is covalency, which leads to the formation of molecular orbitals hybridizing metal d and ligand p states. The resulting level repulsion between bonding and antibonding states renormalizes the crystal-field splitting, such that $\Delta = 10Dq + \Delta_{\mathrm{LF}}$, where $\Delta_{\mathrm{LF}} = V_{e_g} - V_{t_{2g}}$ reflects the energy difference of the hybridization strength between $p - e_g$ and $p - t_{2g}$ hybridization.
For an MX_6 octahedron, there are $10 + 6 \times 6 = 46$ spin orbitals in total. However, only a small subset contributes actively to covalency, since each d orbital only hybridizes with one linear combination of p orbitals that exhibits the same symmetry. Therefore, both models, crystal-field theory and ligand-field theory, exhibit eigenstates with the same symmetry. As such, ligand-field theory does not affect the qualitative structure of the t_{2g} multiplets that we put our focus on. For example, employing ligand-field theory in K_2ReCl_6, the fitted parameters J_{H} and ζ are renormalized by less than 7%, while the quality of the fit remains the same. However, the computational cost for fitting procedures increases dramatically, from a few minutes on a standard computer using crystal-field theory to nearly twenty hours using ligand-field theory. Given the small quantitative change without a qualitative gain, we did not pursue ligand-field theory further in this work.

2.3 Intersite properties

Mott-Hubbard excitations

Going beyond the single-site model, we revisit the correlated electron state in a Mott insulator. Extending the Hubbard model with the Kanamori scheme from Eq. (2.21) adds additional structure to the intersite excitations $|d_i^N d_j^N\rangle \rightarrow |d_i^{N-1} d_j^{N+1}\rangle$ at roughly U. The lowest Mott-Hubbard excitation can be estimated from the energy of the corresponding ground-state multiplets [187] via

$$\Delta = E_0(d^{N+1}) + E_0(d^{N-1}) - 2E_0(d^N). \tag{2.35}$$

Using Tab. 2.1, we find the lowest energies at $\Delta(d^3) = U + 2J_{\mathrm{H}}$ and $\Delta(d^4/d^5) = U - 3J_{\mathrm{H}}$. Although this is only a rough estimate to quantify the excitation energy, it agrees qualitatively with our findings from ellipsometry, which locates the first peaks of the Mott-Hubbard excitations around 2.6 and 2.4 eV for K_2OsCl_6 and K_2IrCl_6, respectively, while for K_2ReCl_6, we find the first peak located around roughly 3.3 eV, see chapter 5, chapter 7, and Fig. 3.12. In comparison to the onsite intra-t_{2g} peaks, these are very broad and form continuous absorption bands. So, although these excitations are directly allowed in optics, we cannot determine the electronic parameters with the same precision as from the intra-t_{2g} excitations using the combination of RIXS and optical spectroscopy.

We utilize the suppression of the transmittance as a means to indicate the onset of the

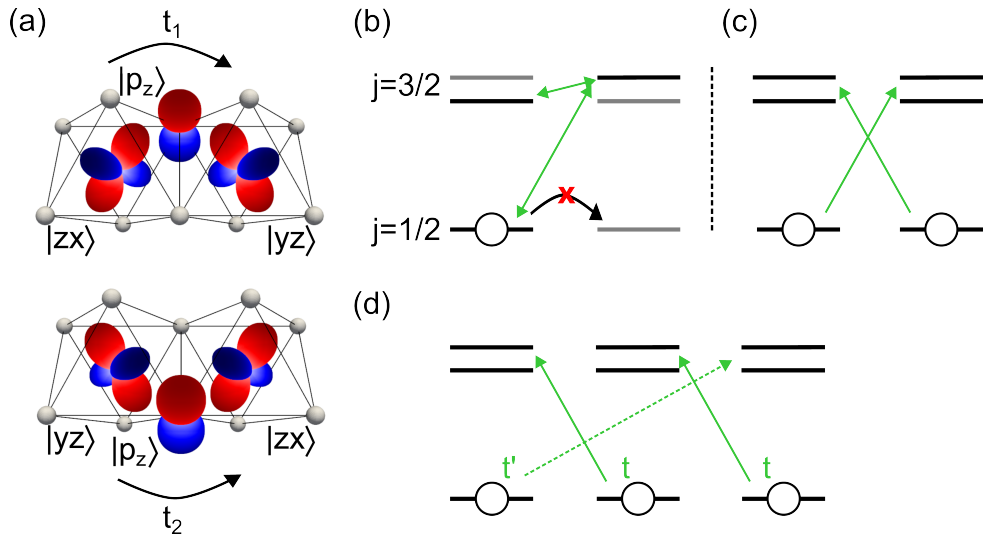

Figure 2.3 Main idea of the Jackeli-Khaliullin mechanism. (a) The two allowed hopping processes for superexchange between edge-sharing octahedra. (b) The resulting hopping is non-zero between $|1/2, \pm 1/2\rangle_i$ and $|3/2, \mp 3/2\rangle_j$ as well as between $|3/2, \pm 1/2\rangle_i$ and $|3/2, \mp 3/2\rangle_j$. (c) The excitation of the double spin-orbit exciton corresponds to the pairwise exchange of two holes, taking the same hopping paths that result in Kitaev interaction. (d) The triple spin-orbit exciton involves nearest-neighbor hopping t and next-nearest-neighbor hopping t'. Breaking inversion symmetry on the honeycomb, this excitation is directly infrared-active in α-$RuCl_3$.

Mott gap, which marks the boundary between the transparent and strongly absorbing part of the spectrum.

Exchange interaction and the Jackeli-Khaliullin mechanism

As mentioned in the introduction, Mott insulators often exhibit a magnetic ground state at low temperatures. The manifestation of magnetic order originates from exchange interactions, which provide a means of reducing the energy by virtual electron hopping to neighboring sites. For $U \gg t$, hopping can be applied in the Hubbard model as a second-order perturbation, where an electron hops to a neighboring site and back instantaneously. The energy gain and the excitation spectrum can be mapped onto the Heisenberg model (for isotropic coupling) [194]:

$$H_{\text{Heisenberg}} = \sum_{i,j} J_{ij} \mathbf{S}_i \cdot \mathbf{S}_j, \tag{2.36}$$

where the exchange coupling $J_{i,j} \sim -t_{ij}^2/U$ reflects this energy gain of the hopping process [19]. The sign of J dictates if the exchange is ferromagnetic or antiferromagnetic. The underlying cause is the symmetry of the two orbitals and their overlap. In the simplest case

of one electron and one orbital per site, this yields antiferromagnetic exchange between nearest neighbors, since two parallel spins on the same orbital are not allowed by the Pauli priciple.
Ferromagnetic exchange can manifest if hopping between unequal orbitals on neighboring sites is allowed, since Hund's coupling favors parallel alignment. For more general scenarios, the exchange between two sites can become more intricate, especially if several hopping paths are possible. For 3*d* orbitals, direct overlap between neighboring sites is typically very small. In this case, the dominating exchange is typically superexchange, mediated via virtual hopping involving ligand orbitals. The resulting type of exchange can be estimated from the Goodenough-Kanamori-Anderson rules, predicting strong antiferromagnetic exchange for nearly linear 180° metal-ligand-metal bonds and weak ferromagnetic exchange for 90° bonds [195, 196]. The resulting exchange can still be depicted as an exchange process between neighboring sites $J \sim -t_{\mathrm{eff}}^2/U$, but with an effective hopping parameter t_{eff} that incorporates all underlying contributions [19]. For 4*d* and 5*d* orbitals, exchange interactions are particularly intricate, since the larger orbital extent gives rise to additional hopping paths and stronger direct hopping. Considering the spin-orbit entangled moments, the exchange Hamiltonian between neighboring $j = 1/2$ moments can take the form [197]

$$H = \sum_{i,j} J_{i,j}\, \mathbf{S}_i \cdot \mathbf{S}_j + \mathbf{D}_{ij} \cdot \left(\mathbf{S}_i \times \mathbf{S}_j\right) + \mathbf{S}_i \cdot \mathbf{\Gamma}_{i,j} \cdot \mathbf{S}_j, \tag{2.37}$$

which shows a combination of isotropic Heisenberg exchange, antisymmetric Dzyaloshinskii-Moriya interaction, and anisotropic exchange mediated via the pseudo-dipolar tensor $\mathbf{\Gamma}$. Neglecting direct exchange for the moment, Jackeli and Khaliullin [38] have identified that superexchange on the honeycomb lattice with edge-sharing octahedra gives rise to the Kitaev Hamiltonian

$$H_{\mathrm{Kitaev}} = \sum_{\gamma=\{x,y,z\}} K\, S_i^{\gamma} S_j^{\gamma}. \tag{2.38}$$

This Hamiltonian describes the bond-selective coupling of spin components, where on each nearest-neighbor bond only one spin component is active. This bond-directional anisotropy leads to strong exchange frustration, since the exchange cannot be satisfied on all bonds simultaneously, and paves the way for the realization of the proposed Kitaev spin liquid [63].
In the case of ideal octahedra with a 90° metal-ligand-metal bonding angle, the edge-sharing geometry provides two mirror-symmetric hopping paths across the edge that remain non-zero. These are illustrated in Fig. 2.3(a). Considering a z bond, an electron or hole can hop from $|zx,\sigma\rangle_i$ via $|p_z,\sigma\rangle_1$ to $|yz,\sigma\rangle_j$ on the neighboring site. The mirror-symmetric path via the second ligand ion yields hopping from $|yz,\sigma\rangle_i$ to $|zx,\sigma\rangle_j$. These two contributions interfere according to the symmetry of the wavefunctions involved: exchange between $|1/2,\pm 1/2\rangle$ states cancels as a result of destructive interference, whereas

the hopping between $|1/2, \pm 1/2\rangle$ and $|3/2, \mp 3/2\rangle$, and between $|3/2, \pm 1/2\rangle$ and $|3/2, \mp 3/2\rangle$ states adds constructively. This orbital-selective interference suppresses isotropic Heisenberg exchange while leaving bond-dependent terms finite, generating the Kitaev Hamiltonian from Eq. (2.38).

In α-$RuCl_3$, we observe a double and a triple spin-orbit exciton. The double spin-orbit exciton can be understood as two interchanging transitions from $j = 1/2$ to adjacent $j = 3/2$ states, see Fig. 2.3. The large spectral weight can be understood as a consequence of the suppression of Heisenberg exchange, since hopping between neighboring $j = 1/2$ states is suppressed, see chapter 4. For the double spin-orbit exciton, the excitation process preserves inversion symmetry. It can thus be observed directly by Raman scattering but not by optical spectroscopy. Similarly to the spin-orbit exciton, it acquires its spectral weight in optics from the simultaneous excitation of an odd-parity phonon that breaks inversion between neighboring sites. On the honeycomb lattice, the triple spin-orbit exciton, however, does break inversion symmetry and is hence directly allowed in optics. The directly allowed three-electron process shows a similar spectral weight as the phonon-assisted two-electron excitation in this case.

3 Linear optical spectroscopy and resonant inelastic x-ray scattering

Linear optical spectroscopy and resonant inelastic x-ray scattering (RIXS) are the main experimental methods used in this thesis. Employing these techniques, the goal is typically to use light to probe excitations in crystals and to link these to the microscopic properties of the material. With a focus on 4*d* and 5*d* Mott insulators, we use these methods to study the effect of the large spin-orbit coupling on the electronic structure. Our focus lies on intrasite *dd* excitations, which are most sensitive to the local symmetry and hierarchy of the energy scales at play. In addition, we also observe intersite excitations, most prominently excitations across the Mott gap and charge-transfer excitations. This chapter lays out some groundwork for both experimental methods. The first part is dedicated to optical spectroscopy and focuses on linear response functions and their extraction from the experiment. Typically, an experiment yields the transmission and reflection spectra of a sample. Analyzing these, we retrieve the optical response functions of the material, such as the index of refraction $N(\omega)$ or the optical conductivity $\sigma(\omega)$, which can be interpreted within a microscopic framework. We make particular use of the transparency window in Mott insulators located above the phonon energies and below the Mott gap. In this energy range, we exploit the great sensitivity of transmission experiments to study the weak, dipole-forbidden spin-orbital excitations activated by the simultaneous excitation of symmetry-breaking phonons. In the range above the Mott gap, the transmission is suppressed by the strong absorption. There, we rely on ellipsometry instead to observe Mott-Hubbard and charge-transfer excitations. In this light, we will discuss the two spectroscopic methods Fourier-transform infrared spectroscopy (FTIR) and spectroscopic ellipsometry. The last part of this chapter discusses basic concepts of RIXS. As a scattering technique, the general goal is to shine x-ray photons onto the sample and to collect the scattered photons with high accuracy. The differences in energy, momentum, and polarization of the incident and outgoing photons directly relate to excitations in the samples. Hence, RIXS can be employed as a photon-in photon-out spectroscopy. Compared to optics, RIXS stands out in two ways. First, it utilizes resonance behavior to target element- and site-specific transitions, and second, the two-step process allows us to observe intrasite excitations directly without the need of symmetry-breaking phonons. Additionally, the large momentum of x-ray photons enables us to probe the dispersion of these excitations across the full Brillouin zone.

3.1 Linear response theory, optical constants, and waves at interfaces

Linear response and Kramers-Kronig relations

In general, response functions capture how a system, e.g., a crystal or a material, responds to external stimuli. The response $\mathcal{A}(\mathbf{r}, t)$ of the system emerges as a reaction to the stimulus $S(\mathbf{r}', t')$ and is mediated by the response function $\chi(\mathbf{r}, \mathbf{r}', t, t')$. This function encodes the physical properties of the system, linking the macroscopic properties of the probed sample with microscopic mechanisms. The structure of the response function can be quite intricate. However, imposing specific constraints on the system simplifies its description. Spatial and temporal invariance ensures that the response function depends only on the difference in spatial coordinates and time, $\chi(\mathbf{r}, \mathbf{r}', t, t') = \chi(\mathbf{r} - \mathbf{r}', t - t')$. Moreover, causality imposes a retarded response, meaning that $\chi(\mathbf{r} - \mathbf{r}', t - t') = 0$ for $t \leq t'$ [198]. Additionally, we perform our experiments in the weak perturbation limit, allowing us to consider only the response that is linear in S. Together, this yields

$$\mathcal{A}(\mathbf{r}, t) = \int \int_{-\infty}^{t} \chi(\mathbf{r} - \mathbf{r}', t - t') S(\mathbf{r}', t') \, \mathrm{d}t' \, \mathrm{d}\mathbf{r}', \tag{3.1}$$

which can be written in Fourier space as

$$\mathcal{A}(\mathbf{k}, \omega) = \chi(\mathbf{k}, \omega) S(\mathbf{k}, \omega), \tag{3.2}$$

and describes the generalized form of a linear response function [199]. As a direct consequence, the stimulus, in our case electromagnetic radiation with wave vector $\mathbf{k}$ and frequency ω, can only induce a response exactly at this momentum and frequency. For the optical response, we omit the explicit $\mathbf{k}$ dependence of the response function. This can be reasoned from the fact that photon wavelengths λ in the infrared and visible regime are in the range of hundreds to thousands of nm, roughly $10^3 - 10^6$ times larger than typical lattice constants a of crystals. From $\frac{a}{\lambda} \to 0$ and $|\mathbf{k}| = 2\pi/\lambda$, this restricts the accessible range of optical probes in crystals typically to $|\mathbf{k}| \approx 0$, i.e., the vicinity of the Γ point of the Brillouin zone. From the perspective of the photons, the crystal appears to be homogeneous. An exception to this rule are multi-particle excitations. Here, finite momenta can be distributed among the constituent particles, but the total momentum still amounts to $\mathbf{k} \approx 0$. Due to the Fourier transform, $\chi(\omega) = \chi_1(\omega) + \mathrm{i}\chi_2(\omega)$ is generally complex, where the real part is even in ω and the imaginary part is odd. This poses the general challenge that two quantities are required to determine the response function. In the ideal case, this would be the amplitude and phase of the transmitted or reflected waves; however, most optical techniques are sensitive only to the intensity, i.e., the phase information is lost. Common workarounds are to determine both transmittance and reflectance, see Sec. 3.1, or to measure the reflection coefficients for different polarization, yielding the two ellipsometric angles Ψ and Δ as done in spectroscopic ellipsometry, see Sec. 3.3. A profound

consequence of causality actually imposes that the real and imaginary parts of $\chi(\omega)$ are not independent of each other [198]. Instead, they are linked via the Kramers-Kronig relations [199].

$$\begin{aligned}\chi_1(\omega) &= \frac{2}{\pi}\mathcal{P}\int_0^\infty \frac{\omega'\chi_2(\omega')}{\omega'^2-\omega^2}\,\mathrm{d}\omega',\\ \chi_2(\omega) &= -\frac{2\omega}{\pi}\mathcal{P}\int_0^\infty \frac{\chi_1(\omega')}{\omega'^2-\omega^2}\,\mathrm{d}\omega'.\end{aligned} \tag{3.3}$$

Here, $\mathcal{P}$ denotes the principal value of the integral, which omits the singularity at $\omega' = \omega$. This means that, in case either the real or imaginary part is known for all frequencies from zero to infinity, the other part can be precisely determined. Unfortunately, all experiments are limited in their frequency range, which usually demands suitable extrapolations of the data to low and high frequencies when this ansatz is chosen. Alternatively, a Kramers-Kronig consistent fitting model can be used, e.g., the Lorentz oscillator model, see Sec. 3.1.1.

Optical response functions

In vacuum, light is a transversal electromagnetic wave with perpendicular electric and magnetic field components, $\mathbf{k} \perp \mathbf{E} \perp \mathbf{B}$. Obeying the wave equation,

$$\begin{aligned}\Delta\mathbf{E}(\mathbf{r},t) - \frac{1}{c^2}\frac{\partial^2\mathbf{E}(\mathbf{r},t)}{\partial t^2} &= 0\\ \Rightarrow \mathbf{E}(\mathbf{r},t) &= E_0\hat{\epsilon}\exp\left[i(\mathbf{kr}-\omega t)\right],\end{aligned} \tag{3.4}$$

the electric field component can be described as a plane wave with polarization $\hat{\epsilon}$ that is traveling in space along $\mathbf{k}$ and oscillating in time with frequency ω [198]. The description of the magnetic field component $\mathbf{B}$ is analogous. In the case of non-magnetic materials, however, it is sufficient to consider only the response of the material to the electric field. With our focus on the excitations of the system, this can be reasoned from the relative strength between electric and magnetic dipole transitions, where the former are typically five orders of magnitude larger than the latter [85]. The responses we consider are the electric polarization density $\mathbf{P}$ and current density $\mathbf{j}$ [199], which can be written analogously to Eq. (3.2) as

$$\begin{aligned}\mathbf{P}(\omega) &= \varepsilon_0(\varepsilon(\omega)-1)\mathbf{E}(\omega)\\ \mathbf{j}(\omega) &= \sigma(\omega)\mathbf{E}(\omega).\end{aligned} \tag{3.5}$$

The linear response functions are the dielectric function $\varepsilon(\omega) = \varepsilon_1(\omega) + \mathrm{i}\varepsilon_2(\omega)$ and the optical conductivity $\sigma(\omega) = \sigma_1(\omega) + \mathrm{i}\sigma_2(\omega)$. In the static case $\omega = 0$, σ describes the current induced by the free charges in a metal, whereas ε describes the polarization of bound charges in an insulator. For general frequencies, the dynamics of free and bound

charges have to be considered. The time-varying polarization creates a bound charge-current density [199]

$$\begin{aligned} \frac{\partial \mathbf{P}(t)}{\partial t} &= \mathbf{j}_b(t), \\ \Rightarrow -\mathrm{i}\omega \mathbf{P}(\omega) &= \mathbf{j}_b(\omega). \end{aligned} \tag{3.6}$$

However, for non-zero ω we cannot distinguish if the response originates from free or bound charges, hence, we can say $\mathbf{j}(\omega) = \mathbf{j}_b(\omega)$ [199]. Combining Eq. (3.5) and (3.6) then yields

$$\varepsilon(\omega) = 1 + \mathrm{i}\frac{\sigma(\omega)}{\varepsilon_0 \omega}, \tag{3.7}$$ [1]

which makes clear that both response functions govern permittivity and dissipation in the dynamic case. In crystalline samples, $\varepsilon(\omega)$ and $\sigma(\omega)$ are tensors that reflect the underlying symmetry of the crystal. In isotropic media, e.g., cubic materials such as the antifluorite halides, these tensors can be reduced to a single component, hence, they are treated as scalars here. In crystals with hexagonal symmetry, e.g, α-$RuCl_3$, the tensor displays uniaxial symmetry, which yields an in-plane and out-of-plane component with respect to the hexagonal lattice structure [200]. For an experiment, this requires aligning these samples such that the electric field of the incident beam oscillates parallel to the targeted component.

Optical experiments do not measure $\mathbf{P}$ or $\mathbf{j}$ directly. Instead, we obtain the intensities of transmitted and reflected light. For this purpose, it is helpful to introduce another response function, the complex index of refraction $N(\omega) = n(\omega) + \mathrm{i}\kappa(\omega)$, which facilitates the description of propagating waves in matter. The index of refraction affects the dispersion relation of the electromagnetic wave inside a medium [2],

$$|\mathbf{k}|^2 = \frac{N^2(\omega)}{c^2}\omega^2. \tag{3.8}$$

Applied to Eq. (3.4), this yields

$$\mathbf{E}(\mathbf{r}, t) = E_0 \hat{\epsilon} \exp\left[\mathrm{i}\left(\frac{\omega n}{c}\hat{\mathbf{e}}_k \mathbf{r} - \omega t\right) - \frac{\omega \kappa}{c}\hat{\mathbf{e}}_k \mathbf{r}\right], \tag{3.9}$$

where the real part of the refractive index n alters the phase velocity $v_p = \frac{c}{n}$ and the imaginary part κ, the so-called extinction coefficient, attenuates the amplitude of the propagating

[1] We see that the real part of ε is linked to the imaginary part of σ and vice versa. This phase difference of $\pi/2$ becomes evident, if we recall that the polarization is proportional to the electric dipole moment, i.e., the displacement of the charges $\mathbf{P} \sim e\mathbf{r}$, whereas the current density follows the velocity of the charges $\mathbf{j} \sim e\dot{\mathbf{r}}$.

[2] More precisely, it affects the dispersion of the polariton, a quasiparticle that couples the photon to the transversal eigenmodes of a material [199], see Sec. 3.1.1.

wave. The refractive index is linked to the dielectric function via

$$\frac{c}{N} = \frac{1}{\sqrt{\varepsilon_0 \varepsilon \, \mu_0 \mu}} \overset{\mu \approx 1}{=} \frac{c}{\sqrt{\varepsilon}}, \tag{3.10}$$

where the approximation of the magnetic permeability $\mu \approx 1$ has been motivated in the beginning by considering non-magnetic materials only.
Since our experiments measure the intensity instead of the amplitude, it is convenient to introduce the absorption coefficient

$$\alpha(\omega) = \frac{2\omega\kappa(\omega)}{c}, \tag{3.11}$$

which yields the attenuation of intensity via Lambert's law $I(r) = I_0 \mathrm{e}^{-\alpha r}$. The absorption coefficient is not a microscopic response function itself. Being a measure of the absorbed power density of a sample for a given incident radiation intensity [201], however, it is a helpful quantity to bridge the macroscopic absorption of radiation and the microscopic excitation of charges, see Sec. 3.1.1.
Combining Eq. (3.7), Eq. (3.10), and Eq. (3.11), we can translate the optical response functions into each other. For instance, the optical conductivity reads as

$$\begin{aligned} \sigma_1(\omega) &= \omega\varepsilon_0 \, \varepsilon_2(\omega) = 2\omega\varepsilon_0 \, n(\omega)\kappa(\omega) = \varepsilon_0 c n(\omega)\alpha(\omega), \\ \sigma_2(\omega) &= \omega\varepsilon_0 \, (1 - \varepsilon_1(\omega)) = \omega\varepsilon_0 \left(1 - n^2(\omega) + \kappa^2(\omega)\right). \end{aligned} \tag{3.12}$$

.

The optical conductivity is a particularly useful representation of the excitation spectrum. Its real part is proportional to the absorption coefficient and, thus, directly linked to the microscopic excitation probabilities. Using $\sigma_1(\omega)$ has the advantage that the weight of an excitation feature is preserved irrespective of its energy. Therefore, the spectral weight of an excitation feature can be determined directly via integration

$$SW = \int_{\omega_1}^{\omega_2} \sigma_1(\omega) \, \mathrm{d}\omega, \tag{3.13}$$

when it is located in the energy range between $\hbar\omega_2$ and $\hbar\omega_1$. The spectral weight is a sensitive measure for the size of the transition dipole moment. For instance, comparing the size of SW, this can be used to discern allowed from forbidden transitions [86]. In the case of parity-forbidden excitations such as *dd* excitations, we can identify the phonon-assisted character by tracing the temperature dependence of the spectral weight that follows the thermal population of the symmetry-breaking phonon modes [85, 202]

$$SW(T) = \alpha + \sum_i \beta_i \coth\left(\frac{\hbar\omega_i}{2k_\mathrm{B}T}\right), \tag{3.14}$$

where α and β are fitting parameters. The coth term emerges from considering both phonon-creation and phonon-annihilation processes, see Sec. 3.1.1. Typically, several

symmetry-breaking phonons with their corresponding energies $\hbar\omega_i$ can contribute to phonon-assisted excitations, and as a result the line shape can become broad and smeared. In case a single phonon mode is dominating, the analysis of the temperature dependence can be used as a tool to determine the energy of this mode, see chap. 4.
Reflecting the size of the matrix elements, the temperature dependence of the spectral weight can also be used as a sensitive gauge for nearest-neighbor spin and orbital correlations when studying intersite excitations, e.g., in 3d manganites and ferrites [203–205]. It can also be used to discriminate different scenarios based on competing energy scales, as shown for Ca_2RuO_4 [155]. In α-$RuCl_3$, we distinguish the onsite and intersite character of the single and double spin-orbit exciton from the temperature dependence of the spectral weight.

Electromagnetic waves at interfaces

Experimentally, we have to determine the optical response functions from the transmitted and reflected light. Equation (3.9) describes the propagation of an electromagnetic wave within the sample. Additionally, we have to account for transmission and reflection at the interfaces between the sample and its surrounding. The Fresnel formulas yield the transmission and reflection amplitudes when light passes under the angle of incidence Θ through an interface between two media with N_1 and N_2. For nonzero Θ, two cases have to be distinguished: the electric field is polarized either parallel or perpendicular with respect to the scattering plane. Arbitrary polarization can be decomposed into these two. Following [199], the reflection and transmission coefficients r_α and t_α, with $\alpha = p, s$ for parallel and perpendicular (German: senkrecht) read

$$\begin{aligned} r_p &= \frac{E_{r,p}}{E_{i,p}} = \frac{N_2 \cos\Theta - N_1 \cos\Theta'}{N_2 \cos\Theta + N_1 \cos\Theta'}, \\ r_s &= \frac{E_{r,s}}{E_{i,s}} = \frac{N_1 \cos\Theta - N_2 \cos\Theta'}{N_1 \cos\Theta + N_2 \cos\Theta'}, \\ R_\alpha &= |r_\alpha|^2, \end{aligned} \tag{3.15}$$

and

$$\begin{aligned} t_p &= \frac{E_{t,p}}{E_{i,p}} = \frac{2N_1 \cos\Theta}{N_2 \cos\Theta + N_1 \cos\Theta'}, \\ t_s &= \frac{E_{t,s}}{E_{i,s}} = \frac{2N_1 \cos\Theta}{N_1 \cos\Theta + N_2 \cos\Theta'}, \end{aligned} \tag{3.16}$$

where Θ' denotes the angle of the refracted beam according to Snell's law. Figure 3.1(a) shows the reflection and refraction of the electromagnetic wave with p polarization. For normal incidence ($\Theta = \Theta' = 0$), parallel and perpendicular polarization cannot be discriminated, and the distinction is omitted. The reflectance of that single interface R_α is the absolute square of the reflection coefficient r_α, in other words, the intensity ratio. For

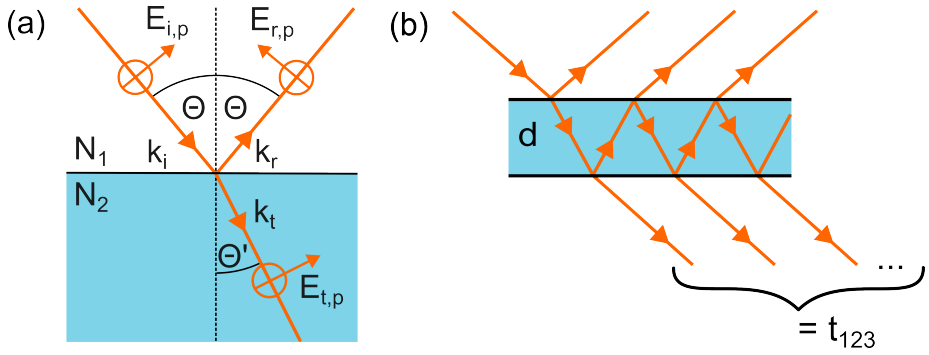

Figure 3.1 (a) Depiction of refraction and reflection of an electromagnetic wave that hits an interface between two media with N_1 and N_2 under a given angle of incidence Θ according to Snell's law. The large arrows indicate the propagation direction of the incident, reflected, and transmitted waves. The smaller arrows tell the polarization direction for the electric field oscillating parallel to the plane of incidence. The perpendicular component is also indicated by the circled crosses. (b) Sketch of reflection and transmission through a slab with thickness d. Multiple reflections lead to multiple partial beams that contribute to the total transmission and reflection coefficients according to Eq. (3.17).

a transmission experiment on a bulk single crystal, the incident waves have to cross the front and the rear interface between the sample and its surrounding. For simplicity, we assume that the sample is surrounded by vacuum. As such, we can write $N_1 = N_3 = 1$ for the refractive index in front of and behind the sample and $N_2 = N$ for the sample itself. At each interface, the waves will obey the Fresnel equations, which will result in multiple reflections within the sample. The reflectance and transmittance of a sample with parallel surfaces and a thickness d can be calculated by taking the coherent sum over all partial waves. Combined with Eq. (3.9), each partial wave acquires a complex phase $\exp[\mathrm{i}N\omega d/c]$ when passing through the sample. Labeling the transmission and reflection amplitude of the first interface from vacuum into the sample $t_{1,2}$ and $r_{1,2}$, and analogously of the second interface from the sample into vacuum $t_{2,3}$ and $r_{2,3}$, the total reflectance R_{123} and transmittance T_{123} under normal incidence are given by [199]

$$\begin{aligned} R_{123} &= |r_{123}|^2 = \left| \frac{r_{1,2} + r_{2,3} \exp[i2N\omega d/c]}{1 - r_{2,1} r_{2,3} \exp[i2N\omega d/c]} \right|^2 , \\ T_{123} &= |t_{123}|^2 = \left| \frac{t_{1,2} t_{2,3} \exp[\mathrm{i}N\omega d/c]}{1 - r_{2,1} r_{2,3} \exp[i2N\omega d/c]} \right|^2 . \end{aligned} \tag{3.17}$$

A conceptual sketch of multiple reflections within a sample is depicted in Fig. 3.1(b). For sufficiently thin samples, the transmittance and reflectance will acquire a discernible intensity modulation, i.e., Fabry-Pérot interference fringes, based on the interference of the partial waves. We will analyze the interference fringes as a tool to determine the index of refraction $n(\omega)$ in Sec. 3.2. In case we can neglect the effect of Fabry-Pérot fringes,

e.g., for sufficiently thick samples[3] or by filtering out the interference fringes, we can use a simplified expression for the reflectance and transmittance. In this case the total reflectance is obtained from the reflection from the first interface as in Eq. (3.15) and the transmittance is obtained by performing an incoherent sum, i.e., adding the intensities of the partial waves. Then, for transparent samples with $n \gg \kappa$, the total reflectance and transmittance read

$$\begin{aligned} R &= \frac{(n-1)^2+\kappa^2}{(n+1)^2+\kappa^2} \approx \frac{(n-1)^2}{(n+1)^2} \\ T &= \frac{(1-R)^2 \exp\left[-2\kappa\omega d/c\right]}{1-R^2 \exp\left[-4\kappa\omega d/c\right]}, \end{aligned} \tag{3.18}$$

which can be inverted to yield the complex index of refraction $N(\omega) = n(\omega) + i\kappa(\omega)$ and subsequently the dielectric function and optical conductivity via Eq. (3.12).

3.1.1 Probing electronic excitations

Electric dipole transitions

Microscopically, excitations arise as transitions between an initial ground state $|i\rangle$ and an excited final state $|f\rangle$ that are rooted, for example, in the phenomena discussed in Chapter 2. Using linear optical spectroscopy, we probe these excitations via the absorption of light, where the frequency of the absorbed radiation is indicative of the excitation energy between these states, while the absorption strength is linked to the transition probability between them. The goal of the following discussion is to motivate the selection rules and mechanisms that allow us to study the excitations of interest. The typical starting point of this discussion treats the interaction between the incident radiation and the charges in the crystal as a perturbation and determines the transition rates via Fermi's golden rule. This section follows [198, 199, 201], which are suggested for further reading. Semiclassically, the Hamiltonian describing the interaction of a bound electron in the presence of an electromagnetic field can be written as

$$H = H_0 + \underbrace{\frac{e}{m}\mathbf{A}(\mathbf{r},t)\cdot\mathbf{p} + \frac{e^2}{2m}\mathbf{A}^2(\mathbf{r},t)}_{:=H'}, \tag{3.19}$$

where H_0 denotes the unperturbed electronic Hamiltonian, and e, m, and $\mathbf{p}$ represent the electron's charge, mass, and momentum, respectively. $\mathbf{A}(\mathbf{r},t)$ is the vector potential used to express the incident electromagnetic radiation. Note that Eq. (3.19) is expressed using the Coulomb gauge $\nabla\cdot\mathbf{A}(\mathbf{r},t) = 0$, and as a result, the vector potential can be treated as a transverse plane wave $\mathbf{A}(\mathbf{r},t) = A_0\,\hat{\epsilon}\left(\mathrm{e}^{\mathrm{i}(\mathbf{kr}-\omega t)} + \mathrm{e}^{-\mathrm{i}(\mathbf{kr}-\omega t)}\right)$. Treating the incident radiation

[3] For a transmission measurement, the sample has to be still thin enough to yield a measurable signal.

as a weak perturbation, we can apply Fermi's golden rule

$$w_{fi} = \frac{2\pi}{\hbar} |\langle f|H'|i\rangle|^2 \delta(E_f - E_i - \hbar\omega), \tag{3.20}$$

to determine the transition rate w_{fi} between initial and final states. In linear response, H' is treated as a first-order perturbation, which means the $\mathbf{A}^2(\mathbf{r}, t)$ term is discarded. In the picture of field quantization, this restricts the excitations we probe to single-photon processes. In the long-wavelength limit of optics, we apply the dipole approximation, which implies that the amplitude of the vector potential is considered constant across a characteristic length scale of the system, e.g., the ionic radius of a bound electron. As such, the vector potential $A_0\, \mathrm{e}^{\mathrm{i}\mathbf{kr}} \approx A_0$ acts as a prefactor instead of an operator [206].[4] Consequently, the matrix elements of H' reduce to matrix elements of the momentum operator. Given the operator identity $\mathbf{p} = \mathrm{i}\frac{m}{\hbar}[H_0, \mathbf{r}]$ and the fact that $|i\rangle$ and $|f\rangle$ are eigenstates of H_0, we can express the matrix elements of the momentum operator as

$$\langle f|\mathbf{p}|i\rangle = \mathrm{i}\frac{m}{\hbar}\langle f|\,[H_0, \mathbf{r}]\,|i\rangle = \mathrm{i}\frac{m}{\hbar}\left(E_f - E_i\right)\langle f|\mathbf{r}|i\rangle, \tag{3.21}$$

and subsequently the transition rate

$$\begin{aligned} w_{fi} &= \frac{2\pi}{\hbar} A_0^2 \omega^2 e^2 |\langle f|\hat{\epsilon}\cdot\mathbf{r}|i\rangle|^2 \\ \Leftrightarrow\ w_{fi} &= \frac{2\pi}{\hbar} |\mathbf{E}|^2 e^2 |\langle f|\hat{\epsilon}\cdot\mathbf{r}|i\rangle|^2. \end{aligned} \tag{3.22}$$

where we used $\mathbf{E}(\mathbf{r}, t) = -\partial_t \mathbf{A}(\mathbf{r}, t)$ in the last step. As mentioned above, we can use the absorption coefficient $\alpha(\omega)$ to link the transition rates to the response functions. With the absorbed power density $P(\omega) \propto \hbar\omega w_{fi} N_f$, where N_f is the density of absorbing states and the incident radiation intensity $I(\omega) = \varepsilon_0\, cn(\omega)|\mathbf{E}(\omega)|^2$, we find

$$\alpha(\omega) = \frac{P(\omega)}{I(\omega)} \propto \frac{\hbar\omega w_{fi} N_f}{\varepsilon_0\, cn(\omega)|\mathbf{E}(\omega)|^2}. \tag{3.23}$$

Thus, we see that the optical response functions, in particular $\sigma_1(\omega)$, are well-suited quantities to reflect the excitation spectrum of a material. In-depth discussions on the optical sum rules that govern the relation between dissipation and particle density are found in [201, 207].

Selection rules

The matrix elements in Eq. (3.22) are conventionally called transition dipole moments and determine the selection rules for electric-dipole transitions. The photon polarization

[4] Despite the much smaller wavelength used in RIXS, the dipole approximation is still valid to describe the leading-order contribution of the RIXS process [206].

selects the component of the position operator, which in turn yields the matrix elements. The symmetry of the initial and final states dictates whether the excitation has a non-zero value. For

$$\langle f|\mathbf{r}|i\rangle = \int \Psi_f^* \mathbf{r} \Psi_i \, \mathrm{d}\mathbf{r}' \neq 0, \tag{3.24}$$

we see immediately that the integrand must be even in symmetry. Since the position operator has odd symmetry, this implies that the symmetry between the initial and final states must change from even to odd or vice versa. The two main rules governing non-zero matrix elements are the Laporte rule and the spin-selection rule [176], from which the electric-dipole selection rules can be inferred. The Laporte rule applies for systems with inversion symmetry, such as octahedral complexes, where parity $\hat{\pi}$ is a good quantum number. In these cases, the initial and final states must have opposite parity $\hat{\pi}_f \cdot \hat{\pi}_i = -1$ to yield non-zero matrix elements. In the single-electron picture, the parity operator is determined by the orbital quantum number as $\hat{\pi} = (-1)^l$, leading to the selection rule $\Delta l = \pm 1$. It allows, for instance, the transition of an electron between the p and the d shell but inhibits transitions within the same shell. At the same time, the spin-selection rule states $\Delta S = 0$, meaning spin-flip excitations are forbidden. Intersite excitations, such as Mott-Hubbard and charge-transfer excitations, break inversion symmetry, making parity no longer a good quantum number. This typically results in large dipole moments and strong absorption. For general electron configurations, intrasite excitations within LS coupling follow $\Delta L = 0, \pm 1$, excluding transitions from $L = 0 \rightarrow 0$ [208]. This implies that the change of the orbital moment can be shared among the electrons to the extent that ΔL can remain zero. Similarly, under LS or jj coupling, where J is a good quantum number, the selection rule is $\Delta J = 0 \pm 1$, except for $J = 0 \rightarrow 0$ [208]. Finally, the polarization of the light imposes further constraints. For a given magnetic quantum number m_J, linearly polarized light allows transitions with $\Delta m_J = 0$. Circularly polarized light permits transitions with $\Delta m_J = \pm 1$ [208]. Experiments with unpolarized light typically allow both.

Phonon-assisted mechanism

At first glance, the Laporte rule prohibits accessing intrasite dd excitations with optical spectroscopy. Defects or crystals with broken inversion symmetry can (partially) lift these restrictions, but when inversion symmetry is present, tools like Raman scattering or RIXS, which are sensitive to parity-preserving excitations, appear as a better choice. The remedy for this constraint arises in our cases in the form of phonon-assisted excitations. The main idea is sketched in Fig. 3.2. A phonon mode with odd symmetry admixes p character into the wavefunction and breaks inversion symmetry. In this scenario the initial and final wavefunctions can be written as a mixture of d and p character [209, 210]. Hence, we find

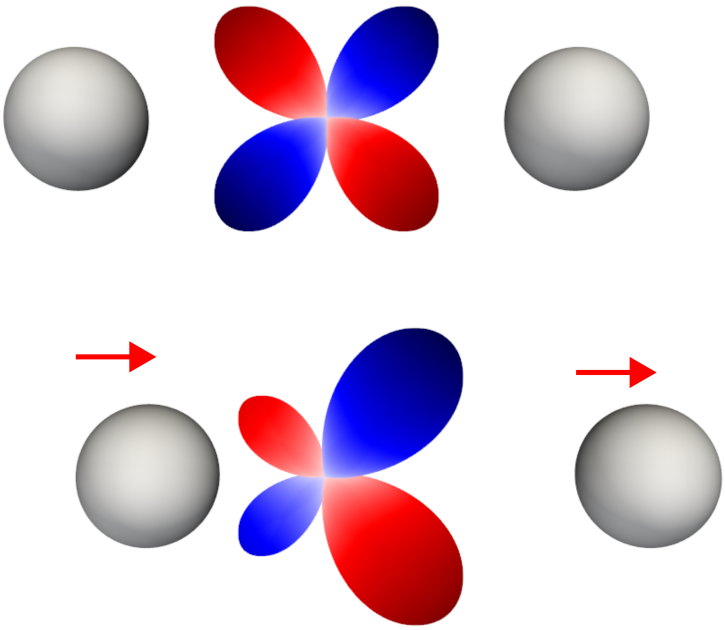

Figure 3.2 Sketch of the symmetry breaking process due to an odd-parity phonon. The upper part shows the $|xy\rangle$ orbital of a transition metal ion between two ligands (gray spheres). The lower part shows how a shift of these ligands, i.e., an odd-parity phonon, breaks inversion symmetry.

for the matrix elements

$$\langle \alpha' d_f + \beta' p_f | \mathbf{r} | \alpha d_i + \beta p_i \rangle = \underbrace{\langle \alpha' d_f | \mathbf{r} | \alpha d_i \rangle}_{=0} + \underbrace{\langle \beta' p_f | \mathbf{r} | \beta p_i \rangle}_{=0} + \underbrace{\langle \beta' p_f | \mathbf{r} | \alpha d_i \rangle}_{\neq 0} + \underbrace{\langle \alpha' d_f | \mathbf{r} | \beta p_i \rangle}_{\neq 0}, \tag{3.25}$$

where α, α', β, and β' are the mixing coefficients. While the first two terms vanish, we find that the latter two are generally in agreement with the selection rules stated above. Thus, the simultaneous excitation of an intrasite electronic excitation and an odd-parity phonon mode is, albeit not very strong, dipole-allowed. Correspondingly, the excitation energy is found as the sum of the electronic excitation energy and the odd-parity phonon $E = E_{el} + E_{\text{odd}}$. The weight of this feature scales with $1 + n(T)$, where $n(T)$ is the thermal occupation of the phonon. Conversely, at elevated temperatures, the complementary process to annihilate an odd-parity phonon to create an electronic excitation at $E = E_{el} - E_{\text{odd}}$ can also be observed and scales with $n(T)$. Using the identity $1 + 2n(T) = \coth \frac{1}{2T}$, we can recover the temperature dependence of the spectral weight of the entire feature in Eq. (3.14). In principle, all infrared-active phonons can couple in this manner to electronic excitations. Depending on lattice geometry and symmetry, the strength of this mechanism will differ. For α-$RuCl_3$ with edge-sharing octahedra arranged on a honeycomb lattice,

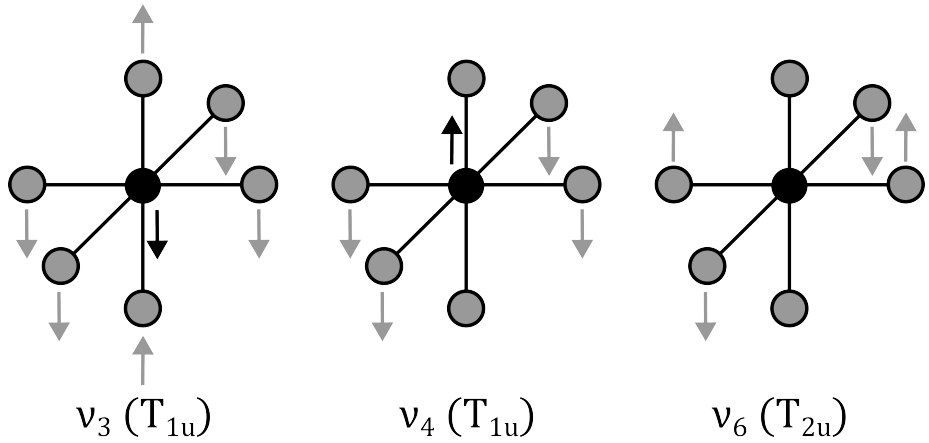

Figure 3.3 The normal modes of an octahedral complex that exhibit odd symmetry. The label ν_i typically orders the modes in a descending manner with respect to their frequency [211]. The term in brackets denotes their symmetry label in Mulliken notation, where *u* refers to *ungerade*, i.e., odd [85].

we find that the phonon-assisted excitations couple predominantly to one single phonon mode. For the isolated octahedra in the antifluorites, a superposition of several phonon modes is displayed. The internal odd-parity phonons of octahedral complexes are shown in Fig. 3.3.

As multiparticle excitations, phonon-assisted features are orders of magnitude weaker than directly dipole-allowed excitations. As such, they are easily masked by any directly allowed excitation in their vicinity. A clear example is the excitation from the $J = 0$ ground state to the $^1A_1$ multiplet at about 2.1 eV in K_2OsCl_6, see chap. 5. Above 150 K, this excitation is masked by the Urbach tail of the Mott gap. Only at lower temperatures, where the Mott gap is at higher energy, can the weak and narrow peak structure of the $^1A_1$ multiplet be resolved. In the corresponding bromide compound K_2OsBr_6, the energy of the onset of the Mott gap is lowered to around 1.8 eV at 5 K, such that the transition into the $^1A_1$ multiplet is buried for all temperatures.

Analogous to the discussion above, spin-orbit coupling can circumvent the spin-selection rule $\Delta S = 0$ [207]. In the presence of spin-orbit coupling, the Hund's multiplets are not eigenstates of the system. Typically, 4*d* and 5*d* states show an admixture of several multiplets. As such, terms with the same spin multiplicity can yield non-zero matrix elements. Again, compared to spin-allowed transitions, these are orders of magnitude weaker. An interesting comparison between phonon-assisted excitations is given by $5d^5$ K_2IrCl_6 and $5d^3$ K_2ReCl_6, see chap. 7 and 6. In the Ir compound, the spin-orbit exciton is an excitation that originates from strong spin-orbit coupling, and it shows a spectral weight of roughly $0.2\,\mathrm{eV}\,\Omega^{-1}\,\mathrm{cm}^{-1}$ at 10 K. In the Re compound, the t_{2g}^3 configuration has a quenched orbital moment, which diminishes the effect of spin-orbit coupling. The ground state shows $S = 3/2$, and all five intra-t_{2g} excitations have $S = 1/2$, i.e., they include a spin flip.

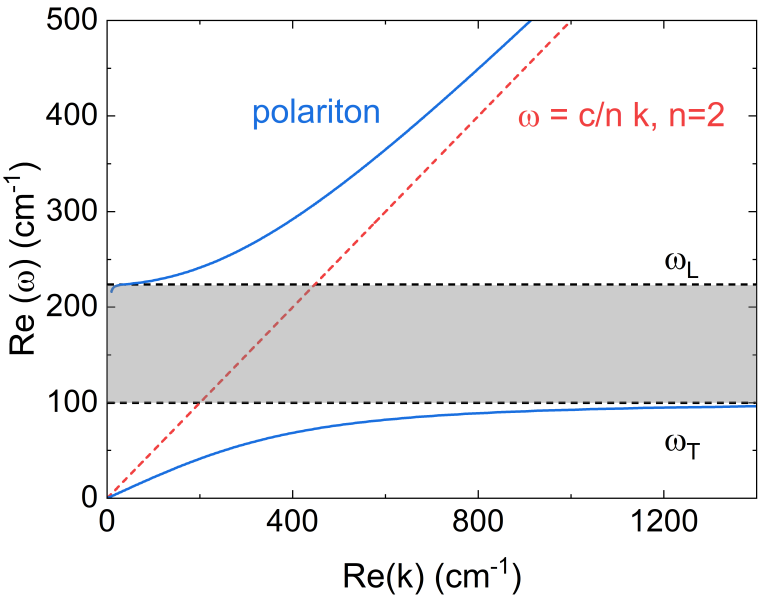

Figure 3.4 Dispersion relation of a polariton following Eq. (3.8) (blue curve) and a photon assuming a constant $n = 2$ (red dashed curve). The underlying model for $N(\omega)$ is based on a Lorentz oscillator with $\omega_0 = 100\,\mathrm{cm}^{-1}$, $\omega_p = 400\,\mathrm{cm}^{-1}$, damping $\gamma = 2\,\mathrm{cm}^{-1}$, and $\varepsilon_\infty = 4$. The gray area marks the highly reflective Reststrahlenbande [199] between ω_0 and ω_L, where no photon states are available. The longitudinal frequency can be calculated via the Lydanne-Sachs-Teller relation [199, 212].

Thereby, we observe much weaker intensities of any of these five excitations with spectral weights up to $0.01\,\mathrm{eV}\,\Omega^{-1}\,\mathrm{cm}^{-1}$ at 18 K. In both compounds, we can identify weaker features within these absorption bands that possibly originate from magnetic dipole transitions.

The Lorentz oscillator model and line profiles

The classical analogue of the electric-dipole transitions from Sec. 3.1.1 can be described by the Lorentz oscillator model. It yields a widely used model function for the dielectric function $\varepsilon(\omega)$ to describe the response of bound charges in terms of harmonic oscillators [199]. It is commonly expressed as

$$\begin{aligned} \varepsilon(\omega) &= \varepsilon_\infty + \sum_j \frac{\omega_{p,j}^2}{\omega_{0,j}^2 - \omega^2 - \mathrm{i}\gamma_j\omega} \\ \Leftrightarrow\ \varepsilon(\omega) &= \varepsilon_\infty + \sum_j \left(\frac{\omega_{p,j}^2 \left(\omega_{0,j}^2 - \omega^2\right)}{\left(\omega_{0,j}^2 - \omega^2\right)^2 + \gamma_j^2\omega^2} + \mathrm{i}\frac{\omega_{p,j}^2\gamma_j\omega}{\left(\omega_{0,j}^2 - \omega^2\right)^2 + \gamma_j^2\omega^2} \right), \end{aligned} \tag{3.26}$$

and describes the response from a set of j individual dipole oscillators with transverse eigenfrequency $\omega_{0,j}$, damping coefficient γ_j, and plasma frequency $\omega_{p,j}$, which determines the strength of the dipole moment. The term ε_∞ accounts for any high-energy contribution that is not explicitly considered in the sum of oscillators. On a microscopic level, Eq. (3.8) describes the dispersion of the polariton, a quasiparticle that results from the coupling of a photon to a dipole-carrying mode in a crystal. Based on the Lorentz model, we show the dispersion of the polariton in Fig. 3.4. Far away from any mode in a material, the dispersion of the polariton resembles the linear dispersion of the photon, meaning it behaves *photon-like*. However, as it approaches a transverse mode from lower frequencies, the polariton adopts the character of that mode. Assuming for simplicity an optical phonon, the polariton is said to behave *phonon-like* and fully acquires the phonon character at resonance. This corresponds to the case discussed earlier when the photon is absorbed to create an excitation. Neglecting damping, $\varepsilon_1(\omega = \omega_0)$ diverges. While the transverse character of photons does not allow coupling to the longitudinal modes directly, these modes with their frequency ω_L can create strong depolarization fields, which in turn yield $\varepsilon_1(\omega) < 0$ for frequencies $\omega_0 < \omega < \omega_L$. As a consequence, there are no real states for photons to occupy available, and the material exhibits strong reflectivity.
Accounting for both dispersion and dissipation, the Lorentz model is Kramers-Kronig consistent and a versatile model for describing optical properties [213–216]. It works particularly well when the observed excitations correspond to discrete, well-defined transitions indicated by the Lorentzian profiles in $\varepsilon_2(\omega)$. In cases where absorption features display a distribution of excited states, such as overlapping Mott-Hubbard excitations [155, 217], or due to dispersion or higher-order couplings in the vibronic sidebands of Franck-Condon-type excitations [209, 218, 219], it is common practice to describe $\varepsilon_2(\omega)$ with Gaussian profiles,

$$\varepsilon_2(\omega) = \sum_j \frac{A_j}{\gamma_j \sqrt{\pi}} \exp\left(-\frac{(\omega - \omega_{0,j})^2}{\gamma_j^2}\right), \tag{3.27}$$

where $\omega_{0,j}$ are the transverse eigenfrequencies, $2\sqrt{\ln 2}\,\gamma_j$ the full-widths-at-half-maximum, and A_j the weights of that oscillators. A special case is the Tauc-Lorentz model [216, 220], which empirically describes the asymmetric lineshape of excitations across the "band" gap, showing a steep increase coming from lower frequencies and a long tail above its peak frequency,

$$\varepsilon_2(\omega) = \frac{1}{\omega} \frac{A\omega_0\gamma\left(\omega - \omega_g\right)^2}{(\omega - \omega_0)^2 + \gamma^2\omega^2} H(\omega - \omega_g). \tag{3.28}$$

Here, ω_0, A, and γ are again the transverse eigenfrequency, the oscillator strength, and the damping coefficient. The Heaviside function $H(\omega - \omega_g)$ is zero below the gap frequency ω_g and unity above it. The real part of the dielectric function of these oscillators is typically obtained from the Kramers-Kronig relations [221, 222].

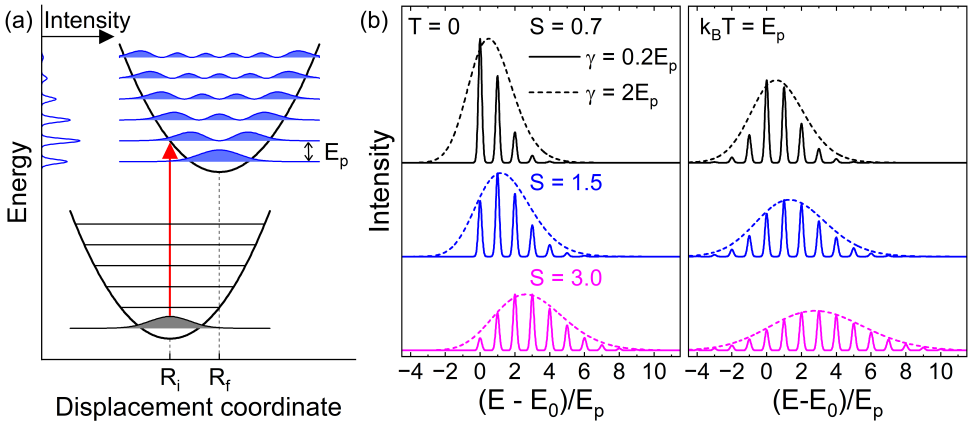

Figure 3.5 (a) Sketch of the Franck-Condon principle. The two parabolas correspond to the harmonic lattice potential for two different electronic states that show different equilibrium positions at $\mathbf{R}_i$ and $\mathbf{R}_f$. The Franck-Condon principle states that an electronic excitation occurs instantaneously. This is depicted by the vertical red arrow. The shaded areas indicate the squared amplitude of the vibrational states. These are separated by the energy E_p. At $T = 0$, the intensity distribution between different vibrational levels follows Eq. (3.31). The left side shows an intensity spectrum of narrow Gaussian lines with $S = 1.5$. (b) Comparison between line shapes with different parameters. The left panel shows the case for $T = 0$ for narrow and fully resolved sideband peaks (solid lines) and broad unresolved sidebands (dashed lines). The colors depict cases for different Huang-Rhys factors. The right panel shows the same lineshapes at finite temperature $k_\mathrm{B}T = E_\mathrm{p}$.

Vibronic excitations

Vibronic excitations are excitations of mixed vibrational and electronic character, where the absorption or emission of radiation induces a change in both electronic and lattice energy. A central ingredient in vibronic excitations is electron-phonon coupling. In solids, electron-phonon coupling manifests in many ways, ranging from the formation of charge density waves and the Peierls transition in one-dimensional systems [223], to the conventional mechanism of phonon-mediated superconductivity [224], and to the formation of polarons, quasiparticles that describe an electron dressed by a cloud of virtual phonons [225].

For this work, we restrict the discussion of vibronic excitations to the case of weak electron-phonon coupling. In the limit of vanishing electron-phonon coupling, the Born-Oppenheimer approximation applies, which decouples the dynamics of the electrons and ions [226]. In this limit, vibronic excitations can be described by the Franck-Condon principle, which was originally formulated for molecules but can also be applied to crystals [227–230]. The Franck-Condon principle states that the transition during an electronic excitation (or relaxation) occurs instantaneously with respect to the timescale of the lattice dynamics. If the lattice potential in the ground state has its minimum energy at the

equilibrium position $\mathbf{R}_i$, an electronic transition may shift this equilibrium position to $\mathbf{R}_f$ in the excited state. This shift reflects the change of the charge distribution and the corresponding change of the effective potential felt by the ions. Since the electronic transition is "vertical", the lattice will be in an excited state with excited phonons. Thus, the final state incorporates both the electronic transition and a change in the phonon occupation. Experimentally, this gives rise to phonon sidebands that accompany the electronic excitation feature. To first order, the phonon sidebands are equidistant, separated by the phonon energy E_p. The schematic idea of the Franck-Condon principle is depicted in Fig. 3.5(a). A characteristic signature of vibronic excitations is the intensity distribution of these sidebands. We make use of this intensity distribution to identify a vibronic character and discard other effects that might create a multipeak structure. As a consequence of the Born-Oppenheimer approximation, the vibronic wavefunction can be written as a product state, $|\Psi(\mathbf{r},\mathbf{R})\rangle = |\psi(\mathbf{r},\mathbf{R})\,\phi(\mathbf{R})\rangle$, where $|\psi\rangle$ is the electronic wavefunction and $|\phi\rangle$ the vibrational wavefunction [231]. The corresponding transition dipole moment gives [5]

$$\langle\Psi_f|\mathbf{d}|\Psi_i\rangle = \langle\psi_r|e\mathbf{r}|\psi_i\rangle\langle\phi_f(\mathbf{R}_f)|\phi_i(\mathbf{R}_i)\rangle. \tag{3.29}$$

The Franck-Condon parameters are a measure of the intensity of the vibronic sidebands and are calculated from the squared overlap of the vibrational wavefunctions. At $T = 0$ with no thermally occupied phonons, the Franck-Condon parameters read

$$F_0^m = |\langle\phi_m|\phi_0\rangle|^2 = \frac{\mathrm{e}^{-S}S^m}{m!}. \tag{3.30}$$

Here, m is the number of excited phonons and S the Huang-Rhys factor that characterizes the vibronic band. The envelope of the intensity follows a Poisson distribution with the mean value S. The full intensity spectrum becomes

$$I(E) = \underbrace{\left|\langle\psi_f|e\mathbf{r}|\psi_i\rangle\right|^2}_{:=\,I_0} \sum_{m=0}^{\infty} \frac{\mathrm{e}^{-S}S^m}{m!}\,\delta(E_0 + mE_p - E). \tag{3.31}$$

Note that for *dd* excitations in crystals with inversion symmetry, we have to include the phonon-assisted mechanism in optics, hence , $E_0 = E_{el} + E_{\mathrm{odd}}$. For better agreement with experimental data, the sharp δ peaks are replaced by Gaussians shown in Eq. (3.27). The resulting lineshape shows a progression of equidistant peaks separated by E_p starting from E_0. The largest overlap, i.e., the maximum intensity, is typically found between $E_{\max} = S - \frac{1}{2}$ and $E_{\max} = S$ and depends on the value of S and the Gaussian broadening γ [232]. Examples for different S are shown in Fig. 3.5(b).

[5] Note that the analogous case of a phonon excitation accompanied by electronic sidebands is suppressed, since the overlap $\langle\psi_f|\psi_i\rangle$ vanishes due to the orthogonality between electronic wavefunctions. Physically, this reflects the Born-Oppenheimer approximation: due to the vast mass difference, the lighter electrons can follow the ions and occupy their respective ground state instantaneously.

At finite temperatures, the thermal phonon occupation $n_p = 1/\left(\mathrm{e}^{E_p/k_\mathrm{B}T} - 1\right)$ has to be included. Following [85], the intensity distribution becomes

$$I(E) = I_0 \sum_{m=-\infty}^{\infty} \left(\frac{n_p+1}{n_p}\right)^{\frac{m}{2}} \mathrm{e}^{-S(2n_p+1)} J_m\left(2S\sqrt{n_p(n_p+1)}\right) \frac{A}{\gamma\sqrt{\pi}} \mathrm{e}^{-\frac{\left(E_0+mE_p-E\right)^2}{\gamma^2}} \tag{3.32}$$

where J_m is the modified Bessel function of mth order. The main effect of temperature is a broadening of the full lineshape, redistributing weight to outer sidebands.
The Franck-Condon picture has been applied successfully to many different compounds. In solids, the existence of several or even many phonon branches and the finite dispersion of phonons typically washes out the detailed structure of the sidebands, such that basically only the envelope is observed. Therefore it is usually not possible to probe aspects that go beyond the Franck-Condon picture. In contrast, the quasimolecular structure of the antifluorite halides allows us to precisely resolve the individual sidebands. In K_2IrCl_6, we use this opportunity to discuss effects that are arise due to finite electron-phonon coupling. In particular, Iwahara and Furukawa have addressed the role of electron-phonon coupling in K_2IrCl_6 [137]. They calculate that the coupling of the $j = 3/2$ state to E_g phonon modes induces a dynamic Jahn-Teller effect that is responsible for the splitting of the spin-orbit exciton in this compound. This scenario is very similar to our discussion of vibronic excitations with the Franck-Condon principle, but it describes the case of considerable electron-phonon coupling. In this case, the vibronic states are not simply product states of electronic and vibrational wavefunctions due to hybridization. In terms of vibronic excitations, this goes beyond the Franck-Condon picture.
To analyze this, we still describe the data of K_2IrCl_6 with the simple Franck-Condon picture. The dynamic Jahn-Teller effect comes into play when looking at the resulting parameters. The Huang-Rhys factors indicate a considerable increase of coupling to the phonons as a function of temperature. In addition, the energy of the progression increases beyond the energy of bare phonon modes, which cannot be motivated from the ideal Franck-Condon scenario. This effect is a manifestation of spin-orbit entangled states coupled to phonons conglomerating to spin-orbital-lattice entanglement.

3.2 Fourier-transform infrared spectroscopy

Fourier-transform infrared spectroscopy (FTIR) is a widely used technique to measure the optical response of samples over a broad range of frequencies. Instead of utilizing dispersive elements like gratings to monochromatize the beam, this method relies on an interferometer to modulate the intensity temporally and a computer to extract the intensity spectrum $I(\omega)$ via a Fourier transform of that modulated signal. Detailed descriptions of this method can be found in [199, 233–235], hence, only the basic principle is outlined in the following. A lamp emits polychromatic light, which is focused and guided to a Michelson interferometer, the central pillar of the spectrometer. The Michelson interferometer consists of a beam splitter and two mirrors. The incident light is separated by the

beam splitter into two partial beams, which travel towards one of the mirrors each and bounce back to meet at the beam splitter, where they interfere. After interference, the light is then focused onto the sample to probe either transmission or reflection and to be subsequently collected by the detector. Of central importance for the interferometer is the temporally modulated movement of one of the mirrors, which is called the scanner. A uniform displacement of the scanner modulates the path length difference between the two partial beams, which in turn modulates the intensity based on constructive and destructive interference among the various frequency components of the polychromatic beam. This spatially modulated intensity profile $I(x)$ is the interferogram. In motion, the position of the scanner can be determined precisely by a parallel measurement of the intensity modulation of a HeNe laser with a fixed wavelength $\lambda = 633\,\text{nm}$. The resulting intensity spectrum $I(\omega)$ is then recovered from a discrete Fourier transform of the interferogram [233]. Due to the Fourier transform of the interferogram, the intensity spectra are typically given in wavenumbers $\nu\,[\text{cm}^{-1}]$. The corresponding frequency is $\omega = 2\pi c\nu$. A sketch of the utilized FTIR spectrometer, the Bruker IFS 66/v, is shown in Fig. 3.6.
One key advantage of FTIR over dispersive methods is a greatly enhanced signal-to-noise ratio, which compensates for the weaker light intensity for photons with lower energy. This results from three factors. First, the resolution is not limited by the slit width of the aperture. Instead, it is determined by the maximum path length difference given by the displacement of the scanner. This allows the use of circular apertures, significantly increasing intensity and enhancing the signal-to-noise ratio compared to slit-like apertures. By measuring all frequency components simultaneously, it further improves the signal-to-noise ratio, particularly for frequency components with weak intensity. Collecting and averaging multiple scans further enhances the signal-to-noise ratio. However, due to the finite displacement of the scanner, the interferogram is truncated, which affects the Fourier transformation. To minimize truncation artifacts, an appropriate apodization function is applied to smooth the interferogram at the edges. Additionally, the spectral point density can be increased numerically through zero-filling, i.e., adding zeros at both ends of the interferogram. This is an effective method to interpolate the intensity spectrum without distorting the line shape. A comprehensive discussion on the properties of the Fourier transform is given in [233].

Range	Energy (cm^{-1})	Lamp	Beam splitter	detector
MIR	500 to 8000	Globar	KBr	MCT
NIR	3000 to 14 000	tungsten lamp	CaF_2 NIR	MCT
VIS	8500 to 26 000	tungsten lamp	CaF_2 UV	Si diode

Table 3.1 List of combinations of optical components used for the measurements in different frequency ranges. Abbreviations: MIR: mid infrared, NIR: near infrared, VIS: visible, Globar: glow bar – a thermal light source made out of SiC, MCT: Mercury Cadmium Telluride detector.

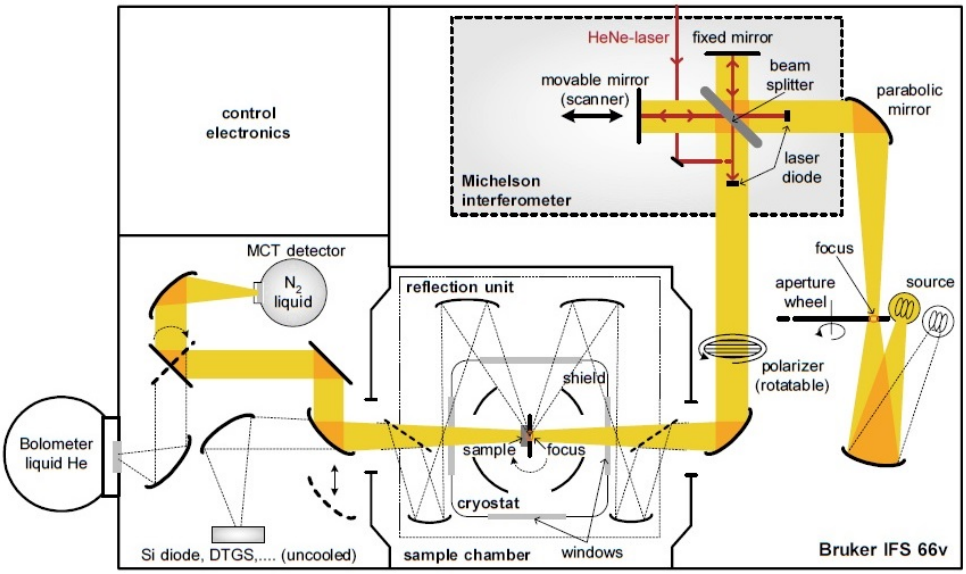

Figure 3.6 Experimental setup and beam path inside the Bruker IFS 66/v. Taken from [210]. The highlighted part marks the light path through the components of the spectrometer for a transmittance measurement. Additionally, an optional polarizer and the reflectivity unit for reflectance measurements are depicted.

Experimental setup and measurement considerations

The FTIR spectrometer is a versatile setup that can measure optical properties from the far infrared up to the ultraviolet range. This is achieved by using several optical components, i.e., suitable light sources, beam splitters, cryostat windows, and detectors. In this work, we cover the range from mid-infrared (MIR) over the near-infrared (NIR) up to the visible/near-UV frequency range (VIS), notably from 60 meV up to 3.2 eV ($\approx$ 500 cm^{-1} - 26 000 cm^{-1}). As lamps, we use either a Globar or a tungsten halogen lamp, thermal radiators that emit a black-body-like spectrum with their spectral intensity distributions governed by the source's temperature. The beam splitters consist of a thin film of Si or Ge deposited on a transparent substrate, such as KBr, CaF_2, or SiO_2, for measurements in MIR, NIR, and VIS, respectively. The cryostat windows are plane-parallel and optically polished slabs of KBr. For the mid- and near-infrared region, we utilize an MCT detector, a narrow-gap semiconductor, cooled down to 77 K with liquid nitrogen to reduce the density of thermally excited carriers. In the visible region, a Si diode is the detector of choice with its band gap of around 1 eV ($\approx$ 8065 cm^{-1}). It can be operated effectively at room temperature without cooling. Table 3.1 summarizes the utilized combinations of optical components in their respective frequency region.
The beam path for a transmission experiment is highlighted in Fig. 3.6. The measured spectrum will depend on the sample properties, but also on every component along the beam path, e.g., the intensity spectrum of the light source, the sensitivity of the detector,

and the optical properties of the beam splitters, optical windows, and mirrors. To account for those, an additional measurement under the very same conditions without the sample has to be taken. For a transmission experiment this requires a measurement through an identical, empty sample holder. The transmittance of the sample

$$T(\omega) = I_{\text{sample}}(\omega)/I_{\text{reference}}(\omega) \tag{3.33}$$

is obtained from the ratio of the intensity spectrum transmitted through the sample and the intensity spectrum of the reference. Equally, the reflectance

$$R(\omega) = I_{\text{sample},R}(\omega)/I_{\text{reference},R}(\omega) \tag{3.34}$$

is determined experimentally by measuring the intensity reflected from the sample and from a suitable reference spectrum, typically a "perfect" mirror, e.g., gold mirrors in MIR and NIR and silver or aluminum mirrors in the visible regime[6]. In this study, we do not measure the reflectance explicitly. Instead, we determine it from the interference pattern that dresses the transmittance spectrum as a result of multiple reflections within the sample. Above the Mott gap, where transmission is suppressed, we employ spectroscopic ellipsometry instead.

To operate the spectrometer and to ensure a stable measurement, the spectrometer is evacuated and continuously flushed with 2-3 mbar of N_2 gas to remove infrared-active residues present in air, e.g., water vapor that can leave fingerprints in the intensity spectrum. At the same time, the flow of N_2 gas keeps the scanner afloat and ensures an almost frictionless movement of the scanner.

One focus of the experiments presented in this thesis is the temperature dependence of the electronic excitations. To change and control the sample temperature, we glue the sample onto a copper aperture with thermally conductive silver paint and mount it on a cold finger of a continuous-flow cryostat. The cryostat isolates the sample from the external environment, and the sample can be illuminated only through the windows of the cryostat. This allows the sample to be cooled down using a continuous flow of ^{4}He to reach temperatures down to 5 K and requires to evacuate the sample compartment of the cryostat to a pressure below 10^{-5} mbar in order to prevent the condensation of crystal ice or other contaminants on the sample or the windows of the cryostat. Nonetheless, weak signatures of crystalline ice and asymmetric O-H bond stretches thereof can be identified in the spectra, especially of the hygroscopic A_2MX_6-type samples, see Fig. 3.7. The sample temperature is monitored by a thermometer in contact with the cold finger and is controlled by adjusting the helium flow and via a PID-controlled heater. The cold finger is constructed such that it can take two sample holders, one with the sample and one for the reference measurement. By moving the cold finger, either the sample or the reference can be moved into the focus of the light beam.

[6] The reflectance is considerably more sensitive to surface roughness than the transmittance. To properly account for this aspect, an often employed strategy is to evaporate a thin film of gold onto the sample and to use this as a reference.

Analysis of the transmittance spectrum

For a transparent sample with flat, parallel surfaces and a well-defined thickness d, the total transmittance is expressed by Eq. (3.17). As mentioned in Sec. 3.1, the transmittance is exponentially sensitive to $\kappa(\omega)$ but is dressed also by Fabry-Pérot interference fringes. These show a maximum in transmittance whenever the real part of the phase $\mathrm{Re}\left(\exp\left[\mathrm{i}N\omega/c\right]\right) = \pm 1$, i.e.,

$$\mathrm{Re}\left(\frac{N\omega d}{c}\right) \stackrel{!}{=} m\pi, \tag{3.35}$$

where m is an integer value. Rewriting Eq. 3.35, we can determine the index of refraction at these frequencies

$$n(\omega_{max,m}) = \frac{m\pi c}{d\omega_{max,m}}, \tag{3.36}$$

particularly useful to determine the dispersion of $n(\omega)$. An example of the Fabry-Pérot fringes is shown in the inset of Fig. 3.7(a). Being limited in frequency, it is most certainly not possible to collect the lowest interference maxima from the infrared and visible regime. The main challenge is to determine the correct order m of the observed interference maximum. For insulating samples $n(\omega)$ usually changes very little in the transparent region above the phonon and below the gap. In a first step, we neglect dispersion and approximate n from the frequencies between $\omega_{max,m}$ and its jth neighbor, $n = \frac{j\pi c}{d(\omega_{max,m}-\omega_{max,m+j})}$, which we use for a rough estimate of m. Then, including dispersion, m has to be adapted to yield a monotonic $n(\omega)$ in absence of strong excitations. To corroborate the correct order of m, we fit the calculated index of refraction either with a purely dispersive Cauchy model

$$n(\omega) = A + \frac{B}{\omega^2} + \frac{C}{\omega^4}, \quad \kappa(\omega) = 0, \tag{3.37}$$

or a Lorentz oscillator model including a strong phonon excitation below the transparent range and an interband excitation characterized by a Tauc-Lorentz oscillator above, as shown in Fig. 3.7(b). From $n(\omega)$, we can reversely calculate the reflectance via Eq. (3.18) and use it to determine the optical response functions.

The procedure to determine the dielectric function and the optical conductivity from the transmittance is illustrated exemplarily in Fig. 3.7 and Fig. 3.8 for a sample of K_2ReCl_6 with a thickness of $d = 471\,\mu$m at 300 K and an energy resolution of 1 cm^{-1} (≈ 0.13 meV). Figure 3.7 shows the measured transmittance, the index of refraction $n(\omega)$ calculated from the fringes, and the resulting reflectance $R(\omega)$. The order of the first observed fringe, $m_1 = 104$, gave the best agreement with a simple fit of a Lorentz model with a phonon mode fixed at 39 meV (320 cm^{-1}) and a Tauc-Lorentz oscillator at (2.5 eV) (20000 cm^{-1}). The resulting response functions $\varepsilon(\omega)$ and $\sigma_1(\omega)$ are shown in Fig. 3.8. This approach of determining the optical constants from $R(\omega)$ and $T(\omega)$ directly works particularly well to study weak absorption features in the transparent region with $n \gg \kappa$. The alternative approach of a Kramers-Kronig analysis of the reflectance alone is often not sensitive enough to capture these weak, dipole-forbidden excitations that are at the center of this work.

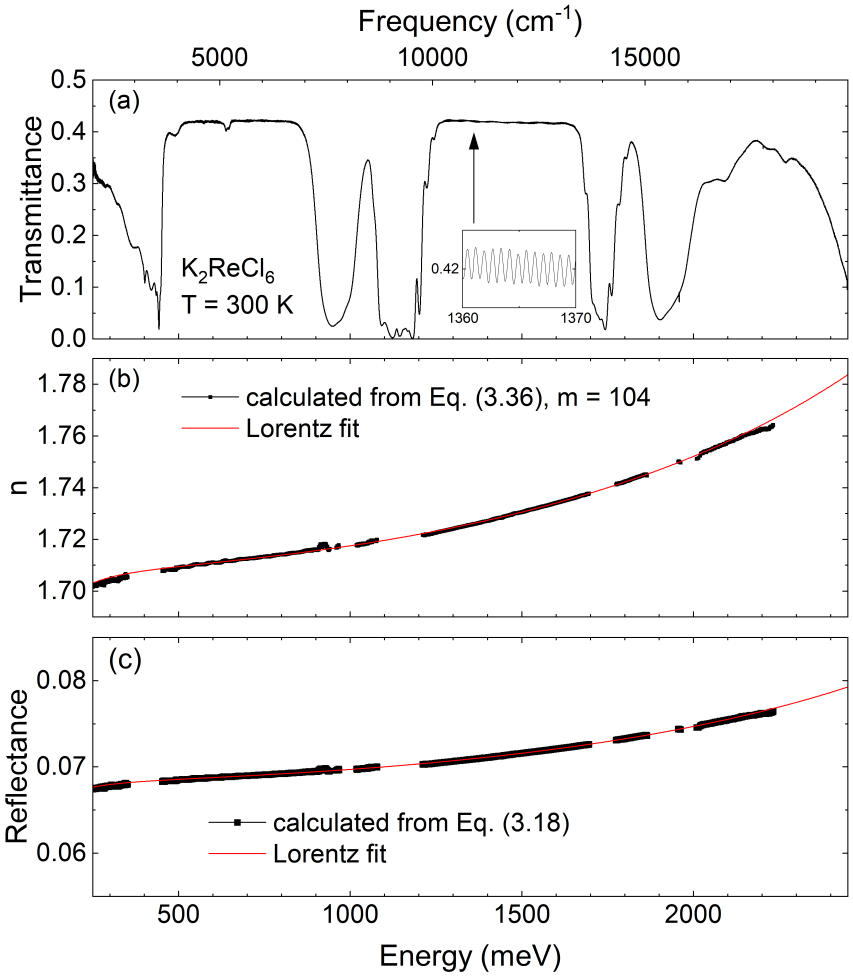

Figure 3.7 Analysis of the transmittance to obtain the index of refraction and the reflectance, illustrated for a measurement of a K_2ReCl_6 sample with a thickness of d=471 mu at 300 K. (a) Transmittance over the transparent range from 0.25 to 2.45 eV, displaying absorption features from local intra-t_{2g} excitations at around 0.95, 1.1, 1.7, and 1.9 eV. Above 2 eV, weaker features from double excitations become apparent. The upper limit of the transparent energy range sets in at 2.4 eV and is given by the onset of the Mott gap . The narrow oscillations of roughly 0.75 meV ($\approx 6\,\mathrm{cm}^{-1}$) are Fabry-Pérot interference fringes. (b) Calculation of $n(\omega)$ using Eq. (3.36), starting the counting of the first maximum at $m = 104$. The red line is a fit of $n(\omega)$ for m =104 using a phonon at 39 meV and a Tauc-Lorentz oscillator for the Mott gap with an excitation energy of around 2.5 eV. (c) Reflectance spectrum calculated from $n(\omega)$ using Eq. (3.18) (black). Additionally, the reflectance from the fit of $n(\omega)$ in (b) is shown (red curve), yielding a great agreement.

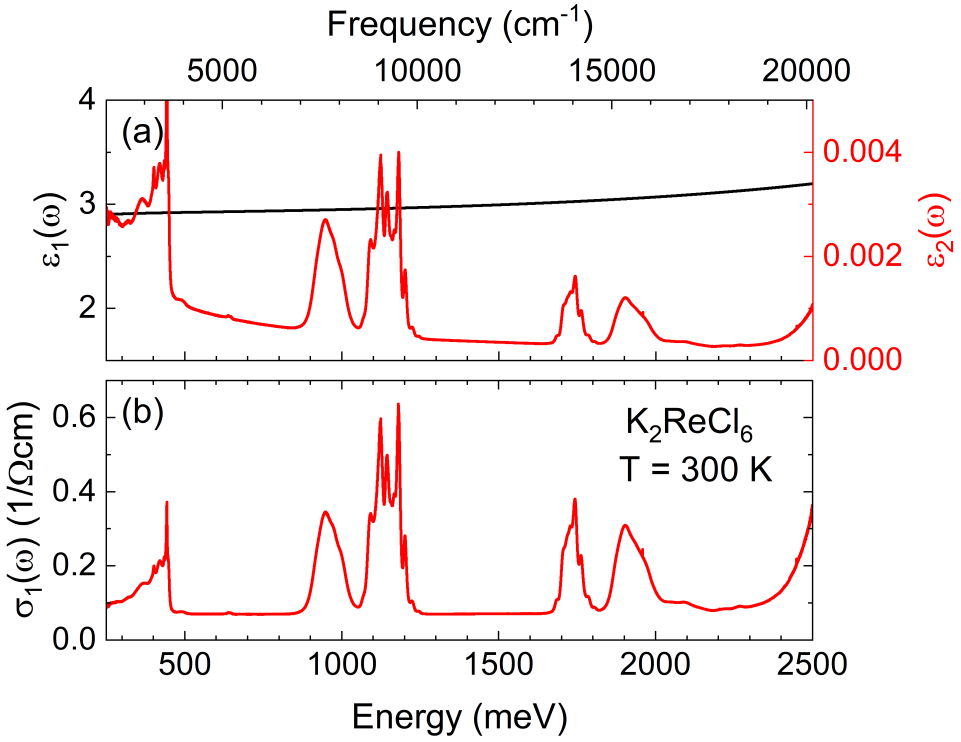

Figure 3.8 Optical constants obtained from the transmittance and the fitted reflectance from Fig. 3.7. (a) Real and imaginary parts $\varepsilon_1(\omega)$ (black curve, left axis) and $\varepsilon_2(\omega)$ (red curve, right axis). (b) Real part of the optical conductivity $\sigma_1(\omega)$. Below 0.5 eV ε_2 and σ_1 are dominated by the response of crystal water on the sample surface.

3.3 Spectroscopic ellipsometry

In the spectral region of strong absorptions, ellipsometry measurements yield an accurate, self-normalizing method to determine the optical response functions. Ellipsometry is rooted in the analysis of the polarization state of light upon reflection from the sample surface under an oblique angle. The basic idea is sketched in the following: monochromatic and linearly polarized light shines onto a sample under the angle of incidence Θ and is reflected thereof. Upon reflection, the polarization of light changes in general from linear to elliptical, as illustrated in Fig. 3.9. This is due to the angle dependence of r_p and r_s of the Fresnel equations, see Eq. (3.15). The ratio of the reflection coefficients is manifested in the two ellipsometric angles Ψ and Δ that encode the relative change in amplitude and the phase shift of the reflected waves [199]

$$\rho = \frac{r_p}{r_s} = \tan(\Psi)\, e^{i\Delta}. \tag{3.38}$$

These fully characterize the polarization ellipse, see Fig. 3.10. The angles Ψ and Δ link to relative quantities, in comparison to, e.g., transmission experiments that measure the

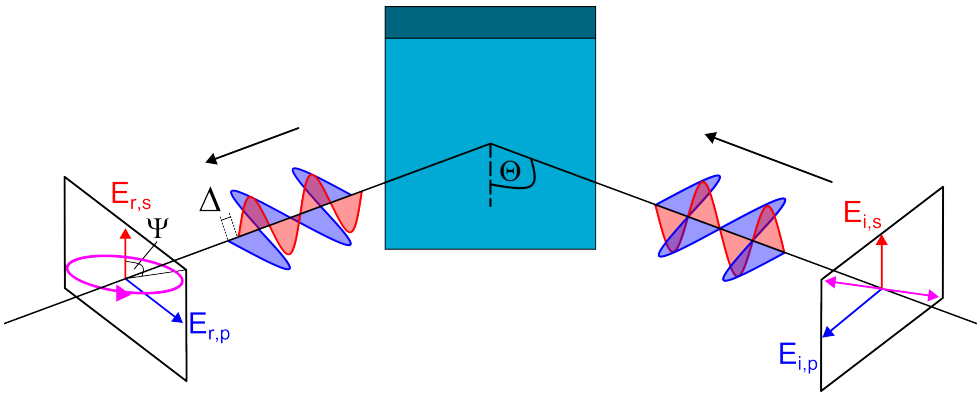

Figure 3.9 Sketch of an ellipsometric measurement illustrating the basic principle. From the right side, the incident light shines under a given angle of incidence Θ on the sample surface (blue cube) and is reflected thereof to the left. The linear polarization of the incident light shown in pink can be decomposed into an electric field component parallel $\mathbf{E}_{i,p}$ (blue) and perpendicular $\mathbf{E}_{i,s}$ (red) to the plane of incidence. Upon reflection from the sample surface, the reflection coefficients r_p and r_s follow Eq. (3.15), which induces a phase shift between the reflected components of the electric field $\mathbf{E}_{r,p}$ and $\mathbf{E}_{r,s}$, as well as a change in their amplitudes. As a result, the polarization of the reflected light is now elliptical, as indicated by the pink ellipse. From the analysis of the polarization of the reflected light, the ellipsometric angles Ψ and Δ are retrieved.

absolute light intensity. This has the advantage that ellipsometric measurements do not require taking a reference. This reduces the sensitivity to intensity fluctuation and makes ellipsometry a very precise tool to track changes of the material's response with respect to external parameters, e.g., the temperature. The setup of the ellipsometer is shown in Fig. 3.11. A very detailed description of the properties of the employed setup can be found in [235–237], which allows us to be brief in the discussion of the main components. Starting from the light source, we utilize a Xe lamp that covers the energy range roughly from 0.6 to 6.5 eV. The light passes through a dispersive double monochromator and is coupled via optical fibers into the input unit. This unit contains a collimator, a linear polarizer with an adjustable polarization angle P, and the retarder unit. The retarder can add an arbitrary phase shift to the polarized light to increase the sensitivity to determine Δ, see below. The polarized light then hits the sample, which is placed on a rotatable sample stage to adjust the angle of incidence Θ, but also to change the sample orientation with respect to the lab frame. The latter allows us to probe different components of the dielectric tensor *in situ* in case of anisotropic samples. The light reflected from the sample is then measured by a detector. The utilized ellipsometer works under the principle of a rotating analyzer ellipsometer (RAE). The key of this ellipsometer type is to equip the detector with an analyzer, which revolves continuously during data acquisition. As a result, the detector will measure a temporally modulated intensity. A Fourier analysis yields the Fourier coefficients of this signal, which encode the properties of the incident polarization

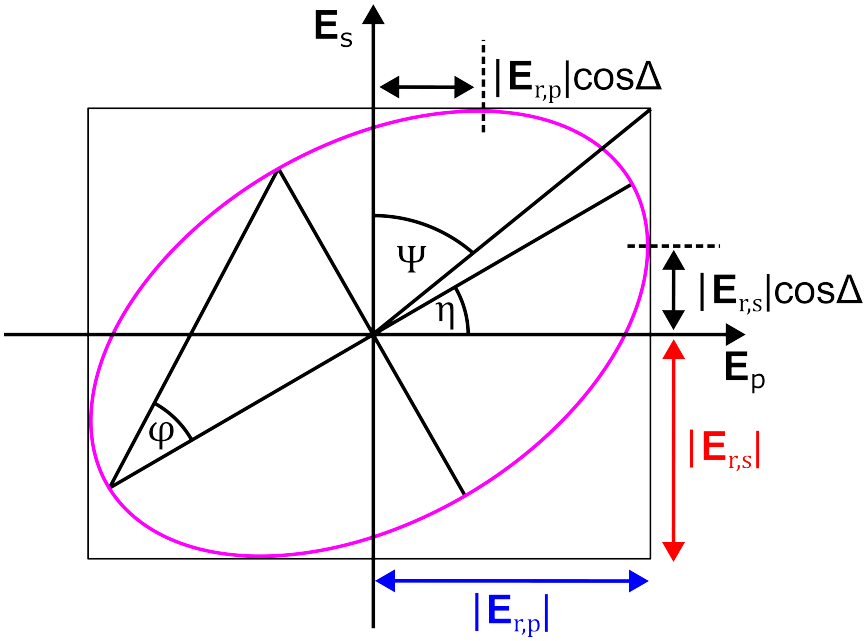

Figure 3.10 Characteristic angles of the polarization ellipse. Geometrically, the ellipse is characterized by its azimuthal angle η and the elliptic angle φ that reflects the ratio between the main axes of the ellipse. The ratio between the reflection components for p and s polarization yields the ellipsometric angle Ψ and their acquired phase difference is Δ. Both sets of angles η and φ as well as Ψ and Δ fully characterize the ellipse and can be transformed into each other [235].

state and the effect of the sample. The time-varying intensity takes the form

$$I(t) = I_0 \left[1 + a\cos(2\omega_A t) + b\sin(2\omega_A t)\right], \tag{3.39}$$

with the Fourier coefficients a and b and the analyzer frequency ω_A. Derived in [236], the coefficients read as

$$\begin{aligned} a &= \frac{\tan^2(\Psi) - \tan^2(P)}{\tan^2(\Psi) + \tan^2(P)} \\ b &= \frac{2\tan\Psi\cos\Delta\tan P}{\tan^2\Psi + \tan^2 P}, \end{aligned} \tag{3.40}$$

which yield

$$\begin{aligned} \tan\Psi &= \sqrt{\frac{1+a}{1-a}}\,|\tan P| \\ \cos\Delta &= \frac{b}{\sqrt{1-a^2}}\,\frac{\tan P}{|\tan P|}. \end{aligned} \tag{3.41}$$

Based on Eq. (3.39), we see that the measured intensity can be strongly modulated as a function of time. Periods of high intensity yield a good signal, whereas low intensities

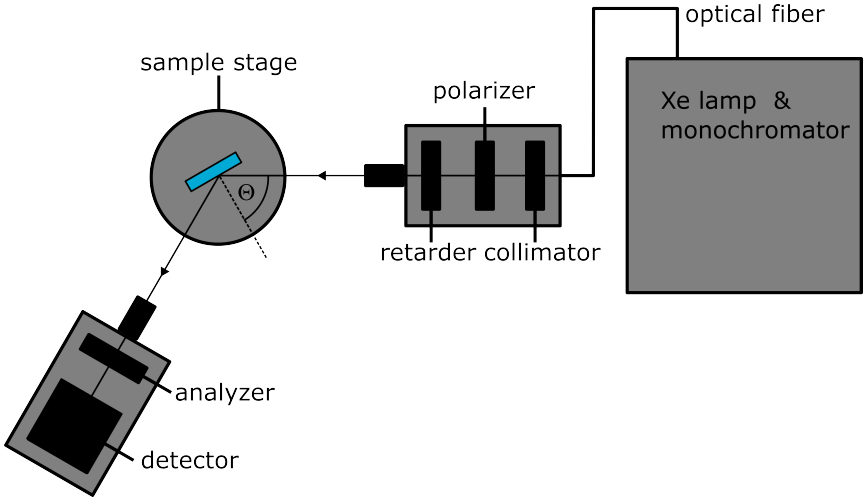

Figure 3.11 Sketch of the ellipsometry setup with its main components. Following the beam path, the light is emitted, monochromatized, and coupled into the input, where the beam is collimated and the polarization state prepared. Under an angle of incidence Θ, it is focused on the sample and subsequently reflected. Passing through an analyzer, the reflected light is detected.

are prone to noise. The most stable situation corresponds to $a = b = 0$, when the overall intensity is constant. In particular $b = 0$ is found for $\Delta = \frac{\pi}{2}$, i.e., circularly polarized light. Conversely, we find the strongest modulation in intensity for $\Delta = 0$, which yields linearly polarized light. To prevent measurements with strongly fluctuating noise levels, one can improve the overall signal-to-noise ratio by measuring the intensity of several analyzer revolutions, and particularly by adding a phase shift δ_r via the retarder to compensate for cases with $\Delta \approx 0$.
Generally, having two independent quantities, Ψ and Δ, avoids the pitfalls of requiring a Kramers-Kronig analysis. However, Ψ and Δ do not translate into the optical response functions directly. Instead, these have to be obtained typically by fitting the data to an optical model. Such a model generally is built of oscillator models for the dielectric tensor, but it can also include effects like surface roughness or interface mixing, especially because Δ is very prone to interfaces. On the flip side, this is a particular strength of ellipsometry, which turns it into a particularly sensitive tool to study thin films or multilayer systems. A useful starting point for a model is the pseudo-dielectric function

$$\tilde{\varepsilon}(\omega) = \sin^2\Theta + \sin^2\Theta \tan^2\Theta \left(\frac{1-\rho}{1+\rho}\right)^2, \tag{3.42}$$

which assumes a homogeneous, isotropic, and semi-infinite sample with a perfect sample surface. Luckily for us, all antifluorite samples measured in this thesis are cubic at room temperature and sufficiently large. Thus, our optical models only have to take a scalar dielectric function and the extra surface roughness into account. In this case sur-

face roughness can be recognized in a region of low absorption by comparing the $\tilde{\varepsilon}(\omega)$ for different angles of incidence. Ideally the curves fall on top of each other and are only altered by the surface roughness layer. Figure 3.12 shows ellipsometric measurements of K_2ReCl_6 on an as-grown (111) surface for three different angles of incidence between 2.5 and 5 eV at room temperature. The fit of the optical model in panels (c) and (d) shows the combined effect of the modeled dielectric function and a surface roughness layer of $d = 21$ nm in cyan and the bare dielectric function in red. The corresponding optical conductivity $\sigma_1(\omega)$ is shown in panel (e) resolving the individual contributions of the fit. These features correspond to intersite Mott-Hubbard excitations, as discussed in Sec. 2.3. The typically stronger charge-transfer excitations lie at energies above 5 eV, revealed by the RIXS resonance map in chap. 6. The data show a stark contrast between the directly allowed features and the dipole-forbidden excitations below the Mott gap in Fig. 3.8. For the case of the dipole-allowed transitions, the values of $\sigma_1(\omega)$ are roughly three orders of magnitude larger. In this context, transmittance measurements offer high sensitivity to weak excitations, while spectroscopic ellipsometry reliably captures strong absorption bands. Used in conjunction, the two techniques provide a comprehensive picture of both subtle and dominant optical responses.

3.4 Resonant inelastic x-ray scattering

The second pillar of experimental methods in this work is resonant inelastic x-ray scattering. The excitation mechanism of this technique can be depicted in a two-step process. The absorption of a photon promotes an electron from a core level to an unoccupied valence state, followed by the recombination of the core hole with a valence electron under the emission of a photon. Resonant enhancement of this electronic core-to-valence transition turns RIXS into a highly sensitive method to probe the local electronic structure of the $5d$ orbitals in our samples. Compared to optics, RIXS suffers from an inherently small scattering cross-section. Thus, it is a very photon-hungry technique that requires intense light sources found at synchrotrons or free-electron lasers [208, 238]. Technical advancements to improve brilliance and the instrumentation of such facilities have led to a rapid development of RIXS in the last two to three decades [206] and as a result, RIXS has presently become a benchmark method to probe various degrees of electronic excitations to investigate the electronic structure [239, 240]. For our purposes, we utilize RIXS to probe the onsite spin-orbital excitations at the L_3 edge of the $5d$ transition metals. It does not only allow us to determine the excitation energies and their dispersion, the resonance behavior also reveals the character of the excited states. In the following, we briefly introduce the direct RIXS process, as well as some technical aspects of the setup in the hard x-ray regime. The RIXS experiments in this work have been carried out at the hard x-ray beamline ID20 at the European Synchrotron Radiation Facility (ESRF) in Grenoble, France.

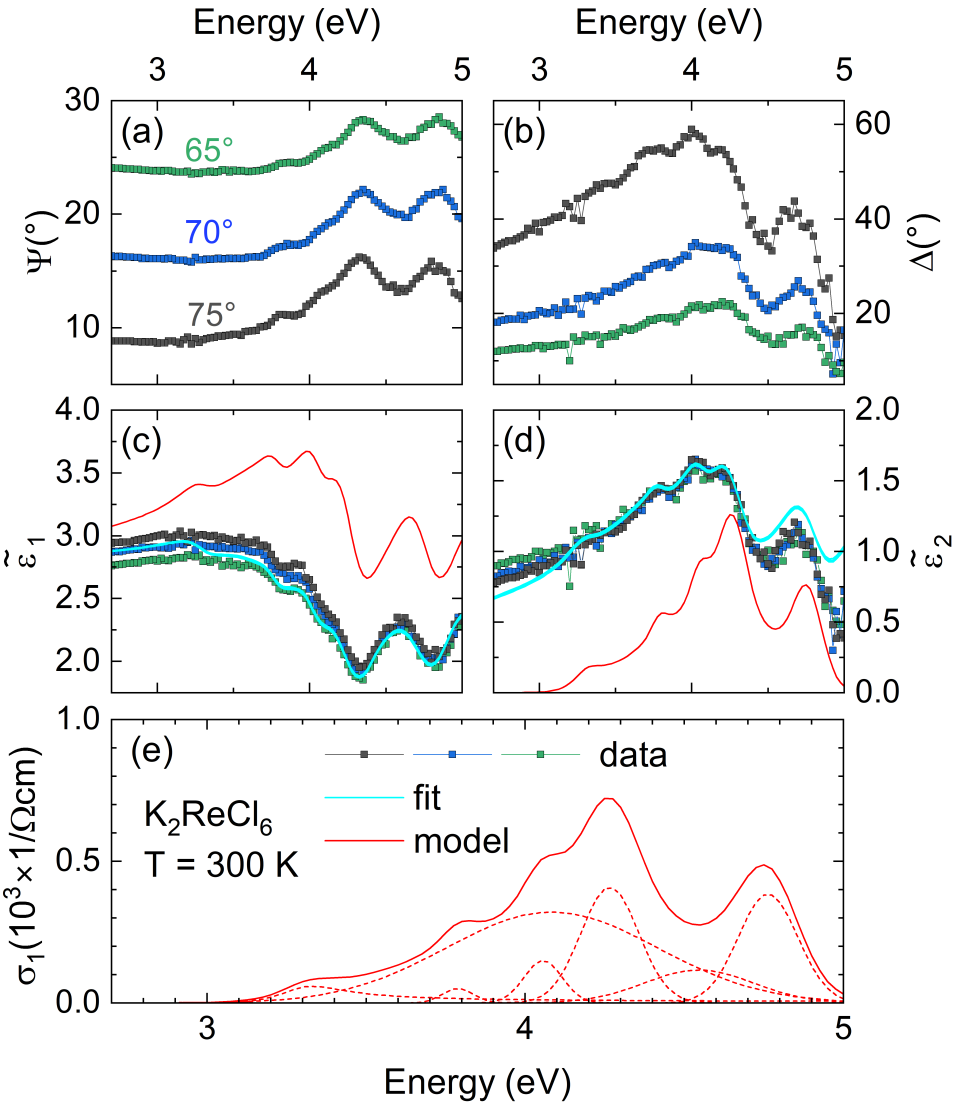

Figure 3.12 Analysis of ellipsometric data on the example of K_2ReCl_6 at 300 K. (a) and (b) Measurement of ellipsometric angles Ψ and Δ for three different angles of incidence $\Theta = 65°$, 70°, and 75°. (c)-(d) Using Eq. (3.42), the pseudo-dielectric function $\tilde{\varepsilon}(\omega)$ is plotted. The real part is shown in the left panel, the imaginary part in the right. The cyan line is a fit of the data based on an oscillator model and a surface roughness model with a thickness of 21 nm. The response function from the oscillator model is shown in red. (e) The real part of the optical conductivity $\sigma_1(\omega)$ computed from the oscillator model using Eq. (3.12). The red dashed lines show the contributions of the individual oscillators used in the fit. Note that the scale of σ_1 is 1000 times larger than compared to Fig. 3.8(c).

The RIXS process

Analogous to Eq. (3.4), we label incident photon energy, momentum, and polarization $\hbar\omega$, $\hbar\mathbf{k}$, and $\hat{\epsilon}$, and the outgoing photon with $\hbar\omega'$, $\hbar\mathbf{k}'$, and $\hat{\epsilon}'$. The central quantities of RIXS are the energy loss $E_{\text{loss}} = \hbar(\omega - \omega')$, the momentum transfer $\hbar\mathbf{q} = \hbar(\mathbf{k} - \mathbf{k}')$, and the double differential cross section $\frac{\mathrm{d}^2\sigma}{\mathrm{d}\Omega\mathrm{d}\hbar\omega'}$. The former two capture the energy and momentum that have been transferred to the sample to create the excited states, while the latter is a measure of the intensity of emitted photons per unit solid angle $\mathrm{d}\Omega$ and per unit energy range $\mathrm{d}\hbar\omega'$. A defining feature of RIXS is the possibility to employ resonant enhancement by matching the incident energy with the x-ray absorption edge of the targeted ion. The resulting double-differential cross section can thus be expressed by the Heisenberg-Kramers formula [206]:

$$\begin{aligned} \frac{\mathrm{d}^2\sigma}{\mathrm{d}\Omega\mathrm{d}\hbar\omega'} &\propto \sum_f |M_{fi}|^2 \delta(E_f - E_i + \hbar\omega - \hbar\omega') \\ M_{fi} &= \sum_n \frac{\langle f|\mathcal{D}^\dagger_{\omega',\mathbf{k}',\epsilon'}|n\rangle\langle n|\mathcal{D}_{\omega,\mathbf{k},\epsilon}|i\rangle}{E_n - E_i - \hbar\omega + \mathrm{i}\Gamma_n}. \end{aligned} \tag{3.43}$$

Here, $\mathcal{D}^{(\dagger)}$ represents the annihilation (creation) operator for x-ray photons, which induces the transitions between the ground state $|i\rangle$, the intermediate state $|n\rangle$, and the final state $|f\rangle$. The matrix elements depict the two subsequent dipole-allowed transitions. First, an absorption process to create the intermediate state characterized by a highly localized core hole. In a second step, the core hole recombines with a valence electron under the emission of a photon. We can recall the RIXS process treating the $\mathbf{A}\cdot\mathbf{p}$ term in the Hamiltonian in Eq. (3.19) as a second-order perturbation and repeating the same steps to find the dipole transition moments. The energies of the absorption edges are ion-specific and solely boost transitions of the targeted ion. The matrix elements are the largest for transitions with $\Delta l = \pm 1$. Focusing on the properties of the $5d$ orbitals, the choice of the $2p$ L edge is ideal. Specifically, RIXS at the L_3 edge, which targets the transition $|2p^4_{3/2}5d^N\rangle \rightarrow |2p^3_{3/2}5d^{N+1}\rangle$, effectively probes all intra-t_{2g} excitations of the $5d^3$, $5d^4$, and $5d^5$ electron configurations with sufficient intensity. Selecting an inner shell such as the $2p$ is advantageous for RIXS. On the one hand, typical $5d$ L_3 edges have energies of around 10 keV [120], corresponding to wave vectors $|\mathbf{k}| \approx 1\,\text{Å}^{-1}$. These allow us to probe the dispersion of excitations across the entire Brillouin zone by selecting the scattering geometry, see Fig.3.13(b). On the other hand, the strong Coulomb interaction experienced by the $2p_{3/2}$ core hole results in an extremely short lifetime of the intermediate state before it decays into the final state. To first order, this short lifetime – on the order of femtoseconds [239] – freezes out any dynamics in the intermediate state. As such, we can understand the properties of the excitation effectively based on the direct scattering from the initial state to the final state, which simplifies the calculation of the excitation energies and the simulation of the RIXS spectrum. In Eq. (3.43), this is encoded in the lineshape broadening Γ_n associated with the lifetime of the intermediate state and is several eV broad. This situation is partly different

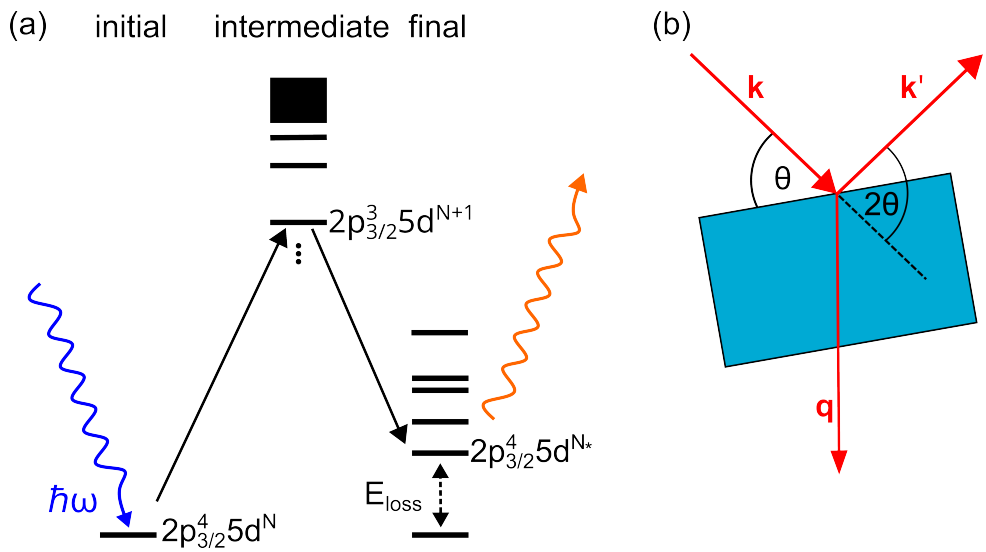

Figure 3.13 (a) Sketch of a direct RIXS process at the L_3 edge of a $5d$ ion with a d^N electron configuration. The energy levels denote eigenstates of a multi-electron system. In the ground state, all shells are completely filled except for the valence shell. In the absorption step, an x-ray photon with energy $\hbar\omega$ excites an electron from the $2p_{3/2}$ shell into the $5d$ shell, creating a $2p^3_{3/2}5d^{N+1}$ configuration. In the emission step, a $5d$ electron recombines with the $2p_{3/2}$ core hole, and a photon with energy $\hbar\omega'$ is emitted. The spacing of the energy level is not up to scale. (b) Sketch of the scattering geometry indicating the incident and outgoing momenta $\mathbf{k}$ and $\mathbf{k}'$ that define the transferred momentum $\mathbf{q}$. In the conventional nomenclature, θ depicts the angle of incidence and 2θ depicts the scattering angle. Note that in general, $2 \cdot \theta \neq 2\theta$.

with L-edge RIXS on, e.g., $3d$ orbitals, where the narrower Γ_n requires considering the substructure of the intermediate state [241]. Figure 3.13(a) depicts the RIXS process.

Sensitivity of RIXS and optics

Because of the different excitation mechanisms, RIXS and optical spectroscopy obey different selection rules. As a two-photon process, direct RIXS is sensitive to excitations that preserve parity and this directly yields *dd* excitations. By contrast, in optical spectroscopy such processes can occur only in a phonon-assisted manner, which complicates the lineshape if several phonon modes contribute. Optical spectroscopy is instead particularly sensitive to infrared-active phonons and delocalized electronic excitations. Phonons can also be detected typically only via *indirect* RIXS, for instance by tuning the incident energy to the ligand K edge, where the core-hole potential is much weaker.
The complementary sensitivities of the two methods are illustrated in Fig. 3.14(b), which compares the optical conductivity $\sigma_1(\omega)$ above the Mott gap with the high-energy RIXS data of K_2OsCl_6. In this range $\sigma_1(\omega)$ is primarily dominated by delocalized Mott-Hubbard

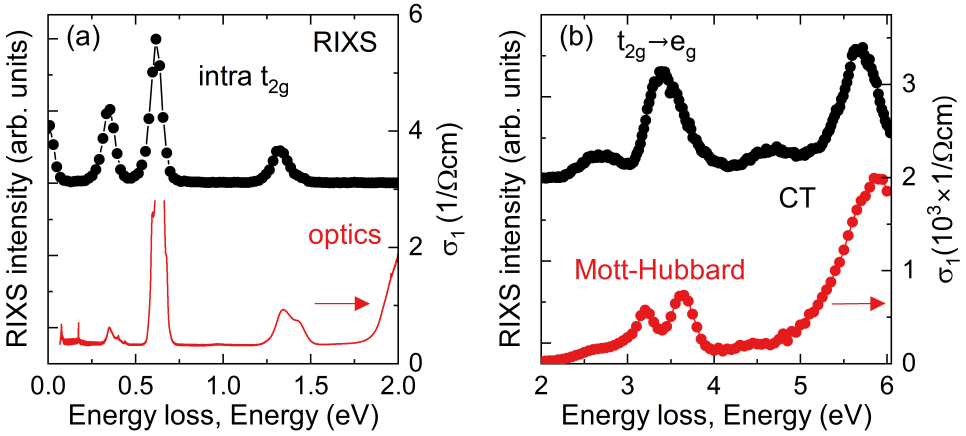

Figure 3.14 Comparison between the excitation spectra in RIXS (left axis) and $\sigma_1(\omega)$ (right axis) of K_2OsCl_6 at $T = 300$ K. The RIXS spectra are measured with $\mathbf{q} = (7\ 7\ 6)$, which corresponds to an X point. (a) Low-energy region displaying the intra-t_{2g} excitations. In the optically transparent window between phonons and the Mott gap, $\sigma_1(\omega)$ reveals the same excitations as RIXS enabled by the phonon-assisted mechanism. Around 1.8 eV $\sigma_1(\omega)$ shows the onset of the Mott gap. (b) Above the onset of the Mott gap, RIXS and $\sigma_1(\omega)$ are sensitive to different processes: RIXS to onsite $|t_{2g}^4\rangle \rightarrow |t_{2g}^{4-m}e_g^m\rangle$ excitations and $\sigma_1(\omega)$ to delocalized $|t_{2g}^4\rangle_i\,|t_{2g}^4\rangle_j \rightarrow |t_{2g}^3\rangle_i\,|t_{2g}^5\rangle_j$ Mott-Hubbard excitations. Note that σ_1 increases by roughly three orders of magnitude across the Mott gap. Above 4 eV both RIXS and optics reveal $|5d_{\mathrm{Os}}^4 3p_{\mathrm{Cl}}^6\rangle \rightarrow |5d_{\mathrm{Os}}^3 3p_{\mathrm{Cl}}^5\rangle$ charge-transfer excitations (CT).

excitations $|t_{2g}^4\rangle_i\,|t_{2g}^4\rangle_j \rightarrow |t_{2g}^3\rangle_i\,|t_{2g}^5\rangle_j$, which primarily reflect Hubbard U and the structure t_{2g}^3 t_{2g}^5 final states. RIXS, on the other hand, reveals onsite crystal-field excitations $|t_{2g}^N\rangle \rightarrow |t_{2g}^{N-1}e_g\rangle$, indicative of the crystal-field splitting $10Dq$. In this sense, optics and RIXS provide different insights.

In contrast, when focusing on onsite spin-orbital excitations, the two methods can augment one another: RIXS yields the electronic excitation energies directly, while optical spectroscopy provides finer spectral detail due to its superior energy resolution (typically <1 meV for FTIR and around 25 meV for RIXS at the Ir L_3 edge), Fig. 3.14(a).

A further distinction lies in the capability to probe dispersion. Optical spectroscopy is typically limited to excitations in the vicinity of the Γ point, but RIXS in the hard x-ray regime can typically probe excitations across the full Brillouin zone. For the antifluorite halides, we can find a lack of a sizeable dispersion, highlighting the local character of the eigenstates.

Experimental considerations

The working principles, properties, and technical benchmarks of the ID20 beamline and the RIXS spectrometer are found in [242, 243]. In the following, we discuss a qualitative overview of the main components of the beamline. The beam path is sketched in Fig. 3.15.

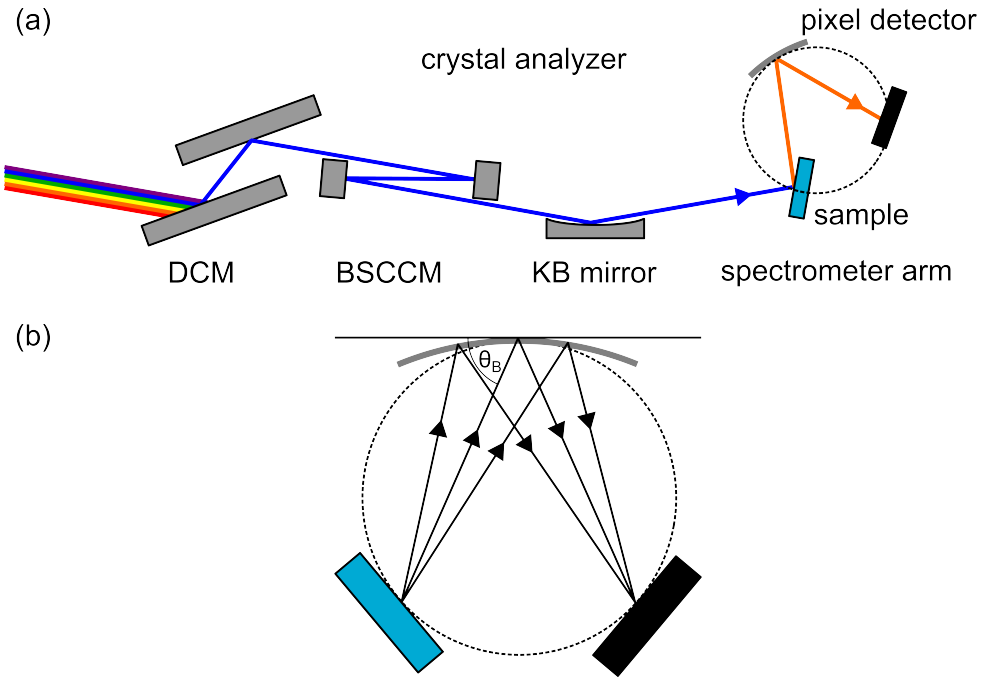

Figure 3.15 Sketch of the RIXS setup. (a) RIXS beam path following the double crystal monochromator (DCM), the back-scattering-channel-cut monochromator (BSCCM), the focusing Kirpatrick-Baez mirror (KB mirror), and the RIXS spectrometer arm with the sample marked in blue, the diced and spherically bent crystal analyzers, and the pixel detector. (b) The Rowland-circle geometry ensures that every photon scattered with energy $\hbar\omega'$ from the sample is focused on the detector, fulfilling the Bragg condition of the analyzer with the respective Bragg angle θ_B.

In a first step, the strongly accelerated electrons in the synchrotron emit a highly brilliant beam of spatially coherent photons when passing through the undulators, i.e., precise arrays of alternating dipole magnets with a fixed periodicity [244]. For the RIXS experiment, the incident photons have to be monochromatized. In the hard x-ray regime, this is typically achieved with crystal monochromators utilizing Bragg reflections [206]. A liquid-nitrogen-cooled Si double monochromator in tandem with a back-scattering-channel-cut Si monochromator tunes the energy and reduces the overall heat load of the incident beam, achieving a typical bandwidth of <0.1 eV at an incident energy of around 10 keV, which yields a relative energy resolution $\Delta E/E \approx 10^{-6} - 10^{-5}$. Then, the monochromatized beam is focused onto the sample, passing through a Kirkpatrick-Baez mirror [244] with a spot size of about $20 \times 10\,\mu m^2$ in vertical and horizontal directions. The sample itself is mounted in a cryostat placed on a sample stage that can be oriented very precisely along all three spatial directions (within specific limitations) to select the scattering geometry. The scattered photons pass through the spectrometer arm, which contains five diced spherically bent Si crystal analyzers, which select the outgoing energy, and a 2D pixelated area detector that records the intensity. Geometrically, the sample together with the crystal analyzers

and the detector are placed within a Rowland circle [238]. This ensures that a broad energy range and a large solid angle can be covered. It also ensures that the energy can be steadily scanned when measuring a RIXS spectrum.
This setup is not sensitive to inelastic scattering processes only. The dominating signals originate from elastic scattering, e.g., Bragg reflection if the scattering conditions are fulfilled, or Thomson scattering [238]. This type of scattering can be recalled from the $\mathbf{A}(\mathbf{r}, t)^2$ term in Eq. (3.19), and its scattering cross-section is proportional to $|\hat{\epsilon}_f \cdot \hat{\epsilon}_i|^2$. To suppress the intensity of Thomson scattering, the scattering geometry is, thus, typically chosen to yield $2\theta = 90°$ [244]. However, this scattering geometry also nullifies the intensity of excitations that persist in the parallel polarization channel only. A good example of this polarization dependence can be seen for the $|T_1^3\,(J = 0)\rangle \rightarrow |A_1^1\rangle$ excitation in K_2OsCl_6 at $E \approx 5J_H$, see chap. 5.

4 Multiple spin-orbit excitons and the electronic structure of α-$RuCl_3$

The following chapter presents the results on α-$RuCl_3$, which have been published as Warzanowski *et al.*, *Multiple spin-orbit excitons and the electronic structure of α-$RuCl_3$*, Phys. Rev. Research **2**, 042007(R) (2020).

Author contributions

M. Grüninger and P. H. M. van Loosdrecht conceived the experiment. P. Warzanowski took the infrared spectroscopy data shown in the publication and analyzed the spectral weight. N. Borgwardt took an initial set of data and performed a first analysis published in [119]. K. Hopfer and T. C. Koethe performed the Raman scattering experiments. P. Becker and V. Tsurkan, and A. Loidl synthesized and characterized the single crystals. J. Attig performed the numerical exact diagonalization of the two-site cluster. P. Warzanowski and M. Hermanns analyzed the data within the single-site model with support from M. Grüninger. P. Warzanowski and M. Grüninger wrote the manuscript with input from all authors.

Sample and data availability

The samples used in this project are stored within the labs of the Institute of Physics II at the University of Cologne. The raw data and the analysis files are stored on the servers of the Institute of Physics II.

Rapid Communications

Multiple spin-orbit excitons and the electronic structure of α-$RuCl_3$

P. Warzanowski,[1] N. Borgwardt,[1] K. Hopfer,[1] J. Attig,[2] T. C. Koethe,[1] P. Becker,[3] V. Tsurkan,[4,5] A. Loidl,[4] M. Hermanns,[6,7] P. H. M. van Loosdrecht,[1] and M. Grüninger[1]

[1]*Institute of Physics II, University of Cologne, D-50937 Cologne, Germany*
[2]*Institute for Theoretical Physics, University of Cologne, D-50937 Cologne, Germany*
[3]*Section Crystallography, Institute of Geology and Mineralogy, University of Cologne, D-50674 Cologne, Germany*
[4]*Experimental Physics V, Center for Electronic Correlations and Magnetism, University of Augsburg, D-86135 Augsburg, Germany*
[5]*Institute of Applied Physics, MD-2028 Chisinau, Moldova*
[6]*Department of Physics, Stockholm University, AlbaNova University Center, SE-106 91 Stockholm, Sweden*
[7]*Nordita, KTH Royal Institute of Technology and Stockholm University, SE-106 91 Stockholm, Sweden*

(Received 20 November 2019; accepted 21 September 2020; published 13 October 2020)

The honeycomb compound α-$RuCl_3$ is widely discussed as a proximate Kitaev spin-liquid material. This scenario builds on spin-orbit entangled $j = 1/2$ moments arising for a t_{2g}^5 electron configuration with strong spin-orbit coupling λ and a large cubic crystal field. The actual low-energy electronic structure of α-$RuCl_3$, however, is still puzzling. In particular, infrared absorption features at 0.30, 0.53, and 0.75 eV seem to be at odds with a $j = 1/2$ scenario. Also the energy of the spin-orbit exciton, the excitation from $j = 1/2$ to $3/2$, and thus the value of λ, are controversial. Combining infrared and Raman data, we show that the infrared features can be attributed to single, double, and triple spin-orbit excitons. We find $\lambda = 0.16$ eV and $\Delta = 42(4)$ meV for the observed noncubic crystal-field splitting, supporting the validity of the $j = 1/2$ picture for α-$RuCl_3$. The unusual strength of the double excitation is related to the underlying hopping interactions, which form the basis for dominant Kitaev exchange.

DOI: 10.1103/PhysRevResearch.2.042007

The exactly solvable Kitaev model [1] describes bond-anisotropic exchange interactions on tricoordinated lattices. Exchange frustration embodied in the model yields a rich phase diagram with gapless and gapped quantum spin liquids in which spins fractionalize into emergent Majorana fermions and gauge fluxes. Gapless Majorana fermions form a metal which on a honeycomb lattice is equivalent to magnetic Dirac matter [2]. Jackeli and Khaliullin [3] demonstrated that the Kitaev model may be realized in honeycomb compounds such as Na_2IrO_3 or α-$RuCl_3$ [4] with edge-sharing IrO_6 or $RuCl_6$ octahedra, t_{2g}^5 configuration, and strong spin-orbit coupling. This triggered an avalanche of experimental and theoretical research [5–10].

At low temperatures, α-$RuCl_3$ orders magnetically due to exchange interactions beyond the Kitaev model [11–13]. The term proximate Kitaev spin liquid [14] was coined for α-$RuCl_3$ based on fingerprints of dominant Kitaev interactions in spectroscopy, e.g., above the magnetic ordering temperature. In particular, inelastic neutron scattering, Raman scattering, and THz spectroscopy revealed an intriguing continuum of magnetic excitations [14–21] for which a fermionic character [18,21] and the restriction of dynamical spin-spin correlations to nearest neighbors [15] were reported. However, a more conventional interpretation in terms of overdamped magnons has also been proposed [13]. The Kitaev picture is in line with the stunning claim of a half-quantized thermal Hall effect [22].

In the light of these far-reaching results, it is surprising that the low-energy electronic structure of α-$RuCl_3$ remains controversial. In the related iridates, the approximate validity of the $j = 1/2$ scenario is well established by resonant inelastic x-ray scattering (RIXS) data of the spin-orbit exciton [23–27], i.e., the excitation to $j = 3/2$, but high-resolution RIXS at the Ru L or M edges is challenging [28,29]. In α-$RuCl_3$, conflicting energies of 145, 195, and 231 meV were reported for the spin-orbit exciton by Raman, inelastic neutron scattering, and Ru M edge RIXS, respectively [14,29,30]. Furthermore, several groups reported on infrared absorption bands at 0.30, 0.53, and 0.75 eV [4,30–35]. The 0.30 eV peak was assigned to the Mott gap [4,33,34], but a gap of about 1 eV is well established by different techniques [30–32,36–41]. Thus far, there is no convincing explanation for this multitude of excitations below the gap.

A scenario first proposed in 1971 attributes the infrared features to $t_{2g}^4 e_g^1$ excited states [30–32,34,41]. This contradicts results of quantum chemistry and spectroscopy [39,42,43] which show the $t_{2g}^4 e_g^1$ states above 1.3 eV. Low-lying e_g states would severely affect exchange interactions and the role of Kitaev coupling [3,44]. Alternatively, the infrared bands were discussed as possible evidence for a large non-cubic crystal-field splitting $\Delta \approx 180$ meV [35], which contrasts with the much smaller values found by x-ray absorption, $\Delta \approx -10$ meV [42], quantum chemistry,

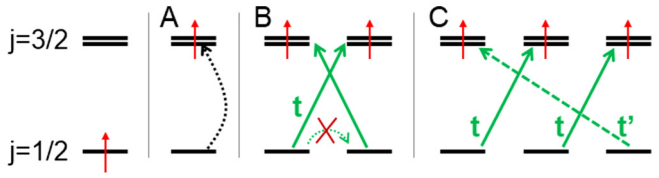

FIG. 1. Sketch of the different excitations from a ground state with $j = 1/2$ moments on each site. The spin-orbit exciton, peak A in Fig. 2, is an on-site excitation from $j = 1/2$ to 3/2. A double spin-orbit exciton, peak B, results from the exchange of two holes between adjacent sites. Nearest-neighbor hopping t (solid green arrows) connects $j = 1/2$ and 3/2 on adjacent sites, it is suppressed between $j = 1/2$ states. The triple process, peak C, involves hopping t' between next-nearest neighbors. The sketch neglects the noncubic crystal field.

$\Delta = 39$ meV [43], density functional theory, $\Delta = 37$ meV [45,46], and M edge RIXS, $\Delta < 40$ meV [29]. Note that $\Delta \approx 180$ meV would strongly mix $j = 1/2$ and 3/2 states, again with dramatic consequences for the exchange interactions [7,47]. Finally, an exact diagonalization study interpreted the 0.3 eV peak as the spin-orbit exciton, activated by direct d-d intersite hopping [48], leaving the features at 0.53 and 0.75 eV unexplained.

In this Rapid Communication, we report on infrared absorption and Raman scattering measurements which resolve the puzzle. Our Raman data feature the spin-orbit exciton, split by the non-cubic crystal field, at 248 and 290 meV. The three infrared bands correspond to phonon-assisted excitations of single and double spin-orbit excitons and the direct excitation of a triple spin-orbit exciton (see Fig. 1). We find that the phonon-assisted excitation of double spin-orbit excitons in Kitaev materials is closely related to the Lorenzana-Sawatzky-type two-magnon-plus-phonon absorption in the high-T_c cuprate parent compounds [49,50]. Our data yield $\lambda = 0.16$ eV within the Ru $4d$ shell. The ratio of noncubic crystal-field splitting and λ is very similar to the case of Na_2IrO_3, supporting the validity of the $j = 1/2$ picture in α-$RuCl_3$.

Single crystals of α-$RuCl_3$ were prepared by sublimation growth in evacuated SiO_2 glass ampoules after purification of the compound by recrystallization in vacuum. Infrared transmittance was measured using a Bruker IFS 66/v Fourier-transform spectrometer equipped with a ^{4}He cryostat. We studied samples with a thickness of (67 ± 5) and (30 ± 3) μm. The polarization of the electric field was parallel to the honeycomb layers. We used the Fabry-Perot interference fringes to determine the refractive index n, which is approximately constant for frequencies below the Mott gap and far above the phonons. Knowing $n(\omega)$ and transmittance $T(\omega)$, one can calculate the optical conductivity $\sigma_1(\omega)$. Raman measurements were performed in backscattering geometry using a micro-Raman setup with a TriVista spectrometer and an incident laser wavelength of 462 nm.

We compare the optical conductivity $\sigma_1(\omega)$ and the Raman data in Fig. 2. In α-$RuCl_3$, phonons are restricted to below 40 meV [16,34,35] and the energy of magnetic excitations is even smaller [14–16]. Above 0.9 eV, $\sigma_1(\omega)$ shows the onset of excitations across the Mott gap, reaching about 10^3 $(\Omega\,\mathrm{cm})^{-1}$

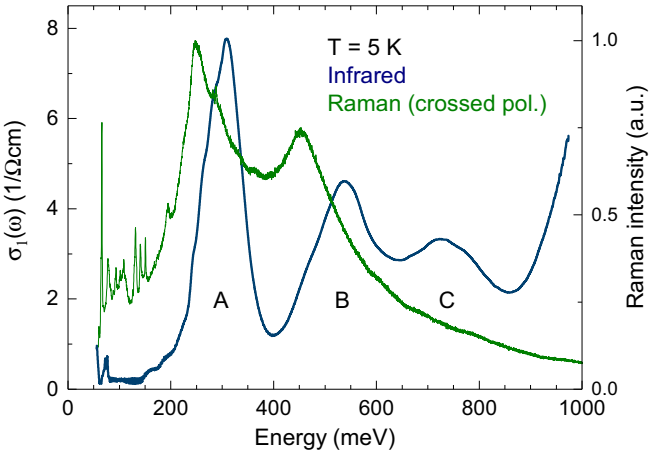

FIG. 2. Optical conductivity $\sigma_1(\omega)$ (left axis) and Raman data (right) of α-$RuCl_3$. Features A, B, and C correspond to (phonon-assisted) single, double, and triple spin-orbit excitons, respectively, cf. Fig. 1. The increase of $\sigma_1(\omega)$ above 0.9 eV indicates the Mott gap. Above 1 eV, $\sigma_1(\omega)$ reaches about 10^3 $(\Omega\,\mathrm{cm})^{-1}$ [38,41]. The much smaller values of $\sigma_1(\omega)$ below the gap are typical for weak phonon-assisted or higher-order absorption features [53].

above 1 eV [30–32,36–41]. The prominent infrared peaks A, B, and C at 0.30, 0.53, and 0.75 eV agree very well with previous reports [4,30–35], demonstrating that these features reflect the local electronic structure. They are robust against the widely discussed sample issues in α-$RuCl_3$ which are related to the stacking sequence of honeycomb layers [35]. Our Raman data reveal two strong peaks at 248 meV and 450 meV and a clear shoulder at 290 meV. The pronounced difference between infrared and Raman spectra originates from the selection rules, offering a key to the assignment.

A given mode is Raman active if it modulates the polarizability and infrared active if it carries an electric dipole moment. The spin-orbit exciton is a local excitation between $4d$ orbitals (see Fig. 1). It is closely related to an on-site d-d excitation. Its Raman activity was demonstrated in Sr_2IrO_4 [51]. Such an electronic transition between even d orbitals does not carry a dipole moment but becomes infrared active by the simultaneous excitation of a symmetry-breaking phonon [52,53]. Such phonon-assisted infrared excitations from $j = 1/2$ to 3/2 were observed in host crystals doped with $5d^5$ Ir^{4+} ions [54], equivalent to $4d^5$ Ru^{3+}. In the honeycomb lattice the Ru sites do not show inversion symmetry. However, the corresponding admixture of p or odd character to the d orbitals usually is neglected. We thus expect the infrared peak of the spin-orbit exciton to be shifted with respect to the Raman peak by a phonon frequency, as observed for peak A.

For phonon-assisted features located between ω_1 and ω_2, the phonon energy $\hbar\omega_{\mathrm{ph}}$ can be determined by the temperature dependence of the spectral weight (SW) [52],

$$SW = \int_{\omega_1}^{\omega_2} \sigma_1(\omega)\, d\omega = \alpha + \beta \coth\left(\frac{\hbar\omega_{\mathrm{ph}}}{2k_B T}\right), \qquad (1)$$

where α and β are fit parameters. Thermal population of the phonon yields an increase of SW. Figure 3 depicts the temperature dependence of $\sigma_1(\omega)$. Figure 4(a) shows SW of peaks A, B, and C. The spectral weight of peak C is constant below

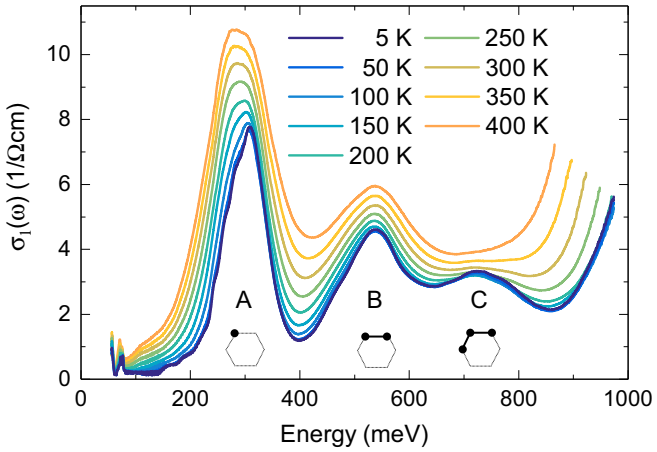

FIG. 3. Temperature dependence of $\sigma_1(\omega)$. With increasing temperature, the Mott gap softens or smears out, partially covering peak C, while peaks A and B show a pronounced increase of spectral weight, typical for phonon-assisted excitations [see Fig. 4(a)]. The high-energy cutoff reflects the suppression of the measured transmittance. Sketches denote the different excitations (cf. Fig. 1).

200 K. The increase above 200 K is due to the softening of the gap, see Fig. 3. Accordingly, peak C is not phonon-assisted but directly infrared active, in agreement with the absence of a corresponding Raman feature. For peaks A and B, fits using Eq. (1) yield $\hbar\omega_{\rm ph} = 19.6$ meV and 39.3 meV, respectively [see Fig. 4(a)] [55]. Note that excitations across the gap have a negligible effect on SW of peaks A and B. An independent analysis of the temperature dependence of $\sigma_1(\omega)$ using an oscillator model (not shown) yields very similar results for the frequencies of the symmetry-breaking phonons.

The phonon energies of 19.6 and 39.3 meV agree with phonon studies using Raman and infrared spectroscopy

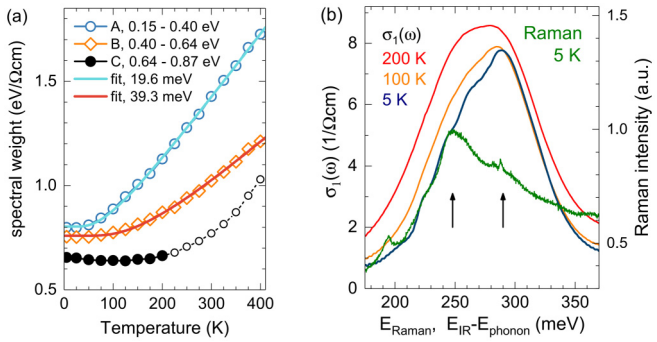

FIG. 4. Spectral weight (left) and zoom in on peak A (right). (a) Using Eq. (1), fits of the spectral weight, integrated over the indicated ranges, yield $\hbar\omega_{\rm ph} = 19.6$ meV for peak A and 39.3 meV for peak B. For peak C, the behavior above 200 K (small symbols) is hidden by the softening of the gap (cf. Fig. 3) while the spectral weight below 200 K (solid symbols) is independent of temperature. (b) Green: Raman data (right axis). Other curves: $\sigma_1(\omega)$ (left axis), shifted by 20 meV to compensate for the phonon shift $\hbar\omega_{\rm ph}$ of the phonon-assisted process. Arrows at 248 and 290 meV indicate peak positions of the spin-orbit exciton split by the noncubic crystal field. Additional phonon sidebands reflect the vibronic character.

[16,34,35]. The fact that two phonon energies are observed is remarkable. It is hard to reconcile with the scenario of excitations to various $t_{2g}^4\, e_g^1$ multiplets [30–32,34,41], because the phonon should be equally effective in breaking the symmetry for all on-site excitations. However, two different phonon modes have to be expected if we assign peaks A and B to single and double spin-orbit excitons. The former is an on-site process for which a phonon has to break the symmetry (on the honeycomb lattice: enhance the odd-symmetry character) on a Ru site. The double excitation, in contrast, involves the exchange of holes between two neighboring sites and becomes infrared active via a different phonon mode breaking the symmetry between a Ru-Ru pair. Note that this scenario of (multiple) spin-orbit excitons — excitations within the t_{2g} shell — is the only plausible explanation for the observed features, considering the accepted energy scales (see above) of phonons, magnons, the Mott gap, and the t_{2g}-e_g splitting.

Single spin-orbit exciton. The closer look on peak A provided in Fig. 4(b) strongly supports its spin-orbit exciton nature. As discussed in the following, its energy yields a reasonable value of λ, and the data support the phonon shift between Raman and infrared data as well as the vibronic character expected for an excitation involving orbitals. Shifting the infrared data by 20 meV to compensate for the phonon-assisted character, we find a stunning agreement with the Raman data which peak at 248 meV and show a second feature at 290 meV. Both coincide with peaks in the shifted infrared data. The data show further sidebands shifted by 19 meV. These can be understood as vibronic sidebands according to the Franck-Condon principle [52,53]. The $j = 1/2$ ground state and the $j = 3/2$ excited state differ in the spatial distributions of electronic charge and thus also in the relaxed configurations of the lattice [56]. Therefore, these excitations mix with phonons, which causes phonon sidebands. We emphasize that this vibronic mixture is a property of the eigenstates which is independent of the spectroscopic technique. In particular, the phonon sidebands should not be confused with the additional phonon that is necessary for breaking the symmetry in the infrared case.

The spin-orbit exciton can be described by the single-site Hamiltonian for the t_{2g} states [3,57],

$$H_{\rm single} = \lambda_{\rm eff}\, \mathbf{S}\cdot\mathbf{L} + \Delta_{\rm CF}\, L^2_{[111]}\,, \qquad (2)$$

where $L_{[111]}$ denotes the component of $\mathbf{L}$ along the trigonal [111] axis. The trigonal crystal field parameterized by $\Delta_{\rm CF}$ yields a splitting of the excited $j = 3/2$ quartet. For $\Delta_{\rm CF}/\lambda_{\rm eff} \ll 1$, the observed splitting is $\Delta = \frac{2}{3}\Delta_{\rm CF}$. With Raman peaks at 248(1) meV and 290(4) meV, there are two different solutions of Eq. (2), $\lambda_{\rm eff} = 175(1)$ meV and $\Delta_{\rm CF} = 70(9)$ meV for trigonal elongation, or $\lambda_{\rm eff} = 177(1)$ meV and $\Delta_{\rm CF} = -59(7)$ meV for compression. Accordingly, the $j = 1/2$ wave function carries more than 98 % of the weight of the local ground state, corroborating the applicability of the $j = 1/2$ picture for α-$RuCl_3$. The ratio $\Delta/\lambda_{\rm eff} \approx 1/4.5$ is very similar in Na_2IrO_3, where RIXS finds $\lambda_{\rm eff} = 0.4$–0.5 eV and $\Delta = 0.11$ eV [25].

Quantum chemistry calculations predicted the spin-orbit exciton at 195 meV and 234 meV with a splitting $\Delta =$ 39 meV [43]. These values, in particular the splitting, agree

very well with our result. Density functional theory finds $\Delta = 37$ meV [45,46], while a somewhat smaller splitting of $\Delta_{\mathrm{CF}} = (-12 \pm 10)$ meV was derived from linear dichroism in x-ray absorption spectroscopy [42]. Note that our experimental splitting $\Delta = 42(4)$ meV is still smaller than the vibronic peak width, and one may speculate whether the considerable overlap of the two excitations explains the reduced dichroism. With the currently available resolution, RIXS data measured at the Ru M edge at 300 K support our assignment of peak A but cannot resolve the splitting [29].

The effective parameter $\lambda_{\mathrm{eff}} \approx 176$ meV applies to the single-site Hamiltonian restricted to t_{2g} orbitals, Eq. (2). Considering the full $4d$ shell including the e_g orbitals with $10\,\mathrm{Dq} = 2.2$ eV [30,39], we find $\lambda = 0.16$ eV. In the literature on α-$RuCl_3$, typical values for λ fall in the range 0.13–0.15 eV [29,37,42,44,58], but a precise experimental value was missing thus far.

Our interpretation of peak A as spin-orbit exciton poses the question of the origin of the features at lower energy that previously were attributed to this excitation. The claim of a neutron mode at 195 meV [14] needs to be substantiated by high-energy neutron data with improved signal-to-noise ratio. In Raman scattering with a 532-nm laser, a weak mode was reported at 145 meV [30]. Our Raman data show a multitude of weak modes below 200 meV, see Fig. 2. In particular we find three narrow peaks at 131, 141, and 151 meV. We tentatively attribute all of these weak features to multiphonon excitations. Their strength depends on the laser wavelength and the sample quality and may be boosted by a flat phonon dispersion. In the infrared data, the feature at 73 meV, i.e., about half the energy, has been explained as a strong two-phonon excitation [34].

Double spin-orbit exciton. To explain this process, we consider the phonon-assisted two-magnon absorption described by Lorenzana and Sawatzky [49,50]. It is a powerful tool for the study of magnetic excitations in, e.g., the $S = 1/2$ cuprate parent compounds [59]. There, exchanging two antiparallel spins on adjacent sites is equivalent to a double spin flip. This process is Raman active but does not carry a dipole moment. It becomes infrared active by the simultaneous excitation of a high-energy breathing phonon which yields different on-site energies on the two sites, breaking the symmetry on the bond. In the edge-sharing geometry of α-$RuCl_3$, this role is played by the highest E_u phonon mode [34], which agrees with our result $\hbar\omega_{\mathrm{ph}} = 39$ meV for peak B. The spectral weight in $\sigma_1(\omega)$ is proportional to the effective charge $q_{\mathrm{eff}} = \frac{\partial^2 J}{\partial u\, \partial |\mathbf{E}|}$ where J denotes the exchange coupling constant, u the ionic displacement, and $\mathbf{E}$ the applied electric field. For α-$RuCl_3$, we estimate the order of magnitude of the leading-order contribution [60], which yields similar results as in the cuprates. Experimentally, peak B reaches about 4 $(\Omega\,\mathrm{cm})^{-1}$ and has a width of about 0.1 eV. Indeed, similar spectral weights are found in the cuprates [59].

Compared to magnetic excitations, the observation of a double excitation involving orbitals is unusual but not unprecedented. The strength of this process depends on the particular form of intersite hopping. For the two-magnon process in the cuprates, it is sufficient to consider a half-filled x^2-y^2 orbital per site and hopping between them. In contrast, the double-orbital excitation is boosted if hopping predominantly connects the ground state orbital on site i with an excited orbital on site j. For instance, two-orbiton infrared absorption was observed in the Mott insulator YVO_3 [61] which shows antiferro-orbital order of xz and yz along c. Hopping between adjacent sites i and j is diagonal in xz and yz. Starting from $|0\rangle = |xz\rangle_i\,|yz\rangle_j$, the exchange of electrons leads to the final state $|yz\rangle_i\,|xz\rangle_j$ with orbital excitations on both sites. In α-$RuCl_3$, the double excitation proceeds via a similar path. Nearest-neighbor hopping from $|j = 1/2\rangle_i$ is only finite to $|3/2\rangle_j$ but vanishes to $|1/2\rangle_j$ (see Fig. 1). From $|0\rangle = |1/2\rangle_i\,|1/2\rangle_j$, the leading contribution of particle exchange yields $|3/2\rangle_i|3/2\rangle_j$, the double spin-orbit exciton. Interaction effects change this picture only slightly, the double spin-orbit exciton remains the dominant contribution (see Supplemental Material [62]). This property of the hopping interactions is the source for vanishing Heisenberg and dominant Kitaev exchange [3]. In this sense, the strength of the double excitation is a direct consequence of dominant Kitaev exchange.

The precise energy of the double excitation is more subtle. Naively, one may expect combination tones of 248 and 290 meV. However, for the double excitation one has to consider dispersion, even if the total wavevector has to vanish, and in particular interaction effects. For two-magnon absorption, this dramatically affects the peak energies, in particular in the case of bound states [63]. In α-$RuCl_3$, it is, e.g., feasible to consider a lattice distortion which lowers the spin-orbit exciton excitation energy on both sites. The observed energies of 450 meV in Raman scattering and $(490 + 39)$ meV in infrared absorption are thus plausible. Following Fig. 1, the infrared peak invokes excitations to $|3/2\rangle_i|3/2\rangle_j$ due to nearest-neighbor hopping t. Raman scattering proceeds via a high-energy intermediate state which may favor a different flavor of the double spin-orbit exciton, explaining the lower energy. A thorough investigation of interaction effects is beyond the scope of our study, which is focused on the detection and identification of the double spin-orbit exciton. Note, however, that our assignment is supported by exact diagonalization of a two-site cluster which reproduces the observed Raman energies (see Supplemental Material [62]). In the related iridates, RIXS at the Ir L edge strongly favors on-site excitations such as the single spin-orbit exciton. However, a close look at the RIXS data of Na_2IrO_3 reveals a small feature at about twice the energy of the spin-orbit exciton [25].

Triple spin-orbit exciton. A triple spin-orbit exciton excitation is possible on three neighboring sites i, j, k of the honeycomb lattice. It results from nearest-neighbor hopping t from i to j and from j to k and next-nearest-neighbor hopping t' from k to i (see Fig. 1). Following the logic of Lorenzana-Sawatzky-type phonon-assisted absorption [49,50], the different hopping amplitudes, in combination with the absence of inversion symmetry for this group of three sites, result in a finite dipole moment, i.e., the excitation is directly infrared active.

A triple excitation is unusual as the spectral weight strongly decreases with increasing particle number. In the present case, this is partially compensated by the fact that a directly infrared-active process such as the triple excitation is much stronger than phonon-assisted processes such as the single and double excitations. Moreover, next-nearest-neighbor hopping is of considerable size in α-$RuCl_3$, which is partially

caused by the strong hopping between the large Cl ions. Band-structure calculations find $t'/t \approx 0.38$ [45].

In conclusion, we solved a long-standing puzzle concerning the low-energy electronic structure of α-$RuCl_3$. The prominent features below the Mott gap can be identified as single, double, and triple spin-orbit excitons. In α-$RuCl_3$, the spin-orbit exciton is far below the gap, which allows Raman scattering and infrared absorption to take over the important role that RIXS plays in iridates. We determine $\lambda = 0.16$ eV, a central parameter for the theoretical modeling of α-$RuCl_3$, and $\Delta = 42(4)$ meV, corroborating the $j = 1/2$ scenario. The observation of a double spin-orbit exciton highlights the prominent role of Kitaev coupling and calls for studies of the interactions between excited $j = 3/2$ states in Kitaev materials.

We acknowledge funding from the Deutsche Forschungsgemeinschaft (DFG, German Research Foundation) – Project No. 277146847 – CRC 1238 (Projects A02, B02, B03, and C02).

[1] A. Kitaev, Anyons in an exactly solved model and beyond, Ann. Phys. **321**, 2 (2006).

[2] K. O'Brien, M. Hermanns, and S. Trebst, Classification of gapless Z_2 spin liquids in three-dimensional Kitaev models, Phys. Rev. B **93**, 085101 (2016).

[3] G. Jackeli and G. Khaliullin, Mott Insulators in the Strong Spin-Orbit Coupling Limit: From Heisenberg to a Quantum Compass and Kitaev Models, Phys. Rev. Lett. **102**, 017205 (2009).

[4] K. W. Plumb, J. P. Clancy, L. J. Sandilands, V. Vijay Shankar, Y. F. Hu, K. S. Burch, H.-Y. Kee, and Y.-J. Kim, α-$RuCl_3$: A spin-orbit assisted Mott insulator on a honeycomb lattice, Phys. Rev. B **90**, 041112(R) (2014).

[5] W. Witczak-Krempa, G. Chen, Y. B. Kim, and L. Balents, Correlated quantum phenomena in the strong spin-orbit regime, Annu. Rev. Condens. Matter Phys. **5**, 57 (2014).

[6] J. G. Rau, E. K.-H. Lee, and H.-Y. Kee, Spin-orbit physics giving rise to novel phases in correlated systems: Iridates and related materials, Annu. Rev. Condens. Matter Phys. **7**, 195 (2016).

[7] S. M. Winter, A. A. Tsirlin, M. Daghofer, J. van den Brink, Y. Singh, P. Gegenwart, and R. Valentí, Models and materials for generalized Kitaev magnetism, J. Phys.: Condens. Matter **29**, 493002 (2017).

[8] S. Trebst, Kitaev Materials, arXiv:1701.07056.

[9] M. Hermanns, I. Kimchi, and J. Knolle, Physics of the Kitaev model: fractionalization, dynamical correlations, and material connections, Annu. Rev. Condens. Matter Phys. **9**, 17 (2018).

[10] H. Takagi, T. Takayama, G. Jackeli, G. Khaliullin and S. E. Nagler, Concept and realization of Kitaev quantum spin liquids, Nat. Rev. Phys. **1**, 264 (2019).

[11] M. Majumder, M. Schmidt, H. Rosner, A. A. Tsirlin, H. Yasuoka, and M. Baenitz, Anisotropic $Ru^{3+}4d^5$ magnetism in the α-$RuCl_3$ honeycomb system: Susceptibility, specific heat, and zero-field NMR, Phys. Rev. B **91**, 180401(R) (2015).

[12] R. D. Johnson, S. C. Williams, A. A. Haghighirad, J. Singleton, V. Zapf, P. Manuel, I. I. Mazin, Y. Li, H. O. Jeschke, R. Valentí, and R. Coldea, Monoclinic crystal structure of α-$RuCl_3$ and the zigzag antiferromagnetic ground state, Phys. Rev. B **92**, 235119 (2015).

[13] S. M. Winter, K. Riedl, P. A. Maksimov, A. L. Chernyshev, A. Honecker, and R. Valentí, Breakdown of magnons in a strongly spin-orbital coupled magnet, Nat. Commun. **8**, 1152 (2017).

[14] A. Banerjee, C. A. Bridges, J.-Q. Yan, A. A. Aczel, L. Li, M. B. Stone, G. E. Granroth, M. D. Lumsden, Y. Yiu, J. Knolle, S. Bhattacharjee, D. L. Kovrizhin, R. Moessner, D. A. Tennant, D. G. Mandrus, and S. E. Nagler, Proximate Kitaev quantum spin liquid behaviour in a honeycomb magnet, Nat. Mater. **15**, 733 (2016).

[15] A. Banerjee, J. Yan, J. Knolle, C. A. Bridges, M. B. Stone, M. D. Lumsden, D. G. Mandrus, D. A. Tennant, R. Moessner, and S. E. Nagler, Neutron scattering in the proximate quantum spin liquid α-$RuCl_3$, Science **356**, 1055 (2017).

[16] L. J. Sandilands, Y. Tian, K. W. Plumb, Y.-J. Kim, and K. S. Burch, Scattering Continuum and Possible Fractionalized Excitations in α-$RuCl_3$, Phys. Rev. Lett. **114**, 147201 (2015).

[17] A. Glamazda, P. Lemmens, S.-H. Do, Y. S. Kwon, and K.-Y. Choi, Relation between Kitaev magnetism and structure in α-$RuCl_3$, Phys. Rev. B **95**, 174429 (2017).

[18] Y. Wang, G. B. Osterhoudt, Y. Tian, P. Lampen-Kelley, A. Banerjee, T. Goldstein, J. Yan, J. Knolle, H. Ji, R. J. Cava, J. Nasu, Y. Motome, S. E. Nagler, D. Mandrus, and K. S. Burch, The range of non-Kitaev terms and fractional particles α-$RuCl_3$, npj Quantum Mater. **5**, 14 (2020).

[19] A. Little, L. Wu, P. Lampen-Kelley, A. Banerjee, S. Patankar, D. Rees, C. A. Bridges, J.-Q. Yan, D. Mandrus, S. E. Nagler, and J. Orenstein, Antiferromagnetic Resonance and Terahertz Continuum in α-$RuCl_3$, Phys. Rev. Lett. **119**, 227201 (2017).

[20] Z. Wang, S. Reschke, D. Hüvonen, S.-H. Do, K.-Y. Choi, M. Gensch, U. Nagel, T. Rõõm, and A. Loidl, Magnetic Excitations and Continuum of a Possibly Field-Induced Quantum Spin Liquid in α-$RuCl_3$, Phys. Rev. Lett. **119**, 227202 (2017).

[21] J. Nasu, J. Knolle, D. L. Kovrizhin, Y. Motome, and R. Moessner, Fermionic response from fractionalization in an insulating two-dimensional magnet, Nat. Phys. **12**, 912 (2016).

[22] Y. Kasahara, T. Ohnishi, Y. Mizukami, O. Tanaka, S. Ma, K. Sugii, N. Kurita, H. Tanaka, J. Nasu, Y. Motome, T. Shibauchi, and Y. Matsuda, Majorana quantization and half-integer thermal quantum Hall effect in a Kitaev spin liquid, Nature (London) **559**, 227 (2018).

[23] J. Kim, D. Casa, M. H. Upton, T. Gog, Y.-J. Kim, J. F. Mitchell, M. van Veenendaal, M. Daghofer, J. van den Brink, G. Khaliullin, and B. J. Kim, Magnetic Excitation Spectra of Sr_2IrO_4 Probed by Resonant Inelastic X-Ray Scattering: Establishing Links to Cuprate Superconductors, Phys. Rev. Lett. **108**, 177003 (2012).

[24] J. Kim, M. Daghofer, A. H. Said, T. Gog, J. van den Brink, G. Khaliullin, and B. J. Kim, Excitonic quasiparticles in a spin-orbit Mott insulator, Nat. Commun. **5**, 4453 (2014).

[25] H. Gretarsson, J. P. Clancy, X. Liu, J. P. Hill, E. Bozin, Y. Singh, S. Manni, P. Gegenwart, J. Kim, A. H. Said, D. Casa,

T. Gog, M. H. Upton, H.-S. Kim, J. Yu, V. M. Katukuri, L. Hozoi, J. van den Brink, and Y.-J. Kim, Crystal-Field Splitting and Correlation Effect on the Electronic Structure of A_2IrO_3, Phys. Rev. Lett. **110**, 076402 (2013).

[26] M. Rossi, M. Retegan, C. Giacobbe, R. Fumagalli, A. Efimenko, T. Kulka, K. Wohlfeld, A. I. Gubanov, and M. Moretti Sala, Possibility to realize spin-orbit-induced correlated physics in iridium fluorides, Phys. Rev. B **95**, 235161 (2017).

[27] A. Revelli, C. C. Loo, D. Kiese, P. Becker, T. Fröhlich, T. Lorenz, M. Moretti Sala, G. Monaco, F. L. Buessen, J. Attig, M. Hermanns, S. V. Streltsov, D. I. Khomskii, J. van den Brink, M. Braden, P. H. M. van Loosdrecht, S. Trebst, A. Paramekanti, and M. Grüninger, Spin-orbit entangled $j = 1/2$ moments in Ba_2CeIrO_6: A frustrated fcc quantum magnet, Phys. Rev. B **100**, 085139 (2019).

[28] H. Gretarsson, H. Suzuki, Hoon Kim, K. Ueda, M. Krautloher, B. J. Kim, H. Yava, G. Khaliullin, and B. Keimer, Observation of spin-orbit excitations and Hund's multiplets in Ca_2RuO_4, Phys. Rev. B **100**, 045123 (2019).

[29] B. W. Lebert, S. Kim, V. Bisogni, I. Jarrige, A. M. Barbour, and Y.-J. Kim, Resonant inelastic x-ray scattering study of α-$RuCl_3$: A progress report, J. Phys.: Condens. Matter **32**, 144001 (2020).

[30] L. J. Sandilands, Y. Tian, A. A. Reijnders, H.-S. Kim, K. W. Plumb, Y.-J. Kim, H.-Y. Kee, and K. S. Burch, Spin-orbit excitations and electronic structure of the putative Kitaev magnet α-$RuCl_3$, Phys. Rev. B **93**, 075144 (2016).

[31] L. Binotto, I. Pollini, and G. Spinol, Optical and transport properties of the magnetic semiconductor α-$RuCl_3$, Phys. Status Solidi B **44**, 245 (1971).

[32] G. Guizzetti, E. Reguzzoni, and I. Pollini, Fundamental optical properties of α-$RuCl_3$, Phys. Lett. A **70**, 34 (1979).

[33] S. Reschke, F. Mayr, Z. Wang, S.-H. Do, K.-Y. Choi, and A. Loidl, Electronic and phonon excitations in α-$RuCl_3$, Phys. Rev. B **96**, 165120 (2017).

[34] Y. Hasegawa, T. Aoyama, K. Sasaki, Y. Ikemoto, T. Moriwaki, T. Shirakura, R. Saito, Y. Imai, and K. Ohgushi, Two-phonon absorption spectra in the layered honeycomb compound α-$RuCl_3$, J. Phys. Soc. Jpn. **86**, 123709 (2017).

[35] S. Reschke, F. Mayr, S. Widmann, H.-A. Krug von Nidda, V. Tsurkan, M. V. Eremin, S.-H. Do, K.-Y. Choi, Z. Wang, and A. Loidl, Sub-gap optical response in the Kitaev spin-liquid candidate α-$RuCl_3$, J. Phys.: Condens. Matter **30**, 475604 (2018).

[36] I. Pollini, Photoemission study of the electronic structure of $CrCl_3$ and $RuCl_3$ compounds, Phys. Rev. B **50**, 2095 (1994).

[37] H.-S. Kim, V. Shankar, A. Catuneanu, and H.-Y. Kee, Kitaev magnetism in honeycomb $RuCl_3$ with intermediate spin-orbit coupling, Phys. Rev. B **91**, 241110(R) (2015).

[38] L. J. Sandilands, C. H. Sohn, H. J. Park, S. Y. Kim, K. W. Kim, J. A. Sears, Y.-J. Kim, and T. W. Noh, Optical probe of Heisenberg-Kitaev magnetism in α-$RuCl_3$, Phys. Rev. B **94**, 195156 (2016).

[39] A. Koitzsch, C. Habenicht, E. Müller, M. Knupfer, B. Büchner, H. C. Kandpal, J. van den Brink, D. Nowak, A. Isaeva, and Th. Doert, J_{eff} Description of the Honeycomb Mott Insulator α-$RuCl_3$, Phys. Rev. Lett. **117**, 126403 (2016).

[40] A. Koitzsch, E. Müller, M. Knupfer, B. Büchner, D. Nowak, A. Isaeva, T. Doert, M. Grüninger, S. Nishimoto, and J. van den Brink, Low temperature enhancement of ferromagnetic Kitaev correlations in α-$RuCl_3$, Phys. Rev. Materials **4**, 094408 (2020).

[41] T. Biesner, S. Biswas, W. Li, Y. Saito, A. Pustogow, M. Altmeyer, A. U. B. Wolter, B. Büchner, M. Roslova, T. Doert, S. M. Winter, R. Valentí, and M. Dressel, Detuning the honeycomb of α-$RuCl_3$: Pressure-dependent optical studies reveal broken symmetry, Phys. Rev. B **97**, 220401(R) (2018).

[42] S. Agrestini, C.-Y. Kuo, K.-T. Ko, Z. Hu, D. Kasinathan, H. B. Vasili, J. Herrero-Martin, S. M. Valvidares, E. Pellegrin, L.-Y. Jang, A. Henschel, M. Schmidt, A. Tanaka, and L. H. Tjeng, Electronically highly cubic conditions for Ru in α-$RuCl_3$, Phys. Rev. B **96**, 161107(R) (2017).

[43] R. Yadav, N. A. Bogdanov, V. M. Katukuri, S. Nishimoto, J. van den Brink, and L. Hozoi, Kitaev exchange and field-induced quantum spin-liquid states in honeycomb α-$RuCl_3$, Sci. Rep. **6**, 37925 (2016).

[44] W. Wang, Z.-Y. Dong, S.-L. Yu, and J.-X. Li, Theoretical investigation of magnetic dynamics in α-$RuCl_3$, Phys. Rev. B **96**, 115103 (2017).

[45] S. M. Winter, Y. Li, H. O. Jeschke, and R. Valentí, Challenges in design of Kitaev materials: Magnetic interactions from competing energy scales, Phys. Rev. B **93**, 214431 (2016).

[46] Winter *et al.* [45] report the crystal-field parameters $\Delta_1 = -19.8$ meV, $\Delta_2 = -17.5$ meV, and $\Delta_3 = -12.5$ meV with energies E_i of the pure crystal-field Hamiltonian of $-\Delta_1$ and $\frac{1}{2}(\Delta_1 + \Delta_3 \pm \sqrt{(\Delta_1 - \Delta_3)^2 + 8\Delta_2^2})$. This yields $E_1 = -41.2$ meV, $E_2 = 8.9$ meV, $E_3 = 19.8$ meV, and $\Delta_{\text{CF}} \approx (E_2 + E_3)/2 - E_1 \approx 55$ meV. With our result for λ, this is equivalent to $\Delta \approx \frac{2}{3}\Delta_{\text{CF}} \approx 37$ meV.

[47] J. Chaloupka and G. Khaliullin, Hidden symmetries of the extended Kitaev-Heisenberg model: Implications for the honeycomb-lattice iridates A_2IrO_3, Phys. Rev. B **92**, 024413 (2015).

[48] B. H. Kim, T. Shirakawa, and S. Yunoki, From a Quasimolecular Band Insulator to a Relativistic Mott Insulator in t_{2g}^5 Systems with a Honeycomb Lattice Structure, Phys. Rev. Lett. **117**, 187201 (2016).

[49] J. Lorenzana and G. A. Sawatzky, Phonon Assisted Multimagnon Optical Absorption and Long Lived Two-Magnon States in Undoped Lamellar Copper Oxides, Phys. Rev. Lett. **74**, 1867 (1995).

[50] J. Lorenzana and G. A. Sawatzky, Theory of phonon-assisted multimagnon optical absorption and bimagnon states in quantum antiferromagnets, Phys. Rev. B **52**, 9576 (1995).

[51] J.-A. Yang, Y.-P. Huang, M. Hermele, T. Qi, G. Cao, and D. Reznik, High-energy electronic excitations in Sr_2IrO_4 observed by Raman scattering, Phys. Rev. B **91**, 195140 (2015).

[52] B. Henderson and G. F. Imbusch, *Optical Spectroscopy of Inorganic Solids* (Oxford University Press, Oxford, 1989).

[53] R. Rückamp, E. Benckiser, M. W. Haverkort, H. Roth, T. Lorenz, A. Freimuth, L. Jongen, A. Möller, G. Meyer, P. Reutler, B. Büchner, A. Revcolevschi, S.-W. Cheong, C. Sekar, G. Krabbes, and M. Grüninger, Optical study of orbital excitations in transition-metal oxides, New J. Phys. **7**, 144 (2005).

[54] R. K. Yoo and T. A. Keiderling, Intraconfigurational absorption spectroscopy of $IrCl_6^{2-}$ and IrB_6^{2-} in A_2MX_6-type host crystals, Chem. Phys. **108**, 317 (1986).

[55] A previous SW analysis of a different data set was reported in the Ph.D. thesis of one of the authors, N. Borgwardt [64]. This analysis finds phonon energies of 25 meV for peak A, 40 meV for peak B, and that peak C is not phonon assisted, in good agreement with our claims.

[56] E. M. Plotnikova, M. Daghofer, J. van den Brink, and K. Wohlfeld, Jahn-Teller Effect in Systems with Strong On-Site Spin-Orbit Coupling, Phys. Rev. Lett. **116**, 106401 (2016).

[57] Y. Sizyuk, C. Price, P. Wölfle, and N. B. Perkins, Importance of anisotropic exchange interactions in honeycomb iridates: Minimal model for zigzag antiferromagnetic order in Na_2IrO_3, Phys. Rev. B **90**, 155126 (2014).

[58] S. Sinn, C. H. Kim, B. H. Kim, K. D. Lee, C. J. Won, J. S. Oh, M. Han, Y. J. Chang, N. Hur, H. Sato, B.-G. Park, C. Kim, H.-D. Kim, and T. W. Noh, Electronic structure of the Kitaev material α-$RuCl_3$ probed by photoemission and inverse photoemission spectroscopies, Sci. Rep. **6**, 39544 (2016).

[59] M. Grüninger, M. Windt, E. Benckiser, T. S. Nunner, K. P. Schmidt, G. S. Uhrig, and T. Kopp, Optical spectroscopy of low-dimensional quantum spin systems, Adv. Solid State Phys. **43**, 95 (2003).

[60] In leading order one finds $q_{\rm eff} \propto ea\frac{J}{\Delta_{is}^2}\frac{\partial \Delta E_M}{\partial u}$, where e denotes the electric charge, a the metal-metal distance, Δ_{is} the effective intersite excitation energy, and ΔE_M the phonon-induced difference in metal on-site energies. In the cuprates, exchange is an order of magnitude larger than in α-$RuCl_3$, and Δ_{is} is about a factor of 2 larger. We thus find that $q_{\rm eff}$ is of the same order of magnitude.

[61] E. Benckiser, R. Rückamp, T. Möller, T. Taetz, A. Möller, A. A. Nugroho, T. T. M. Palstra, G. S. Uhrig, and M. Grüninger, Collective orbital excitations in orbitally ordered YVO_3 and $HoVO_3$, New J. Phys. **10**, 053027 (2008).

[62] See Supplemental Material at http://link.aps.org/supplemental/10.1103/PhysRevResearch.2.042007 for a theoretical analysis of interaction effects on the weight of the double spin-orbit exciton and for an exact diagonalization study of a two-site cluster.

[63] M. Windt, M. Grüninger, T. Nunner, C. Knetter, K. P. Schmidt, G. S. Uhrig, T. Kopp, A. Freimuth, U. Ammerahl, B. Büchner, and A. Revcolevschi, Observation of Two-Magnon Bound States in the Two-Leg Ladders of $(Ca, La)_{14}Cu_{24}O_{41}$, Phys. Rev. Lett. **87**, 127002 (2001).

[64] N. Borgwardt, Optics on materials with strong spin-orbit coupling: topological insulators $Bi_{2-x}Sb_xTe_{3-y}Se_y$ and the $j = 1/2$ compounds Na_2IrO_3 and α-$RuCl_3$, Ph.D. thesis, University of Cologne, 2019.

Supplemental Material: Multiple Spin-Orbit Excitons and the Electronic Structure of α-$RuCl_3$

P. Warzanowski,[1] N. Borgwardt,[1] K. Hopfer,[1] J. Attig,[2] T. C. Koethe,[1] P. Becker,[3] V. Tsurkan,[4,5] A. Loidl,[4] M. Hermanns,[6,7] P. H. M. van Loosdrecht,[1] and M. Grüninger[1]

[1]*Institute of Physics II, University of Cologne, 50937 Cologne, Germany*
[2]*Institute for Theoretical Physics, University of Cologne, 50937 Cologne, Germany*
[3]*Sect. Crystallography, Institute of Geology and Mineralogy, University of Cologne, 50674 Cologne, Germany*
[4]*Experimental Physics V, Center for Electronic Correlations and Magnetism, University of Augsburg, 86135 Augsburg, Germany*
[5]*Institute of Applied Physics, MD 2028 Chisinau, Moldova*
[6]*Department of Physics, Stockholm University, AlbaNova University Center, SE-106 91 Stockholm, Sweden*
[7]*Nordita, KTH Royal Institute of Technology and Stockholm University, SE-106 91 Stockholm, Sweden*

(Dated: August 14, 2020)

DOUBLE SPIN-ORBIT EXCITON

A: Weights of final states

The observation of a double spin-orbit exciton is unusual but double excitations involving orbitals are not unprecedented, as discussed in the main text. Figure 1(B) of the main text shows a simplified sketch which illustrates how the double spin-orbit exciton is boosted by the nearest-neighbor hopping amplitudes in α-$RuCl_3$. The main simplification lies in neglecting interactions in the intermediate state after the first hopping process, when two holes reside on the same site. Here, we shortly demonstrate that Fig. 1(B) describes the essential physics correctly, even in the presence of interactions.

We consider two neighboring sites a and b and the four possible initial states with $j = 1/2$ moments on each site,

$$\begin{aligned}
|\text{initial}, 1\rangle &= |1/2, 1/2\rangle_a \otimes |1/2, 1/2\rangle_b \\
|\text{initial}, 2\rangle &= (|1/2, 1/2\rangle_a \otimes |1/2, -1/2\rangle_b + a \leftrightarrow b)/\sqrt{2} \\
|\text{initial}, 3\rangle &= |1/2, -1/2\rangle_a \otimes |1/2, -1/2\rangle_b \\
|\text{initial}, 4\rangle &= (|1/2, 1/2\rangle_a \otimes |1/2, -1/2\rangle_b - a \leftrightarrow b)/\sqrt{2}\,,
\end{aligned}$$

where the first number denotes the quantum number j and the second j_z. Note that the general arguments do not depend on the details of the initial spin configuration, i.e., the final results of states 1 and 3 (2 and 4) are identical. Hence we will only discuss the first two states.

We first focus on $|\text{initial}, 1\rangle$. As expressed in Fig. 1(B) of the main text, edge-sharing octahedra allow for only very few non-zero hopping amplitudes. In particular, $|1/2, 1/2\rangle_a$ can only hop to $|3/2, -3/2\rangle_b$, leading to the intermediate state

$$|\text{inter}\rangle = (|1/2, 1/2\rangle_a \otimes |3/2, -3/2\rangle_a + a \leftrightarrow b)/\sqrt{2}\,.$$

If both Hund's coupling J_H and the crystal-field splitting Δ_{CF} vanish, this state is an eigenstate of the interaction Hamiltonian. In this case, a second hopping process leads to only three possible final states,

$$\begin{aligned}
|\text{final}, 1\rangle &= |1/2, 1/2\rangle_a \otimes |1/2, 1/2\rangle_b \\
|\text{final}, 2\rangle &= (|1/2, 1/2\rangle_a \otimes |3/2, 1/2\rangle_b + a \leftrightarrow b)/\sqrt{2} \\
|\text{final}, 3\rangle &= |3/2, -3/2\rangle_a \otimes |3/2, -3/2\rangle_b\,.
\end{aligned}$$

The first two are due to the hole in $|3/2, -3/2\rangle$ hopping back to its original site, bringing us either back to $|\text{initial}, 1\rangle = |\text{final}, 1\rangle$ or to a single spin-orbit exciton $|\text{final}, 2\rangle$. State $|\text{final}, 3\rangle$ is the one we are interested in, corresponding to a double spin-orbit exciton. It carries a large part of the weight, see Fig. S1.

If either J_H or Δ_{CF} are non-vanishing, we need to project on the 15 true two-hole eigenstates for the intermediate state, which in turn will give non-vanishing amplitudes to additional final states such as $|3/2, 1/2\rangle_a \otimes |3/2, 1/2\rangle_b$. This projector is implemented as

$$\mathcal{P} = \sum_{j=1}^{15} \frac{1}{\epsilon_j} |\xi_j\rangle\langle\xi_j|,$$

where ϵ_j are the eigenenergies of the interacting eigenstates $|\xi_j\rangle$. Thus, we can find the non-vanishing amplitudes for, say, two sites along a z bond by computing

$$M = T_z^\dagger \mathcal{P} T_z$$

where T_z denotes the full hopping matrix for this bond. We find that the largest part of the weight is shared by the initial state $|\text{final}, 1\rangle$ and the double spin-orbit exciton $|\text{final}, 3\rangle$, both for $J_H = 0$ and in the realistic range $0.3\,\text{eV} \leq J_H \leq 0.4\,\text{eV}$, see Fig. S1. For $J_H = 0.4\,\text{eV}$, the double spin-orbit exciton has only 3.2 % contribution from states other than $|\text{final}, 3\rangle$ (or, starting from $|\text{inital}, 2\rangle$, 7.8 % other than $|3/2, 3/2\rangle_a \otimes |3/2, 3/2\rangle_b$). This shows that the simple picture of Fig. 1(B) remains qualitatively correct in the presence of interactions, supporting our interpretation of the experimental features as double spin-orbit excitons.

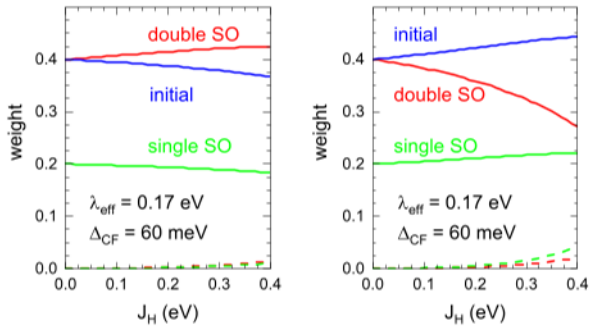

FIG. S1: Weight (absolute value squared of the amplitude) of final states reached after two hopping processes, starting from either $|\text{initial}, 1\rangle$ (left) or $|\text{inital}, 2\rangle$ (right). The weight is plotted as a function of Hund's coupling J_H for $\Delta_{\text{CF}} = 60\,\text{meV}$, $\lambda_{\text{eff}} = 0.17\,\text{eV}$, and $U = 2\,\text{eV}$. The sign of Δ_{CF} and the exact size of U have very little influence on the result. Blue/green/red solid lines: weights of the initial state $|\text{final}, 1\rangle$ / a single spin-orbit exciton $|\text{final}, 2\rangle$ / a double spin-orbit exciton $|\text{final}, 3\rangle$. The red (green) dashed line denotes the *total* weight of all other states contributing to the double (single) spin-orbit exciton.

B: Energies

A full discussion of the energies of double spin-orbit excitons – including the effects of dispersion and interactions – is beyond the scope of our study. However, to support the plausibility of our assignment we employ exact diagonalization of a two-site cluster, equivalent to a z bond in edge-sharing geometry. We study the effect of nearest-neighbor hopping t_{xz-yz} between the xz (yz) orbital on site i and the yz (xz) orbital on site j, which forms the basis for dominant Kitaev exchange. Direct hopping between the xy orbitals is neglected. We use $U = 2\,\text{eV}$ and $J_H = 0.4\,\text{eV}$, resulting in an effective 'gap' for double occupancy of about 1 eV, as observed experimentally. The energies for all states below the gap are plotted in Fig. S2 as a function of t_{xz-yz}. We estimate $t_{xz-yz} \approx t_{pd\pi}^2/\Delta_{\text{CT}} \approx 0.16\,\text{eV}$ (vertical dashed line) from the hopping between Ru xz/yz and Cl p_z orbitals, $t_{pd\pi} = $-0.9 eV, and the charge-transfer energy $\Delta_{\text{CT}} = 5\,\text{eV}$ [1, 2]. For this choice of t_{xz-yz}, the magnetic excitations within the $j = 1/2$ sector reach up to about 10 meV, in reasonable agreement with the energy scale observed in different experiments.

For the considered two-site cluster with a finite trigonal crystal-field splitting $\Delta_{\text{CF}} = \pm 60\,\text{meV}$, finite hopping gives rise to a bonding-antibonding type of splitting of the spin-orbit exciton states, see Fig. S2. In this figure, we also plot the observed Raman energies (blue symbols). Remarkably, the two dominant Raman features at 248 meV and 290 meV (full symbols) coincide with several branches of calculated energies, and even the weaker Raman features (open symbols) observed at 195 meV and 224 meV tentatively can be attributed to the two lowest branches of single spin-orbit excitons. The hopping-induced splitting on the two-site cluster partially mimics dispersion in an infinite lattice, and Raman scattering is sensitive to momentum $k = 0$ only. Hence, not all the modes depicted in Fig. S2 will contribute to the Raman signal, but some of the calculated splittings still may provide a possible explanation for the smaller structures observed in experiment. Note that the chosen value of $\lambda_{\text{eff}} = 165\,\text{meV}$ is slightly smaller than the value of 175 meV to 177 meV discussed in the main text for a single site. This is due to the fact that most energies of single spin-orbit excitons increase with increasing t_{xz-yz}.

For finite hopping t_{xz-yz}, the energies of double spin-orbit excitons no longer correspond to simple combination tones of single spin-orbit excitons, which reflects interactions. The lowest double spin-orbit exciton energy found for $t_{xz-yz} = 0.16\,\text{eV}$ coincides with the 450 meV observed in Raman scattering. We thus conclude that this simple model on a two-site cluster is able to reproduce the experimentally determined Raman energies for a realistic set of parameters. While this may not yet serve as a definite proof of our assignment, it strongly confirms the plausibility of the scenario discussed in the main text.

[1] S. Sinn, C. H. Kim, B. H. Kim, K. D. Lee, C. J. Won, J. S. Oh, M. Han, Y. J. Chang, N. Hur, H. Sato, B.-G. Park, C. Kim, H.-D. Kim, and T. W. Noh, Sci. Rep. **6**, 39544 (2016).

[2] S. M. Winter, Y. Li, H. O. Jeschke, and R. Valentí, Phys. Rev. B **93**, 214431 (2016).

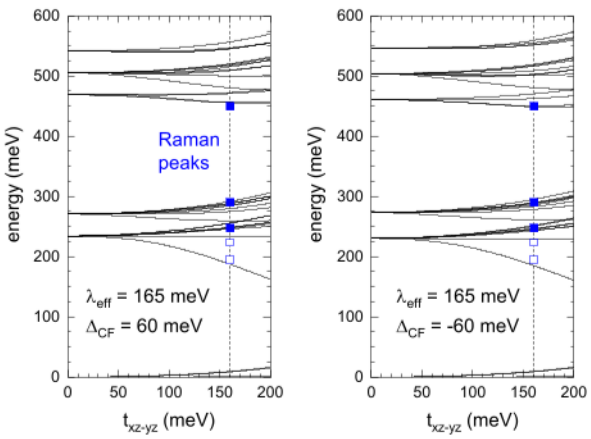

FIG. S2: Exact diagonalization result for the energies of two holes on adjacent sites forming a z bond. We employ $U = 2\,\text{eV}$, $J_H = 0.4\,\text{eV}$, $\lambda_{\text{eff}} = 165\,\text{meV}$, and trigonal crystal-field splitting $\Delta_{\text{CF}} = 60\,\text{meV}$ (left) or -60 meV (right). The expected value for hopping $t_{xz-yz} = 0.16\,\text{eV}$ [2] is marked by the vertical dashed line. In this case, magnetic excitations reach up to about 10 meV, single spin-orbit excitons cover the range from about 200 meV to 300 meV, while double spin-orbit excitons occur between about 460 meV and 560 meV. Full (open) symbols denote the energies of strong (weak) Raman features observed in our experimental data.

5 Electronic excitations in $5d^4$ $J = 0$ Os^{4+} halides studied by resonant inelastic x-ray scattering and optical spectroscopy

The following chapter presents the results on the Os-based $5d^4$ $J = 0$ antifluorite halides, which have been published as Warzanowski *et al.*, *Electronic excitations in* $5d^4$ $J = 0$ Os^{4+} *halides studied by resonant inelastic x-ray scattering and optical spectroscopy*, Phys. Rev. B **108**, 125120 (2023).

Author contributions

M. Grüninger and P. Warzanowski conceived the experiment. P. Warzanowski carried out the optical spectroscopy experiments. P. Warzanowski, M. Magnaterra, P. Stein, Q. Faure, Ch. J. Sahle, and M. Grüninger carried out the RIXS experiments at the ID20 beamline at the ESRF, supported by M. Moretti Sala, G. Monaco, and P. H. M. van Loosdrecht. G. Schlicht supported P. Warzanowski on the optical spectroscopy experiments on K_2OsBr_6. T. Lorenz contributed the magnetic susceptibility data. P. Becker and L. Bohatý synthesized and characterized the samples. P. Warzanowski analyzed the data and performed the numerical single-site calculations with support from M. Magnaterra, T. Lorenz, and M. Grüninger. P. Warzanowski and M. Grüninger wrote the manuscript with input from all authors.

Sample and data availability

The samples used in this project are stored within the labs of the Institute of Physics II at the University of Cologne. The raw data and the analysis files are stored on the servers of the Institute of Physics II.

Editors' Suggestion

Electronic excitations in $5d^4$ $J = 0$ Os^{4+} halides studied by resonant inelastic x-ray scattering and optical spectroscopy

P. Warzanowski,[1] M. Magnaterra,[1] P. Stein,[1] G. Schlicht,[1] Q. Faure,[2,3] Ch. J. Sahle,[2] T. Lorenz,[1] P. Becker,[4] L. Bohatý,[4] M. Moretti Sala,[5] G. Monaco,[6] P. H. M. van Loosdrecht,[1] and M. Grüninger[1]

[1]*Institute of Physics II, University of Cologne, 50937 Cologne, Germany*
[2]*ESRF, The European Synchrotron, 71 Avenue des Martyrs, CS40220, 38043 Grenoble Cedex 9, France*
[3]*Laboratoire Léon Brillouin, CEA, Centre National de la Recherche Scientifique, Université Paris-Saclay, CEA-Saclay, 91191 Gif-sur-Yvette, France*
[4]*Sect. Crystallography, Institute of Geology and Mineralogy, University of Cologne, 50674 Cologne, Germany*
[5]*Dipartimento di Fisica, Politecnico di Milano, I-20133 Milano, Italy*
[6]*Dipartimento di Fisica e Astronomia "Galileo Galilei," Università di Padova, I-35121 Padova, Italy*

(Received 21 June 2023; accepted 29 August 2023; published 14 September 2023)

We demonstrate that the cubic antifluorite-type halides K_2OsCl_6, K_2OsBr_6, and Rb_2OsBr_6 are excellent realizations of nonmagnetic $J = 0$ compounds. The magnetic susceptibility shows the corresponding Van Vleck type of behavior and no sign of defects. We investigate the electronic excitations with two complementary techniques, resonant inelastic x-ray scattering and optical spectroscopy. This powerful combination allows us to thoroughly study, e.g., on-site intra-t_{2g} excitations and t_{2g}-to-e_g excitations as well as intersite excitations across the Mott gap and an exciton below the gap. In this way, we determine the electronic parameters with high accuracy, altogether yielding a comprehensive picture. In K_2OsCl_6, we find the spin-orbit coupling constant $\zeta = 0.34$ eV, Hund's coupling $J_H = 0.43$ eV, the onset of excitations across the Mott gap at $\Delta = 2.2$ eV, the cubic crystal-field splitting $10Dq = 3.3$ eV, and the charge-transfer energy $\Delta_{CT} = 4.6$ eV. With $J_H/\zeta = 1.3$, K_2OsCl_6 is in the intermediate-coupling regime. In a t_{2g}-only Kanamori picture, the above values correspond to $\zeta^{\text{eff}} = 0.41$ eV and $J_H^{\text{eff}} = 0.28$ eV, which is very close to results reported for related $5d^4$ iridates. In the tetragonal phase at 5 K, the noncubic crystal field causes a peak splitting of the $J = 1$ state as small as 4 meV. Compared to K_2OsCl_6, the bromides K_2OsBr_6 and Rb_2OsBr_6 show about 12–14% smaller values of $10Dq$ and Δ_{CT}, while the spin-orbit entangled intra-t_{2g} excitations below 2 eV and hence ζ and J_H are reduced by less than 4%. Furthermore, the Mott gap in K_2OsBr_6 is reduced to about 1.8 eV.

DOI: 10.1103/PhysRevB.108.125120

I. INTRODUCTION

The family of $5d$ transition-metal compounds features Mott-insulating quantum materials in which strong spin-orbit coupling plays the central role [1–5]. Prominent examples are t_{2g}^5 iridates with spin-orbit entangled $J = 1/2$ moments [6–8]. Compounds with edge-sharing IrO_6 octahedra have been predicted to show bond-directional Kitaev-type exchange couplings [9]. This has raised hopes to realize the Kitaev model on tricoordinated lattices, where strong exchange frustration yields an intriguing quantum spin liquid [10–12]. Experimentally, the dominant bond-directional character of exchange interactions has been demonstrated for honeycomb Na_2IrO_3 [13,14]. Remarkably, Kitaev exchange has been found to have a very different effect for $J = 1/2$ moments on an fcc lattice with corner-sharing IrO_6 octahedra as realized in the double perovskite Ba_2CeIrO_6. There, antiferromagnetic Kitaev coupling counteracts the geometric frustration of isotropic Heisenberg exchange [15]. For face-sharing IrO_6 octahedra as in the Ir_2O_9 dimer compounds $Ba_3MIr_2O_9$, spin-orbit coupling competes with strong intradimer hopping that yields quasimolecular orbitals. Still, resonant inelastic x-ray scattering (RIXS) studies for $M = Ce^{4+}$ and In^{3+} established the spin-orbit entangled $J_{\text{dim}} = 0$ and 3/2 character of the respective quasimolecular magnetic moments [16,17].

For a t_{2g}^4 configuration in cubic symmetry, dominant spin-orbit coupling ζ is expected to yield a nonmagnetic $J = 0$ ground state. However, strong exchange interactions give rise to a dispersion of magnetic excited states, and if the dispersion is large enough, these may condense and drive magnetism of excitonic Van Vleck type that is also called singlet magnetism [18–22]. In this scenario, a magnetic amplitude mode equivalent to a Higgs mode is expected, which has been proposed for antiferromagnetic Ca_2RuO_4 [18,23]. In this layered $4d^4$ compound, one has to consider the tetragonal crystal-field splitting Δ_{CF} [21,24–33] and that spin-orbit coupling is smaller than in $5d$ materials such that the physics is governed by the ratio $\Delta_{CF}/\zeta > 2$ [32,33]. For dominant noncubic Δ_{CF}, d^4 compounds turn into spin $S = 1$ magnets. Considering (nearly) cubic symmetry, the local intra-t_{2g} excitations from the $J = 0$ state have been studied by RIXS in $4d^4$ K_2RuCl_6 [34] and in the $5d^4$ Ir^{5+} double perovskites A_2BIrO_6 (A = Ba, Sr; B = Y, Gd, Lu, Sc) [35–39]. Among these, Sr_2YIrO_6 and Ba_2YIrO_6 were reported to host magnetic order [40,41] which has been attributed to the presence of $5d^5$ Ir^{4+} and $5d^3$ Ir^{6+} defects [42]. Pyrochlore $Yb_2Os_2O_7$ with $5d^4$ Os^{4+} ions exhibits a

trigonal distortion and a defect-induced magnetic response [43]. For K_2RuCl_6, the possible role of vibronic effects has been discussed [44].

Here, we employ RIXS at the Os L_3 edge and optical spectroscopy to study stoichiometric single crystals of the $5d^4$ halides K_2OsCl_6 and A_2OsBr_6 with A = K and Rb. In the magnetic susceptibility, we do not find any indication of magnetic defects. Our results establish these materials as a reference for $J = 0$ systems in the intermediate regime between LS coupling for $J_H/\zeta \to \infty$ and jj coupling for $J_H/\zeta \to 0$. We show that $J_H/\zeta = 1.3$ is equivalent to $J_H^{\rm eff}/\zeta^{\rm eff} = 0.8$ in the Kanamori scheme [45], which considers only t_{2g} orbitals. Our result for $J_H^{\rm eff}/\zeta^{\rm eff}$ is in excellent agreement with the values reported for $5d^4$ iridates [35–38]. The antifluorite-type Os compounds combine several properties which are advantageous for a precise determination of the electronic parameters. At room temperature, they show cubic symmetry [46–48], and for the purpose of studying the local electronic excitations the compounds may be viewed as being composed of undistorted, well-separated OsX_6 octahedra with, to first approximation, negligible interactions between them. This yields well-defined, narrow RIXS peaks even at high energy such as the charge-transfer excitations at 4.6, 5.7, and 8.0 eV in K_2OsCl_6, allowing for a straightforward determination of the charge-transfer energy $\Delta_{\rm CT}$.

For the study of orbital and electronic excitations in Mott insulators, RIXS and optical spectroscopy are complementary techniques. In the case of inversion symmetry, RIXS at the transition-metal L edge is in particular sensitive to local, parity-conserving excitations between d orbitals [32,34–37,43,49]. In contrast, optical spectroscopy is most sensitive to electric dipole active absorption features such as inter-site excitations across the Mott gap or excitons [33,50,51], while local excitations between d orbitals mainly contribute in a phonon-assisted process, i.e., they become electric dipole active by the simultaneous excitation of a symmetry-breaking phonon [52–55]. Interesting examples studied by both techniques are, e.g., the $3d^2$ vanadates RVO_3 [51,55,56] or the excitations from $J = 1/2$ to $3/2$ in the $4d^5$ Kitaev material $\alpha - RuCl_3$ [57–59]. In the infrared data, weak phonon-assisted absorption features can only be detected in the transparent range with excitation energies smaller than the Mott gap. In comparison, RIXS offers the possibility to observe the corresponding orbital excitations also for larger excitation energies but with limited energy resolution. At the Os L_3 edge with an incident energy $E_{\rm in} = 10.870$ keV, we achieve a resolution $\delta E = 63$ meV, i.e., $\delta E/E_{\rm in} \approx 6 \times 10^{-6}$. In contrast, the Fourier spectrometer employed for infrared measurements offers a resolution better than 0.1 meV. Accordingly, it is more difficult to determine the electronic parameters by using only one of the two techniques, as discussed, e.g., for RIXS on $Yb_2Os_2O_7$ [43] or infrared spectroscopy on K_2OsCl_6 [60]. For K_2OsCl_6, we will show below that the combination of the two techniques resolves all ambiguities.

II. SINGLE-CRYSTAL GROWTH AND CRYSTAL STRUCTURE

Single crystals of K_2OsCl_6 and of the bromides A_2OsBr_6 with A = K and Rb were grown starting from commercially available dihydrogen hexahalogenoosmate (IV) H_2OsCl_6, respectively H_2OsBr_6, and the respective halide KCl or ABr. The educts were dissolved in a stoichiometric ratio in diluted hydrochloric (respectively hydrobromic) acid. For the potassium compounds, single crystals of several millimeters size were achieved by slow, controlled evaporation of the solvent at 293 K during a typical growth period of one to two weeks. For the Rb compound, crystals were of submillimeter size due to the low solubility. Examples of K_2OsBr_6 and K_2OsCl_6 are shown in Fig. 1.

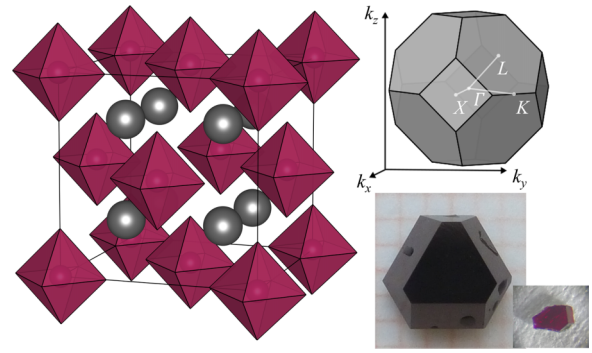

FIG. 1. Left: Face-centered cubic crystal structure of A_2OsX_6 at 300 K. The OsX_6 octahedra (X = Cl, Br) are plotted in red and the A^+ ions (A = K, Rb) are shown in gray. Top right: Sketch of the first Brillouin zone of the fcc lattice with the high-symmetry points Γ, X, K, and L. Lower right: Photos of a K_2OsBr_6 crystal and of the thin, transparent sample of K_2OsCl_6 that has been studied in infrared transmittance. The size of the latter amounts to $\approx 0.5\,\text{mm} \times 0.3\,\text{mm} \times 0.12\,\text{mm}$.

At room temperature, these K_2PtCl_6-type compounds show a cubic crystal structure with space group $Fm\bar{3}m$ [46–48] (see Fig. 1). The Os^{4+} ions are located on an fcc lattice. The stoichiometry of all three compounds has been verified on small crystals by x-ray diffraction in the cubic phase [61]. At 45 K, K_2OsCl_6 exhibits a phase transition to a tetragonal phase [47]. For K_2OsBr_6, the structural transition at 220 K to a phase with tetragonal symmetry is followed by a phase transition to a monoclinic phase at 200 K [48].

III. MAGNETIC SUSCEPTIBILITY

The magnetic susceptibility χ of K_2OsCl_6 and K_2OsBr_6 is plotted in Fig. 2. We observe a temperature-independent susceptibility without any indication of a Curie-Weiss contribution of defects. The constant value $\chi = 7.5 \times 10^{-4}$ emu/mol can be attributed to a dominant Van Vleck term and a small diamagnetic contribution of the closed shells of K^+, Os^{4+}, Cl^-, and Br^-, $\chi = \chi_{\rm VV} + \chi_{\rm dia}$. Via tabulated values [62], we estimate $\chi_{\rm dia}^{\rm Cl} = -2.1 \times 10^{-4}$ emu/mol and $\chi_{\rm dia}^{\rm Br} = -2.7 \times 10^{-4}$ emu/mol. This yields experimental values of the Van Vleck contribution of $\chi_{\rm VV}^{\rm Cl} = 9.6 \times 10^{-4}$ emu/mol and $\chi_{\rm VV}^{\rm Br} = 10.2 \times 10^{-4}$ emu/mol.

Our spectroscopic data establish a $J = 0$ ground state of the $5d^4$ configuration of Os^{4+} (see Sec. V), in agreement with predictions of density functional theory [63]. The

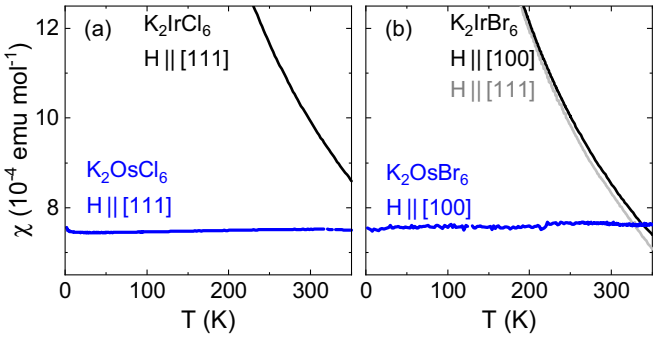

FIG. 2. Magnetic susceptibility χ of K_2OsCl_6 and K_2OsBr_6. Both compounds show dominant temperature-independent Van Vleck paramagnetism. For comparison, we show χ of the $J = 1/2$ iridium sister compounds with a sizable Curie-Weiss contribution.

corresponding Van Vleck susceptibility is given by

$$\chi_{\mathrm{VV}} = \frac{N}{V} 2\mu_B^2 \sum_n \frac{|\langle n|L_z + gS_z|0\rangle|^2}{E_n - E_0}, \tag{1}$$

where $|0\rangle$ and $|n\rangle$ denote the ground state and excited states, respectively, $E_n - E_0$ is the respective energy difference, S_z and L_z refer to the z components of spin and orbital angular momentum, μ_B is the Bohr magneton, and N/V denotes the density of Os ions. In the most simple picture, one can consider only the matrix elements from the $J = 0$ ground state to the lowest excited state, the $J = 1$ triplet, assuming that all other excitation energies are infinite. Only the matrix element to the $J_z = 0$ state of the triplet is finite. Using an $|M_S, M_L\rangle$ basis [18], the relevant states are $|0\rangle = (|1,-1\rangle - |0,0\rangle + |-1,1\rangle)/\sqrt{3}$ and $|1\rangle = (|1,-1\rangle - |-1,1\rangle)/\sqrt{2}$. With $\mathbf{M} = 2\mathbf{S} - \mathbf{L}$ [18] for the t_{2g} states with $L_{\mathrm{eff}} = -1$, the corresponding matrix element equals $|\langle 1|L_z - 2S_z|0\rangle|^2 = 6$. With an excitation energy of 0.35 eV (see below), this yields $\chi_{\mathrm{VV}}^{J=1} = 11 \times 10^{-4}$ emu/mol. As a more sophisticated alternative, we calculate the matrix elements via QUANTY [64,65], using the electronic parameters that result from our thorough analysis of the spectroscopic data discussed below. For the 209 possible excited states of a $5d^4$ configuration, we find that only two states contribute significantly. About 90% arise from the $J = 1$ state at about 0.35 eV, while 10% stem from a state with one electron in the e_g orbitals at about 3.5 eV. The two matrix elements are similar, hence the contribution of the second term is suppressed by about a factor 10 due to the higher excitation energy. We find $\chi_{\mathrm{VV,mod}}^{\mathrm{Cl}} = 8.8 \times 10^{-4}$ emu/mol and $\chi_{\mathrm{VV,mod}}^{\mathrm{Br}} = 8.6 \times 10^{-4}$ emu/mol, in reasonable agreement with the experimental result.

IV. SPECTROSCOPIC MEASUREMENTS

All RIXS experiments were performed at beamline ID20 of the European Synchrotron Radiation Facility. Incident photons from three consecutive U26 undulators were monochromatized by a Si(111) high-heat-load monochromator and either a successive Si(664) backscattering-channel-cut or a Si(311) channel-cut postmonochromator at 10.870 keV with a final bandwidth of 18 meV or 0.29 eV, respectively. The monochromatic x-ray beam was focused by a mirror system in Kirkpatrick-Baez geometry to 8×50 μm^2 (V × H) at the sample position. Incident π polarization in the horizontal scattering plane was used. We specify the transferred momentum $\mathbf{q}$ in reciprocal lattice units. First, we studied the resonance behavior of K_2OsCl_6 at the Os L_3 edge by measuring low-energy-resolution RIXS spectra with the incident energy in the range from 10.866 to 10.880 keV. Then, the incident energy was tuned to 10.870 keV to maximize the intra-t_{2g} excitations. RIXS spectra were measured using the 2 m analyzer/detector arm of the spectrometer. The Si(6,6,4) reflection of a diced Si(5,5,3) analyzer crystal was utilized in conjunction with a pixelated area detector [66–68]. The overall energy resolution of the setup was 63 meV for the high-energy-resolution spectra and 0.29 eV for the low-energy-resolution spectra, respectively, as estimated by the full width at half maximum of quasielastic scattering from a piece of adhesive tape. To determine the energy-loss scale of the spectrometer, we first define its origin at the center of mass of the rocking curve of a diced Si(664) analyzer crystal using quasielastic scattering from a piece of adhesive tape. Then, the increment of the scale is determined mainly by the analyzer Bragg angle and detector position. The combination of RIXS and optics allows us to examine the accuracy of this approach up to high energies. Comparing the excitation energy of a RIXS peak with the corresponding feature in the optical data at 2117 meV (see below), we find that the two values agree within about 1%. This excellent result is in line with a previous study of the precision of the RIXS energy scale for energies up to 150 meV [69]. For a consistent analysis, we have anchored the RIXS energy-loss scale using the optical value of 2117 meV. The RIXS measurements were performed using a dynamic helium gas flow cryostat as described elsewhere [70]. RIXS data were collected at 20 and 300 K on a (111) surface, with (001) and (110) lying in the horizontal scattering plane. All RIXS spectra are corrected for energy-dependent self-absorption [71].

In the complex optical conductivity $\sigma(\omega) = \sigma_1(\omega) + i\sigma_2(\omega)$, we address very weak absorption features as well as strong ones. This requires two different approaches [50,72,73]. For the strong absorption bands above the Mott gap, we performed ellipsometry measurements on a shiny (111) surface of a K_2OsCl_6 crystal at 300 K in the range from 1 to 6 eV using a Woollam VASE ellipsometer. The ellipsometric data of a cubic single crystal directly yield $\sigma(\omega)$ [74]. In the transparent range below the gap, the transmittance $T(\omega)$ is the appropriate tool, and we obtain complex $\sigma(\omega)$ via determining the complex index of refraction $n(\omega) + i\kappa(\omega)$ with $\kappa \ll n$ and $\sigma_1 \propto n\kappa$ [75]. In particular, $T(\omega)$ depends exponentially on $\kappa(\omega)$, offering high sensitivity. The real part $n(\omega)$ is dominated by contributions from strong absorption bands at higher energy while the weak absorption features leave only very small signatures in $n(\omega)$. For our purpose, $n(\omega)$ can reasonably be approximated as a constant that we derive from the period of the Fabry-Pérot interference fringes in $T(\omega)$ which arise from multiple reflections within the sample. We measured $T(\omega)$ from 0.1 to 2.5 eV at several temperatures in the range from 5 to 300 K using a Bruker IFS 66/v Fourier-transform spectrometer equipped with a continuous-flow ^{4}He cryostat. We employed thin plane-parallel samples with a cubic (111) surface. The sample of K_2OsCl_6 was lapped to

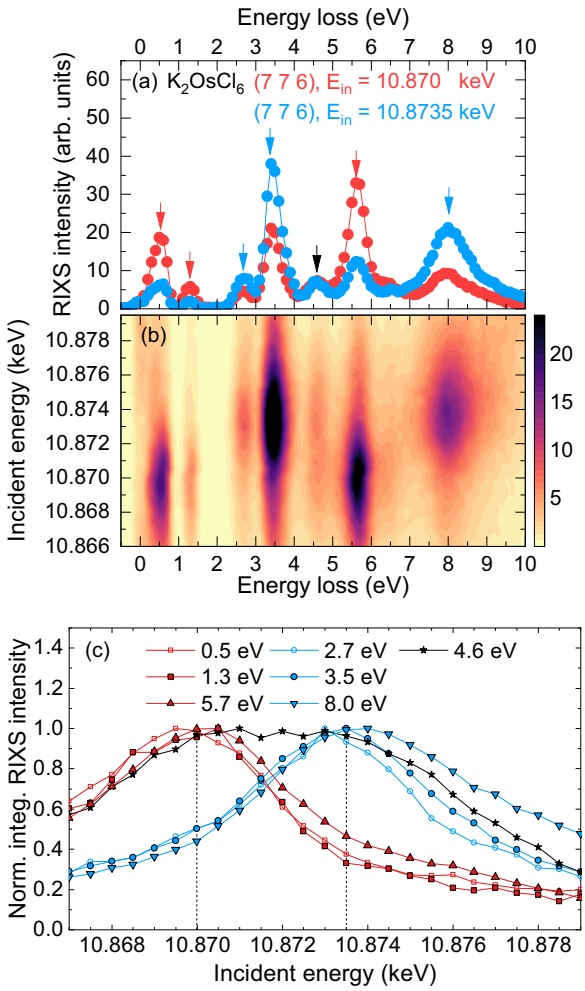

FIG. 3. Resonance behavior of K_2OsCl_6 at $T = 20$ K. (a) Low-resolution RIXS spectra for incident energy $E_{in} = 10.870$ keV and 10.8735 keV, i.e., at t_{2g} and e_g resonance, respectively. Arrows indicate peak energies and their color symbolizes the resonance behavior. (b) Low-resolution resonance map of the RIXS intensity based on RIXS spectra measured with different E_{in} for $\mathbf{q} = (7\ 7\ 6)$. (c) Normalized integrated intensity of the RIXS peaks as a function of E_{in}. The integration interval is chosen to be ± 0.4 eV around the peak energy. With the exception of the 4.6 eV peak, all peaks show either t_{2g} or e_g resonance.

a suitable thickness and polished with CeO_2 in propanol, while the sample of K_2OsBr_6 was measured as grown. The sample thickness amounts to $d = 120(5)$ μm for K_2OsCl_6 and $d = 170(7)$ μm for K_2OsBr_6.

V. RESULTS ON K_2OsCl_6

A. Resonance behavior

To study the resonance behavior and to maximize the RIXS intensity, we collected low-resolution RIXS spectra of K_2OsCl_6 for different incident energies at $T = 20$ K for a transferred momentum $\mathbf{q} = (7\ \ 7\ \ 6)$ [see Fig. 3(b)]. With the energy loss being independent of E_{in} for all of the observed RIXS peaks, we find the two distinct resonance energies $E_{in} = 10.870$ keV and 10.8735 keV, as shown in Fig. 3(c). These can be attributed to t_{2g} resonance and e_g resonance, i.e., resonance enhancement of the initial x-ray absorption part of the RIXS process in which a $2p$ core electron is promoted to either a t_{2g} or an e_g orbital, respectively. The difference of the two resonance energies gives a first estimate of the cubic crystal-field splitting $10Dq \approx 3.5$ eV. This agrees with the strong RIXS peak at about 3.5 eV energy loss that exhibits e_g resonance behavior and corresponds to an excitation from a t_{2g} orbital to an e_g orbital. Cuts of the resonance map at the two resonance energies are shown in Fig. 3(a).

B. Character of RIXS features

Based on the resonance behavior, we distinguish three different kinds of excitations: intra-t_{2g} excitations, crystal-field excitations to e_g orbitals, and charge-transfer excitations. At low energy loss, up to about 2 eV, all RIXS features exhibit t_{2g} resonance and can be attributed to intra-t_{2g} excitations. Their excitation energies mainly reflect spin-orbit coupling ζ and Hund's coupling J_H. These intra-t_{2g} excitations will be addressed below by high-resolution RIXS measurements and optical transmission measurements. At higher energy loss, the RIXS peaks in the range from 2.7 to 4.6 eV are resonantly enhanced for $E_{in} = 10.8375$ keV and correspond to crystal-field excitations to e_g orbitals, $|t_{2g}^4\rangle \rightarrow |t_{2g}^3 e_g^1\rangle$. We will show below that the lowest e_g excitation at 2.7 eV can be identified with the high-spin $S = 2$ multiplet with ^5E symmetry. The energy of this high-spin state is reduced by Hund's coupling J_H, and the ^5E multiplet becomes the d^4 ground state if J_H dominates over the cubic crystal-field splitting $10Dq$.

At still higher energy loss, we observe charge-transfer excitations, $|5d_{Os}^4\, 3p_{Cl}^6\rangle \rightarrow |5d_{Os}^5 3p_{Cl}^5\rangle$. The peaks at 4.6 and 5.7 eV both show t_{2g} resonance and hence can be attributed to $|t_{2g}^5\, 3p_{Cl}^5\rangle$ final states. Roughly, these two excited states with t_{2g}^5 configuration can be identified with $J = 1/2$ and $3/2$ on the Os site. The peak at 8.0 eV energy loss shows e_g resonance and corresponds to excitations from Cl $3p$ to Os $5d$ e_g orbitals. The RIXS peak at 4.6 eV is the only one that resonates at both 10.870 and 10.8735 keV (see lower panel of Fig. 3). This suggests an overlap between an on-site crystal-field excitation to e_g orbitals and the lowest charge-transfer excitation to t_{2g} orbitals. Note that the energy difference of about 3.4 eV between the peaks at 8.0 and 4.6 eV confirms our first rough estimate of $10Dq \approx 3.5$ eV. Accordingly, we identify the peak energy of the lowest charge-transfer excitation with the charge-transfer energy, $\Delta_{CT} = 4.6$ eV.

The occurrence of both t_{2g} resonance and e_g resonance behavior of charge-transfer excitations has previously been observed in, e.g., $5d^5$ K_2IrBr_6 [76], $5d^4$ $Yb_2Os_2O_7$ [43], and $5d^2$ Ba_2YReO_6 [35]. In the present case of K_2OsCl_6, the charge-transfer excitations are particularly well defined and yield comparably narrow RIXS peaks. For instance the 5.7 eV peak shows a full width at half maximum of 0.6 eV. This suggests that the charge-transfer excitations to t_{2g} orbitals are well localized in nonmagnetic K_2OsCl_6, in agreement with the notion that interactions between the well-separated $OsCl_6$ octahedra are very small, at least for t_{2g} orbitals.

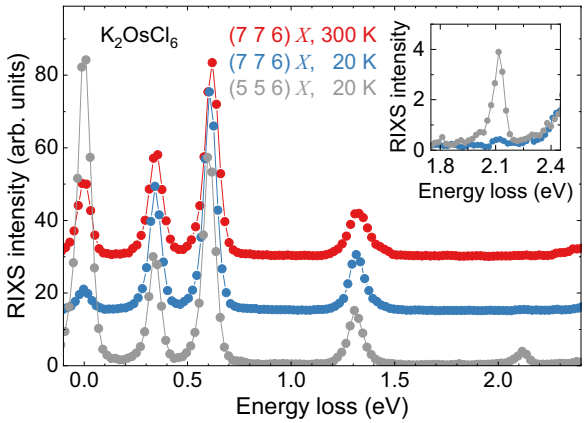

FIG. 4. Intra-t_{2g} excitations of K_2OsCl_6 at the X point. RIXS spectra at $\mathbf{q} = (5\ 5\ 6)$ and $(7\ 7\ 6)$ reveal four peaks at 0.3, 0.6, 1.3, and 2.1 eV with little temperature dependence. For clarity, the data are plotted with an offset. The inset highlights the $^1A_1$ peak at 2.1 eV which is suppressed for a scattering angle $2\theta = 90°$ (see main text).

C. Intra-t_{2g} excitations of K_2OsCl_6 in RIXS

High-resolution RIXS spectra of the intra-t_{2g} excitations reveal four peaks at about 0.3, 0.6, 1.3, and 2.1 eV (see Fig. 4). The local, on-site character of these excitations is highlighted by the insensitivity of the peak energies to the transferred momentum $\mathbf{q}$, i.e., the absence of a measurable dispersion (see Fig. 5). For a first assignment, we neglect spin-orbit coupling, $\zeta = 0$, and assume $10Dq = \infty$ for the cubic crystal-field splitting. In this case, the effect of the e_g orbitals on the intra-t_{2g} excitations vanishes. In a d^4 configuration there are 15 t_{2g}^4 states. Interorbital Coulomb interactions lift their degeneracy and yield a ninefold degenerate $^3T_1$ ground state and the $^1T_2$, ^1E, and $^1A_1$ excited states. The latter is expected at $5J_H$, while $^1T_2$ and ^1E show an energy of $2J_H$ [26,45]. Note, however, that these values correspond to a t_{2g}-only scenario, i.e., $10Dq = \infty$; they are not suitable to estimate J_H for realistic values of $10Dq$ and ζ, as discussed below. The low-energy RIXS peaks at 0.3 and 0.6 eV reflect the effect of spin-orbit coupling, which splits the $^3T_1$ multiplet into the $J = 0$ ground state with Γ_1 symmetry and two excited states of $J = 1$ (Γ_4) and $J = 2$ ($\Gamma_3 + \Gamma_5$) character, respectively. The two contributions to the $J = 2$ peak at about 0.6 eV are expected to split in energy for finite values of the cubic crystal-field splitting $10Dq$. The fact that our RIXS data still show a single peak (see Fig. 5) indicates that the splitting is much smaller than the energy resolution $\delta E = 63$ meV. A finite Coulomb-induced splitting of the $J = 2$ states is most relevant in cubic $5d^2$ compounds. In these electron analogs of the two-t_{2g}-hole $5d^4$ configuration, the $J = 2$ multiplet has the lowest energy and its splitting for finite $10Dq$ determines the local ground state, which may lead to exotic multipolar phases [77–82]. For both $5d^4$ and $5d^2$, also the degeneracy of the $^1T_2$ and ^1E multiplets is lifted for finite $10Dq$. The asymmetric line shape of the RIXS peak around 1.3 eV at 20 and 300 K (see Fig. 4) indeed indicates a finite splitting between the cubic multiplets with a weaker feature on the high-energy side, as discussed in K_2RuCl_6 and Ba_2YIrO_6 [34,36].

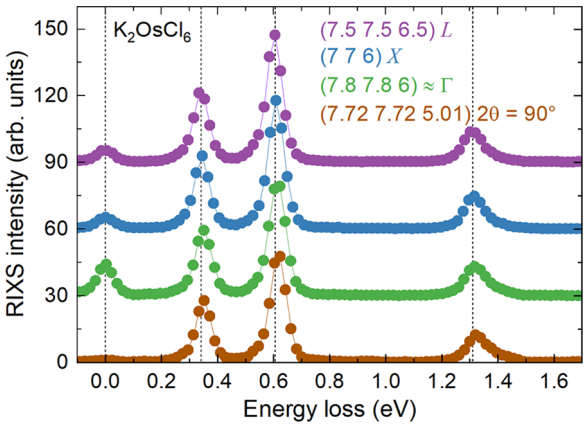

FIG. 5. Low-energy RIXS features in K_2OsCl_6 at 20 K at L, at X, and close to Γ. The latter data were measured in the vicinity of Γ to avoid the strong contribution of Bragg scattering right at Γ. Dashed lines indicate peak positions at X. The dispersion is negligible, highlighting the local character of the intra-t_{2g} excitations. Additionally, data at $(7.72\ \ 7.72\ \ 5.01)$ demonstrate the suppression of elastic Thomson scattering for $2\theta = 90°$.

Overall, the excitation spectrum agrees with previous RIXS results on $5d^4$ iridates [35–38]. RIXS data of $Yb_2Os_2O_7$ [43] also show the two low-energy modes below 1 eV but the intra-t_{2g} features at higher energies are hidden by a broad band that has been attributed to defects. Furthermore, the energy of the lowest excitation is much smaller in $Yb_2Os_2O_7$ due to a trigonal distortion [43]. In $4d^4$ K_2RuCl_6, the equivalent of the lower three features has been observed [34]. The $^1A_1$ peak at 2.1 eV thus far was only observed as a very weak feature in Sr_2YIrO_6 [35]. Comparing two data sets measured at the equivalent X points $(5\ \ 5\ \ 6)$ and $(7\ \ 7\ \ 6)$ (see Fig. 4), we find that the $^1A_1$ peak is suppressed in the latter, which has been recorded with a scattering angle 2θ close to 90°. This geometry typically is chosen to suppress elastic Thomson scattering, explaining the absence of this peak in previous measurements on $5d^4$ compounds. An example for the successful suppression of the elastic line for $2\theta = 90°$ is given by the data for $(7.72\ \ 7.72\ \ 5.01)$ in Fig. 5. In contrast, the data for $(5\ \ 5\ \ 6)$ were measured with $2\theta = 66°$ and accordingly show a more pronounced elastic line. For $2\theta = 90°$, the polarization of the scattered light is perpendicular to the incident π polarization. This suggests that the $^1A_1$ feature is observable only for parallel polarization, which is supported by simulations using QUANTY [64,65].

Our peak assignment assumes cubic symmetry and neglects the phase transition from cubic to tetragonal symmetry at 45 K. However, the RIXS data measured at 20 and 300 K fully agree with each other (see Fig. 4), suggesting that the noncubic splitting is much smaller than the energy resolution $\delta E = 63$ meV. This is supported by the infrared data, which were measured with $\delta E = 0.25$ meV. A thorough analysis of the temperature dependence of the infrared data reveals a noncubic splitting of about 4 meV, as discussed below.

D. Optical conductivity of K_2OsCl_6

Based on the different selection rules, optical spectroscopy and RIXS are complementary techniques. The optical conduc-

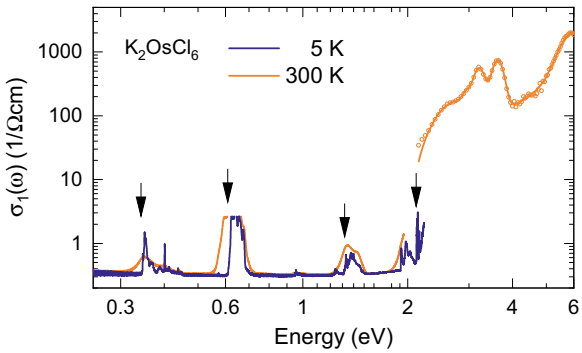

FIG. 6. Optical conductivity $\sigma_1(\omega)$ of K_2OsCl_6. Note the logarithmic scales. The strong absorption features above the Mott gap at 2.2 eV have been measured by ellipsometry, while the data in the transparent range below the gap with much smaller values of $\sigma_1(\omega)$ are based on the transmittance $T(\omega)$. The latter is suppressed below the noise level above 2.2 eV and around 0.6 eV, limiting the maximum value of $\sigma_1(\omega)$ that can be determined via $T(\omega)$ for the given sample thickness. Below the Mott gap, $\sigma_1(\omega)$ shows (phonon-assisted) intra-t_{2g} excitations in agreement with RIXS (arrows depict the RIXS intra-t_{2g} peak energies). Additionally, $\sigma_1(\omega)$ at 5 K reveals an exciton around 2.0 eV and two tiny features at about 0.95 and 1.25 eV that can be assigned to intersite overtones of the low-energy intra-t_{2g} excitations. For the ellipsometry data, symbols depict the result obtained from direct inversion of the raw data, while the solid line shows a fit of the raw data that additionally takes into account the low values of σ_1 below 2 eV. Around the gap, in the transition range from weak to strong absorption, the fit yields a very reasonable estimate of $\sigma_1(\omega)$.

tivity $\sigma_1(\omega)$ is dominated by electric dipole active transitions. Considering the orbital and electronic excitations in a Mott insulator, the dominant absorption features arise from *intersite* processes such as excitations across the Mott gap, in our case $|d_i^4\, d_j^4\rangle \rightarrow |d_i^3\, d_j^5\rangle$, or charge-transfer excitations $|5d_{\rm Os}^4\, 3p_{\rm Cl}^6\rangle \rightarrow |5d_{\rm Os}^5\, 3p_{\rm Cl}^5\rangle$. In Fig. 6, the Mott gap corresponds to the steep rise of $\sigma_1(\omega)$ above 2.2 eV. In contrast, RIXS at the Os L edge is dominated by on-site excitations [35–37,43,49], as discussed above, in particular for incident energies tuned to t_{2g} resonance. In the presence of inversion symmetry, on-site crystal-field excitations such as the intra-t_{2g} excitations are parity forbidden in $\sigma_1(\omega)$ but can become weakly allowed for instance in a phonon-assisted process. The corresponding spectral weight is several orders of magnitude smaller. Such weak features can only be studied for energies below the Mott gap where they are not hidden by stronger absorption processes (see Fig. 6).

1. Intersite excitations in $\sigma_1(\omega)$

Concerning the strong absorption features in $\sigma_1(\omega)$ above the Mott gap, we have to distinguish charge-transfer excitations between Cl and Os states from Mott-Hubbard excitations between Os states on different sites. One expects a larger spectral weight for the charge-transfer excitations due to the larger hopping matrix elements between Cl $3p$ and Os $5d$ states compared to Os intersite hopping. Accordingly, the strongest peak at about 6 eV can be assigned to a charge-transfer excitation, in agreement with the RIXS feature at 5.7 eV. The three peaks in $\sigma_1(\omega)$ between 2 and 4 eV correspond to Mott-Hubbard excitations involving t_{2g} states, $|t_{2g_i}^4\, t_{2g_j}^4\rangle \rightarrow |t_{2g_i}^3\, t_{2g_j}^5\rangle$. Their energy mainly reflects the on-site Coulomb repulsion U, while the splitting is caused by J_H and ζ. In $4d^4$ Ca_2RuO_4, the relative spectral weight of these bands has been employed to estimate ζ [33]. Comparing $\sigma_1(\omega)$ with the RIXS data, we emphasize that the origin of the RIXS features between 2 and 4 eV is very different. RIXS shows on-site excitations to e_g states, as demonstrated by the resonance behavior. The pronounced difference between the two techniques is based on the on-site energy U that has to be paid in the optical Mott-Hubbard excitations. In $\sigma_1(\omega)$, Mott-Hubbard excitations to e_g states $|t_{2g_i}^4\, t_{2g_j}^4\rangle \rightarrow |t_{2g_i}^3\, (t_{2g}^4 e_g^1)_j\rangle$ are expected to occur roughly $10Dq$ higher in energy than the corresponding t_{2g} bands, i.e., above about 6 eV. In K_2OsCl_6, these processes hence overlap with the charge-transfer excitations discussed above.

The onset of excitations across the Mott gap can be determined very well from the transmittance $T(\omega)$ which is strongly suppressed by the steep increase of absorption. This limits the accessible frequency window in our measurement on a single crystal with thickness $d = 120$ μm (see Fig. 6). At 5 K, the onset is at $\Delta = 2.2$ eV. With increasing temperature, the onset shifts to lower energy, roughly to 1.9 eV at 300 K, while the slope of the steep increase in $\sigma_1(\omega)$ is reduced [see Fig. 7(a)]. The change of slope shows that the main origin of this shift is not a possible small temperature dependence of the gap itself. The enhanced absorption below 2.2 eV predominantly can be attributed to thermally activated phonon-assisted excitations across the gap, i.e., the Urbach tail.

Below the Mott gap, the optical data show three additional absorption bands that are absent in the RIXS data. The strongest one is observed between 1.9 and 2.1 eV, which is very close to the Mott gap [see Fig. 7(a)]. This feature is well separated from the $^1A_1$ intra-t_{2g} excitation at 2.117 eV. Its spectral weight is comparable to the weak intra-t_{2g} excitations but the absence of a corresponding RIXS feature strongly points to a different origin. We therefore assign it to an exciton with $5d^3$ and $5d^5$ configurations on neighboring Os sites. This exciton is stabilized by nearest-neighbor Coulomb attraction and may induce a local relaxation of the Cl_6 octahedra. In this case, the substructure of this absorption feature tentatively can be attributed to phonon sidebands. The exciton scenario is strongly supported by the data of K_2OsBr_6, in which both the Mott gap and the excitonic absorption feature are shifted to lower energy by about 0.3–0.4 eV [see Fig. 7(b)]. In contrast, the intra-t_{2g} excitation energies are very similar in K_2OsBr_6 and K_2OsCl_6, as discussed in Sec. VI.

The two other below-gap absorption bands without a counterpart in RIXS are the two tiny features in $\sigma_1(\omega)$ at about 0.95 and 1.25 eV (see Fig. 6). We attribute also these bands to intersite excitations. They can be explained as a combination and overtone of the intra-t_{2g} excitations at about 0.35 and 0.65 eV, i.e., the simultaneous excitation of intra-t_{2g} excitations on two neighboring Os sites. In the honeycomb compound $\alpha - RuCl_3$ it has been shown that such double or even triple excitations may carry sizable spectral weight [58].

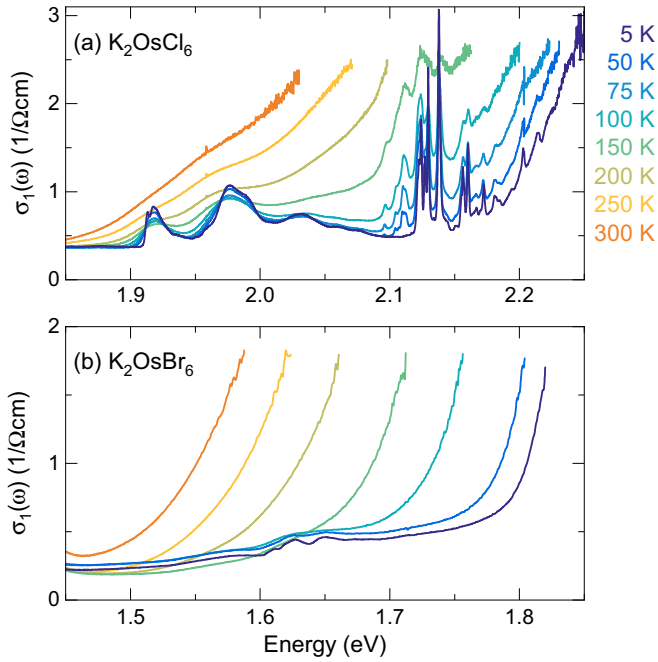

FIG. 7. Temperature dependence of $\sigma_1(\omega)$ close to the Mott gap in (a) K_2OsCl_6 and (b) K_2OsBr_6. In K_2OsCl_6, the onset of excitations across the Mott gap is observed at 2.2 eV at 5 K. This onset is washed out with increasing temperature since additional processes with simultaneous annihilation of thermally excited phonons reduce the total excitation energy in the Urbach tail. The $^1A_1$ intra-t_{2g} excitation is observed at 2.117 eV, and the many narrow lines around it correspond to phonon sidebands. In contrast to the $^1A_1$ peak, the absorption band between 1.9 and 2.1 eV has no counterpart in RIXS and can be assigned to an exciton. For comparison, the data of K_2OsBr_6 show the Mott gap at 1.8 eV at 5 K and a very similar temperature dependence. In K_2OsBr_6, the exciton is observed around 1.6–1.7 eV.

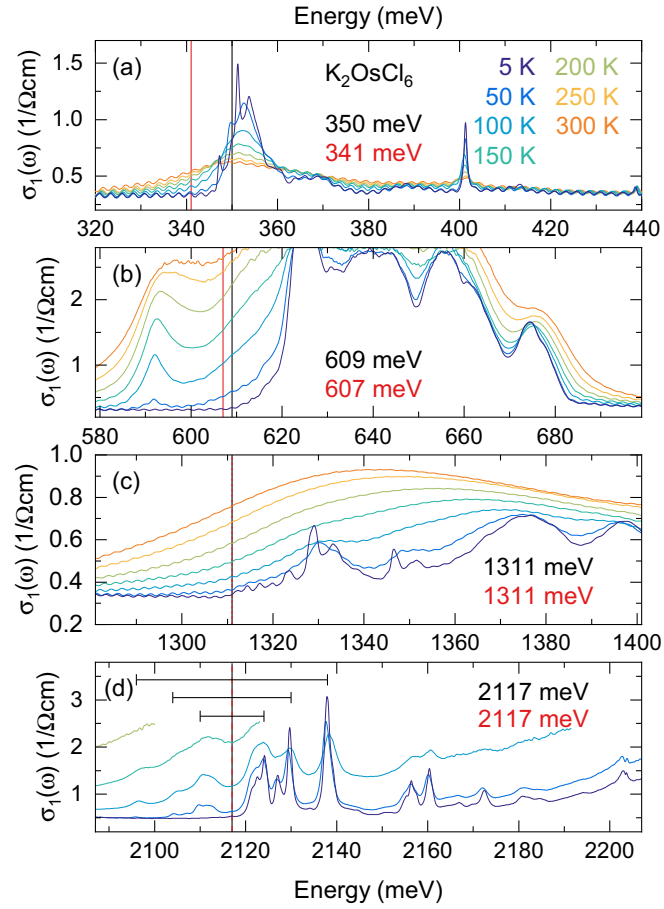

FIG. 8. Intra-t_{2g} excitations of K_2OsCl_6 in $\sigma_1(\omega)$. The panels depict excitations from $J = 0$ to (a) $J = 1$, i.e., Γ_1 to Γ_4; (b) the split $J = 2$ states, i.e., Γ_1 to Γ_5 and Γ_3; (c) the split $^1T_2$ and ^1E states; and (d) $^1A_1$. Each panel covers a window of the same width, 120 meV. In each panel, the vertical black line denotes the bare electronic (zero-phonon) energy, while the red line shows the fit result of the RIXS data. In $\sigma_1(\omega)$, the spectral weight is dominated by phonon sidebands. In (b), the transmittance around the peak maximum is suppressed below the noise level, which limits the measurable range of $\sigma_1(\omega)$. In (d), the horizontal black lines denote phonon sidebands at $E_{^1A_1} \pm E_{\text{ph}}$ with $E_{\text{ph}} = 7$, 13, and 21 meV. The small periodic wiggles, most pronounced at lower frequency, i.e., panel (a), are caused by Fabry-Pérot interference fringes in the transmittance. In $\sigma_1(\omega)$, they are an artifact of our analysis and have to be ignored.

Due to interaction effects, the peak energies do not have to perfectly match the simple sum of the individual excitation energies.

2. *Intra-t_{2g} excitations in $\sigma_1(\omega)$*

Considering the intra-t_{2g} excitations (see Figs. 4 and 8), the optical data show a rich structure where RIXS finds a single peak. Apart from the very different energy resolution, the selection rules and hence the excitation mechanisms are different. K_2OsCl_6 shows inversion symmetry, therefore the electric dipole matrix element for a local, even-parity $d - d$ excitation vanishes. Finite spectral weight appears in $\sigma_1(\omega)$ based on either a phonon-assisted process, or in the magnetic dipole channel, or due to electric quadrupolar or higher-order moments. We exemplify this by the data on the $^1A_1$ multiplet [see Fig. 8(d)].

At 5 K, we find a tiny zero-phonon magnetic-dipole mode at $E_{^1A_1} = 2117$ meV. This assignment is based on the temperature dependence of the phonon-assisted electric dipole features observed at $E_{^1A_1} \pm E_{\text{ph}}$. At 5 K, we only find modes at $E_{^1A_1} + E_{\text{ph}}$ for different symmetry-breaking phonons with, e.g., $E_{\text{ph}} = 7$, 13, or 21 meV, as indicated in Fig. 8(d) by the right ends of the horizontal black lines. With increasing temperature, these phonon modes become thermally populated and the corresponding phonon-annihilation features appear at $E_{^1A_1} - E_{\text{ph}}$, strongly supporting our assignment. The spectral weight of the phonon-annihilation peaks is governed by the Boltzmann factor. Hence peaks at lower energy $E_{^1A_1} - E_{\text{ph}}$ with larger E_{ph} become noticeable at higher temperature. Further features above 2150 meV correspond to a progression of phonon sidebands in a vibronic Franck-Condon picture [52,54]. Typically, this rich phonon-related pattern of crystal-field excitations can be resolved in measurements of transition-metal ions substituted into a host crystal [60]. In single crystals, this pattern usually is washed out. Exceptions have been observed in quasimolecular crystals such

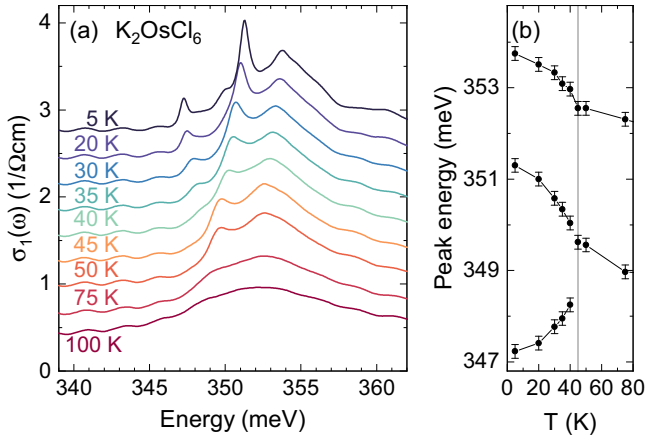

FIG. 9. Temperature dependence of $\sigma_1(\omega)$ in K_2OsCl_6 across the structural phase transition at 45 K. (a) Excitations to $J = 1$ [see Fig. 8(a)]. Data have been offset for clarity. (b) Corresponding peak energies as a function of temperature. Below 45 K, the peak splitting of the mode at $E_0 \approx 349$ meV reflects the noncubic crystal field. The feature at 352–354 meV is a phonon sideband that is present already in the cubic phase.

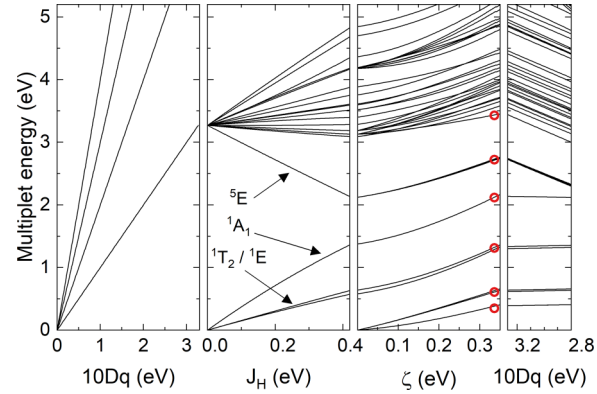

FIG. 10. Energies of on-site $d - d$ excitations for a $5d^4$ configuration in a cubic crystal field. Left: First switching on $10Dq$ separates the t_{2g}^4 states at zero energy from $t_{2g}^3 e_g^1$ states and states with more than one electron in the e_g orbitals. Middle left: Effect of J_H for $10Dq = 3.3$ eV and $\zeta = 0$. Here, the $^3T_1$ multiplet forms the ground state. Middle right: Spin-orbit coupling ζ yields a $J = 0$ ground state and four groups of intra-t_{2g} excitations. Red circles denote the experimental energies of K_2OsCl_6 used to determine the electronic parameters. Right: Effect of a reduction of $10Dq$ for finite J_H and ζ, mimicking the trend from K_2OsCl_6 to K_2OsBr_6.

as K_3NiO_2 with isolated NiO_2 units [53], and the rich optical spectra of K_2OsCl_6 most probably reflect the weak interactions between well-separated $OsCl_6$ octahedra. A detailed assignment of the sidebands in K_2OsCl_6 has been discussed previously [60].

Similar to the analysis of the $^1A_1$ peak, we use the optical data to find the bare electronic excitation energies of the intra-t_{2g} excitations at 350, 609, and 1311 meV. The value 350 meV corresponds to the energy of a feature that can be assigned to a magnetic-dipole transition from $J = 0$ to 1, i.e., Γ_1 to Γ_4 [83]. This peak splits below 45 K (see Fig. 9 and discussion below), but for comparison with theory, we employ the value at 50 K in the cubic phase. The two further energies 609 and 1311 meV are deduced from the temperature dependence of those absorption bands in $\sigma_1(\omega)$, in agreement with Ref. [60].

To compare the excitation energies found in RIXS and optics, we extract the RIXS peak energies for the intra-t_{2g} excitations from a fit that uses a series of Voigt profiles. We anchor the RIXS energy scale via the optical result of 2117 meV for the highest intra-t_{2g} excitation energy, as mentioned in Sec. IV. For the other low-energy RIXS peaks, this yields 341(1), 607(1), 1311(9), and 1373(140) meV, where the values in parentheses state the error bar of the fit. Remarkably, the first three values agree with the optical data within less than 10 meV (see Fig. 8). This excellent result once more corroborates the local character of these excitations. For the small shoulder around 1.37 eV, the uncertainty of the peak energy is much larger. We hence neglect this value for the further analysis.

The effect of the structural phase transition at 45 K is addressed in Fig. 9. In the antifluorite halides, a noncubic crystal-field splitting Δ_{CF} is driven by tilts and rotary or librational modes of the metal-ligand octahedra [84–87]. In $\sigma_1(\omega)$, an intra-t_{2g} excitation at E_0 gives rise to phonon-assisted peaks at $E_0 + E_{ph}$ already in the cubic phase, as discussed above for the $^1A_1$ mode. For the absorption band around 350 meV, we find a magnetic-dipole excitation at $E_0 \approx 349$ meV [83] and a phonon sideband at 352 meV, both at 50 and 75 K in the cubic phase. However, the peak at E_0 exhibits a noncubic peak splitting below 45 K. At 5 K, we observe peaks at $E_{0,a} = 347$ meV and $E_{0,b} = 351$ meV, i.e., $\Delta_{exp} \approx 4$ meV. This splitting scenario is supported by the temperature dependence. With decreasing temperature, $E_{0,a}$ decreases whereas the upper two peak energies $E_{0,b}$ and $E_{0,b} + E_{ph}$ show a common increase [see Fig. 9(b)]. Further support stems from the small shoulder observed at $E_{0,a} + E_{ph} = 350$ meV at 5 K [see Fig. 9(a)]. A similar behavior is observed for the $^1T_2$ excitation at 1.3 eV (not shown). This peak splitting $\Delta_{exp} \approx 4$ meV of the $J = 1$ band sets the energy scale of Δ_{CF} of K_2OsCl_6. For instance for a small tetragonal field $|\Delta_{CF}| \ll \zeta$, one finds $|\Delta_{CF}| \approx 2\Delta_{exp}$ [33].

E. Calculation of energy levels of K_2OsCl_6

For the analysis of the electronic parameters, we stick to cubic symmetry. In a single-site model, the relevant parameters for the energy levels are the cubic crystal-field splitting $10Dq$ between t_{2g} and e_g levels, spin-orbit coupling ζ, and the Coulomb interaction within the $5d$ shell. In spherical approximation, the latter can be described by the Slater integrals F^2 and F^4, which are used to calculate Hund's coupling $J_H = 1/14\,(F^2 + F^4)$ within the entire $5d$ shell [45]. Note that F^0, equivalent to Hubbard U, does not contribute to the energy splitting for a single site with a fixed number of electrons. We calculate the multiplet energies using QUANTY [64,65]. Figure 10 displays the behavior as a function of $10Dq$, J_H, and ζ. Starting with $J_H = \zeta = 0$, the cubic crystal field yields a t_{2g}^4 ground state and raises the excitation energies of the $t_{2g}^{4-n} e_g^n$ states with $n = 1$ to 4 electrons in the e_g subshell.

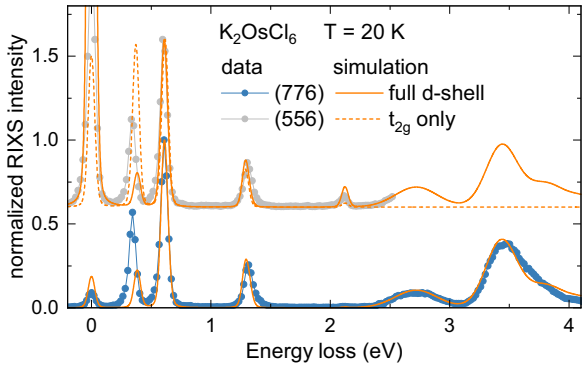

FIG. 11. Measured and calculated RIXS spectra of K_2OsCl_6. Solid orange lines: Simulation based on the fit result for the full d-shell model (see Table I). To account for the polarization dependence of the $^1A_1$ transition at 2.1 eV, we consider two different values of **q**. Dashed: Corresponding result of the Kanamori model for $J_H^{\text{eff}} = 0.28$ eV and $\zeta^{\text{eff}} = 0.41$ eV. Peak widths are adapted to the data. Offsets have been used for clarity.

Switching on J_H splits each of these five branches. We focus on the 15 t_{2g}^4 states. These are split into the $^3T_1$ ground state and the $^1T_2$, ^1E, and $^1A_1$ excited states. The excitation energies of roughly $3/2\,J_H$ and $4\,J_H$ are approximately 20–25% lower than for $10Dq = \infty$, reflecting a small but finite admixture of e_g character. Finally, spin-orbit coupling ζ causes a further fanning out of the energies and splits the $^3T_1$ ground state into three branches. In the limit of $10Dq = J_H = \infty$ these correspond to the eigenstates $J = 0$, 1, and 2. The intra-t_{2g} excitations within the t_{2g}^4 states form four groups of excitations that cover the range up to about 2 eV. The lowest $t_{2g}^3 e_g^1$ level corresponds to the high-spin ^5E state with $S = 2$. With all four spins being parallel, it is strongly favored by J_H. Even though the ^5E state is well separated from other levels (see Fig. 10), the width of this t_{2g}-to-e_g excitation is much larger than observed for the intra-t_{2g} peaks (see Fig. 11). This suggests a finite mixing with excitations across the Mott gap at 2.2 eV.

Optical studies of Os^{4+} impurities in different host crystals have reported different sets of electronic parameters [88–91]. Also for optical data on single crystals of K_2OsCl_6, it has been found that the determination of the electronic parameters is difficult [60], foremost because the crystal-field splitting $10Dq$ is hard to obtain from the optical data. The combined approach of RIXS and optics is pivotal here to resolve these ambiguities.

To determine the parameters of the d-shell model for K_2OsCl_6, we consider the four energies of the intra-t_{2g} excitations from the optical data and the $t_{2g}^3 e_g^1$ excitations observed at 2.72 and 3.43 eV in RIXS (see red circles in Fig. 10). We neglect peaks at higher energies where an unambiguous assignment is hindered by the large number of similar excitation energies. In the fit, we minimize the absolute difference between experimental peak energies and calculated ones. This yields the parameters $10Dq = 3.3$ eV, $\zeta = 0.34$ eV, $F^2 = 3.7$ eV, and $F^4 = 2.2$ eV, resulting in $J_H = 0.43$ eV. Note that the value of $10Dq$ agrees very well with our simple estimate discussed above. Figure 11 compares the calculated result for direct L_3-edge RIXS [49] for this parameter set with the experimental data. Overall, the peak energies as well as the relative peak intensities are well described. Calculations using density functional theory find $10Dq = 3$ eV and $\zeta = 0.4$ eV for K_2OsCl_6 [63], in reasonable agreement with our results.

The calculated excitation energies are given in Table I. For the splittings of the excitations at about 0.6 and 1.3 eV, the model predicts values of 20–35 meV in cubic symmetry, which is well below the RIXS resolution limit and agrees with the energy scale observed in the optical data. Concerning the fitted energies, the deviations are less than 7 meV for four of the six energies, an excellent result. Upon a closer look, the largest deviation of 33 meV is found for the peak lowest in energy, and the intensity of this feature is underestimated. A similar observation has been reported for $4d^4$ K_2RuCl_6, where it has been discussed in terms of a possible role of vibronic coupling, i.e., a dynamic Jahn-Teller splitting of the excited $J = 1$ triplet state [34,44]. For K_2OsCl_6, our optical data resolve the vibronic sidebands in the excited states (see Fig. 8), but do not hint at a particular importance of vibronic effects for the feature around 0.35 eV. We find, however, that a small change in the parameters can eliminate this apparent shortcoming of the model. In a second fit, we minimize the *relative* energy difference between experiment and model. This results in the very similar parameter set $10Dq = 3.4$ eV,

TABLE I. Experimental and calculated excitation energies. The four intra-t_{2g} energies are taken from the optical data; the two e_g levels above 2.7 eV come from RIXS. Dashes denote peaks that are not resolved in the experiment. For K_2OsCl_6 (K_2OsBr_6), the parameters of the d-shell model are $10Dq = 3.27$ eV (2.85 eV), $\zeta = 0.336$ eV (0.325 eV), $F^2 = 3.73$ eV (3.90 eV), and $F^4 = 2.22$ eV (2.01 eV), which corresponds to $J_H = 0.425$ eV (0.422 eV).

Multiplet	Expt. Cl (meV)	Fit Cl (meV)	Expt. Br (meV)	Fit Br (meV)
$\Gamma_4(^3T_1)$	350	383	349	388
$\Gamma_5(^3T_1)$	609	608	604	604
$\Gamma_3(^3T_1)$	–	631	–	632
$^1T_2$	1311	1289	1285	1267
^1E	–	1323	–	1312
$^1A_1$	2117	2123	–	2050
^5E	2721	2716	2391	2381
^3E	3428	3432	3033	3042

$\zeta = 0.34$ eV, and $J_H = 0.42$ eV and yields the energies 358, 600, 1278, and 2139 meV for the four lowest excitations. For all four, the relative difference is less than 2.6%, a very reasonable result. In terms of absolute energy differences, the deviation between fit and experiment is reduced to 8 meV for the peak at 350 meV while the description of the other peaks is slightly worse compared to the first fit. Finally, we have checked that inclusion of the Cl $3p$ orbitals and ligand-to-metal charge-transfer processes [64] yields very similar results. Overall, we find $J_H/\zeta \approx 1.3$ which puts K_2OsCl_6 in the intermediate regime between LS coupling with $J_H/\zeta \to \infty$ and jj coupling for $J_H/\zeta \to 0$.

F. Parameters in the Kanamori model

Thus far we discussed a model that takes the entire d shell into account. In contrast, the related $5d^4$ iridate data in Refs. [35–38] were analyzed using the Kanamori model that assumes $10Dq = \infty$, i.e., it considers only t_{2g} orbitals. For a comparison, it is important to quantify how the parameter values depend on the chosen model. In the Kanamori model, the only parameters are $\zeta^{\rm eff}$ and $J_H^{\rm eff} = 3/49\,F^2 + 20/441\,F^4$ [45]. With $10Dq = \infty$, the Kanamori model restores the degeneracy of $^1T_2$ and ^1E around 1.3 eV and of the Γ_3 and Γ_5 states of $J = 2$ around 0.6 eV, as mentioned in Sec. V C. Hence the model has only four intra-t_{2g} excitation energies. For simplicity, we call these energies $E(1)$ to $E(4)$, in ascending order. Simple expressions for $E(1)$ to $E(4)$ are given in Ref. [44].

A fit of the four intra-t_{2g} excitation energies with the t_{2g}-only Kanamori model yields $J_H^{\rm eff} = 0.28$ eV and $\zeta^{\rm eff} = 0.41$ eV and the energies 371, 616, 1288, and 2125 meV. A corresponding simulated RIXS spectrum is shown in Fig. 11. Similar to the result obtained for the full d shell, the relative deviation between fit and data is largest for the lowest mode. Again, a slightly different set of parameters yields excellent agreement for the lowest excitation energies. Choosing $J_H^{\rm eff} = 310$ meV and $\zeta^{\rm eff} = 399$ meV describes the lowest three peaks of K_2OsCl_6 within 1 meV and $E(4)$ within 6%. Overall, this suggests $J_H^{\rm eff}/\zeta^{\rm eff} \approx 3/4$.

Another possibility to determine this quantity is given by the ratio $E(2)/E(1)$, which varies from 3 for LS coupling to 1 for jj coupling [see Fig. 12(a)]. For K_2OsCl_6 with 609 meV/350 meV ≈ 1.7, this corroborates $J_H^{\rm eff}/\zeta^{\rm eff} \approx 3/4$. Remarkably, very similar values of the ratio $E(2)/E(1)$ have been reported for several $5d^4$ iridates [see Fig. 12(b)], highlighting the close relationship of the properties of this series of $5d^4$ compounds.

As long as the corresponding model is specified, both $J_H/\zeta \approx 1.3$ for the entire $5d$ shell and $J_H^{\rm eff}/\zeta^{\rm eff} \approx 3/4$ in the t_{2g}-only model are valid. For $J_H \approx \zeta$, the two models predict

$$E(J=2) \approx \frac{3}{2}\zeta\left(1 + \frac{2\zeta}{10Dq}\right) \tag{2}$$

$$E(2) \approx \frac{3}{2}\zeta^{\rm eff} \tag{3}$$

for the second excitation energy and hence $\zeta^{\rm eff}/\zeta \approx 1.2$ in the $5d^4$ compounds. Additionally, the different definitions of Hund's coupling yield $J_H^{\rm eff}/J_H \approx 0.77$. Concerning the energies of the intra-t_{2g} excitations, the t_{2g}-only Kanamori model and the model for the full d shell work equally well. The main shortcoming of both models is the intensity of the lowest excitation, which is too small in the d-shell model but too large in the Kanamori model (see Fig. 11). This suggests that the intensity of the lowest RIXS peak depends sensitively on $10Dq$ and on the admixture of e_g character.

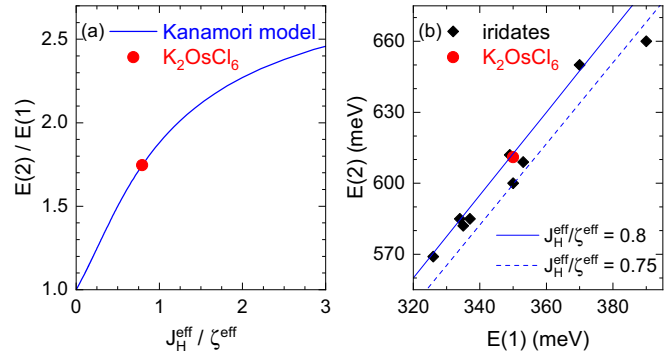

FIG. 12. Analysis based on the t_{2g}-only Kanamori model. (a) The ratio $E(2)/E(1)$ varies between 1 for $J_H^{\rm eff}/\zeta^{\rm eff} \to 0$ and 3 for $J_H^{\rm eff}/\zeta^{\rm eff} \to \infty$. For K_2OsCl_6, it yields $J_H^{\rm eff}/\zeta^{\rm eff} \approx 3/4$. (b) Comparison of the two lowest excitation energies in K_2OsCl_6 and related $5d^4$ iridates [35–38]. For all of them, $J_H^{\rm eff}/\zeta^{\rm eff}$ is very similar.

VI. RESULTS ON THE BROMIDES

RIXS spectra of K_2OsCl_6, K_2OsBr_6, and Rb_2OsBr_6 are compared in Fig. 13. We find a close resemblance of the RIXS data of K_2OsBr_6 and Rb_2OsBr_6, i.e., a very small effect of the A ion. Hence we focus on the comparison of K_2OsBr_6 and K_2OsCl_6. The behavior is different above and below 2 eV. In RIXS we find the intra-t_{2g} excitation energies of K_2OsBr_6 at 0.34, 0.60, and 1.27 eV. Compared to K_2OsCl_6, these are reduced by about 1, 2, and 3%, respectively, i.e., they are almost unaffected by the choice of the halide. In contrast, the peak energies associated to the e_g and charge-transfer excitations

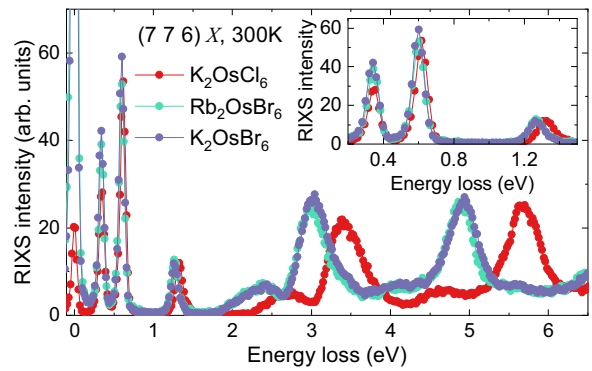

FIG. 13. Comparison of RIXS spectra of K_2OsCl_6, K_2OsBr_6, and Rb_2OsBr_6. The difference in size and electronegativity between Br and Cl ions alters the crystal-field and charge-transfer excitations. In comparison, the intra-t_{2g} peaks are less affected by the change of the ligand, as highlighted in the inset.

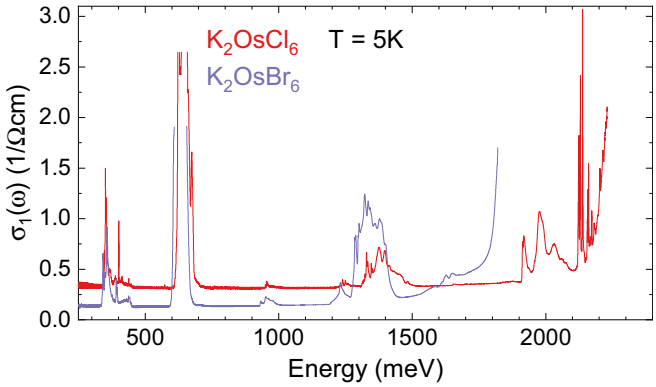

FIG. 14. Optical conductivity of K_2OsCl_6 and K_2OsBr_6. The main change is the shift of the Mott gap from 2.2 to 1.8 eV. The small offset in the K_2OsCl_6 data indicates a possible surface issue. Note that we polished this sample with CeO_2 in propanol, while the K_2OsBr_6 crystal was measured as grown.

are reduced by about 12–14% in K_2OsBr_6 with respect to the chloride. More precisely, the peak energies are 2.4 and 3.0 eV for the strongest $t_{2g}^3 e_g^1$ transitions and 4.0 and 4.9 eV for the charge-transfer excitations $|5d_{\rm Os}^4\, 4p_{\rm Br}^6\rangle \rightarrow |5d_{\rm Os}^5 4p_{\rm Br}^5\rangle$. The very similar intensity profile of the two compounds indicates that the main effect at high energy is captured by a renormalization of the energy scale, i.e., of $10Dq$ and $\Delta_{\rm CT}$. Both parameters are affected by the difference in ionic size and electronegativity. Empirically, the effect of different ligands on $10Dq$ is described by the spectrochemical series [53], and the reduction of $\Delta_{\rm CT}$ from bromides to chlorides has been observed in other transition-metal compounds as well, both in optics and RIXS [92,93]. For $5d$ halides, a very similar shift has been reported from K_2IrCl_6 to K_2IrBr_6 [76].

In analogy to the discussion of K_2OsCl_6 above, we identify $\Delta_{\rm CT}^{\rm Br} = 4.0$ eV via the lowest charge-transfer excitation. Furthermore, a fit of the excitation energies using multiplet calculations yields the parameters $10Dq^{\rm Br} = 2.9$ eV, $\zeta^{\rm Br} = 0.33$ eV, and $J_H^{\rm Br} = 0.42$ eV. Compared to K_2OsCl_6, the spin-orbit coupling constant is reduced by about 4 %, while the change of J_H is negligible (see Table I). These results are in good agreement with predictions of density functional theory for the reduction of $10Dq$, $\Delta_{\rm CT}$, and ζ from K_2OsCl_6 to K_2OsBr_6 [63]. A similar reduction of the spin-orbit coupling constant of about 5 % has been reported from K_2IrCl_6 to K_2IrBr_6 [76]. The effect of a reduction of $10Dq$ on the energy levels of the multiplet model is shown in the right panel of Fig. 10. While the $t_{2g}^3 e_g^1$ levels decrease linearly in energy, the t_{2g}^4 states hardly change. In general, lower values of $10Dq$ and $\Delta_{\rm CT}$ indicate a stronger admixture of e_g and $4p$ ligand character into the t_{2g} states. This, in turn, reduces the effective value of ζ. However, the large ratio of $10Dq/\zeta \approx 10$ explains why the sizable reduction of $10Dq$ has only a small effect on ζ.

The optical conductivity $\sigma_1(\omega)$ of K_2OsBr_6 is depicted in Figs. 14 and 7(b). Note that the larger thickness $d^{\rm Br} = 170\,\mu$m of the bromide sample limits the accessible values of $\sigma_1(\omega)$ to below $2\,(\Omega\,{\rm cm})^{-1}$, somewhat lower than in the thinner chloride sample. The most pronounced difference to the data of K_2OsCl_6 is the value of the Mott gap, which is shifted down by about 0.4 eV to 1.8 eV at 5 K. This shift masks the $^1A_1$ excitation which occurs at 2.1 eV in K_2OsCl_6. Along with the Mott gap, also the excitation energy of the exciton is reduced, as already discussed in connection with Fig. 7. At lower energy, the small shifts of the intra-t_{2g} excitations of less than 1% for the lowest excitation and about 1–2 % for the bands at 0.6 and 1.3 eV agree with the RIXS results.

VII. CONCLUSION

In conclusion, we have probed the local electronic structure of the $5d^4$ hexahalogenoosmates K_2OsCl_6, K_2OsBr_6, and Rb_2OsBr_6 with magnetic and spectroscopic methods. These measurements reveal nonmagnetic $J = 0$ behavior, as expected for a clean $5d^4$ system in which both defects and exchange interactions are negligible. Combining RIXS and optical spectroscopy, we can assign the multiplet excitation energies with high accuracy and extract the electronic parameters by comparison with local multiplet calculations. RIXS at the transition-metal L edge is most sensitive to on-site $d - d$ excitations, which in the optical data give rise to weak, typically phonon-assisted features. For the antifluorite-type Os halides, a central advantage of RIXS is the ability to determine $10Dq$ via the observation of local excitations into the e_g subshell also above the Mott gap. Due to the weak interactions between OsX_6 (X = Cl, Br) octahedra, both the e_g excitations and the charge-transfer excitations are narrow and very well defined in RIXS. As a complementary technique, optical spectroscopy allows us to determine the small noncubic crystal-field splitting of 4 meV below 45 K in K_2OsCl_6. Furthermore, it is sensitive to intersite processes such as excitations across the Mott gap at 2.2 eV and reveals an exciton around 1.9–2.1 eV. These results establish the presented compounds as realizations of clean cubic $J = 0$ systems in the intermediate coupling regime with $J_H/\zeta \approx 1.3$ or $J_H^{\rm eff}/\zeta^{\rm eff} \approx 3/4$. Accordingly, Coulomb interaction and spin-orbit coupling have to be taken on equal footing. This value of $J_H^{\rm eff}/\zeta^{\rm eff}$ is very similar to results reported for $5d^4$ iridates [35–38], highlighting the close relationship between these compounds. The comparison of the data from chloride and bromide samples shows a 20% decrease of the Mott gap as well as a reduction of about 12–14% of $10Dq$ and of the charge-transfer energy $\Delta_{\rm CT}$, in agreement with predictions of density functional theory [63]. Due to the large size of $10Dq$ and $\Delta_{\rm CT}$ with respect to J_H and ζ, this sizable change has only a marginal effect on intra-t_{2g} energies, which are reduced by 1–3%. In contrast to previous studies on $5d^4$ $J = 0$ compounds, where the determination of ζ and J_H has turned out to be difficult, we find that both chloride and bromide samples are well described by $\zeta = 0.33$–0.34 eV and $J_H = 0.42$–0.43 eV. These values may serve as a solid reference for future studies on Os compounds.

ACKNOWLEDGMENTS

We gratefully acknowledge H. Schwab for experimental assistance in sample characterization and the European Synchrotron Radiation Facility for providing beam time and

technical support. Furthermore, we acknowledge funding from the Deutsche Forschungsgemeinschaft (DFG, German Research Foundation) through Project No. 277146847 - CRC 1238 (projects No. A02, No. B01, No. B02, and No. B03).

[1] W. Witczak-Krempa, G. Chen, Y. B. Kim, and L. Balents, Correlated quantum phenomena in the strong spin-orbit regime, Annu. Rev. Condens. Matter Phys. **5**, 57 (2014).

[2] J. G. Rau, E. K.-H. Lee, and H.-Y. Kee, Spin-orbit physics giving rise to novel phases in correlated systems: Iridates and related materials, Annu. Rev. Condens. Matter Phys. **7**, 195 (2016).

[3] R. Schaffer, E. K.-H. Lee, B.-J. Yang, and Y. B. Kim, Recent progress on correlated electron systems with strong spin-orbit coupling, Rep. Prog. Phys. **79**, 094504 (2016).

[4] T. Takayama, J. Chaloupka, A. Smerald, G. Khaliullin, and H. Takagi, Spin-orbit-entangled electronic phases in 4*d* and 5*d* transition-metal compounds, J. Phys. Soc. Jpn. **90**, 062001 (2021).

[5] D. I. Khomskii and S. V. Streltsov, Orbital effects in solids: Basics, recent progress, and opportunities, Chem. Rev. **121**, 2992 (2021).

[6] S. M. Winter, A. A. Tsirlin, M. Daghofer, J. van den Brink, Y. Singh, P. Gegenwart, and R. Valentí, Models and materials for generalized Kitaev magnetism, J. Phys.: Condens. Matter **29**, 493002 (2017).

[7] G. Cao and P. Schlottmann, The challenge of spin-orbit-tuned ground states in iridates, Rep. Prog. Phys. **81**, 042502 (2018).

[8] S. Trebst and C. Hickey, Kitaev materials, Phys. Rep. **950**, 1 (2022).

[9] G. Jackeli and G. Khaliullin, Mott Insulators in the Strong Spin-Orbit Coupling Limit: From Heisenberg to a Quantum Compass and Kitaev Models, Phys. Rev. Lett. **102**, 017205 (2009).

[10] M. Hermanns, I. Kimchi, and J. Knolle, Physics of the Kitaev model: Fractionalization, dynamic correlations, and material connections, Annu. Rev. Condens. Matter Phys. **9**, 17 (2018).

[11] H. Takagi, T. Takayama, G. Jackeli, G. Khaliullin and S. E. Nagler, Concept and realization of Kitaev quantum spin liquids, Nat. Rev. Phys. **1**, 264 (2019).

[12] Y. Motome and J. Nasu, Hunting Majorana fermions in Kitaev magnets, J. Phys. Soc. Jpn. **89**, 012002 (2020).

[13] S. H. Chun, J.-W. Kim, J. Kim, H. Zheng, C. C. Stoumpos, C. D. Malliakas, J. F. Mitchell, K. Mehlawat, Y. Singh, Y. Choi, T. Gog, A. Al-Zein, M. Moretti Sala, M. Krisch, J. Chaloupka, G. Jackeli, G. Khaliullin, and B. J. Kim, Direct evidence for dominant bond-directional interactions in a honeycomb lattice iridate Na_2IrO_3, Nat. Phys. **11**, 462 (2015).

[14] M. Magnaterra, K. Hopfer, Ch. J. Sahle, M. Moretti Sala, G. Monaco, J. Attig, C. Hickey, I.-M. Pietsch, F. Breitner, P. Gegenwart, M. H. Upton, Jungho Kim, S. Trebst, P. H. M. van Loosdrecht, J. van den Brink, and M. Grüninger, RIXS observation of bond-directional nearest-neighbor excitations in the Kitaev material Na_2IrO_3, arXiv:2301.08340

[15] A. Revelli, C. C. Loo, D. Kiese, P. Becker, T. Fröhlich, T. Lorenz, M. Moretti Sala, G. Monaco, F. L. Buessen, J. Attig, M. Hermanns, S. V. Streltsov, D. I. Khomskii, J. van den Brink, M. Braden, P. H. M. van Loosdrecht, S. Trebst, A. Paramekanti, and M. Grüninger, Spin-orbit entangled $j = 1/2$ moments in Ba_2CeIrO_6: A frustrated fcc quantum magnet, Phys. Rev. B **100**, 085139 (2019).

[16] A. Revelli, M. Moretti Sala, G. Monaco, P. Becker, L. Bohatý, M. Hermanns, T. C. Koethe, T. Fröhlich, P. Warzanowski, T. Lorenz, S. V. Streltsov, P. H. M. van Loosdrecht, D. I. Khomskii, J. van den Brink, and M. Grüninger, Resonant inelastic x-ray incarnation of Young's double-slit experiment, Sci. Adv. **5**, eaav4020 (2019).

[17] A. Revelli, M. Moretti Sala, G. Monaco, M. Magnaterra, J. Attig, L. Peterlini, T. Dey, A. A. Tsirlin, P. Gegenwart, T. Fröhlich, M. Braden, C. Grams, J. Hemberger, P. Becker, P. H. M. van Loosdrecht, D. I. Khomskii, J. van den Brink, M. Hermanns, and M. Grüninger, Quasimolecular electronic structure of the spin-liquid candidate $Ba_3InIr_2O_9$, Phys. Rev. B **106**, 155107 (2022).

[18] G. Khaliullin, Excitonic Magnetism in Van Vleck–type d^4 Mott Insulators, Phys. Rev. Lett. **111**, 197201 (2013).

[19] O. N. Meetei, W. S. Cole, M. Randeria, and N. Trivedi, Novel magnetic state in d^4 Mott insulators, Phys. Rev. B **91**, 054412 (2015).

[20] D. I. Khomskii, *Transition Metal Compounds* (Cambridge University, New York, 2014).

[21] A. Akbari and G. Khaliullin, Magnetic excitations in spin-orbit coupled d^4 Mott insulator on square lattice, Phys. Rev. B **90**, 035137 (2014).

[22] N. Kaushal, J. Herbrych, G. Alvarez, and E. Dagotto, Magnetization dynamics fingerprints of an excitonic condensate t_{2g}^4 magnet, Phys. Rev. B **104**, 235135 (2021).

[23] A. Jain, M. Krautloher, J. Porras, G. H. Ryu, D. P. Chen, D. L. Abernathy, J. T. Park, A. Ivanov, J. Chaloupka, G. Khaliullin, B. Keimer, and B. J. Kim, Higgs mode and its decay in a two-dimensional antiferromagnet, Nat. Phys. **13**, 633 (2017).

[24] S. Kunkemöller, D. Khomskii, P. Steffens, A. Piovano, A. A. Nugroho, and M. Braden, Highly Anisotropic Magnon Dispersion in Ca_2RuO_4: Evidence for Strong Spin-Orbit Coupling, Phys. Rev. Lett. **115**, 247201 (2015).

[25] S. Kunkemöller, E. Komleva, S. V. Streltsov, S. Hoffmann, D. I. Khomskii, P. Steffens, Y. Sidis, K. Schmalzl, and M. Braden, Magnon dispersion in $Ca_2Ru_{1-x}Ti_xO_4$: Impact of spin-orbit coupling and oxygen moments, Phys. Rev. B **95**, 214408 (2017).

[26] G. Zhang and E. Pavarini, Mott transition, spin-orbit effects, and magnetism in Ca_2RuO_4, Phys. Rev. B **95**, 075145 (2017).

[27] G. Zhang and E. Pavarini, Higgs mode and stability of xmy − orbital ordering in Ca_2RuO_4, Phys. Rev. B **101**, 205128 (2020).

[28] T. Feldmaier, P. Strobel, M. Schmid, P. Hansmann, and M. Daghofer, Excitonic magnetism at the intersection of spin-orbit coupling and crystal-field splitting, Phys. Rev. Res. **2**, 033201 (2020).

[29] B. J. Kim and G. Khaliullin, Resonant inelastic x-ray scattering operators for t_{2g} orbital systems, Phys. Rev. B **96**, 085108 (2017).

[30] C. G. Fatuzzo, M. Dantz, S. Fatale, P. Olalde-Velasco, N. E. Shaik, B. Dalla Piazza, S. Toth, J. Pelliciari, R. Fittipaldi, A. Vecchione, N. Kikugawa, J. S. Brooks, H. M. Rønnow, M. Grioni, Ch. Rüegg, T. Schmitt, and J. Chang, Spin-orbit-induced orbital excitations in Sr_2RuO_4 and Ca_2RuO_4:

A resonant inelastic x-ray scattering study, Phys. Rev. B **91**, 155104 (2015).

[31] L. Das, F. Forte, R. Fittipaldi, C. G. Fatuzzo, V. Granata, O. Ivashko, M. Horio, F. Schindler, M. Dantz, Y. Tseng, D. E. McNally, H. M. Rønnow, W. Wan, N. B. Christensen, J. Pelliciari, P. Olalde-Velasco, N. Kikugawa, T. Neupert, A. Vecchione, T. Schmitt *et al.*, Spin-Orbital Excitations in Ca_2RuO_4 Revealed by Resonant Inelastic X-Ray Scattering, Phys. Rev. X **8**, 011048 (2018).

[32] H. Gretarsson, H. Suzuki, Hoon Kim, K. Ueda, M. Krautloher, B. J. Kim, H. Yavaş, G. Khaliullin, and B. Keimer, Observation of spin-orbit excitations and Hund's multiplets in Ca_2RuO_4, Phys. Rev. B **100**, 045123 (2019).

[33] I. Vergara, M. Magnaterra, P. Warzanowski, J. Attig, S. Kunkemöller, D. I. Khomskii, M. Braden, M. Hermanns, and M. Grüninger, Spin-orbit coupling and crystal-field splitting in Ti-doped Ca_2RuO_4 studied by ellipsometry, Phys. Rev. B **106**, 085103 (2022).

[34] H. Takahashi, H. Suzuki, J. Bertinshaw, S. Bette, C. Mühle, J. Nuss, R. Dinnebier, A. Yaresko, G. Khaliullin, H. Gretarsson, T. Takayama, H. Takagi, and B. Keimer, Nonmagnetic $J = 0$ State and Spin-Orbit Excitations in K_2RuCl_6, Phys. Rev. Lett. **127**, 227201 (2021).

[35] B. Yuan, J. P. Clancy, A. M. Cook, C. M. Thompson, J. Greedan, G. Cao, B. C. Jeon, T. W. Noh, M. H. Upton, D. Casa, T. Gog, A. Paramekanti, and Y.-J. Kim, Determination of Hund's coupling in 5*d* oxides using resonant inelastic x-ray scattering, Phys. Rev. B **95**, 235114 (2017).

[36] M. Kusch, V. M. Katukuri, N. A. Bogdanov, B. Büchner, T. Dey, D. V. Efremov, J. E. Hamann-Borrero, B. H. Kim, M. Krisch, A. Maljuk, M. Moretti Sala, S. Wurmehl, G. Aslan-Cansever, M. Sturza, L. Hozoi, J. van den Brink, and J. Geck, Observation of heavy spin-orbit excitons propagating in a nonmagnetic background: The case of $(Ba, Sr)_2YIrO_6$, Phys. Rev. B **97**, 064421 (2018).

[37] A. Nag, S. Bhowal, A. Chakraborty, M. M. Sala, A. Efimenko, F. Bert, P. K. Biswas, A. D. Hillier, M. Itoh, S. D. Kaushik, V. Siruguri, C. Meneghini, I. Dasgupta, and S. Ray, Origin of magnetic moments and presence of spin-orbit singlets in Ba_2YIrO_6, Phys. Rev. B **98**, 014431 (2018).

[38] A. A. Aczel, Q. Chen, J. P. Clancy, C. dela Cruz, D. Reig-i-Plessis, G. J. MacDougall, C. J. Pollock, M. H. Upton, T. J. Williams, N. LaManna, J. P. Carlo, J. Beare, G. M. Luke, and H. D. Zhou, Spin-orbit coupling controlled ground states in the double perovskite iridates A_2BIrO_6 (A = Ba, Sr; B = Lu, Sc), Phys. Rev. Mater. **6**, 094409 (2022).

[39] A. Paramekanti, D. J. Singh, B. Yuan, D. Casa, A. Said, Y.-J. Kim, and A. D. Christianson, Spin-orbit coupled systems in the atomic limit: rhenates, osmates, iridates, Phys. Rev. B **97**, 235119 (2018).

[40] G. Cao, T. F. Qi, L. Li, J. Terzic, S. J. Yuan, L. E. DeLong, G. Murthy, and R. K. Kaul, Novel Magnetism of $Ir^{5+}(5d^4)$ Ions in the Double Perovskite Sr_2YIrO_6, Phys. Rev. Lett. **112**, 056402 (2014).

[41] J. Terzic, H. Zheng, F. Ye, H. D. Zhao, P. Schlottmann, L. E. De Long, S. J. Yuan, and G. Cao, Evidence for a low-temperature magnetic ground state in double-perovskite iridates with $Ir^{5+}(5d^4)$ ions, Phys. Rev. B **96**, 064436 (2017).

[42] S. Fuchs, T. Dey, G. Aslan-Cansever, A. Maljuk, S. Wurmehl, B. Büchner, and V. Kataev, Unraveling the Nature of Magnetism of the $5d^4$ Double Perovskite Ba_2YIrO_6, Phys. Rev. Lett. **120**, 237204 (2018).

[43] N. R. Davies, C. V. Topping, H. Jacobsen, A. J. Princep, F. K. K. Kirschner, M. C. Rahn, M. Bristow, J. G. Vale, I. da Silva, P. J. Baker, Ch. J. Sahle, Y.-F. Guo, D.-Y. Yan, Y.-G. Shi, S. J. Blundell, D. F. McMorrow, and A. T. Boothroyd, Evidence for a $J_{\text{eff}} = 0$ ground state and defect-induced spin glass behavior in the pyrochlore osmate $Y_2Os_2O_7$, Phys. Rev. B **99**, 174442 (2019).

[44] N. Iwahara and S. Shikano, Vibronic excitations in resonant inelastic x-ray scattering spectra of K_2RuCl_6, Phys. Rev. Res. **5**, 023051 (2023).

[45] A. Georges, L. de'Medici, and J. Mravlje, Strong correlations from Hund's coupling, Annu. Rev. Condens. Matter Phys. **4**, 137 (2013).

[46] J. E. Fergusson and P. F. Heveldt, The influence of π-bonding and steric factors on hexahalogeno-metallates, Aust. J. Chem. **27**, 661 (1974).

[47] R. L. Armstrong, D. Mintz, B. M. Powell, and W. J. L. Buyers, Ferrorotative transition in the antifluorite crystal K_2OsCl_6, Phys. Rev. B **17**, 1260 (1978).

[48] M. Saura-Múzquiz, M. Avdeev, H. E. A. Brand, and B. J. Kennedy, Structural and magnetic properties of some vacancy-ordered osmium halide perovskites, Inorg. Chem. **61**, 15961 (2022).

[49] L. J.P. Ament, M. van Veenendaal, T. P. Devereaux, J. P. Hill, and J. van den Brink, Resonant inelastic x-ray scattering studies of elementary excitations, Rev. Mod. Phys. **83**, 705 (2011).

[50] A. Gössling, R. Schmitz, H. Roth, M. W. Haverkort, T. Lorenz, J. A. Mydosh, E. Müller-Hartmann, and M. Grüninger, Mott-Hubbard exciton in the optical conductivity of $YTiO_3$ and $SmTiO_3$, Phys. Rev. B **78**, 075122 (2008).

[51] J. Reul, A. A. Nugroho, T. T. M. Palstra, and M. Grüninger, Probing orbital fluctuations in RVO_3 (R = Y, Gd, or Ce) by ellipsometry, Phys. Rev. B **86**, 125128 (2012).

[52] B. Henderson and G. F. Imbusch, *Optical Spectroscopy of Inorganic Solids* (Oxford, New York, 1989).

[53] B. N. Figgis and M. A. Hitchman, *Ligand Field Theory and its Applications* (Wiley, New York, 1999).

[54] R. Rückamp, E. Benckiser, M. W. Haverkort, H. Roth, T. Lorenz, A. Freimuth, L. Jongen, A. Möller, G. Meyer, P. Reutler, B. Büchner, A. Revcolevschi, S.-W. Cheong, C. Sekar, G. Krabbes, and M. Grüninger, Optical study of orbital excitations in transition-metal oxides, New J. Phys. **7**, 144 (2005).

[55] E. Benckiser, R. Rückamp, T. Möller, T. Taetz, A. Möller, A. A. Nugroho, T. T. M. Palstra, G. S. Uhrig, and M. Grüninger, Collective orbital excitations in orbitally ordered YVO_3 and $HoVO_3$, New J. Phys. **10**, 053027 (2008).

[56] E. Benckiser, L. Fels, G. Ghiringhelli, M. Moretti Sala, T. Schmitt, J. Schlappa, V. N. Strocov, N. Mufti, G. R. Blake, A. A. Nugroho, T. T. M. Palstra, M. W. Haverkort, K. Wohlfeld, and M. Grüninger, Orbital superexchange and crystal field simultaneously at play in YVO_3: Resonant inelastic x-ray scattering at the V L edge and the O K edge, Phys. Rev. B **88**, 205115 (2013).

[57] B. W. Lebert, S. Kim, V. Bisogni, I. Jarrige, A. M. Barbour, and Y.-J. Kim, Resonant inelastic x-ray scattering study of $\alpha - RuCl_3$: a progress report, J. Phys.: Condens. Matter **32**, 144001 (2020).

[58] P. Warzanowski, N. Borgwardt, K. Hopfer, J. Attig, T. C. Koethe, P. Becker, V. Tsurkan, A. Loidl, M. Hermanns, P. H. M. van Loosdrecht, and M. Grüninger, Multiple spin-orbit excitons and the electronic structure of $\alpha - RuCl_3$, Phys. Rev. Res. **2**, 042007(R) (2020).

[59] H. Suzuki, H. Liu, J. Bertinshaw, K. Ueda, H. Kim, S. Laha, D. Weber, Z. Yang, L. Wang, H. Takahashi, K. Fürsich, M. Minola, B. V. Lotsch, B. J. Kim, H. Yavaş, M. Daghofer, J. Chaloupka, G. Khaliullin, H. Gretarsson, and B. Keimer, Proximate ferromagnetic state in the Kitaev model material $\alpha - RuCl_3$, Nat. Commun. **12**, 4512 (2021).

[60] B. A. Kozikowski and T. A. Keiderling, Intraconfigurational absorption spectroscopy of Os^{4+} ion in K_2SnCl_6 and K_2OsCl_6 crystals, J. Phys. Chem. **87**, 4630 (1983).

[61] A. Bertin, L. Kiefer, and M. Braden (private communication).

[62] G. A. Bain and J. F. Berry, Diamagnetic corrections and pascal's constants, J. Chem. Educ. **85**, 532 (2008).

[63] Y. Zhang, L.-F. Lin, A. Moreo, and E. Dagotto, $J = 0$ nonmagnetic insulating state in K_2OsX_6 ($X =$ F, Cl, and Br), Phys. Rev. B **106**, 155148 (2022).

[64] M. W. Haverkort, M. Zwierzcki, and O. K. Andersen, Multiplet ligand-field theory using Wannier orbitals, Phys. Rev. B **85**, 165113 (2012).

[65] M. W. Haverkort, Quanty for core level spectroscopy - excitons, resonances and band excitations in time and frequency domain, J. Phys.: Conf. Ser. **712**, 012001 (2016).

[66] S. Huotari, G. Vankó, F. Albergamo, C. Ponchut, H. Graafsma, C. Henriquet, R. Verbeni, and G. Monaco, Improving the performance of high-resolution x-ray spectrometers with position-sensitive pixel detectors, J. Synchrotron Rad. **12**, 467 (2005).

[67] S. Huotari, F. Albergamo, G. Vankó, R. Verbeni, and G. Monaco, Resonant inelastic hard x-ray scattering with diced analyzer crystals and position-sensitive detectors, Rev. Sci. Instrum. **77**, 053102 (2006).

[68] M. Moretti Sala, C. Henriquet, L. Simonelli, R. Verbeni, and G. Monaco, High energy-resolution set-up for Ir L_3 edge RIXS experiments, J. Electron Spectrosc. Relat. Phenom. **188**, 150 (2013).

[69] M. Moretti Sala, K. Martel, C. Henriquet, A. Al Zein, L. Simonelli, Ch. J. Sahle, H. Gonzalez, M.-C. Lagier, C. Ponchut, S. Huotari, R. Verbeni, M. Krisch, and G. Monaco, A high-energy-resolution resonant inelastic X-ray scattering spectrometer at ID20 of the European Synchrotron Radiation Facility, J. Synchrotron Rad. **25**, 580 (2018).

[70] P. J. E. M. van der Linden, M. Moretti Sala, C. Henriquet, M. Rossi, K. Ohgushi, F. Fauth, L. Simonelli, C. Marini, E. Fraga, C. Murray, J. Potter, and M. Krisch, A compact and versatile dynamic flow cryostat for photon science, Rev. Sci. Instr. **87**, 115103 (2016).

[71] M. Minola, G. Dellea, H. Gretarsson, Y. Y. Peng, Y. Lu, J. Porras, T. Loew, F. Yakhou, N. B. Brookes, Y. B. Huang, J. Pelliciari, T. Schmitt, G. Ghiringhelli, B. Keimer, L. Braicovich, and M. Le Tacon, Collective Nature of Spin Excitations in Superconducting Cuprates Probed by Resonant Inelastic X-Ray Scattering, Phys. Rev. Lett. **114**, 217003 (2015).

[72] J. Reul, L. Fels, N. Qureshi, K. Shportko, M. Braden, and M. Grüninger, Temperature-dependent optical conductivity of layered $LaSrFeO_4$, Phys. Rev. B **87**, 205142 (2013).

[73] N. Borgwardt, J. Lux, I. Vergara, Z. Wang, A. A. Taskin, K. Segawa, P. H. M. van Loosdrecht, Y. Ando, A. Rosch, and M. Grüninger, Self-organized charge puddles in a three-dimensional topological material, Phys. Rev. B **93**, 245149 (2016).

[74] R. M. A. Azzam and N. M. Bashara, *Ellipsometry and Polarized Light* (Elsevier, New York, 1987).

[75] M. Grüninger, M. Windt, T. Nunner, C. Knetter, K. P. Schmidt, G. S. Uhrig, T. Kopp, A. Freimuth, U. Ammerahl, B. Büchner, and A. Revcolevschi, Magnetic excitations in two-leg spin 1/2 ladders: Experiment and theory, J. Phys. Chem. Solids **63**, 2167 (2002).

[76] D. Reig-i-Plessis, T. A. Johnson, K. Lu, Q. Chen, J. P. C. Ruff, M. H. Upton, T. J. Williams, S. Calder, H. D. Zhou, J. P. Clancy, A. A. Aczel, and G. J. MacDougall, Structural, electronic, and magnetic properties of nearly ideal $J_{\text{eff}} = 1/2$ iridium halides, Phys. Rev. Mater. **4**, 124407 (2020).

[77] A. Paramekanti, D. D. Maharaj, and B. D. Gaulin, Octupolar order in d-orbital Mott insulators, Phys. Rev. B **101**, 054439 (2020).

[78] S. W. Lovesey and D. D. Khalyavin, Lone octupole and bulk magnetism in osmate $5d^2$ double perovskites, Phys. Rev. B **102**, 064407 (2020).

[79] G. Khaliullin, D. Churchill, P. P. Stavropoulos, and H.-Y. Kee, Exchange interactions, Jahn-Teller coupling, and multipole orders in pseudospin one-half $5d^2$ Mott insulators, Phys. Rev. Res. **3**, 033163 (2021).

[80] S. Voleti, A. Haldar, and A. Paramekanti, Octupolar order and Ising quantum criticality tuned by strain and dimensionality: Application to d-orbital Mott insulators, Phys. Rev. B **104**, 174431 (2021).

[81] L. V. Pourovskii, D. F. Mosca, and C. Franchini, Ferro-octupolar order and low-energy excitations in d^2 double perovskites of osmium, Phys. Rev. Lett. **127**, 237201 (2021).

[82] A. Rayyan, D. Churchill, and H.-Y. Kee, Field-induced Kitaev multipolar liquid in spin-orbit coupled d^2 honeycomb Mott insulators, Phys. Rev. B **107**, L020408 (2023).

[83] H. Homborg, Absorptions- und elektronische Raman-Spektren von Intrakonfigurationsübergängen der Hexahalogenokomplexe von Os^{IV} (X = CI, I) und Ir^{IV} (X = CI, Br), Z. Anorg. Allg. Chem. **493**, 121 (1982).

[84] D. Mintz, R. L. Armstrong, B. M. Powell, and W. J. L. Buyers, Soft rotary mode in the antifluorite crystal K_2OsCl_6, Phys. Rev. B **19**, 448 (1979).

[85] G. P. O'Leary and R. G. Wheeler, Phase transitions and soft librational modes in cubic crystals, Phys. Rev. B **1**, 4409 (1970).

[86] N. Khan, D. Prishchenko, M. H. Upton, V. G. Mazurenko, and A. A. Tsirlin, Towards cubic symmetry for Ir^{4+}: Structure and magnetism of the antifluorite K_2IrBr_6, Phys. Rev. B **103**, 125158 (2021).

[87] A. Bertin, T. Dey, D. Brüning, D. Gorkov, K. Jenni, A. Krause, P. Becker, L. Bohatý, D. Khomskii, M. Braden, and T. Lorenz, Interplay of weak ferromagnetism, ferroelasticity and shape-memory effects in the spin-orbit coupled antiferromagnet K_2ReCl_6, arXiv:2207.11101

[88] B. A. Kozikowski and T. A. Keiderling, Intraconfigurational absorption and magnetic circular dichroism spectra of Os^{4+} in Cs_2ZrCl_6 and in Cs_2ZrBr_6, Mol. Phys. **40**, 477 (1980).

[89] H. U. Rahman, Analysis of the Magnetic Susceptibility of K_2OsCl_6, Phys. Rev. B **3**, 729 (1971).

[90] P. B. Dorain, H. H. Patterson, and P. C. Jordan, Optical spectra of Os^{4+} in single cubic crystals at 4.2 °K, J. Chem. Phys. **49**, 3845 (1968).

[91] S. B. Piepho, J. R. Dickinson, J. A. Spencern, and P. N. Schatz, High resolution absorption and magnetic circular dichroism spectra of Cs_2ZrCl_6: Os^{4+}, Mol. Phys. **24**, 609 (1972).

[92] Y. Moritomo and Y. Tokura, Charge-transfer type excitations in layered cupric halides, Jpn. J. Appl. Phys. **32**, 344 (1993).

[93] R.-P. Wang, B. Liu, R. J. Green, M. U. Delgado-Jaime, M. Ghiasi, T. Schmitt, M. M. van Schooneveld, and F. M. F. de Groot, Charge-transfer analysis of $2p3d$ resonant inelastic X-ray scattering of cobalt sulfide and halides, J. Phys. Chem. C **121**, 24919 (2017).

6 Spin-orbit coupling in a half-filled t_{2g} shell: The case of $5d^3$ K_2ReCl_6

The following chapter presents the results on K_2ReCl_6, which have been published as Warzanowski *et al.*, *Spin-orbit coupling in a half-filled t_{2g} shell: The case of $5d^3$ K_2ReCl_6*, Phys. Rev. B **109**, 155149 (2024).

Author contributions

M. Grüninger and P. Warzanowski conceived the experiment. P. Warzanowski carried out the optical spectroscopy experiments with support from G. Schlicht. P. Warzanowski, M. Magnaterra, Q. Faure, Ch. J. Sahle, and M. Grüninger carried out the RIXS experiments at the ID20 beamline of the ESRF, supported by M. Moretti Sala, G. Monaco, and P. H. M. van Loosdrecht. P. Becker and L. Bohatý synthesized and characterized the samples. P. Warzanowski analyzed the data and performed the numerical single-site calculations with support from M. Grüninger. P. Warzanowski, M. Hermanns, and M. Grüninger analyzed the eigenstates within the t_{2g}-only model. P. Warzanowski, M. Hermanns, and M. Grüninger wrote the manuscript with input from all authors.

Sample and data availability

The samples used in this project are stored within the labs of the Institute of Physics II at the University of Cologne. The raw data and the analysis files are stored on the servers of the Institute of Physics II.

Spin-orbit coupling in a half-filled t_{2g} shell: The case of $5d^3$ K_2ReCl_6

P. Warzanowski,[1] M. Magnaterra,[1] G. Schlicht,[1] Q. Faure,[2,3] Ch. J. Sahle,[2] P. Becker,[4] L. Bohatý,[4] M. Moretti Sala,[5] G. Monaco,[6] M. Hermanns,[7] P. H. M. van Loosdrecht,[1] and M. Grüninger[1]

[1]*Institute of Physics II, University of Cologne, 50937 Cologne, Germany*
[2]*ESRF, The European Synchrotron, 71 Avenue des Martyrs, CS40220, 38043 Grenoble Cedex 9, France*
[3]*Laboratoire Léon Brillouin, CEA, CNRS, Université Paris-Saclay, CEA-Saclay, 91191 Gif-sur-Yvette, France*
[4]*Sect. Crystallography, Institute of Geology and Mineralogy, University of Cologne, 50674 Cologne, Germany*
[5]*Dipartimento di Fisica, Politecnico di Milano, I-20133 Milano, Italy*
[6]*Dipartimento di Fisica e Astronomia "Galileo Galilei," Università di Padova, I-35121 Padova, Italy*
[7]*Department of Physics, Stockholm University, AlbaNova University Center, SE-106 91 Stockholm, Sweden*

(Received 25 November 2023; accepted 29 March 2024; published 17 April 2024)

The half-filled t_{2g} shell of the t_{2g}^3 configuration usually, in *LS* coupling, hosts a $S = 3/2$ ground state with quenched orbital moment. This state is not Jahn-Teller active. Sufficiently large spin-orbit coupling ζ has been predicted to change this picture by mixing in orbital moment, giving rise to a sizable Jahn-Teller distortion. In $5d^3$ K_2ReCl_6 we study the electronic excitations using resonant inelastic x-ray scattering and optical spectroscopy. We observe on-site intra-t_{2g} excitations below 2 eV and corresponding overtones with two intra-t_{2g} excitations on adjacent sites, the Mott gap at 2.7 eV, t_{2g}-to-e_g excitations above 3 eV, and charge-transfer excitations at still higher energy. The intra-t_{2g} excitation energies are a sensitive measure of ζ and Hund's coupling J_H. The sizable value of $\zeta \approx 0.29$ eV places K_2ReCl_6 into the intermediate coupling regime, but $\zeta/J_H \approx 0.6$ is not sufficiently large to drive a pronounced Jahn-Teller effect. We discuss the ground state wave function in a Kanamori picture and find that the $S = 3/2$ multiplet still carries about 97% of the weight. However, the finite admixture of orbital moment allows for subtle effects. We discuss small temperature-induced changes of the optical data and find evidence for a lowering of the ground state by about 3 meV below the structural phase transitions.

DOI: 10.1103/PhysRevB.109.155149

I. INTRODUCTION

Strong spin-orbit coupling ζ is a fertile source of rich physics in correlated $5d$ transition-metal compounds [1–6]. Consider a single metal site with the electronic configuration t_{2g}^n in cubic symmetry. For $n = 1$, 2, 4, or 5 and $\zeta = 0$, the ground state shows either spin $S = 1/2$ or 1 and threefold orbital degeneracy and the latter is expected to be lifted by the Jahn-Teller effect [4]. In all four cases, strong spin-orbit coupling changes the character of the magnetic moments in a decisive way, forming spin-orbit-entangled moments from the spin and the effective orbital moment of the t_{2g} states. The t_{2g}^5 configuration hosts $J = 1/2$ moments that open the door for the realization of bond-directional Kitaev exchange [7–11]. Similarly, $n = 1$ yields $J = 3/2$ moments with bond-dependent multipolar interactions and a corresponding rich phase diagram [12–16]. Exotic multipolar phases have also been predicted for t_{2g}^2 compounds where the degeneracy of the $J = 2$ states is lifted if one considers the admixture of e_g orbitals for a finite cubic crystal-field splitting $10Dq$ [17–22]. Finally, t_{2g}^4 compounds show a nonmagnetic $J = 0$ state [23–30] that, in the case of strong dispersion of magnetic excited states, may give way to excitonic magnetism based on the condensation of these excited states [31–34].

In this series, the case of $n = 3$ stands out due to its half-filled t_{2g} shell, which typically is assumed to give rise to a spin-only $S = 3/2$ state with quenched orbital moment. Spin-orbit coupling hence is not expected to play a prominent role, at least in the commonly adopted *LS* coupling scheme for $\zeta/J_H \to 0$, where J_H denotes Hund's coupling. Recently, Streltsov and Khomskii [4] pointed out that this common point of view fails for large ζ/J_H, highlighting a particularly interesting case of the interplay of spin-orbit coupling and Jahn-Teller physics. In the $S = 3/2$ scenario, the three electrons equally occupy the three t_{2g} orbitals such that a distortion away from cubic symmetry does not lower the energy. In contrast, for large ζ/J_H in jj coupling one obtains $j = 3/2$ for each electron individually and the corresponding three-electron ground state is found to be Jahn-Teller active [4]. More precisely, a significant Jahn-Teller distortion is expected for $\zeta^{\rm eff}/J_H^{\rm eff} \gtrsim 1.5$; see Fig. 1(b). The effective parameters $\zeta^{\rm eff}$ and $J_H^{\rm eff}$ refer to a t_{2g}-only Kanamori scheme, i.e., to the case of an infinite cubic crystal-field splitting, $10Dq = \infty$.

Experimentally, the electronic parameters ζ and J_H can be determined via the energies of intra-t_{2g} excitations that can be observed in resonant inelastic x-ray scattering (RIXS) or optical spectroscopy. Based on RIXS data, the $5d^3$ osmates Ca_3LiOsO_6 and Ba_2YOsO_6 have been claimed to realize a novel spin-orbit-entangled $J = 3/2$ ground state for which, however, about 95% of the wave function stem from the $S = 3/2$ state [35]. The admixture of low-spin $S = 1/2$ character and the corresponding finite orbital moment are supposed

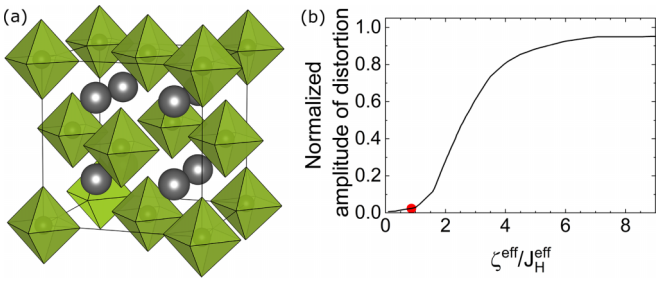

FIG. 1. (a) Sketch of the room-temperature crystal structure of K_2ReCl_6. The Re^{4+} ions form an fcc lattice. The $ReCl_6$ octahedra are depicted in green and the K^+ ions are gray. (b) Jahn-Teller distortion of a t_{2g}^3 configuration as a function of $\zeta^{\text{eff}}/J_{\text{H}}^{\text{eff}}$, normalized to the value for $\zeta^{\text{eff}}/J_{\text{H}}^{\text{eff}} \rightarrow \infty$ (adapted from [4]). The calculation assumes $J_{\text{H}}B/g^2 = 1/2$, where g and B are electron-phonon coupling parameters of the Jahn-Teller Hamiltonian [4]. Red symbol marks the position of K_2ReCl_6 according to our analysis.

to explain the sizable spin gap observed in both compounds and other $5d^3$ osmates [36–39]. In contrast, gapless magnetic excitations were reported for $4d^3$ $S = 3/2$ Ca_3LiRuO_6 [40]. In the RIXS data of $5d^3$ Ca_3LiOsO_6 and Ba_2YOsO_6, only four of the five intra-t_{2g} excitations were resolved [35]. The analysis yields $\zeta/J_{\text{H}} \approx 1$, placing these compounds within the intermediate coupling range [35].

Here, we address the electronic structure of the $5d^3$ Mott insulator K_2ReCl_6 using RIXS measurements at the Re L_3 edge and optical spectroscopy. At room temperature, K_2ReCl_6 exhibits the cubic K_2PtCl_6-type antifluorite structure with the Re ions forming an fcc lattice; see Fig. 1(a). The structure can be viewed as equivalent to a double perovskite K_2ABX_6 in which the B sites are occupied by Re^{4+} ions while the A sites correspond to "ordered" vacancies. This material has been proposed by Streltsov and Khomskii [4] as a possible candidate for a spin-orbit-driven Jahn-Teller effect, arguing that it shows a series of structural phase transitions at lower temperature [41–43]. Recent Raman scattering results revealed the violation of cubic selection rules already at 300 K [44]. A Curie-Weiss fit of the magnetic susceptibility [43] yields an effective magnetic moment $\mu_{\text{eff}} \approx 3.81\mu_B$, which is close to the value expected for a $S = 3/2$ system, $2\sqrt{S(S+1)}\mu_B \approx 3.87\mu_B$. Below the antiferromagnetic ordering temperature $T_N = 12$ K, the application of a large magnetic field induces weak ferromagnetism and reveals a pronounced magnetoelastic coupling [43]. The structure shows nearly undistorted, unconnected $ReCl_6$ octahedra and the corresponding (nearly) spin-forbidden on-site d-d excitations [45,46] yield narrow features in the optical conductivity that allow for a most accurate determination of the excitation energies. In combination with the value of the cubic crystal-field splitting $10Dq$ seen in RIXS, this allows us to obtain a reliable and accurate set of the electronic parameters. Our analysis is based on calculations of the local multiplet energies using QUANTY [47,48].

The paper is organized as follows. Experimental aspects are described in Sec. II. In Secs. III A and III B 1, we assign the features observed in RIXS and optical spectroscopy, respectively. In optics, the spectral weight of the on-site intra-t_{2g} excitations mainly stems from phonon-assisted processes and the corresponding line shape and temperature-dependent spectral weight are discussed in Secs. III B 2 and III B 3, respectively. Overtones or double d-d excitations are analyzed in Sec. III B 4. Subtle temperature-induced effects in the optical data down to T_N are presented in Sec. III B 5, while the temperature range below T_N is addressed in Appendix A. Results of local multiplet calculations are discussed in Sec. III C. We cover the Kanamori picture with $10Dq = \infty$ but also derive the electronic parameters for finite $10Dq$. We give the analytic expressions for the wave functions in the Kanamori picture, with details described in Appendix B. This allows for a quantitative description of the effect of spin-orbit coupling.

II. EXPERIMENT

Single crystals of K_2ReCl_6 have been grown from HCl solution by controlled slow evaporation of the solvent. The sample batch has been thoroughly characterized by x-ray diffraction and measurements of the magnetic susceptibility and the specific heat [43]. At 300 K, K_2ReCl_6 exhibits the cubic K_2PtCl_6-type antifluorite structure with space group $Fm\bar{3}m$ and lattice parameter $a = 9.8$ Å. Structural phase transitions have been observed at 111, 103, and 77 K [41–43] and are accompanied by rotations and tilts of the $ReCl_6$ octahedra. Note that adjacent $ReCl_6$ octahedra are not connected in this structure, i.e., they do not share a corner, edge, or face. The structure turns tetragonal ($P4/mnc$) at 111 K [43] and monoclinic ($C2/c$) at 103 K. The transition at 77 K from monoclinic $C2/c$ to monoclinic $P2_1/n$ is of first order, while the monoclinic angle is very close to 90° in both phases [43]. Finally, a magnetic phase transition to an antiferromagnetically ordered state occurs at $T_N = 12$ K [43,49,50].

To the best of our knowledge, RIXS at the Re L_3 edge thus far has only been reported in an early study on ReO_2 and ReO_3 [51] and in the $5d^1$ and $5d^2$ double perovskites A_2BReO_6 (A = Ba, Sr, Ca; B = Mg, Y, Cr) [24,27,52,53]. On K_2ReCl_6, resonant magnetic scattering has been studied at the Re L edge [54]. Our RIXS experiments at the Re L_3 edge were performed at beamline ID20 of the European Synchrotron Radiation Facility. Incident photons from three consecutive U26 undulators were monochromatized by a Si(111) high-heat-load monochromator and a successive Si(311) channel-cut postmonochromator. Via a mirror system in Kirkpatrick-Baez geometry, the monochromatic x-ray beam was focused to 8×50 μm^2 (V × H) at the sample position. Energy loss spectra were collected with the high-energy-resolution resonant inelastic x-ray scattering spectrometer equipped with a 2 m analyzer/detector arm. Incident π polarization in the horizontal scattering plane was used. We employed the Si(9,1,1) reflection of a diced Si(11,1,1) analyzer crystal in conjunction with a pixelated area detector [55–57]. To address the resonance behavior, we have measured RIXS spectra at 300 K with the incident energy in the range from 10.530 to 10.545 keV, i.e., across the maximum of the Re $2p_{3/2} \rightarrow 5d$ absorption. The overall energy resolution was 295 meV as estimated by the full width at half maximum of quasielastic scattering from a piece of adhesive tape. The RIXS measurements were performed on a (111) surface, with (001) and (110) lying in the horizontal scattering plane, as sketched in the inset of Fig. 2(b). All RIXS data are corrected for

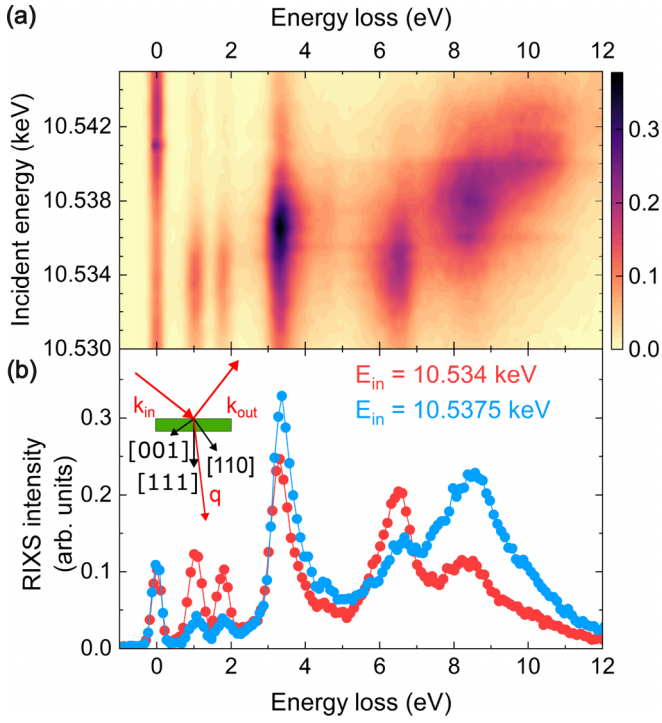

FIG. 2. RIXS data of K_2ReCl_6 at $T = 300$ K. (a) Resonance map of the RIXS intensity based on spectra measured with different incident energy E_{in} for transferred momentum $\mathbf{q} \approx (7.4\ 7.4\ 5.9)$. (b) RIXS spectra for $E_{in} = 10.534$ keV and 10.5375 keV, i.e., at t_{2g} and e_g resonance, respectively. Inset: sketch of the scattering geometry.

the geometrical contribution to self-absorption [58]. We use reciprocal lattice units for the transferred momentum $\mathbf{q}$.

Infrared and optical transmittance measurements were performed using a Bruker IFS 66/v Fourier-transform spectrometer. The energy resolution was set to 1 $cm^{-1} \approx$ 0.12 meV. We measured an as-grown sample with thickness $d = 471(5)$ μm. The light propagated along the cubic (111) direction. Using a continuous-flow ^{4}He cryostat, the measurements were performed at several temperatures between 6 and 300 K.

III. RESULTS

The combination of RIXS and optical spectroscopy is suited very well to examine the local electronic structure of Mott insulators such as K_2ReCl_6. RIXS at the L_3 edge is boosting the intensity of on-site d-d excitations via resonant transitions between the valence $5d$ orbitals and core $2p$ states [10,15,23,24,30,59–61]. In contrast, optical spectroscopy is most sensitive to excitations that involve a change of the electric dipole moment. In Mott insulators, these are in particular intersite excitations such as excitations across the Mott gap, here $|d_i^3 d_j^3\rangle \rightarrow |d_i^2 d_j^4\rangle$ with sites i and j, or charge-transfer processes $|3p_{Cl}^6 5d_{Re}^3\rangle \rightarrow |3p_{Cl}^5 5d_{Re}^4\rangle$ [62–64]. Compared to these strong absorption bands, on-site d-d excitations are observed as weak features [23,65–70]. In the presence of inversion symmetry, on-site d-d excitations are parity forbidden by the Laporte rule. This can be circumvented by means of a phonon-assisted process in which the additional creation or annihilation of an odd-symmetry phonon breaks inversion symmetry. Additionally, we have to consider the spin selection rule $\Delta S = 0$. In a spin-only picture of the t_{2g}^3 configuration of a Re^{4+} ion in K_2ReCl_6, the local ground state exhibits $S = 3/2$, while all excited states show $S = 1/2$; hence all excitations within the t_{2g}^3 manifold are spin forbidden. However, these excitations may acquire finite spectral weight due to spin-orbit coupling or in a magnetic dipole transition. Combining parity and spin selection rules, the spectral weight of on-site d-d excitations in K_2ReCl_6 is orders of magnitude smaller than for strong, directly electric dipole allowed transitions. Nevertheless such weak on-site d-d excitations can be studied very well in transmittance measurements on single crystals with an appropriate thickness; see Sec. III B.

A. RIXS on K_2ReCl_6

The resonance behavior observed in RIXS allows us to assess the character of the electronic excitations in K_2ReCl_6, i.e., to distinguish intra-t_{2g} features, t_{2g}-to-e_g excitations and charge-transfer excitations. Figure 2(a) depicts a resonance map, i.e., an intensity plot of RIXS spectra for different incident energies. The data have been measured at $T = 300$ K for transferred momentum $\mathbf{q} \approx (7.4\ 7.4\ 5.9)$. We find that the resonance enhancement of the RIXS intensity is peaking at $E_{in} = 10.534$ keV and 10.5375 keV, while the energy loss does not depend on E_{in}. Cuts through the resonance map at these two incident energies are shown in Fig. 2(b). The two resonance energies can be attributed to t_{2g} resonance and e_g resonance, i.e., enhancement of the RIXS intensity if E_{in} is tuned to promote a $2p$ core electron to either a t_{2g} or an e_g orbital, respectively.

The two low-energy peaks at 1.0 and 1.8 eV display t_{2g} resonance and therefore can be assigned to intra-t_{2g} excitations. The energy resolution of 295 meV does not allow us to resolve any substructure of these two peaks in the RIXS data. The strong feature peaking at 3.5 eV shows e_g resonance and corresponds to excitations from $|t_{2g}^3\rangle$ to $|t_{2g}^2 e_g^1\rangle$. This assignment is supported by the difference between the two resonance energies, $(10.5375 - 10.534)$ keV $= 3.5$ eV, which provides an approximate measure of the cubic crystal-field splitting $10Dq$. Charge-transfer excitations set in at about 5 eV. They correspond to promoting an electron from the ligand Cl p shell to either Re t_{2g} or e_g orbitals, $|3p_{Cl}^6 5d_{Re}^3\rangle \rightarrow |3p_{Cl}^5 5d_{Re}^4\rangle$. Accordingly, the respective RIXS peaks at about 6.5 and 8.5 eV exhibit t_{2g} or e_g resonance.

Previously, such a coexistence of t_{2g} resonance and e_g resonance of charge-transfer excitations has been reported in, e.g., $5d^2$ Ba_2YReO_6 [24] and the sister compounds $5d^4$ K_2OsCl_6 [23] and $5d^5$ K_2IrBr_6 [61]. Compared to K_2OsCl_6 [23], the charge-transfer peaks are roughly 0.5 to 0.8 eV higher in energy in K_2ReCl_6, while the value of $10Dq$ is very similar. Concerning the intra-t_{2g} excitations, our RIXS data of K_2ReCl_6 resolve the two energies 1.0 and 1.8 eV, while a splitting into four peaks at somewhat lower energies has been reported in RIXS on the $5d^3$ osmates Ca_3LiOsO_6 and Ba_2YOsO_6 [35]. All five intra-t_{2g} energies are revealed by our optical data, which we address in the next section.

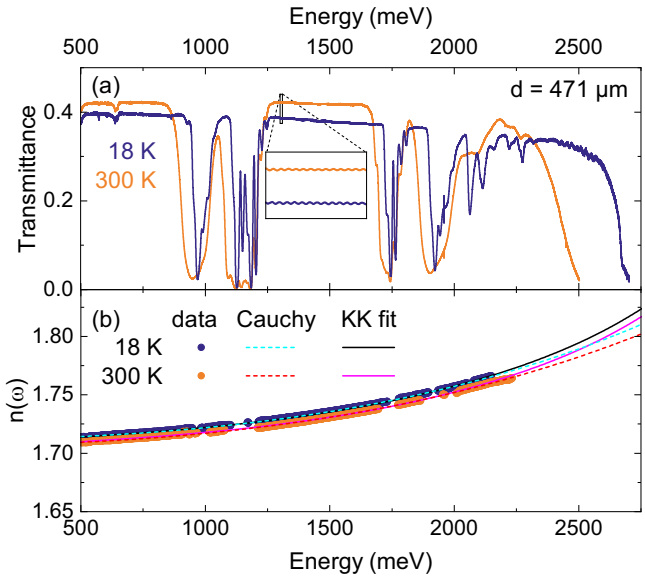

FIG. 3. Optical data of K_2ReCl_6. (a) Transmittance $T(\omega)$ for a sample thickness $d = 471$ μm at 18 and 300 K. The data reveal weak excitations within the t_{2g}^3 subshell, while the onset of excitations across the Mott gap at $\Delta_{\text{exp}} = 2.7$ eV at 18 K marks the upper energy limit of the transparency range. The inset highlights Fabry-Pérot interference fringes. (b) Refractive index $n(\omega)$ extracted from Fabry-Pérot interference fringes in $T(\omega)$ (symbols). Note that $n(\omega)$ is nearly constant below the gap. Dashed: empirical fit using the Cauchy model. Lines: Kramers-Kronig-consistent fit using an oscillator model with an infrared-active phonon at $E_{ph} = 39$ meV and a Tauc-Lorentz oscillator with the measured gap $\Delta_{\text{exp}} = 2.7$ eV.

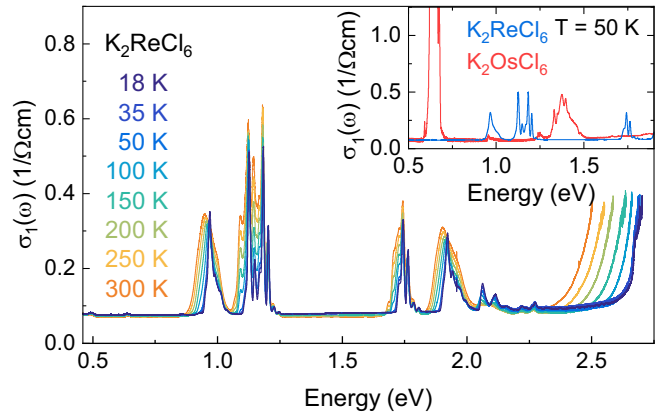

FIG. 4. Optical conductivity $\sigma_1(\omega)$ of K_2ReCl_6 below the Mott gap for several temperatures. The onset of excitations across the Mott gap is at 2.7 eV at 18 K. Below the gap, there are phonon-assisted intra-t_{2g} excitations in the range from 0.9 to 2 eV. Above 2 eV, we observe weak overtones, i.e., intersite pair excitations that correspond to two intra-t_{2g} excitations on neighboring sites. Inset: comparison of intra-t_{2g} excitations of K_2ReCl_6 and its d^4 sister compound K_2OsCl_6 [23]. From the latter, a small constant offset has been subtracted.

B. Optical conductivity of K_2ReCl_6

The experimental task is to obtain the complex optical conductivity $\sigma(\omega) = \sigma_1(\omega) + i\sigma_2(\omega)$ or, equivalently, the complex index of refraction $N(\omega) = n(\omega) + i\kappa(\omega)$, with $\sigma_1 \propto nk$. To address the very weak on-site d-d absorption features in the frequency range below the Mott gap, we employ the sensitivity of the transmittance $T(\omega)$, which depends exponentially on $\kappa(\omega)$; see Fig. 3. In contrast to $\kappa(\omega)$, the real part $n(\omega)$ is not very sensitive to weak absorption bands. In the transparency range $\kappa \ll n$, Fabry-Pérot interference fringes are observed in $T(\omega)$ due to multiple reflections within the sample. From the fringes we determine the optical path length $n(\omega)d$ and hence the real part $n(\omega)$; see Fig. 3. As expected, $n(\omega)$ shows the nearly constant behavior that is typical for an insulator below the gap. Sufficiently far above the phonon range, the small positive dispersion can be described empirically by the Cauchy model, $n = \alpha + \beta/\lambda^2 + \gamma/\lambda^4$, where λ denotes the wavelength and α, β, and γ are fit parameters (dashed lines in Fig. 3).

1. *Assignment of intra-t_{2g} excitations*

The real part of the optical conductivity $\sigma_1(\omega)$ of K_2ReCl_6 is plotted in Fig. 4. We focus on temperatures higher than $T_N = 12$ K to avoid the additional complexity arising from magnetic order; see Appendix A. We observe three different kinds of excitations: the onset of excitations across the Mott gap at about 2.7 eV at 18 K, a series of weak phonon-assisted intra-t_{2g} excitation bands between 0.9 eV and 2 eV that are in agreement with the corresponding RIXS peaks centered at 1.0 and 1.8 eV and with previous optical results [45,46], and even weaker features above 2 eV that can be attributed to double excitations, i.e., combinations and overtones of the intra-t_{2g} excitations, as discussed below. Overall, the values of $\sigma_1(\omega)$ are very small below the gap, reflecting the infrared-forbidden character of the intra-t_{2g} excitations [65,66]. The weak spectral weight of excitations that are both spin forbidden and parity forbidden is most strikingly illustrated by data on compounds where both spin-forbidden and spin-allowed excitations are observed, such as $3d^2$ VOCl [68] or $3d^3$ Cr compounds [69]. Furthermore, it is instructive to compare K_2ReCl_6 with the $5d^4$ $J = 0$ compound K_2OsCl_6 [23]; see inset of Fig. 4. In the absence of spin-orbit coupling, the cubic t_{2g}^4 configuration would show an $S = 1$ ground state and $S = 0$ excited states, i.e., spin-forbidden excitations. Most of the features in $J = 0$ K_2OsCl_6 are as weak as in K_2ReCl_6. However, K_2OsCl_6 also exhibits a stronger band around 0.6 eV that corresponds to the excitation from $J = 0$ to 2, reflecting the prominent role of strong spin-orbit coupling for this absorption feature. This comparison gives a first hint for a smaller effect of spin-orbit coupling for the t_{2g}^3 configuration of K_2ReCl_6.

Our focus is on the intra-t_{2g} excitations of K_2ReCl_6. In total, there are 20 t_{2g}^3 states. In cubic symmetry and neglecting spin-orbit coupling, these are split by Coulomb interactions into four multiplets, i.e., the high-spin $S = 3/2$ $^4A_2$ ground state and the three low-spin $S = 1/2$ excited states ^2E, $^2T_1$, and $^2T_2$; see Fig. 5. In the t_{2g}-only Kanamori scheme, i.e., for a cubic crystal-field splitting $10Dq = \infty$, the excitation energies are $3J_{\text{H}}^{\text{eff}}$ for the ^2E and $^2T_1$ multiplets and $5J_{\text{H}}^{\text{eff}}$ for $^2T_2$ [71–73], where $J_{\text{H}}^{\text{eff}}$ denotes Hund's coupling in the Kanamori scheme [72] (see Sec. III C 1). From the peak energies observed in RIXS, 1.0 and 1.8 eV, we obtain a rough estimate $J_{\text{H}}^{\text{eff}} \approx 0.35$ eV. For finite $10Dq$, in a model con-

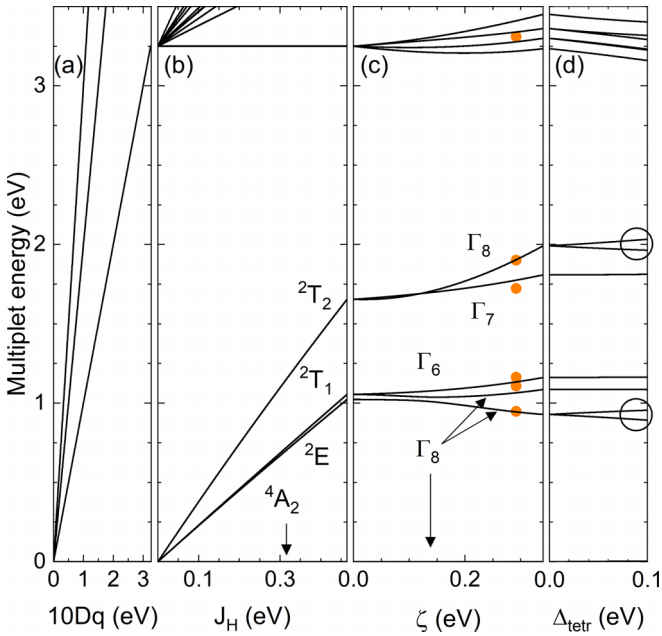

FIG. 5. Energy level diagram for the d^3 configuration. (a)–(c) Using QUANTY [47,48], the cubic multiplet energies were calculated as a function of cubic crystal-field splitting $10Dq$, spin-orbit coupling ζ, and interelectronic Coulomb interaction in terms of the Slater integrals F^2 and F^4. The latter is captured by $J_H = 1/14(F^2 + F^4)$. Panel (a) uses $J_H = \zeta = 0$ and shows the t_{2g}^3 states at $E = 0$ and $t_{2g}^{3-n}e_g^n$ states at higher energy. (b) Coulomb interactions lift the degeneracy of the t_{2g}^3 states. (c) Effect of ζ. Orange symbols: intra-t_{2g} energies taken from $\sigma_1(\omega)$ and the t_{2g}-to-e_g excitation energy of 3.3 eV observed in RIXS. Their position on the ζ axis marks the value obtained from a fit (see Sec. III C 2). For the e_g states, the maximum of the broadened RIXS response was chosen, lying between the second and third energy levels. (d) Effect of a tetragonal crystal field. Circles highlight the splitting of the lowest and highest intra-t_{2g} excitations.

sidering the entire d shell [72], this corresponds to $J_H \approx J_H^{\text{eff}}/0.77 \approx 0.45$ eV; see Fig. 5(b).

Finite $10Dq$ lifts the degeneracy between ^2E and $^2T_1$, while spin-orbit coupling splits both $^2T_1$ and $^2T_2$ into a quartet and a doublet. Altogether, this yields five excited states within the t_{2g}^3 manifold. In Bethe notation, the ground state is given by Γ_8 while the five excited states are described by Γ_8, Γ_8, Γ_6, Γ_7, and Γ_8; see Fig. 5 and Appendix B. In the optical data, the spin-forbidden character of the intra-t_{2g} excitations yields narrow absorption lines that allow for an accurate determination of all five electronic excitation energies $E_{0,i}$ for $i = 1$–5; see Fig. 6. As explained in the next paragraph, we find $E_{0,i} = 948$, 1107, 1164, 1723, and 1901 meV, in agreement with previous results [45,46].

2. *Sideband features of the intra-t_{2g} absorption bands*

For each absorption band, $\sigma_1(\omega)$ shows a series of peaks; see Fig. 6. However, the energies $E_{0,i}$ can be identified based on the common peak structure that becomes evident by plotting the five intra-t_{2g} absorption bands on the shifted energy axis $E - E_{0,i}$, as done in Fig. 7 for 18 K and in Appendix A for 6 K, below T_N. These plots illustrate the existence of the

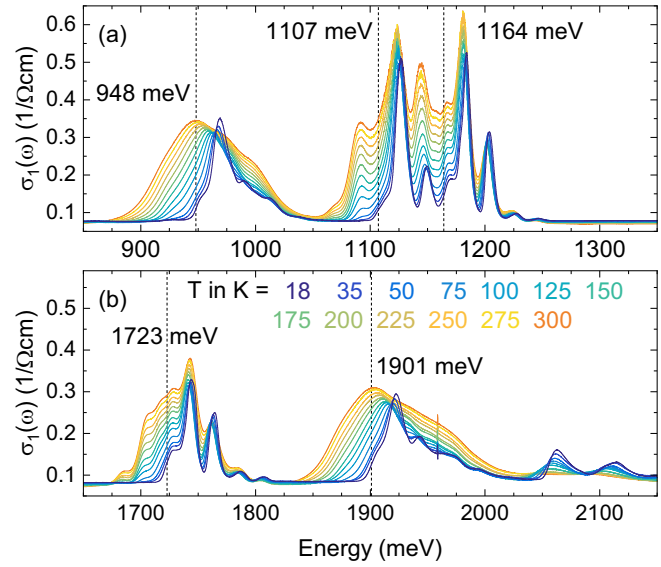

FIG. 6. Temperature dependence of intra-t_{2g} excitations. Both panels depict $\sigma_1(\omega)$ over a range of 0.5 eV. The multipeak structure and the temperature-driven increase of spectral weight indicate the phonon-assisted character; see Fig. 7. Vertical dashed lines denote the bare electronic energies $E_{0,i}$ for the excited states Γ_8 at 948 meV, Γ_8 at 1107 meV, Γ_6 at 1164 meV, Γ_7 at 1723 meV, and Γ_8 at 1901 meV. The tiny feature at 1959 meV (633 nm) is an artifact from a HeNe laser used to calibrate the energy of the Fourier spectrometer.

following three distinct mechanisms. First, we observe very weak magnetic dipole transitions at $E_{0,i}$ [45,46], where $E_{0,i}$ denotes the zero-phonon electronic energy of band i. Second, the spectra show phonon-assisted excitations [65–67,74] at

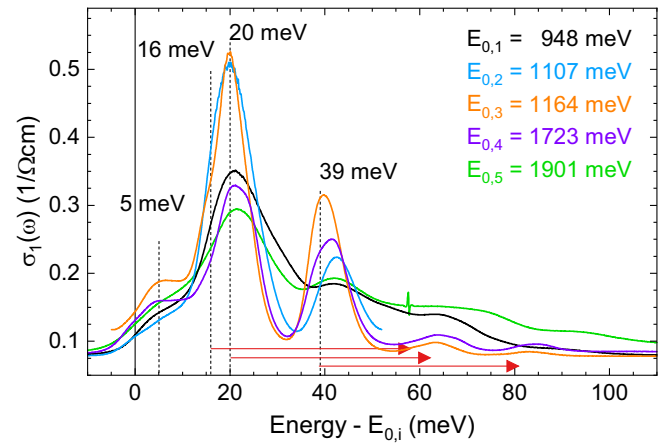

FIG. 7. Common peak structure of intra-t_{2g} excitations at 18 K. Data of the five absorption bands $i = 1$–5, see Fig. 6, are plotted as a function of $E - E_{0,i}$ to highlight the common energies of the symmetry-breaking phonons with $E_{\text{ph}} = 5$, 16, 20, and 39 meV (vertical dotted lines) that yield peaks at $E_{0,i} + E_{\text{ph}}$. Moreover, the plot shows the Franck-Condon phonon sidebands at $E_{0,i} + E_{\text{ph}} + E_{a_{1g}}$ with $E_{a_{1g}} \approx 44$ meV (arrows). Note that the excitations at $E_{0,2} = 1107$ meV and $E_{0,3} = 1164$ meV are close in energy (light blue and orange). To disentangle the corresponding features, the lines have been cut at 1159 meV, i.e., at 52 meV for $E_{0,2}$ and -5 meV for $E_{0,3}$. The corresponding plot for 6 K, below T_N, is given in Appendix A.

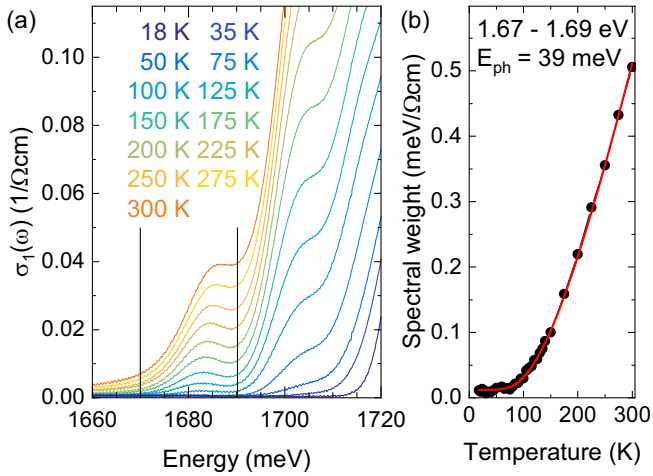

FIG. 8. Temperature dependence of $\sigma_1(\omega)$ around 1.7 eV. (a) Closeup of $\sigma_1(\omega)$ highlighting the thermal population of the phonon mode with $E_{\rm ph} = 39$ meV that yields an intra-t_{2g} excitation at $E_{0,4} - E_{\rm ph}$ for $E_{0,4} = 1723$ meV. For each temperature, an offset has been subtracted that was fixed outside the absorption band, as described for Fig. 9. Vertical black lines denote the energy range used for the integration to calculate the spectral weight. (b) Spectral weight of the phonon-assisted feature shown in (a) (symbols). Red line: fit using a Bose occupation factor with $E_{\rm ph} = 39$ meV.

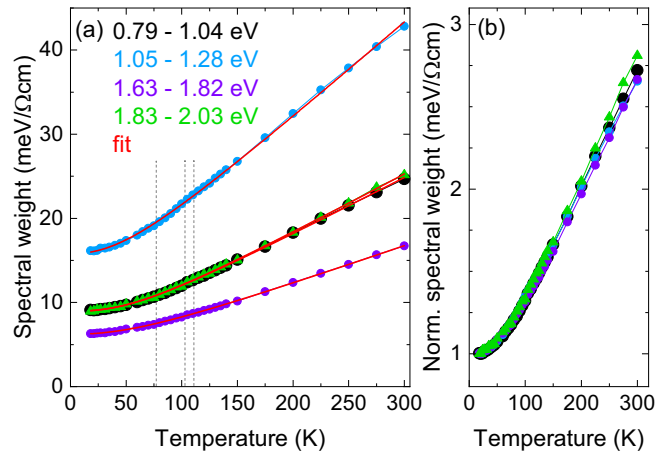

FIG. 9. Spectral weight as function of temperature. (a) Spectral weight (symbols) of the absorption bands with $E_{0,i}$ within the given integration ranges. Note that the data of the close lying bands with $E_{0,2}$ and $E_{0,3}$ have been integrated together (blue). The data for $E_{0,1} = 948$ meV (black) and $E_{0,5} = 1901$ meV (green) nearly fall on top of each other. In each case, the data show the characteristic temperature dependence of a phonon-assisted process, as shown by the fits (red lines) following Eq. (1) with four phonon modes at $E_{{\rm ph},k} = 5$, 16, 20, and 39 meV. For each temperature, a linear offset has been subtracted from $\sigma_1(\omega)$ that was fixed outside the absorption bands, i.e., at 755 and 1275 meV for $E_{0,1}$ to $E_{0,3}$ and at 1400 and 2040 meV for the upper two bands. Vertical dashed lines denote the structural transition temperatures. (b) The normalized spectral weights of the four integration ranges plotted in (a) collapse to a single curve, corroborating the common phonon energies.

$E_{0,i} + E_{\rm ph}$ with phonon energies $E_{\rm ph}$ of about 5, 16, 20, and 39 meV. These phonon energies agree with the temperature dependence of the spectral weight, as discussed below. Third, vibronic Franck-Condon-type absorption peaks with smaller spectral weight are observed at $E_{0,i} + E_{\rm ph} + E_{a_{1g}}$ with $E_{a_{1g}} \approx$ 44 meV.

The upper three energies $E_{\rm ph} = 16$, 20, and 39 meV of symmetry-breaking phonon modes can be motivated by considering a single regular $ReCl_6$ octahedron. It exhibits three odd-symmetry normal modes of vibration that break the inversion symmetry on the Re site and hence contribute to phonon-assisted absorption [45,46]. The additional mode at about 5 meV has to be identified as a lattice phonon mode. Far-infrared data reported a phonon at 5.3 meV that becomes infrared active by backfolding below 103 K [41]. Note that the symmetry-breaking modes do not have to be at the Γ point, i.e., they do not have to be infrared active.

The phonon-assisted scenario is supported by the temperature dependence of the spectral weight. At low temperature such as 18 K, the spectra show absorption peaks at $E_{0,i} + E_{\rm ph}$ in which a phonon and an electronic excitation are excited simultaneously. With increasing temperature, the spectral weight grows at $E_{0,i} - E_{\rm ph}$ due to phonon-annihilation contributions, giving rise to a temperature-induced increase of the spectral weight in particular on the low-energy side of each band. For, e.g., $E_{0,4} = 1723$ meV, the integrated spectral weight around $E_{0,4} - 39$ meV reveals a Bose factor that agrees with a phonon energy of 39 meV; see Fig. 8. A quantitative analysis of the total integrated spectral weight of the absorption bands will be discussed in Sec. III B 3.

In contrast to the peaks at $E_{0,i} \pm E_{\rm ph}$ that reflect the phonon-assisted excitation mechanism, the vibronic Franck-Condon type phonon sidebands at $E_{0,i} + E_{\rm ph} + E_{a_{1g}}$ arise due to the finite coupling of the electronic excitations to the lattice. A change of the orbital occupation upon electronic excitation implies that the lattice is not necessarily in its ground state anymore. This yields a vibronic character of the modes, i.e., mixed electronic and vibrational character, which drives phonon sidebands according to the Franck-Condon principle [67,74]. Considering the dominant contribution [45,46,75] for a t_{2g}^3 configuration in a regular octahedron, both the electronic ground state and the excited states exhibit cubic symmetry. Preserving cubic symmetry, the lattice may relax via a Raman-active breathing mode of the $ReCl_6$ octahedron with a_{1g} symmetry, changing the Re-Cl distance. In Raman scattering, the a_{1g} mode has been observed at 42 meV [44], in good agreement with our result. Note that our optical data probe the Raman mode in an electronically excited state, which may cause small shifts of the phonon energy. Moreover, the local character of the excitation averages over the dispersion across the Brillouin zone.

3. *Spectral weight*

Figure 9(a) shows the integrated spectral weight of the different absorption bands as a function of temperature. The plot depicts data for four different frequency ranges. Three of them correspond to the distinct absorption bands around $E_{0,1}$, $E_{0,4}$, and $E_{0,5}$, while the fourth data set shows the cumulative spectral weight of the two close-lying bands around $E_{0,2} =$ 1107 meV and $E_{0,3} = 1164$ meV; see Fig. 6. The integration ranges are given in Fig. 9. They were chosen sufficiently large

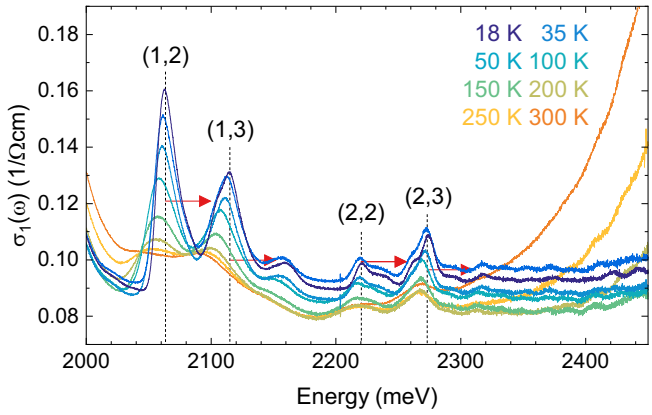

FIG. 10. Intersite d-d overtones in $\sigma_1(\omega)$ of K_2ReCl_6. Above the highest intra-t_{2g} excitation with $E_{0,5} = 1901$ meV, we observe peaks at energies that (nearly) coincide with the sum $E_{0,i} + E_{0,j}$ of two intra-t_{2g} excitation energies. Hence these features are not phonon assisted but directly infrared active, in agreement with their temperature dependence. Still also these higher-order excitations show a Franck-Condon sideband of the a_{1g} breathing mode with $E_{a_{1g}} = 44$ meV (arrows; cf. Fig. 7).

to capture the spectral weight of both phonon-creating and phonon-annihilating processes. For a phonon-assisted process, we can describe the spectral weight of a feature located between ω_1 and ω_2 as

$$SW = \int_{\omega_1}^{\omega_2} \sigma_1(\omega)\mathrm{d}\omega = \alpha + \sum_k \beta_k \coth\left(\frac{E_{\mathrm{ph},k}}{2k_\mathrm{B}T}\right), \qquad (1)$$

where $E_{\mathrm{ph},k}$ denotes the energies of the odd, symmetry-breaking phonon modes and α and β_k are fit parameters. Based on the four phonon energies $E_{\mathrm{ph},k} = 5$, 16, 20, and 39 meV discussed in connection with Fig. 7, we find good agreement between model and data; see Fig. 9. Furthermore, the curves of the normalized spectral weight nearly lie on top of each other, with the largest deviation of 5% observed at 300 K; see Fig. 9(b). This stresses the common energies $E_{\mathrm{ph},k}$ of the relevant phonon modes.

4. Overtones or double d-d excitations

According to RIXS, excitations to e_g orbitals require an energy larger than 3 eV, as discussed above. Having identified the five expected intra-t_{2g} excitations below 2 eV, the series of weak absorption features between 2.0 and 2.4 eV at first sight comes as a surprise; see Fig. 10. The key to their assignment as double d-d excitations, with the two excitations located on adjacent sites, is provided by the peak energies. At 18 K, the values of 2063, 2115, 2221, and 2273 meV agree within 2 to 8 meV with the sums $E_{0,i} + E_{0,j}$ for $(i, j) = (1, 2)$, (1,3), (2,2), and (2,3), respectively, revealing the combination and overtone character [76] (see also [45,77]). Note that the lowest peak of this series is expected at $2E_{0,1} = 1896$ meV, overlapping with the band of the Γ_8 term around $E_{0,5} = 1901$ meV. Like the single-site d-d excitations at $E_{0,i}$, these overtones show a Franck-Condon-type phonon sideband that corresponds to the 44 meV a_{1g} mode; see arrows in Figs. 10 and 7.

The overtone peak energies may deviate from the sum of two single-site excitation energies due to interaction effects. In K_2ReCl_6, these deviations do not exceed 8 meV or 0.4%, a remarkably small value that reflects once more the small coupling of these intra-t_{2g} excitations to the lattice. The excitation energies are mainly determined by J_H and ζ, and even on two adjacent, unconnected $ReCl_6$ octahedra the two excitations hardly interact. Similar overtones of intra-t_{2g} excitations have been reported in the 5d sister compound K_2OsCl_6 [23], in 3d orbitally ordered YVO_3 [68], and in the 4d Kitaev material α-$RuCl_3$. In the latter, both double and triple excitations were observed [70].

With the peak energies coinciding with the sums $E_{0,i} + E_{0,j}$ of the purely electronic zero-phonon energies, these features are directly infrared allowed, i.e., not phonon assisted. This is supported by their temperature dependence, which lacks the temperature-driven increase of spectral weight described by Eq. (1). Previously, the finite spectral weight of these overtones has been attributed to quadrupole-quadrupole interactions between neighboring Re sites [76]. In this scenario, the spectral weight is enhanced by some mixing between the overtones and the single-site excitation at $E_{0,5} = 1901$ meV and this mixing has been claimed to explain the decrease of intensity of the overtones with increasing separation from $E_{0,5}$. In the sister compound K_2OsCl_6, however, the intensity of the overtones is not correlated with the distance in energy to single-site d-d excitations [23]. Alternatively, we consider a hopping-based mechanism related to superexchange. Lorenzana and Sawatzky [78,79] described an analogous process for magnetic excitations. In an antiferromagnet, the exchange of two spins on adjacent sites is equivalent to a double spin flip. This excitation may generate an electric dipole moment if inversion symmetry is broken on the bond between the two sites. In other words, a finite dipole moment arises if the matrix elements for the corresponding electron transfer from site i to site j and *vice versa* are different. In the case of inversion symmetry, finite spectral weight of such a double spin flip can be caused by a phonon-assisted process, the so-called bi-magnon-plus-phonon absorption [78–80]. For double orbital excitations, both the direct process and the phonon-assisted version have been observed [68,70]. In the cubic phase above 111 K, K_2ReCl_6 shows inversion symmetry on the midpoint between two adjacent Re sites [43]. We attribute the larger spectral weight at low temperature to the breaking of inversion symmetry in the low-temperature phases. The finite spectral weight above 111 K tentatively can be attributed to fluctuations of octahedral rotations that according to Raman scattering [44] give rise to a low-energy continuum of excitations that extends up to about 12 meV, both at low temperature and at 300 K.

5. Differences in line shape and temperature dependence

We established that the five absorption bands around $E_{0,i}$ share a common temperature dependence of the spectral weight, see Fig. 9, and a common peak structure with $\sigma_1(\omega)$ at low temperature peaking at $E_{0,i} + E_\mathrm{ph}$ and $E_{0,i} + E_\mathrm{ph} + E_{a_{1g}}$ with common phonon energies; see Fig. 7. However, a closer look at the line shape reveals two different types of behavior

that distinguishes the absorption bands $i = 1$ and 5 from those with $i = 2$–4. The differences are apparent in the width of the individual peaks, the spectral weight of the Franck-Condon sidebands at $E_{0,i} + E_{\rm ph} + E_{a_{1g}}$, and the precise temperature dependence of the peak energies and peak heights. We address these points in the following.

The width of the individual peaks is larger for $i = 1$ and 5 than for $i = 2$–4. Below 111 K we have to consider deviations from cubic symmetry. Figure 5(d) shows that, e.g., a tetragonal crystal field yields clear splittings for $i = 1$ and 5. In contrast, deviations from cubic symmetry cannot split the Kramers doublets for $i = 3$ or 4. For the quartet $i = 2$ we calculate a tiny splitting for finite ζ. This band is related to the ^2E multiplet for $\zeta = 0$, which does not split in a tetragonal crystal field. The noncubic symmetry hence is a plausible explanation for the larger width for $i = 1$ and 5. Note that our optical data do not resolve a peak splitting; we only find a larger width. Therefore, the noncubic crystal-field splitting has to be small. Similarly, Raman data of the phonon modes at low temperature could not resolve a peak splitting [44]. Instead, the Raman data show a low-energy continuum that points towards rotary fluctuations of the orientation of the $ReCl_6$ octahedra. This scenario agrees with an enhanced peak width in $\sigma_1(\omega)$ for $i = 1$ and 5.

The spectral weight of the Franck-Condon-type phonon sidebands at $E_{0,i} + E_{\rm ph} + E_{a_{1g}}$ is larger for $i = 1$ and 5; see Fig. 7. This also affects the line shape at elevated temperatures. For $i = 3$ and 4, the spectral weight with increasing temperature mainly rises on the low-energy side (see above). We expect the same behavior for $i = 2$ but this is covered by the overlap with $i = 3$. In contrast, the spectral weight for $i = 1$ and 5 is also enhanced on the high-energy side, in the range of the Franck-Condon sidebands. These even-symmetry Franck-Condon-type phonon sidebands should not be confused with the odd-symmetry mode that breaks the inversion symmetry in the phonon-assisted process; see Sec. III B 2. If an electronic excitation yields a sizable change of both the orbital occupation and the corresponding charge distribution, the phonon sidebands dominate the spectral weight and determine the line shape in the optical data [67]. Moreover, the existence of several phonon modes, all of them showing dispersion, typically washes out the detailed sideband structure in crystalline samples, giving rise to a broad featureless peak in $\sigma_1(\omega)$ [67,68]. The broader line shape of $i = 1$ and 5 in combination with the larger spectral weight of the Franck-Condon sidebands thus indicates that these excitations correspond to a stronger change of the orbital occupation. In contrast, a nearly pure spin flip with little change of the orbital occupation exhibits a very small coupling to the lattice and the spectral weight in the Franck-Condon sidebands is suppressed. In $5d$ K_2ReCl_6 with well-separated $ReCl_6$ octahedra, the very narrow peaks for $i = 2$–4 underline the marginal coupling to the lattice. The data for $i = 2$–4 qualify as a textbook example of on-site d-d excitations with a predominant spin-flip character.

Concerning the temperature dependence, Streltsov and Khomskii [4] speculated that one of the phase transitions of K_2ReCl_6 could be related to a spin-orbit-induced Jahn-Teller splitting. In the optical data, temperature-related effects are rather subtle above T_N. For instance, Fig. 6 does not show pronounced qualitative changes of $\sigma_1(\omega)$ throughout the entire temperature range and the spectral weight shows a smooth evolution with temperature; see Fig. 9(a). The structural changes hence hardly affect the matrix elements of the phonon-assisted processes. The refractive index $n(\omega)$ in the studied frequency range is governed by the spectral weight of the higher-lying electronic interband excitations. The temperature dependence of $n(\omega)$ is exemplified for two frequencies in Fig. 11(a). The data suggest

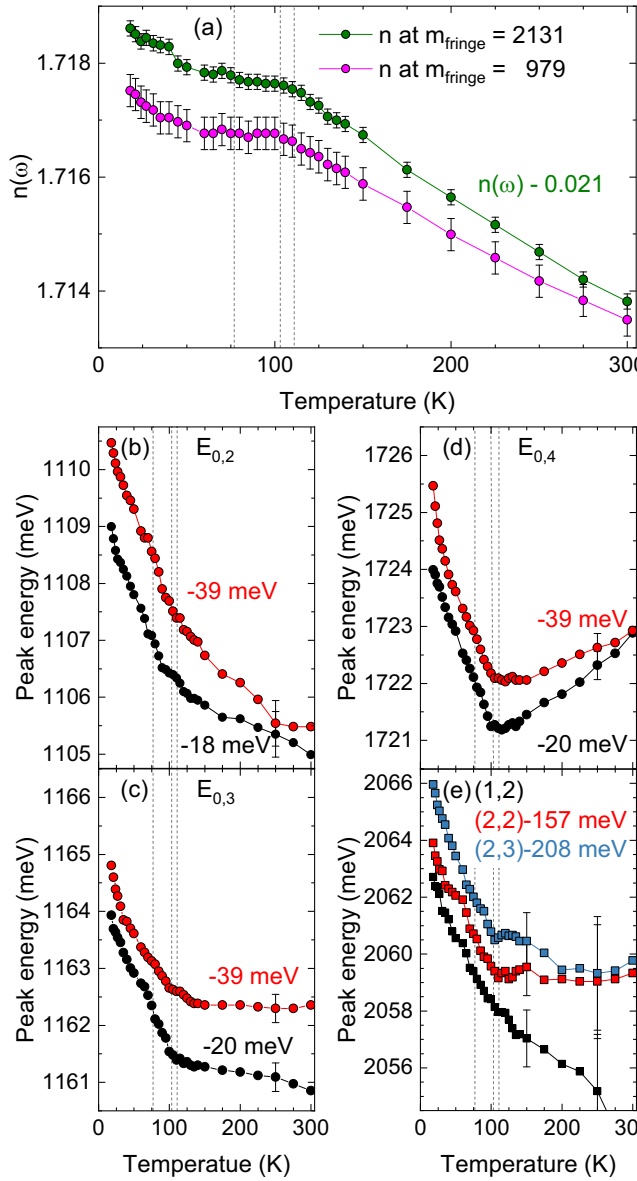

FIG. 11. Temperature dependence of the refractive index $n(\omega)$ and of the intra-t_{2g} energies. (a) $n(\omega)$ extracted from the energies of two Fabry-Pérot interference fringes at around 0.75 and 1.6 eV with order $m_{\rm fringe} = 979$ and 2131, respectively. The curve of n of the latter has been shifted down by 0.021 to facilitate comparison. (b)–(d) Peak energies $E_{0,i} + E_{\rm ph}$ for $i = 2$, 3, and 4 and two different phonon modes. Symbols have been shifted as indicated in the panels. (e) Peak energies of the overtones at $E_{0,i} + E_{0,j}$ for $(i, j) = (1, 2)$, (2,2), and (2,3). In all panels, vertical dashed lines indicate the temperatures of the structural phase transitions, i.e., 77, 103, and 111 K.

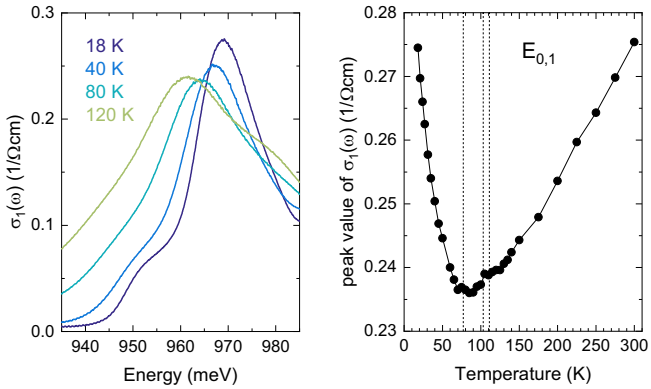

FIG. 12. Value of $\sigma_1(\omega)$ at the peak maximum for the band around $E_{0,1} = 948$ meV. Left: zoom in on $\sigma_1(\omega)$ around the peak at $E_{0,1} + E_{\rm ph}$. A background has been subtracted, as discussed for Fig. 9. Right: the increase of the peak maximum at high temperature reflects the increase of the spectral weight; see Fig. 9. In view of the spectral weight, the opposite behavior of the peak maximum below 77 K indicates a change of the linewidth. Vertical dashed lines mark the temperatures of the structural phase transitions.

small changes of the slope $\partial n/\partial T$ but do not show strong effects.

The clearest signatures of deviations from cubic symmetry below 111 K are detected in the peak energies. We focus on the bands with $i = 2$ to 4 since these allow us to track the individual peaks up to 300 K. In Figs. 11(b)–11(d) we compare the peak energies $E_{0,i} + E_{\rm ph}$, considering two different phonon energies $E_{\rm ph}$. In all three panels, the energies continuously harden by 2.5 to 3 meV from the highest phase transition temperature 111 K down to low temperature. Note that the shift amounts to about 0.2% of the energy, a tiny effect. In each panel, both curves show a very similar shift, even though the phonon energies differ by about a factor of 2. Moreover, the phonon energies in general are expected to exhibit a larger softening above 100 K due to thermal expansion. We thus conclude that the observed behavior below 111 K predominantly reflects the temperature dependence of the electronic energies $E_{0,i}$. This is corroborated by the peak energies of the double excitations at $E_{0,1} + E_{0,2}$, $2E_{0,2}$, and $E_{0,2} + E_{0,3}$; see Fig. 11(e). The temperature-induced shift of the overtones below 111 K amounts to about 5 meV, i.e., it is twice as large as the shift of the single modes. This common increase of the excitation energies $E_{0,i}$ strongly suggests a lowering of the ground state energy by about 3 meV from 111 K to low temperature.

The peak energies of the bands with $i = 1$ and 5 show larger shifts as a function of temperature. For these bands, however, the larger coupling to the lattice implies a larger role of phonons for the line shape, impeding the determination of the temperature dependence of the pure electronic energies. Instead, we address the peak height, i.e., the value of $\sigma_1(\omega)$ at the peak. For $i = 2$–4, the peak height increases with increasing temperature, in agreement with the increase of the spectral weight; see Fig. 6. In contrast, the peak height for $i = 1$ and 5 decreases from low temperature up to the phase transition temperature 77 K; see Figs. 6 and 12. This points towards a change of the linewidth.

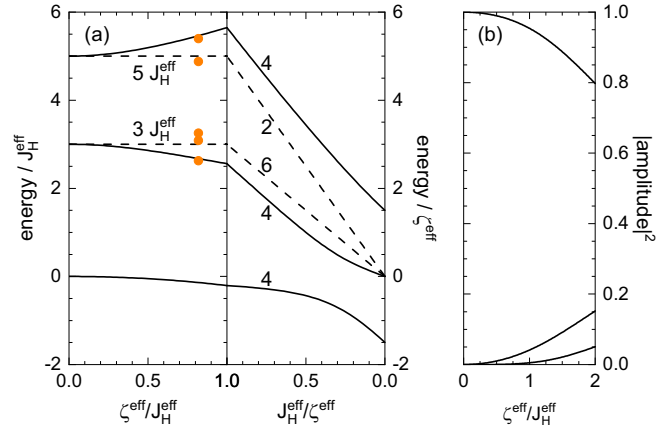

FIG. 13. Absolute energies of the t_{2g}^3 states and ground state wave function for $10Dq = \infty$. (a) To obtain excitation energies, the ground state energy E_0 (lowest line) has to be subtracted; see Eq. (2). For $\zeta^{\rm eff} = 0$, the ground state is at zero while the excited states are at $3J_{\rm H}^{\rm eff}$ and $5J_{\rm H}^{\rm eff}$. Spin-orbit coupling mixes some of the states (solid lines) while other states remain unaffected (dashed), giving rise to, in total, four excitation energies. The best agreement with experiment (symbols) is obtained for $\zeta^{\rm eff}/J_{\rm H}^{\rm eff} = 0.82$ with $J_{\rm H}^{\rm eff} = 343$ meV. Numbers in the right panel denote the number of states. Note the change in scale of the horizontal axis from $\zeta^{\rm eff}/J_{\rm H}^{\rm eff}$ in the left panel to $J_{\rm H}^{\rm eff}/\zeta^{\rm eff}$ in the right panel. This is accompanied by a change of the energy scale, which is given in units of $J_{\rm H}^{\rm eff}$ on the left and $\zeta^{\rm eff}$ on the right. (b) Squared amplitudes of the three contributions to the ground state wave function corresponding to the solid lines in (a).

C. Determination of electronic parameters

Based on the results from RIXS and optical spectroscopy, we turn our focus to the quantitative analysis of the multiplet energies and the effect of spin-orbit coupling on the electronic ground state. Considering a single site in cubic symmetry, the electronic energy levels are determined by the cubic crystal-field splitting $10Dq$, the interelectronic Coulomb interaction captured by the Slater integrals F^2 and F^4, and spin-orbit coupling ζ. The Slater integrals can also be expressed in terms of Hund's coupling $J_{\rm H} = 1/14(F^2 + F^4)$ within the entire $5d$ shell [72]. Using QUANTY [47,48], we calculate the effect of these parameters on the $5d^3$ energy levels; see Fig. 5. As mentioned in Sec. III B 1, $J_{\rm H}$ splits the 20 t_{2g}^3 states into the cubic multiplets $^4A_2$, ^2E, $^2T_1$, and $^2T_2$, while ζ gives rise to a further lifting of degeneracies, yielding the terms Γ_8 (four times), Γ_6, and Γ_7.

1. t_{2g}-only limit for $10Dq = \infty$

We start the quantitative analysis within the t_{2g}-only Kanamori picture for $10Dq = \infty$, neglecting any admixture of e_g states. This approximation is often chosen in theory, for instance in the discussion of the possible role of the Jahn-Teller effect [4]. The matrix elements describing the mixing of the cubic t_{2g}^3 multiplets due to spin-orbit coupling have been reported in, e.g., Refs. [71,81], reducing the problem to two 5×5 matrices that we address in Appendix B. The t_{2g}-only picture shows four excitation energies. As discussed above, the degeneracy between the ^2E and $^2T_1$ states is not lifted for $10Dq = \infty$ and $\zeta = 0$. Figure 13 plots the absolute energies,

covering both limits, LS coupling for $\zeta^{\rm eff}/J_{\rm H}^{\rm eff} \to 0$ and jj coupling for $\zeta^{\rm eff}/J_{\rm H}^{\rm eff} \to \infty$. Three of the absolute energies [solid lines in Fig. 13(a)] are given by

$$\frac{E_n}{J_{\rm H}^{\rm eff}} = \frac{3+5}{3} - \frac{\tau}{3} \times \cos\left[\frac{1}{3}\arccos\left(\frac{4(284-3\tau^2)}{\tau^3}\right) + 2\pi\frac{n}{3}\right], \quad (2)$$

with $n = 0$, 1, and 2 and

$$\tau = 2\sqrt{3^2+5^2-3\times 5+3\left(\frac{3}{2}\frac{\zeta^{\rm eff}}{J_{\rm H}^{\rm eff}}\right)^2}. \quad (3)$$

The expression of τ reflects the energies in the limits $\zeta^{\rm eff}/J_{\rm H}^{\rm eff} \to 0$ and $\zeta^{\rm eff}/J_{\rm H}^{\rm eff} \to \infty$. Two further absolute energies equal $3J_{\rm H}^{\rm eff}$ and $5J_{\rm H}^{\rm eff}$ (dashed lines), unaffected by spin-orbit coupling. Note that $E_1 > E_2$ and that the excitation energies are obtained by subtracting the ground state energy E_0. The states at $3J_{\rm H}^{\rm eff}$ and $5J_{\rm H}^{\rm eff}$ (dashed lines), not mixing with the $S = 3/2$ $^4A_2$ multiplet, correspond to the absorption bands with narrow features, $i = 2$–4, while the states with $n = 1$ and 2 (solid lines) can be identified with the broader bands for $i = 1$ and 5 in the optical conductivity.

The best description of the five experimental intra-t_{2g} energies $E_{0,i}$ is achieved for $\zeta^{\rm eff}/J_{\rm H}^{\rm eff} \approx 0.8$ with $J_{\rm H}^{\rm eff} = 343$ meV; see symbols in Fig. 13(a). This ratio falls within the range of intermediate coupling. It is about a factor of 2 too small to cause a pronounced Jahn-Teller effect; see Fig. 1.

The description of the experimental peak energies is reasonable but not excellent, as illustrated in Fig. 13(a) and by the following example. The energy scale $J_{\rm H}^{\rm eff} = 343$ meV is given by $5J_{\rm H}^{\rm eff} \approx E_{0,4} = 1723$ meV. This predicts a splitting of about 0.7 eV between the states at roughly $5J_{\rm H}^{\rm eff}$ and $3J_{\rm H}^{\rm eff}$, which is substantially larger than the corresponding experimental values $E_{0,4} - E_{0,3} = (1723–1164)$ meV $= 559$ meV and $E_{0,4} - E_{0,2} = (1723–1107)$ meV $= 616$ meV. To achieve a better description of the experimental data, the effect of higher lying states has to be taken into account.

2. *Parameters for the entire d shell*

Going beyond the t_{2g}-only model, we consider the entire $5d$ shell and fit the five intra-t_{2g} energies $E_{0,i}$ taken from $\sigma_1(\omega)$ and the energy of the RIXS peak at 3.3 eV. Using the widely employed value $F^4/F^2 = 36/55$ (equivalent to Racah $C/B = 4$), the best agreement is found for $10Dq = 3.25$ eV, $\zeta = 290$ meV, and $F^2 = 3.93$ eV. This yields $J_{\rm H} = 464$ meV and $\zeta/J_{\rm H} = 0.625$, i.e., intermediate coupling. Note that we can also obtain $J_{\rm H}^{\rm eff} = (3/49)F^2 + (20/441)F^4 \approx 0.36$ eV from these parameters, in good agreement with the analysis described above. The fit yields $E_{0,i}^{\rm fit} = 945$, 1064, 1132, 1773, and 1901 meV for the intra-t_{2g} excitations and 3.31 eV for the t_{2g}-to-e_g transition; see symbols in Fig. 5.

While $E_{0,1}$ and $E_{0,5}$ are described within 3 meV, the fit underestimates $E_{0,2}$ and $E_{0,3}$ but overestimates $E_{0,4}$ by about 3–4%. This corresponds to the difficulty discussed for the t_{2g}-only model concerning the comparably small experimental splitting between the states attributed to about $5J_{\rm H}^{\rm eff}$ and $3J_{\rm H}^{\rm eff}$. A decrease of $10Dq$ indeed lowers $E_{0,4}$ more strongly than $E_{0,3}$ and $E_{0,2}$, i.e., the admixture of e_g states reduces the splitting but does not yet yield perfect agreement for the appropriate value of $10Dq$ that is fixed by the RIXS data. The description of the experimental peak energies can be further improved by, e.g., considering the ratio F^4/F^2 as a fit parameter or by allowing for charge-transfer processes to the ligands, which adds further fit parameters. We refrain from following this path since it has no profound impact on the result for $\zeta/J_{\rm H}$. Overall, our result is supported by a comparison of the experimental RIXS data and a spectrum calculated with QUANTY; see Fig. 14. For the parameters stated above, we find good agreement. Considering the experimental resolution of 295 meV, energy and line shape of the on-site Re d-d excitations are well reproduced.

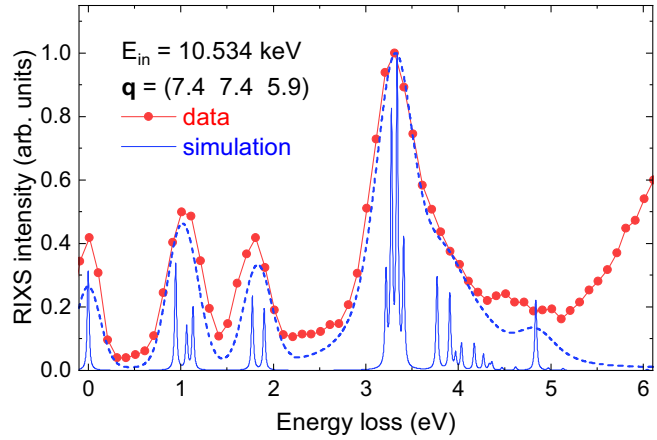

FIG. 14. Comparison of experimental and simulated RIXS data. Red symbols: RIXS result for $E_{\rm in} = 10.534$ keV. Solid blue line: RIXS spectrum simulated using QUANTY for $10Dq = 3.25$ eV, $\zeta = 290$ meV, and $J_{\rm H} = 464$ meV for Voigt oscillators with 10 meV width. Dashed blue line: same data using a Voigt line shape where the width of the Gaussian part is set to the experimental resolution of 295 meV, while the width of the Lorentzian contribution is 10 meV for the intra-t_{2g} excitations and 300 meV for excitations to e_g states above 3 eV. The total intensity is scaled to agree with the experimental data at the maximum. Note that the charge-transfer excitations at higher energies are not included in the simulation.

3. *Effect of spin-orbit coupling on the ground state*

Beyond spin-orbit coupling or $\zeta/J_{\rm H}$, the effective magnetic moment of the $5d^3$ configuration is affected by the cubic crystal-field splitting, by deviations from cubic symmetry, and by exchange interactions [82]. The latter can be expected to be particularly relevant in K_2ReCl_6 due to the strong exchange frustration of the fcc lattice [10]. However, exchange interactions will be rather small due to the large Re-Re distance. The admixture of e_g states for finite $10Dq$ reduces the effective moment, which is $2\sqrt{S(S+1)}\mu_B$ for $\zeta = 0$, approximately by the factor $1 - (4/3)\zeta/10Dq$ [66], which in K_2ReCl_6 equals 0.88 according to our results. In the following, we focus on the effect of spin-orbit coupling.

For $\zeta = 0$, the ground state is given by the $S = 3/2$ $^4A_2$ multiplet with quenched orbital moment. In this state, each t_{2g} orbital is occupied by one electron. It is not split by noncubic distortions. Finite spin-orbit coupling causes an admixture of higher-lying states, in particular of the $^2T_2$ multiplet, which is

the one highest in energy; see Fig. 5. This adds orbital moment and drives the Jahn-Teller activity. For an intuitive picture, we employ the t_{2g}-only Kanamori model.

The five energies have been described in Sec. III C 1 and the eigenstates and expectation values of L_z are discussed in Appendix B. The ground state exhibits contributions from all four cubic t_{2g}^3 multiplets but can be written as a superposition of three terms and their weights or squared amplitudes are depicted in Fig. 13(b). In leading order, the weights of the admixed states increase like $(1/25)\,(\zeta^{\rm eff}/J_{\rm H}^{\rm eff})^2$ and $(1/180)\,(\zeta^{\rm eff}/J_{\rm H}^{\rm eff})^4$. For $\zeta^{\rm eff}/J_{\rm H}^{\rm eff} = 0.8$, as we find for K_2ReCl_6, more than 97% of the weight is still contributed by the $^4A_2$ multiplet. If we include the e_g states and consider the parameters obtained from the fit discussed above, we still find 93% of the ground state weight to be carried by the $S = 3/2$ multiplet.

We focus on the state showing $S_z = 3/2$ for $\zeta = 0$. For finite ζ, we find for the expectation values of L_z and $J_z = S_z - L_z$ in leading order

$$\langle L_z\rangle \approx \tfrac{1}{25}\left(\zeta^{\rm eff}/J_{\rm H}^{\rm eff}\right)^2, \tag{4}$$

$$\langle J_z\rangle \approx \tfrac{3}{2} - \tfrac{2}{15^2}\left(\zeta^{\rm eff}/J_{\rm H}^{\rm eff}\right)^4. \tag{5}$$

The finite expectation value of L_z predominantly arises from the admixture of the $^2T_2$ multiplet into the ground state and this multiplet is Jahn-Teller active. However, for $\zeta^{\rm eff}/J_{\rm H}^{\rm eff} = 0.8$, we find $\langle L_z\rangle \approx 0.027$, which is a small value. In LS coupling, S_z and L_z sum up to 3/2. The deviations from this value describe the gradual transition to jj coupling. This deviation increases slowly in fourth order in $\zeta^{\rm eff}/J_{\rm H}^{\rm eff}$. For $\zeta^{\rm eff}/J_{\rm H}^{\rm eff} = 0.8$, we find $\langle J_z\rangle \approx 1.497$, very close to 3/2. This agrees with the result of a Curie-Weiss fit of the magnetic susceptibility that finds an effective magnetic moment very close to the value expected for a $S = 3/2$ compound [43]. Note, however, that our analysis is restricted to the Kanamori model. Inspection of the energies in Fig. 13 shows that a more pronounced change of the ground state character occurs for $J_{\rm H}^{\rm eff}/\zeta^{\rm eff} \approx 0.5$ in the right panel, which is equivalent to $\zeta^{\rm eff}/J_{\rm H}^{\rm eff} \approx 2$. Note that this agrees with the result of Streltsov and Khomskii [4] for the range where a strong Jahn-Teller effect sets in; see Fig. 1(b).

IV. CONCLUSION

For the half-filled t_{2g} shell of K_2ReCl_6, the effect of spin-orbit coupling is more subtle than for $5d$ transition-metal compounds with other electron configurations. We studied the electronic excitations with RIXS and optical spectroscopy. In the optical conductivity $\sigma_1(\omega)$, the narrow, phonon-assisted intra-t_{2g} features qualify as textbook examples of on-site d-d excitations. We find that spin-orbit coupling is sizable, $\zeta = 0.29$ eV. In the often employed t_{2g}-only Kanamori model, spin-orbit coupling causes an admixture of mainly $^2T_2$ character into the ground state. The corresponding orbital moment opens the door for Jahn-Teller activity, but the admixture in leading order increases only quadratically, $\propto(\zeta/J_{\rm H})^2$, and $\zeta/J_{\rm H} \approx 0.6$ is too small to drive a sizable Jahn-Teller distortion. The $S = 3/2$ multiplet carries about 97% of the ground state weight in the Kanamori picture. Additionally taking into account the e_g states, we find that 93% of the weight stems from the $S = 3/2$ multiplet. However, spin-orbit coupling may still leave its fingerprints, for instance causing anisotropy gaps in the magnon dispersion as discussed for $5d^3$ osmates [36–39] or the pronounced magnetoelastic effects reported for K_2ReCl_6 [43]. Concerning structural changes, we could not resolve a noncubic splitting of the on-site d-d excitations above T_N; the noncubic crystal field hence has to be small. However, we find subtle differences in the line shape comparing the excitations to quartets that are expected to split with the Kramers doublets that are insensitive to a noncubic crystal field. The former show broader features and a stronger coupling to the lattice. Moreover, our careful analysis of the optical data provides evidence for a lowering of the ground state energy by about 3 meV from the highest phase transition temperature 111 K down to low temperature. The question of whether the Jahn-Teller effect plays any role in the structural phase transitions will have to be addressed by thorough structural studies. Still, our results firmly establish that such effects can only be small.

ACKNOWLEDGMENTS

We gratefully acknowledge fruitful discussions with J. van den Brink. We thank the European Synchrotron Radiation Facility for providing beam time at ID20 and technical support. Furthermore, we acknowledge funding from the Deutsche Forschungsgemeinschaft (DFG, German Research Foundation) through Project No. 277146847–CRC 1238 (Projects No. A02, No. B02, and No. B03). M.H. acknowledges partial funding by the Knut and Alice Wallenberg Foundation as part of the Wallenberg Academy Fellows project.

APPENDIX A: LINE SHAPE BELOW T_N

In a state with long-range antiferromagnetic order, the spin-forbidden on-site d-d excitations may show magnon sidebands. The joint excitation carries $\Delta S = 0$ and does not need to involve the excitation of a phonon, as discussed for, e.g., compounds with $3d^3$ Cr^{3+} ions [69]. However, magnon sidebands have also been reported for phonon-assisted features, both in Cr compounds and in K_2ReCl_6 [69,76,83,84]. Below $T_N = 12$ K, we observe a splitting of some of the absorption peaks and this splitting is most pronounced for the band with $E_{0,4} = 1723$ meV; see bottom panel of Fig. 15. A comparison of the line shape of the five absorption bands as a function of $E - E_{0,i}$ at 6 K is given in the top panel of Fig. 15.

APPENDIX B: EIGENSTATES AND L_z IN KANAMORI MODEL

We stick to the t_{2g}-only Kanamori model for analytic expressions of the energies and wave functions of the t_{2g}^3 states. For $\zeta = 0$, Coulomb interactions yield the cubic multiplets $^4A_2$, ^2E, $^2T_1$, and $^2T_2$. The corresponding eigenstates are given below in Sec. B 3, where we use $^2E(u)$ and $^2E(v)$ and, e.g., $^2T_1(u)$, $^2T_1(v)$, and $^2T_1(w)$ to distinguish states with orbital degeneracy. The multiplets are mixed by spin-orbit coupling

$$H_{ls} = \zeta\,\vec{l}\vec{s}, \tag{B1}$$

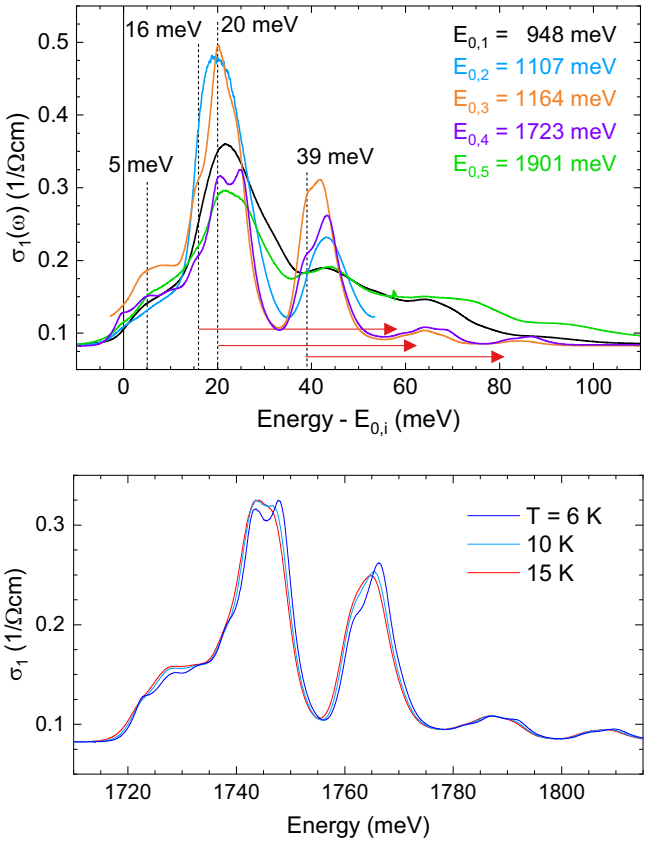

FIG. 15. Peak structure of intra-t_{2g} excitations below T_N. Top: comparison of the line shape of the five absorption bands at 6 K. Bottom: temperature dependence of the band at $E_{0,4} = 1723$ meV.

where $\vec{l}$ and $\vec{s}$ denote the orbital and spin angular momenta of an individual electron. The problem decouples into two 5×5 matrices [71]. Using $x = \zeta^{\text{eff}}/J_{\text{H}}^{\text{eff}}$, the matrix for the basis states ${}^4A_2(\mp\frac{1}{2})$, ${}^2E(v, \mp\frac{1}{2})$, ${}^2T_2(v, \mp\frac{1}{2})$, ${}^2T_1(w, \pm\frac{1}{2})$, and ${}^2T_2(w, \pm\frac{1}{2})$ (see Sec. B 3) is given by

$$H_1 = J_{\text{H}}^{\text{eff}} \begin{pmatrix} 0 & 0 & 2x/\sqrt{6} & 0 & x/\sqrt{3} \\ 0 & 3 & -x/\sqrt{3} & 0 & -x/\sqrt{6} \\ 2x/\sqrt{6} & -x/\sqrt{3} & 5 & -x/\sqrt{2} & 0 \\ 0 & 0 & -x/\sqrt{2} & 3 & -x/2 \\ x/\sqrt{3} & -x/\sqrt{6} & 0 & -x/2 & 5 \end{pmatrix}, \tag{B2}$$

while for the basis states ${}^4A_2(\mp\frac{3}{2})$, ${}^2E(u, \pm\frac{1}{2})$, ${}^2T_1(u, \pm\frac{1}{2})$, ${}^2T_1(v, \mp\frac{1}{2})$, and ${}^2T_2(u, \mp\frac{1}{2})$ it becomes

$$H_2 = J_{\text{H}}^{\text{eff}} \begin{pmatrix} 0 & 0 & 0 & 0 & x \\ 0 & 3 & 0 & 0 & -x/\sqrt{2} \\ 0 & 0 & 3 & 0 & x/\sqrt{2} \\ 0 & 0 & 0 & 3 & x/2 \\ x & -x/\sqrt{2} & x/\sqrt{2} & x/2 & 5 \end{pmatrix}. \tag{B3}$$

We will discuss H_1 first. The analysis of H_2 is very similar.

1. Solutions of H_1 for finite spin-orbit coupling

Among the five eigenstates in the subspace of H_1, there are two states with constant energies, $E(\Gamma_8') = 3J_{\text{H}}^{\text{eff}}$ and $E(\Gamma_7) = 5J_{\text{H}}^{\text{eff}}$; see Fig. 13. These states are given by

$$\begin{aligned} |\Gamma_8'\rangle_1 &= -\sqrt{\frac{3}{5}}\left|{}^2E\left(v, \mp\frac{1}{2}\right)\right\rangle + \sqrt{\frac{2}{5}}\left|{}^2T_1\left(w, \pm\frac{1}{2}\right)\right\rangle, \\ |\Gamma_7\rangle &= -\sqrt{\frac{1}{3}}\left|{}^2T_2\left(v, \mp\frac{1}{2}\right)\right\rangle + \sqrt{\frac{2}{3}}\left|{}^2T_2\left(w, \pm\frac{1}{2}\right)\right\rangle. \end{aligned} \tag{B4}$$

Additionally, we consider the states

$$\begin{aligned} |a\rangle &= \left|{}^4A_2\left(\mp\frac{1}{2}\right)\right\rangle, \\ |b\rangle &= \sqrt{\frac{2}{5}}\left|{}^2E\left(v, \mp\frac{1}{2}\right)\right\rangle + \sqrt{\frac{3}{5}}\left|{}^2T_1\left(w, \pm\frac{1}{2}\right)\right\rangle, \\ |c\rangle &= \sqrt{\frac{2}{3}}\left|{}^2T_2\left(v, \mp\frac{1}{2}\right)\right\rangle + \sqrt{\frac{1}{3}}\left|{}^2T_2\left(w, \pm\frac{1}{2}\right)\right\rangle \end{aligned} \tag{B5}$$

based on which the problem further reduces to the following Hamiltonian matrix that describes the mixing of Γ_8 states:

$$H' = J_{\text{H}}^{\text{eff}} \begin{pmatrix} 0 & 0 & x \\ 0 & 3 & -\sqrt{5}x/2 \\ x & -\sqrt{5}x/2 & 5 \end{pmatrix}. \tag{B6}$$

With $n = 0$, 1, and 2 and the eigenvalues E_n given in Eq. (2), the three eigenstates of H' are described by

$$|n\rangle = \frac{1}{\alpha_n}\left(1, \frac{\sqrt{5}}{2}\frac{E_n}{3J_{\text{H}}^{\text{eff}} - E_n}, \frac{E_n}{\zeta^{\text{eff}}}\right), \tag{B7}$$

$$\alpha_n = \sqrt{1 + \frac{5}{4}\left(\frac{E_n}{3J_{\text{H}}^{\text{eff}} - E_n}\right)^2 + \left(\frac{E_n}{\zeta^{\text{eff}}}\right)^2}. \tag{B8}$$

The ground state, or more precisely one doublet of the Γ_8 ground state quartet, explicitly reads

$$|0\rangle_{\mp\frac{1}{2}} = \frac{1}{\alpha_0}\left|{}^4A_2\left(\mp\frac{1}{2}\right)\right\rangle + \frac{\sqrt{5}}{2\alpha_0}\frac{E_0}{3J_{\text{H}}^{\text{eff}} - E_0}|b\rangle + \frac{E_0}{\alpha_0\,\zeta^{\text{eff}}}|c\rangle. \tag{B9}$$

For $\zeta^{\text{eff}}/J_{\text{H}}^{\text{eff}} = 0.8$, appropriate for K_2ReCl_6, the three amplitudes are 0.9858, −0.0462, and −0.1617. The expectation value for L_z in $|0\rangle_{\mp\frac{1}{2}}$ amounts to

$$\langle L_z\rangle_{\mp\frac{1}{2}} = \frac{3}{5}\left(\frac{\sqrt{5}E_0}{2\alpha_0\left(3J_{\text{H}}^{\text{eff}} - E_0\right)}\right)^2 + \frac{1}{3}\left(\frac{E_0}{\alpha_0\zeta^{\text{eff}}}\right)^2. \tag{B10}$$

In leading order, the ground state energy E_0 for small $\zeta^{\text{eff}}/J_{\text{H}}^{\text{eff}}$ is given by

$$E_0 = -\frac{1}{5}\frac{(\zeta^{\text{eff}})^2}{J_{\text{H}}^{\text{eff}}}, \tag{B11}$$

which gives the approximation

$$|0\rangle_{\mp\frac{1}{2}} \approx \frac{1}{\beta_0}\Big[\Big|{}^4A_2\Big(\mp\frac{1}{2}\Big)\Big\rangle - \frac{\zeta^{\rm eff}}{5J_{\rm H}^{\rm eff}}\Big(\sqrt{\frac{2}{3}}\Big|{}^2T_2\Big(v,\mp\frac{1}{2}\Big)\Big\rangle + \sqrt{\frac{1}{3}}\Big|{}^2T_2\Big(w,\pm\frac{1}{2}\Big)\Big\rangle\Big)\Big], \tag{B12}$$

with $\beta_0 = \sqrt{1+(\zeta^{\rm eff}/5J_{\rm H}^{\rm eff})^2}$. The leading order contribution to L_z in $|0\rangle_{\mp\frac{1}{2}}$ hence reads

$$\langle L_z\rangle_{\mp\frac{1}{2}} \approx \frac{1}{75}\Big(\frac{\zeta^{\rm eff}}{J_{\rm H}^{\rm eff}}\Big)^2. \tag{B13}$$

2. Solutions of H_2 for finite spin-orbit coupling

Also in the subspace of H_2 there are two states with constant energies $E(\Gamma_6) = E(\Gamma_8') = 3J_{\rm H}^{\rm eff}$; see Fig. 13. These read

$$\begin{aligned}|\Gamma_6\rangle &= \sqrt{\frac{1}{3}}\Big|{}^2T_1\Big(u,\pm\frac{1}{2}\Big)\Big\rangle - \sqrt{\frac{2}{3}}\Big|{}^2T_1\Big(v,\mp\frac{1}{2}\Big)\Big\rangle,\\ |\Gamma_8'\rangle_2 &= \sqrt{\frac{3}{5}}\Big|{}^2E\Big(u,\pm\frac{1}{2}\Big)\Big\rangle + \sqrt{\frac{4}{15}}\Big|{}^2T_1\Big(u,\pm\frac{1}{2}\Big)\Big\rangle + \sqrt{\frac{2}{15}}\Big|{}^2T_1\Big(v,\mp\frac{1}{2}\Big)\Big\rangle.\end{aligned} \tag{B14}$$

Choosing the remaining states as

$$\begin{aligned}|a'\rangle &= \Big|{}^4A_2\Big(\mp\frac{3}{2}\Big)\Big\rangle,\\ |b'\rangle &= \sqrt{\frac{2}{5}}\Big[\Big|{}^2E\Big(u,\pm\frac{1}{2}\Big)\Big\rangle - \Big|{}^2T_1\Big(u,\pm\frac{1}{2}\Big)\Big\rangle - \frac{1}{\sqrt{2}}\Big|{}^2T_1\Big(v,\mp\frac{1}{2}\Big)\Big\rangle\Big],\\ |c'\rangle &= \Big|{}^2T_2\Big(u,\mp\frac{1}{2}\Big)\Big\rangle,\end{aligned} \tag{B15}$$

the problem reduces to the same 3×3 matrix as earlier, i.e., Eq. (B6). In particular, the eigenvalues and eigenstates are given by Eqs. (2) and (B7), respectively, but this time with the basis states $|a'\rangle$, $|b'\rangle$, and $|c'\rangle$. The second doublet of the Γ_8 ground state manifold hence reads

$$|0\rangle_{\mp\frac{3}{2}} = \frac{1}{\alpha_0}\Big|{}^4A_2\Big(\mp\frac{3}{2}\Big)\Big\rangle + \frac{\sqrt{5}}{2\alpha_0}\frac{E_0}{3J_{\rm H}^{\rm eff}-E_0}|b'\rangle + \frac{E_0}{\alpha_0\,\zeta^{\rm eff}}|c'\rangle. \tag{B16}$$

The expectation value for L_z in $|0\rangle_{\mp\frac{3}{2}}$ is given by

$$\langle L_z\rangle_{\mp\frac{3}{2}} = \frac{1}{5}\Big(\frac{\sqrt{5}E_0}{2\alpha_0(3J_{\rm H}^{\rm eff}-E_0)}\Big)^2 + \Big(\frac{E_0}{\alpha_0\zeta^{\rm eff}}\Big)^2. \tag{B17}$$

Using the leading order approximation of E_0 in Eq. (B11), one finds that the ground state is approximated by

$$|0\rangle_{\mp\frac{3}{2}} = \frac{1}{\beta_0}\Big[\Big|{}^4A_2\Big(\mp\frac{3}{2}\Big)\Big\rangle - \frac{\zeta^{\rm eff}}{5J_{\rm H}^{\rm eff}}\Big|{}^2T_2\Big(u,\mp\frac{1}{2}\Big)\Big\rangle\Big], \tag{B18}$$

with, as above, $\beta_0 = \sqrt{1+(\zeta^{\rm eff}/5J_{\rm H}^{\rm eff})^2}$. The L_z expectation value is to leading order given by

$$\langle L_z\rangle_{\mp\frac{3}{2}} \approx \frac{1}{25}\Big(\frac{\zeta^{\rm eff}}{J_{\rm H}^{\rm eff}}\Big)^2. \tag{B19}$$

The ${}^2T_2$ multiplet is Jahn-Teller active. Spin-orbit coupling causes a mixing in of ${}^2T_2$ character into the ground state, driving it Jahn-Teller active. In the Kanamori picture for $\zeta^{\rm eff}/J_{\rm H}^{\rm eff} = 0.8$, we find $\langle L_z\rangle_{\mp\frac{3}{2}} \approx 0.027$, a small value.

3. Eigenstates for $\zeta = 0$

The 20 t_{2g}^3 eigenstates for $\zeta = 0$ read

$$\begin{aligned}\Big|{}^4A_2\Big(\mp\frac{3}{2}\Big)\Big\rangle &= c^\dagger_{xy-\sigma}c^\dagger_{xz-\sigma}c^\dagger_{yz-\sigma}|{\rm vac}\rangle,\\ \Big|{}^4A_2\Big(\mp\frac{1}{2}\Big)\Big\rangle &= \frac{1}{\sqrt{3}}(c^\dagger_{xy\sigma}c^\dagger_{xz-\sigma}c^\dagger_{yz-\sigma} + c^\dagger_{xy-\sigma}c^\dagger_{xz\sigma}c^\dagger_{yz-\sigma} + c^\dagger_{xy-\sigma}c^\dagger_{xz-\sigma}c^\dagger_{yz\sigma})|{\rm vac}\rangle,\\ \Big|{}^2E\Big(u,\pm\frac{1}{2}\Big)\Big\rangle &= \frac{1}{\sqrt{2}}(c^\dagger_{xz\sigma}c^\dagger_{yz-\sigma} - c^\dagger_{xz-\sigma}c^\dagger_{yz\sigma})c^\dagger_{xy\sigma}|{\rm vac}\rangle,\\ \Big|{}^2E\Big(v,\mp\frac{1}{2}\Big)\Big\rangle &= \frac{1}{\sqrt{6}}(2c^\dagger_{xy\sigma}c^\dagger_{xz-\sigma}c^\dagger_{yz-\sigma} - c^\dagger_{xy-\sigma}c^\dagger_{xz\sigma}c^\dagger_{yz-\sigma} - c^\dagger_{xy-\sigma}c^\dagger_{xz-\sigma}c^\dagger_{yz\sigma})|{\rm vac}\rangle,\end{aligned}$$

$$\begin{aligned}\Big|{}^2T_1\Big(u,\pm\frac{1}{2}\Big)\Big\rangle &= \frac{i}{\sqrt{2}}(c^\dagger_{xz\sigma}c^\dagger_{xz-\sigma} - c^\dagger_{yz\sigma}c^\dagger_{yz-\sigma})c^\dagger_{xy\sigma}|{\rm vac}\rangle,\\ \Big|{}^2T_1\Big(v,\mp\frac{1}{2}\Big)\Big\rangle &= \frac{1}{2}[(c^\dagger_{yz\sigma}c^\dagger_{yz-\sigma} - c^\dagger_{xy\sigma}c^\dagger_{xy-\sigma})c^\dagger_{xz-\sigma} \mp i(c^\dagger_{xy\sigma}c^\dagger_{xy-\sigma} - c^\dagger_{xz\sigma}c^\dagger_{xz-\sigma})c^\dagger_{yz-\sigma}]|{\rm vac}\rangle,\\ \Big|{}^2T_1\Big(w,\pm\frac{1}{2}\Big)\Big\rangle &= \frac{1}{2}[(c^\dagger_{yz\sigma}c^\dagger_{yz-\sigma} - c^\dagger_{xy\sigma}c^\dagger_{xy-\sigma})c^\dagger_{xz\sigma} \mp i(c^\dagger_{xy\sigma}c^\dagger_{xy-\sigma} - c^\dagger_{xz\sigma}c^\dagger_{xz-\sigma})c^\dagger_{yz\sigma}]|{\rm vac}\rangle,\end{aligned}$$

$$\begin{aligned}\Big|{}^2T_2\Big(u,\mp\frac{1}{2}\Big)\Big\rangle &= \frac{1}{2}[(c^\dagger_{yz\sigma}c^\dagger_{yz-\sigma} + c^\dagger_{xy\sigma}c^\dagger_{xy-\sigma})c^\dagger_{xz-\sigma} \pm i(c^\dagger_{xy\sigma}c^\dagger_{xy-\sigma} + c^\dagger_{xz\sigma}c^\dagger_{xz-\sigma})c^\dagger_{yz-\sigma}]|{\rm vac}\rangle,\\ \Big|{}^2T_2\Big(v,\mp\frac{1}{2}\Big)\Big\rangle &= \frac{i}{\sqrt{2}}(c^\dagger_{xz\sigma}c^\dagger_{xz-\sigma} + c^\dagger_{yz\sigma}c^\dagger_{yz-\sigma})c^\dagger_{xy-\sigma}|{\rm vac}\rangle,\\ \Big|{}^2T_2\Big(w,\pm\frac{1}{2}\Big)\Big\rangle &= \frac{1}{2}[(c^\dagger_{yz\sigma}c^\dagger_{yz-\sigma} + c^\dagger_{xy\sigma}c^\dagger_{xy-\sigma})c^\dagger_{xz\sigma} \pm i(c^\dagger_{xy\sigma}c^\dagger_{xy-\sigma} + c^\dagger_{xz\sigma}c^\dagger_{xz-\sigma})c^\dagger_{yz\sigma}]|{\rm vac}\rangle,\end{aligned}$$

where, e.g., $c^\dagger_{xy\sigma}$ creates an electron with spin σ in the xy orbital and $|{\rm vac}\rangle$ denotes vacuum.

[1] W. Witczak-Krempa, G. Chen, Y. B. Kim, and L. Balents, Correlated quantum phenomena in the strong spin-orbit regime, Annu. Rev. Condens. Matter Phys. **5**, 57 (2014).

[2] J. G. Rau, E. K.-H. Lee, and H.-Y. Kee, Spin-orbit physics giving rise to novel phases in correlated systems: Iridates and related materials, Annu. Rev. Condens. Matter Phys. **7**, 195 (2016).

[3] R. Schaffer, E. K.-H. Lee, B.-J. Yang, and Y. B. Kim, Recent progress on correlated electron systems with strong spin-orbit coupling, Rep. Prog. Phys. **79**, 094504 (2016).

[4] S. V. Streltsov and D. I. Khomskii, Jahn-Teller effect and spin-orbit coupling: Friends or foes? Phys. Rev. X **10**, 031043 (2020).

[5] T. Takayama, J. Chaloupka, A. Smerald, G. Khaliullin, and H. Takagi, Spin–orbit-entangled electronic phases in 4*d* and 5*d* transition-metal compounds, J. Phys. Soc. Jpn. **90**, 062001 (2021).

[6] D. I. Khomskii and S. V. Streltsov, Orbital effects in solids: Basics, recent progress, and opportunities, Chem. Rev. **121**, 2992 (2021).

[7] G. Jackeli and G. Khaliullin, Mott insulators in the strong spin-orbit coupling limit: From Heisenberg to a quantum compass and Kitaev models, Phys. Rev. Lett. **102**, 017205 (2009).

[8] S. M. Winter, A. A. Tsirlin, M. Daghofer, J. van den Brink, Y. Singh, P. Gegenwart, and R. Valentí, Models and materials for generalized Kitaev magnetism, J. Phys.: Condens. Matter **29**, 493002 (2017).

[9] S. H. Chun, J.-W. Kim, J. Kim, H. Zheng, C. C. Stoumpos, C. D. Malliakas, J. F. Mitchell, K. Mehlawat, Y. Singh, Y. Choi, T. Gog, A. Al-Zein, M. Moretti Sala, M. Krisch, J. Chaloupka, G. Jackeli, G. Khaliullin, and B. J. Kim, Direct evidence for dominant bond-directional interactions in a honeycomb lattice iridate Na_2IrO_3, Nat. Phys. **11**, 462 (2015).

[10] A. Revelli, C. C. Loo, D. Kiese, P. Becker, T. Fröhlich, T. Lorenz, M. Moretti Sala, G. Monaco, F. L. Buessen, J. Attig, M. Hermanns, S. V. Streltsov, D. I. Khomskii, J. van den Brink, M. Braden, P. H. M. van Loosdrecht, S. Trebst, A. Paramekanti, and M. Grüninger, Spin-orbit entangled $j = 1/2$ moments in Ba_2CeIrO_6: A frustrated fcc quantum magnet, Phys. Rev. B **100**, 085139 (2019).

[11] M. Magnaterra, K. Hopfer, Ch. J. Sahle, M. Moretti Sala, G. Monaco, J. Attig, C. Hickey, I.-M. Pietsch, F. Breitner, P. Gegenwart, M. H. Upton, J. Kim, S. Trebst, P. H. M. van Loosdrecht, J. van den Brink, and M. Grüninger, RIXS observation of bond-directional nearest-neighbor excitations in the Kitaev material Na_2IrO_3, arXiv:2301.08340.

[12] G. Chen, R. Pereira, and L. Balents, Exotic phases induced by strong spin-orbit coupling in ordered double perovskites, Phys. Rev. B **82**, 174440 (2010).

[13] W. M. H. Natori, E. C. Andrade, E. Miranda, and R. G. Pereira, Chiral spin-orbital liquids with nodal lines, Phys. Rev. Lett. **117**, 017204 (2016).

[14] J. Romhányi, L. Balents, and G. Jackeli, Spin-orbit dimers and noncollinear phases in d^1 cubic double perovskites, Phys. Rev. Lett. **118**, 217202 (2017).

[15] H. Ishikawa, T. Takayama, R. K. Kremer, J. Nuss, R. Dinnebier, K. Kitagawa, K. Ishii, and H. Takagi, Ordering of hidden multipoles in spin-orbit entangled $5d^1$ Ta chlorides, Phys. Rev. B **100**, 045142 (2019).

[16] A. Mansouri Tehrani, J.-R. Soh, J. Pásztorová, M. E. Merkel, I. Živković, H. M. Rønnow, and N. A. Spaldin, Charge multipole correlations and order in Cs_2TaCl_6, Phys. Rev. Res. **5**, L012010 (2023).

[17] A. Paramekanti, D. D. Maharaj, and B. D. Gaulin, Octupolar order in *d*-orbital Mott insulators, Phys. Rev. B **101**, 054439 (2020).

[18] S. W. Lovesey and D. D. Khalyavin, Lone octupole and bulk magnetism in osmate $5d^2$ double perovskites, Phys. Rev. B **102**, 064407 (2020).

[19] G. Khaliullin, D. Churchill, P. P. Stavropoulos, and H.-Y. Kee, Exchange interactions, Jahn-Teller coupling, and multipole orders in pseudospin one-half $5d^2$ Mott insulators, Phys. Rev. Res. **3**, 033163 (2021).

[20] S. Voleti, A. Haldar, and A. Paramekanti, Octupolar order and Ising quantum criticality tuned by strain and dimensionality: Application to *d*-orbital Mott insulators, Phys. Rev. B **104**, 174431 (2021).

[21] L. V. Pourovskii, D. F. Mosca, and C. Franchini, Ferro-octupolar order and low-energy excitations in d^2 double perovskites of osmium, Phys. Rev. Lett. **127**, 237201 (2021).

[22] A. Rayyan, D. Churchill, and H.-Y. Kee, Field-induced Kitaev multipolar liquid in spin-orbit coupled d^2 honeycomb Mott insulators, Phys. Rev. B **107**, L020408 (2023).

[23] P. Warzanowski, M. Magnaterra, P. Stein, G. Schlicht, Q. Faure, Ch. J. Sahle, T. Lorenz, P. Becker, L. Bohatý, M. Moretti Sala, G. Monaco, P. H. M. van Loosdrecht, and M. Grüninger, Electronic excitations in $5d^4$ $J = 0$ Os^{4+} halides studied by RIXS and optical spectroscopy, Phys. Rev. B **108**, 125120 (2023).

[24] B. Yuan, J. P. Clancy, A. M. Cook, C. M. Thompson, J. Greedan, G. Cao, B. C. Jeon, T. W. Noh, M. H. Upton, D. Casa, T. Gog, A. Paramekanti, and Y.-J. Kim, Determination of Hund's coupling in 5*d* oxides using resonant inelastic x-ray scattering, Phys. Rev. B **95**, 235114 (2017).

[25] M. Kusch, V. M. Katukuri, N. A. Bogdanov, B. Büchner, T. Dey, D. V. Efremov, J. E. Hamann-Borrero, B. H. Kim, M. Krisch, A. Maljuk, M. M. Sala, S. Wurmehl, G. Aslan-Cansever, M. Sturza, L. Hozoi, J. van den Brink, and J. Geck, Observation of heavy spin-orbit excitons propagating in a nonmagnetic background: The case of $(Ba, Sr)_2YIrO_6$, Phys. Rev. B **97**, 064421 (2018).

[26] A. Nag, S. Bhowal, A. Chakraborty, M. M. Sala, A. Efimenko, F. Bert, P. K. Biswas, A. D. Hillier, M. Itoh, S. D. Kaushik, V. Siruguri, C. Meneghini, I. Dasgupta, and S. Ray, Origin of magnetic moments and presence of spin-orbit singlets in Ba_2YIrO_6, Phys. Rev. B **98**, 014431 (2018).

[27] A. Paramekanti, D. J. Singh, B. Yuan, D. Casa, A. Said, Y.-J. Kim, and A. D. Christianson, Spin-orbit coupled systems in the atomic limit: rhenates, osmates, iridates, Phys. Rev. B **97**, 235119 (2018).

[28] A. A. Aczel, Q. Chen, J. P. Clancy, C. de la Cruz, D. Reig-i-Plessis, G. J. MacDougall, C. J. Pollock, M. H. Upton, T. J. Williams, N. LaManna, J. P. Carlo, J. Beare, G. M. Luke, and H. D. Zhou, Spin-orbit coupling controlled ground states in the double perovskite iridates A_2BIrO_6 (A = Ba, Sr; B = Lu, Sc), Phys. Rev. Mater. **6**, 094409 (2022).

[29] S. Fuchs, T. Dey, G. Aslan-Cansever, A. Maljuk, S. Wurmehl, B. Büchner, and V. Kataev, Unraveling the nature of magnetism of the $5d^4$ double perovskite Ba_2YIrO_6, Phys. Rev. Lett. **120**, 237204 (2018).

[30] H. Takahashi, H. Suzuki, J. Bertinshaw, S. Bette, C. Mühle, J. Nuss, R. Dinnebier, A. Yaresko, G. Khaliullin, H. Gretarsson, T. Takayama, H. Takagi, and B. Keimer, Nonmagnetic $J = 0$ state and spin-orbit excitations in K_2RuCl_6, Phys. Rev. Lett. **127**, 227201 (2021).

[31] G. Khaliullin, Excitonic magnetism in Van Vleck–type d^4 Mott insulators, Phys. Rev. Lett. **111**, 197201 (2013).

[32] D. I. Khomskii, *Transition Metal Compounds* (Cambridge University Press, Cambridge, UK, 2014).

[33] A. Jain, M. Krautloher, J. Porras, G. H. Ryu, D. P. Chen, D. L. Abernathy, J. T. Park, A. Ivanov, J. Chaloupka, G. Khaliullin, B. Keimer, and B. J. Kim, Higgs mode and its decay in a two-dimensional antiferromagnet, Nat. Phys. **13**, 633 (2017).

[34] N. Kaushal, J. Herbrych, G. Alvarez, and E. Dagotto, Magnetization dynamics fingerprints of an excitonic condensate t_{2g}^4 magnet, Phys. Rev. B **104**, 235135 (2021).

[35] A. E. Taylor, S. Calder, R. Morrow, H. L. Feng, M. H. Upton, M. D. Lumsden, K. Yamaura, P. M. Woodward, and A. D. Christianson, Spin-orbit coupling controlled $J = 3/2$ electronic ground state in $5d^3$ oxides, Phys. Rev. Lett. **118**, 207202 (2017).

[36] E. Kermarrec, C. A. Marjerrison, C. M. Thompson, D. D. Maharaj, K. Levin, S. Kroeker, G. E. Granroth, R. Flacau, Z. Yamani, J. E. Greedan, and B. D. Gaulin, Frustrated fcc antiferromagnet Ba_2YOsO_6: Structural characterization, magnetic properties, and neutron scattering studies, Phys. Rev. B **91**, 075133 (2015).

[37] S. Calder, J. G. Vale, N. A. Bogdanov, X. Liu, C. Donnerer, M. H. Upton, D. Casa, A. H. Said, M. D. Lumsden, Z. Zhao, J.-Q. Yan, D. Mandrus, S. Nishimoto, J. van den Brink, J. P. Hill, D. F. McMorrow, and A. D. Christianson, Spin-orbit-driven magnetic structure and excitation in the $5d$ pyrochlore $Cd_2Os_2O_7$, Nat. Commun. **7**, 11651 (2016).

[38] A. E. Taylor, R. Morrow, R. S. Fishman, S. Calder, A. I. Kolesnikov, M. D. Lumsden, P. M. Woodward, and A. D. Christianson, Spin-orbit coupling controlled ground state in Sr_2ScOsO_6, Phys. Rev. B **93**, 220408(R) (2016).

[39] A. E. Taylor, R. Morrow, M. D. Lumsden, S. Calder, M. H. Upton, A. I. Kolesnikov, M. B. Stone, R. S. Fishman, A. Paramekanti, P. M. Woodward, and A. D. Christianson, Origin of magnetic excitation gap in double perovskite Sr_2FeOsO_6, Phys. Rev. B **98**, 214422 (2018).

[40] S. Calder, D. J. Singh, V. O. Garlea, M. D. Lumsden, Y. G. Shi, K. Yamaura, and A. D. Christianson, Interplay of spin-orbit coupling and hybridization in Ca_3LiOsO_6 and Ca_3LiRuO_6, Phys. Rev. B **96**, 184426 (2017).

[41] G. P. O'Leary and R. G. Wheeler, Phase transitions and soft librational modes in cubic crystals, Phys. Rev. B **1**, 4409 (1970).

[42] R. L. Armstrong, Structural properties and lattice dynamics of $5d$ transition metal antifluorite crystals, Phys. Rep. **57**, 343 (1980).

[43] A. Bertin, T. Dey, D. Brüning, D. Gorkov, K. Jenni, A. Krause, P. Becker, L. Bohatý, D. Khomskii, V. Pomjakushin, L. Keller, M. Braden, and T. Lorenz, Interplay of magnetic order and ferroelasticity in the spin-orbit coupled antiferromagnet K_2ReCl_6, Phys. Rev. B **109**, 094409 (2024).

[44] P. Stein, T. C. Koethe, L. Bohatý, P. Becker, M. Grüninger, and P. H. M. van Loosdrecht, Local symmetry breaking and low-energy continuum in K_2ReCl_6, Phys. Rev. B **107**, 214301 (2023).

[45] L. Pross, K. Rössler, and H. J. Schenk, Optical studies on crystalline hexahalorhenates–I: Low temperature absorption spectra of $K_2[ReCl_6]$ single crystals, J. Inorg. Nucl. Chem. **36**, 317 (1974).

[46] R. K. Yoo, S. C. Lee, B. A. Kozikowski, and T. A. Keiderling, Intraconfigurational absorption spectroscopy of $ReCl_6^{2-}$ in various A_2MCl_6 host crystals, Chem. Phys. **117**, 237 (1987).

[47] M. W. Haverkort, M. Zwierzycki, and O. K. Andersen, Multiplet ligand-field theory using Wannier orbitals, Phys. Rev. B **85**, 165113 (2012).

[48] M. W. Haverkort, Quanty for core level spectroscopy - excitons, resonances and band excitations in time and frequency domain, J. Phys.: Conf. Ser. **712**, 012001 (2016).

[49] R. H. Busey and E. Sonder, Magnetic susceptibility of Potassium Hexachlororhenate (IV) and Potassium Hexabromorhenate (IV) from 5° to 300°K, J. Chem. Phys. **36**, 93 (1962).

[50] H. G. Smith and G. E. Bacon, Neutron-diffraction study of magnetic ordering in K_2ReCl_6, J. Appl. Phys. **37**, 979 (1966).

[51] N. Smolentsev, M. Sikora, A. V. Soldatov, K. O. Kvashnina, and P. Glatzel, Spin-orbit sensitive hard x-ray probe of the occupied and unoccupied $5d$ density of states, Phys. Rev. B **84**, 235113 (2011).

[52] G. Marcaud, A. Taekyung Lee, A. J. Hauser, F. Y. Yang, S. Lee, D. Casa, M. Upton, T. Gog, K. Saritas, Y. Wang, M. P. M. Dean, H. Zhou, Z. Zhang, F. J. Walker, I. Jarrige, S. Ismail-Beigi, and C. Ahn, Low-energy electronic interactions in ferrimagnetic Sr_2CrReO_6 thin films, Phys. Rev. B **108**, 075132 (2023).

[53] F. I. Frontini, G. H. J. Johnstone, N. Iwahara, P. Bhattacharyya, N. A. Bogdanov, L. Hozoi, M. H. Upton, D. M. Casa, D. Hirai, and Y.-J. Kim, Spin-orbit-lattice entangled state in A_2MgReO_6 (A = Ca, Sr, Ba) revealed by resonant inelastic X-ray scattering, arXiv:2311.01621.

[54] D. F. McMorrow, S. E. Nagler, K. A. McEwen, and S. D. Brown, Large enhancement of x-ray magnetic scattering at the L edges of the $5d$ transition metal antiferromagnet K_2ReCl_6, J. Phys.: Condens. Matter **15**, L59 (2003).

[55] S. Huotari, G. Vankó, F. Albergamo, C. Ponchut, H. Graafsma, C. Henriquet, R. Verbeni, and G. Monaco, Improving the performance of high-resolution x-ray spectrometers with position-sensitive pixel detectors, J. Sync. Radiat. **12**, 467 (2005).

[56] S. Huotari, F. Albergamo, G. Vankó, R. Verbeni, and G. Monaco, Resonant inelastic hard x-ray scattering with diced analyzer crystals and position-sensitive detectors, Rev. Sci. Instrum. **77**, 053102 (2006).

[57] M. Moretti Sala, C. Henriquet, L. Simonelli, R. Verbeni, and G. Monaco, High energy-resolution set-up for Ir L_3 edge RIXS experiments, J. Electron Spectrosc. Relat. Phenom. **188**, 150 (2013).

[58] M. Minola, G. Dellea, H. Gretarsson, Y. Y. Peng, Y. Lu, J. Porras, T. Loew, F. Yakhou, N. B. Brookes, Y. B. Huang, J. Pelliciari, T. Schmitt, G. Ghiringhelli, B. Keimer, L. Braicovich, and M. Le Tacon, *Supplementary Information for* Collective nature of spin excitations in superconducting cuprates probed by resonant inelastic x-ray scattering, Phys. Rev. Lett. **114**, 217003 (2015).

[59] L. J.P. Ament, M. van Veenendaal, T. P. Devereaux, J. P. Hill, and J. van den Brink, Resonant inelastic x-ray scattering studies of elementary excitations, Rev. Mod. Phys. **83**, 705 (2011).

[60] N. Khan, D. Prishchenko, Y. Skourski, V. G. Mazurenko, and A. A. Tsirlin, Cubic symmetry and magnetic frustration

on the fcc spin lattice in K_2IrCl_6, Phys. Rev. B **99**, 144425 (2019).

[61] D. Reig-i-Plessis, T. A. Johnson, K. Lu, Q. Chen, J. P. C. Ruff, M. H. Upton, T. J. Williams, S. Calder, H. D. Zhou, J. P. Clancy, A. A. Aczel, and G. J. MacDougall, Structural, electronic, and magnetic properties of nearly ideal $J_{\text{eff}} = 1/2$ iridium halides, Phys. Rev. Mater. **4**, 124407 (2020).

[62] A. Gössling, R. Schmitz, H. Roth, M. W. Haverkort, T. Lorenz, J. A. Mydosh, E. Müller-Hartmann, and M. Grüninger, Mott-Hubbard exciton in the optical conductivity of $YTiO_3$ and $SmTiO_3$, Phys. Rev. B **78**, 075122 (2008).

[63] J. Reul, A. A. Nugroho, T. T. M. Palstra, and M. Grüninger, Probing orbital fluctuations in RVO_3 (R = Y, Gd, or Ce) by ellipsometry, Phys. Rev. B **86**, 125128 (2012).

[64] I. Vergara, M. Magnaterra, P. Warzanowski, J. Attig, S. Kunkemöller, D. I. Khomskii, M. Braden, M. Hermanns, and M. Grüninger, Spin-orbit coupling and crystal-field splitting in Ti-doped Ca_2RuO_4 studied by ellipsometry, Phys. Rev. B **106**, 085103 (2022).

[65] B. Henderson and G. F. Imbusch, *Optical Spectroscopy of Inorganic Solids* (Oxford University Press, Oxford, 1989).

[66] B. N. Figgis and M. A. Hitchman, *Ligand Field Theory and its Applications* (Wiley, New York, 1999).

[67] R. Rückamp, E. Benckiser, M. W. Haverkort, H. Roth, T. Lorenz, A. Freimuth, L. Jongen, A. Möller, G. Meyer, P. Reutler, B. Büchner, A. Revcolevschi, S.-W. Cheong, C. Sekar, G. Krabbes, and M. Grüninger, Optical study of orbital excitations in transition-metal oxides, New J. Phys. **7**, 144 (2005).

[68] E. Benckiser, R. Rückamp, T. Möller, T. Taetz, A. Möller, A. A. Nugroho, T. T. M. Palstra, G. S. Uhrig, and M. Grüninger, Collective orbital excitations in orbitally ordered YVO_3 and $HoVO_3$, New J. Phys. **10**, 053027 (2008).

[69] M. Schmidt, Z. Wang, Ch. Kant, F. Mayr, S. Toth, A. T. M. N. Islam, B. Lake, V. Tsurkan, A. Loidl, and J. Deisenhofer, Exciton-magnon transitions in the frustrated chromium antiferromagnets $CuCrO_2$, α-$CaCr_2O_4$, $CdCr_2O_4$, and $ZnCr_2O_4$, Phys. Rev. B **87**, 224424 (2013).

[70] P. Warzanowski, N. Borgwardt, K. Hopfer, J. Attig, T. C. Koethe, P. Becker, V. Tsurkan, A. Loidl, M. Hermanns, P. H. M. van Loosdrecht, and M. Grüninger, Multiple spin-orbit excitons and the electronic structure of α-$RuCl_3$, Phys. Rev. Res. **2**, 042007(R) (2020).

[71] P. E. Hoggard, Spin-orbit coupling in tetragonal d^3 systems, Z. Naturforsch. A **36**, 1276 (1981).

[72] A. Georges, L. de'Medici, and J. Mravlje, Strong correlations from Hund's coupling, Annu. Rev. Condens. Matter Phys. **4**, 137 (2013).

[73] G. Zhang and E. Pavarini, Mott transition, spin-orbit effects, and magnetism in Ca_2RuO_4, Phys. Rev. B **95**, 075145 (2017).

[74] C. F. Ballhausen, *Introduction to Ligand Field Theory* (McGraw-Hill, New York, 1962).

[75] I. Pollini, G. Spinolo, and G. Benedek, Vibrational structure of crystal-field spectra in layered $3d$-metal dihalides, Phys. Rev. B **22**, 6369 (1980).

[76] M. Bettinelli and C. D. Flint, Magnon sidebands and cooperative absorptions in K_2ReCl_6 and Cs_2ReCl_6, J. Phys. C: Solid State Phys. **21**, 5499 (1988).

[77] R. K. Yoo, B. A. Kozikowski, S. C. Lee, and T. A. Keiderling, Visible region absorption and excitation spectroscopy of K_2ReCl_6 and various $ReCl_6^{2-}$ containing A_2MCl_6 host crystals, Chem. Phys. **117**, 255 (1987).

[78] J. Lorenzana and G. A. Sawatzky, Phonon assisted multimagnon optical absorption and long lived two-magnon states in undoped lamellar copper oxides, Phys. Rev. Lett. **74**, 1867 (1995).

[79] J. Lorenzana and G. A. Sawatzky, Theory of phonon-assisted multimagnon optical absorption and bimagnon states in quantum antiferromagnets, Phys. Rev. B **52**, 9576 (1995).

[80] M. Windt, M. Grüninger, T. Nunner, C. Knetter, K. P. Schmidt, G. S. Uhrig, T. Kopp, A. Freimuth, U. Ammerahl, B. Büchner, and A. Revcolevschi, Observation of two-magnon bound states in the two-leg ladders of $(Ca, La)_{14}Cu_{24}O_{41}$, Phys. Rev. Lett. **87**, 127002 (2001).

[81] H. Kamimura, S. Koide, H. Sekiyama, and S. Sugano, Magnetic properties of the Pd and Pt group transition metal complexes, J. Phys. Soc. Jpn. **15**, 1264 (1960).

[82] B. N. Figgis, J. Lewis, and F. E. Mabbs, The magnetic properties of some d^3-complexes, J. Chem. Soc. **1961**, 3138 (1961).

[83] H. Szymczak, W. Wardzyński, and A. Pajaczkowska, Optical spectrum of antiferromagnetic spinels $ZnCr_2O_4$, J. Magn. Magn. Mater. **15-18**, 841 (1980).

[84] M. V. Eremin and M. A. Fayzullin, Possible mechanisms of magnon sidebands formation in transition metal compounds, J. Phys.: Conf. Ser. **324**, 012022 (2011).

7 Spin orbital lattice entanglement in the ideal $j = 1/2$ compound K_2IrCl_6

The following chapter presents the results on K_2IrCl_6, which have been published as Warzanowski *et al.*, *Spin orbital lattice entanglement in the ideal* $j = 1/2$ *compound* K_2IrCl_6, Phys. Rev. B **110**, 195120 (2024).

Author contributions

M. Grüninger and P. Warzanowski conceived the experiment. P. Warzanowski carried out the optical spectroscopy experiments and analyzed the data. M. Magnaterra, Ch. J. Sahle, M. Moretti Sala, and M. Grüninger carried out the RIXS experiments at the ID20 beamline of the ESRF, with support from P. Warzanowski, G. Monaco, and P. H. M. van Loosdrecht. P. Warzanowski analyzed the optical spectra and the RIXS data with input from M. Grüninger. P. Becker and L. Bohatý synthesized the samples. I. Císařova performed the single-crystal x-ray diffraction experiments and analyzed the structural data. T. Lorenz contributed the part on the discussion of magnetic susceptibility and specific heat. J. van den Brink contributed in particular to the discussion of the vibronic character. P. Warzanowski and M. Grüninger wrote the manuscript with input from all authors.

Sample and data availability

The samples used in this project are stored within the labs of the Institute of Physics II at the University of Cologne. The raw data and the analysis files are stored on the servers of the Institute of Physics II. The data for the figures published in the manuscript are also stored on a Zenodo repository [245].

Editors' Suggestion

Spin orbital lattice entanglement in the ideal $j = \frac{1}{2}$ compound K_2IrCl_6

P. Warzanowski,[1] M. Magnaterra,[1] Ch. J. Sahle,[2] M. Moretti Sala,[3] P. Becker,[4] L. Bohatý,[4] I. Císařová,[5] G. Monaco,[6] T. Lorenz,[1] P. H. M. van Loosdrecht,[1] J. van den Brink,[7,8] and M. Grüninger[1]

[1]*Institute of Physics II, University of Cologne, 50937 Cologne, Germany*
[2]*ESRF, The European Synchrotron, 71 Avenue des Martyrs, CS40220, 38043 Grenoble Cedex 9, France*
[3]*Dipartimento di Fisica, Politecnico di Milano, I-20133 Milano, Italy*
[4]*Sect. Crystallography, Institute of Geology and Mineralogy, University of Cologne, 50674 Cologne, Germany*
[5]*Department of Inorganic Chemistry, Charles University in Prague, 128 43 Prague 2, Czech Republic*
[6]*Dipartimento di Fisica e Astronomia "Galileo Galilei", Università di Padova, I-35121 Padova, Italy*
[7]*Institute for Theoretical Solid State Physics, IFW Dresden, 01069 Dresden, Germany*
[8]*Institute for Theoretical Physics and Würzburg-Dresden Cluster of Excellence ct.qmat, Technische Universität Dresden, 01069 Dresden, Germany*

(Received 16 July 2024; accepted 17 October 2024; published 7 November 2024)

Mott insulators with spin-orbit entangled $j = 1/2$ moments host intriguing magnetic properties. The $j = 1/2$ wave function requires cubic symmetry, while a noncubic crystal field mixes $j = 1/2$ and $3/2$ character. Spectroscopic studies of $5d^5$ iridates typically claim noncubic symmetry, e.g., based on a splitting of the excited $j = 3/2$ quartet. A sizable splitting is particularly puzzling in antifluorite-type K_2IrCl_6, a frustrated fcc quantum magnet with global cubic symmetry. It raises the fundamental question about the stability of $j = 1/2$ moments against magnetoelastic coupling. Combining resonant inelastic x-ray scattering with optical spectroscopy, we demonstrate that the multi-peak line shape in K_2IrCl_6 reflects a vibronic character of the $j = 3/2$ states rather than a noncubic crystal field. The quasimolecular crystal structure with well separated $IrCl_6$ octahedra explains the existence of well-defined sidebands that are usually smeared out in solids. Our results highlight the spin orbital lattice entangled character of cubic K_2IrCl_6 with ideal $j = 1/2$ moments.

DOI: 10.1103/PhysRevB.110.195120

I. INTRODUCTION

The entanglement of spin and orbital degrees of freedom via strong spin-orbit coupling leads to a multitude of novel quantum magnetic phases in $4d$ and $5d$ transition-metal compounds [1–7]. Particular interest has focused on the physics of $j = 1/2$ moments in $4d^5$ Ru^{3+} and $5d^5$ Ir^{4+} compounds. Despite strong spin-orbit coupling, these allow for isotropic Heisenberg exchange in 180° corner-sharing bonding geometry but also yield Ising exchange in 90° edge-sharing configuration [8], opening the door for the realization of Kitaev spin liquids with bond-directional exchange [9,10] on tricoordinated lattices. Such local $j = 1/2$ moments are formed by, e.g., t_{2g}^5 Ir^{4+} ions in octahedral configuration. Resonant inelastic x-ray scattering (RIXS) at the Ir L_3 edge is a sensitive tool to test the $j = 1/2$ character, probing excitations to the $j = 3/2$ quartet, i.e., the spin-orbit exciton. A noncubic crystal-field contribution Δ_{CF} lifts the degeneracy of the quartet, see Fig. 1(c), giving rise to an admixture of $j = 3/2$ character to the $j = 1/2$ ground state wave function [11]. In Ir^{4+} materials, RIXS typically detects such deviations from pure $j = 1/2$ character with crystal-field splittings of roughly 0.1 eV [12–26].

Surprisingly, a sizable splitting of the spin-orbit exciton has even been reported for compounds that are found to exhibit cubic symmetry in x-ray diffraction such as the double perovskite Ba_2CeIrO_6 and the antifluorite-type halides K_2IrX_6 (X = Cl, Br) [15,16,27–33]. The halides show such splitting in Ir L-edge RIXS, Raman spectroscopy, and infrared absorption [29–32]. All three compounds host the local moments on an fcc lattice, giving rise to highly frustrated quantum magnetism where a spin-liquid phase emerges in the phase diagram based on the geometric frustration of antiferromagnetic nearest-neighbor Heisenberg exchange augmented by next-nearest-neighbor exchange [16,34]. Remarkably, finite antiferromagnetic Kitaev exchange in this case reduces the magnetic frustration and stabilizes long-range magnetic order [16,28,30]. However, the pronounced frustration on the fcc lattice can be lifted via magnetoelastic coupling, where even small lattice distortions may cause strong variation of nearest-neighbor exchange couplings [16]. Such small distortions may be reconciled with an apparent global cubic structure in diffraction experiments if distortions are essentially local and exhibit a very short correlation length. This raises the fundamental question on the stability of cubic $j = 1/2$ moments in frustrated quantum magnets.

Recently, Iwahara and Furukawa [35] suggested an alternative scenario for K_2IrCl_6 in which the two-peak structure of the spin-orbit exciton observed in RIXS is attributed to the interplay of spin-orbit coupling and electron-phonon coupling that gives rise to vibronic sidebands, i.e., spin orbital lattice entangled states with a mixed vibrational-electronic character. This scenario of a dynamic Jahn-Teller effect in the

$j = 3/2$ *excited* state [5,36] does not require a local breaking of cubic symmetry in the ground state and hence reconciles the spectroscopic data with the cubic symmetry reported in diffraction [27–29] and in electron spin resonance, where an isotropic g factor is found [33]. However, this explanation raises the puzzling question why distinct vibronic sidebands thus far have not been discussed in the compelling series of experimental L-edge RIXS studies of other $5d^5$ Ir^{4+} oxides and halides [12–25,37]. Based on the excellent energy resolution of optical spectroscopy, vibronic sidebands of the spin-orbit exciton have been observed in optical data of the $4d^5$ $j = 1/2$ Kitaev material α-$RuCl_3$ [38,39]. Furthermore, a dressing of the spin-orbit exciton with phonon sidebands has been claimed in oxygen K-edge RIXS on the related Kitaev material α-Li_2IrO_3 [40]. Compared to L-edge RIXS, however, RIXS at the O K edge is much more sensitive to vibrational features due to the very different character of the intermediate state in the scattering process and the much longer core hole life time. This has recently been demonstrated for $5d^1$ Ba_2NaOsO_6 [41] and is further exemplified by the observation of an entire ladder of strong phononic peaks in α-Li_2IrO_3 at the O K edge [40] and the absence of any phononic features in L-edge RIXS of the same compound [42]. Beyond iridates, the observation of vibronic sidebands of electronic excitations by means of transition-metal L-edge RIXS has been claimed in $3d^9$ $Ca_2Y_2Cu_5O_{10}$ [43], $4d^4$ K_2RuCl_6 [44,45], and $5d^1$ A_2MgReO_6 (A =Ca, Sr, Ba) [46] but the observed features are broad and individual sidebands are not or hardly resolved. This is the typical situation in solids. While molecules like O_2 exhibit distinct vibronic sidebands of electronic excitations [47], in solids the existence of many different phonon modes and their dispersion smear out the sideband structure, most often turning the line shape into a broad hump even in optical data [48–51]. Remarkably, individual vibronic sidebands have been resolved in optical data of quasimolecular crystals such as K_3NiO_2 with isolated NiO_2 units [49], and the same characteristic features have been detected recently in optical data of the sister compounds K_2ReCl_6 and K_2OsCl_6 [52,53].

Here, we join forces of RIXS and optical spectroscopy to thoroughly study the spin-orbit exciton in K_2IrCl_6. Phenomenologically, the two-peak structure seen in RIXS can be explained by either a noncubic crystal field or a vibronic picture. In contrast, the excellent energy resolution of the optical data allows us to resolve a multi-peak structure that highlights the vibronic origin, respecting cubic symmetry. These excitations are particularly well defined in K_2IrCl_6 due to its quasimolecular crystal structure with spatially isolated $IrCl_6$ octahedra. The competition of spin-orbit coupling and electron-phonon coupling gives rise to a dynamic Jahn-Teller effect in the $j = 3/2$ excited state, hybridizing the spin-orbit exciton with vibrational states [35]. Empirically, the overall line shape of these spin orbital lattice entangled excitations can be described by the Franck-Condon approximation, where the eigenstates are product states of electronic and vibrational states. However, the spin orbital lattice entangled nature is evident in the parameters, in particular in the peak splitting and its temperature dependence. We further demonstrate that the contribution of elementary phonon excitations in Ir L_3-edge RIXS is negligible in K_2IrCl_6. In contrast, the vibronic "phonon" sidebands of the spin-orbit exciton contribute in a direct RIXS process and are resonantly enhanced due to the electronic part of the wave function. Finally, we observe the double spin-orbit exciton at 1.3 eV in $\sigma_1(\omega)$ which also shows vibronic sidebands. Our results firmly establish the spin orbital lattice entangled nature of $j = 3/2$ excited states in cubic K_2IrCl_6 with ideal $j = 1/2$ moments.

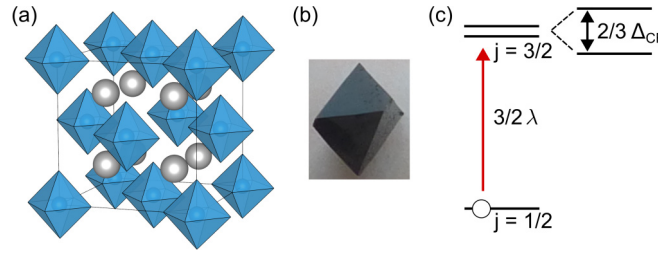

FIG. 1. (a) Sketch of the cubic crystal structure of K_2IrCl_6 with well separated $IrCl_6$ octahedra (blue). The K^+ ions are shown in gray. (b) Example of a grown single crystal of K_2IrCl_6. (c) The spin-orbit exciton denotes the excitation from the local $j = 1/2$ ground state to the $j = 3/2$ excited state. In cubic symmetry, the energy equals 1.5 λ. The degeneracy of the quartet is lifted in a noncubic crystal field.

II. EXPERIMENTAL

High-quality single crystals were grown from a solution of commercially available K_2IrCl_6 in ≈ 5.2 molar HCl by controlled evaporation of the solvent at 293 K. Within typical growth periods of two weeks, crystals of dimensions up to $1 \times 1 \times 2$ mm^3 were obtained, see Fig. 1(b). In single-crystal x-ray diffraction measurements performed at ten different temperatures from 120 to 290 K, we find the cubic space group $Fm\bar{3}m$ (No. 225) and lattice constants $a = 9.7458(2)$ Å (290 K) and 9.6867(3) Å (120 K), see Appendix. Our x-ray diffraction results agree very well with earlier data measured at 80 and 200 K on samples of the same batch [27]. A thorough analysis of the x-ray diffraction data supports the high sample quality with no indication of a significant amount of vacancies, see also Ref. [27]. Measurements of the magnetic susceptibility χ and the specific heat C_p (see Fig. 2) yield results that agree with previous reports [28,29,33,54], e.g., concerning the Néel temperature $T_N = 3.1$ K, the Weiss temperature $\theta_W = -43.9$ K, the sizable frustration parameter $f = |\theta_W|/T_N \approx 14$, and the effective magnetic moment $\mu_{eff} = 1.69\ \mu_B$. The latter is in good agreement with the value $2\sqrt{j(j+1)}\ \mu_B \approx 1.73\ \mu_B$ expected for an ideal $j = 1/2$ ground state in a cubic environment.

RIXS spectra were measured at the Ir L_3 edge at beamline ID20 of the European Synchrotron Radiation Facility. Details of the RIXS setup can be found in Refs. [55,56]. In order to resonantly enhance the spin-orbit exciton, we tuned the energy of the incident photons to 11.214 keV where an energy resolution of 25 meV was achieved [55,56]. RIXS data were collected at 10, 100, 200, and 300 K on a (111) surface with (001) and (110) lying in the horizontal scattering plane. The incident x-ray photons were π polarized. The RIXS spectra at different temperatures have been normalized by the spectral weight of the spin-orbit exciton. The transferred momentum

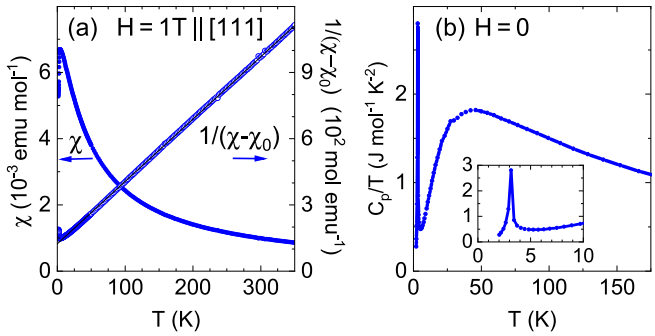

FIG. 2. (a) The magnetic susceptibility χ of K_2IrCl_6 exhibits Curie-Weiss behavior as seen by the straight line of $1/(\chi - \chi_0)$ (right axis) with $\chi_0 = -3.9 \times 10^{-5}$emu/mol representing the sum of core diamagnetism and Van Vleck paramagnetism. The linear fit (black) above 100 K yields a Weiss temperature $\theta_W = -43.9$ K and an effective magnetic moment $\mu_{eff} = 1.69\ \mu_B$. (b) The specific heat shows a pronounced peak signaling antiferromagnetic order at $T_N = 3.1$ K, as plotted on an enlarged scale in the inset.

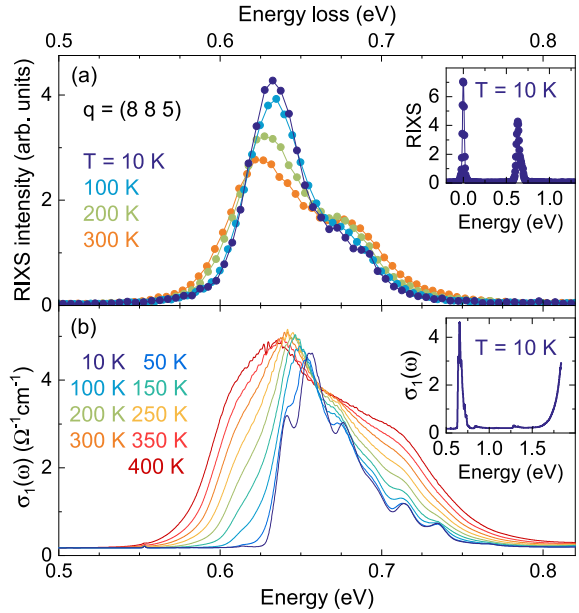

FIG. 3. Spin-orbit exciton in L_3-edge RIXS and optics. (a) RIXS spectra at $\mathbf{q} = (8\ 8\ 5)$ show a two-peak structure around 0.63 eV. (Inset) RIXS data over the entire measured range. The spin-orbit exciton is the only inelastic feature. (b) Optical conductivity $\sigma_1(\omega)$ in the same energy range as used in (a). The shift of the peak energy compared to RIXS at 10 K, the existence of several sidebands, and the strong increase of the spectral weight with increasing temperature highlight the phonon-assisted character. (Inset) The steep onset of excitations across the Mott gap is observed at about 1.7 eV at 10 K.

$\mathbf{q}$ is given in reciprocal lattice units. Furthermore, we study the linear optical response of K_2IrCl_6 in the range from 0.1 to 6 eV, i.e., from the infrared up to the UV. Using a Woollam VASE ellipsometer from 1 to 6 eV, we address the optical response above the Mott gap at 300 K. For cubic symmetry, such ellipsometric measurements directly yield the optical conductivity $\sigma_1(\omega)$ [57]. The VASE setup employs a rotating analyzer and a retarder between polarizer and sample. We collected ellipsometric data with an angle of incidence of 65°, 70°, and 75°. Due to inversion symmetry on the Ir site, the spin-orbit exciton in optics corresponds to a parity-forbidden excitation. However, it acquires finite spectral weight in a phonon-assisted process. For frequencies below the Mott gap, measurements of the infrared transmittance $T(\omega)$ are ideally suited to study such weak absorption features [51], as recently demonstrated on the sister compounds K_2OsCl_6 and K_2ReCl_6 [52,53]. Note that $T(\omega)$ depends exponentially on the sample thickness d and on the imaginary part of the refractive index. By choosing transparent single crystals with appropriate thickness, also very weak absorption features can be determined with high accuracy. For K_2IrCl_6, we studied single-crystalline samples with a thickness $d = 380(8)$, 95(3), and 46(3) μm. Infrared transmittance data for normal incidence were measured from 0.15 to 1.85 eV with an energy resolution of 8 cm^{-1} (≈ 1 meV) using a Bruker IFS 66 v/S Fourier-transform infrared spectrometer equipped with a continuous-flow ^{4}He cryostat. For the determination of the real part of the optical conductivity $\sigma_1(\omega)$ from the measured $T(\omega)$, we refer to Refs. [52,53].

III. SPIN-ORBIT EXCITON IN RIXS

The hallmark excitation of a local $j = 1/2$ ground state is the spin-orbit exciton, i.e., the excitation to the $j = 3/2$ quartet that is expected at 1.5λ in cubic symmetry [8,11], where λ is the spin-orbit coupling constant, see sketch in Fig. 1(c). RIXS data of K_2IrCl_6, measured up to 1.3 eV with transferred momentum $\mathbf{q} = (8\ 8\ 5)$, show the spin-orbit exciton around 0.63 eV, see Fig. 3(a). The absence of further inelastic features in this energy range demonstrates the pure Ir^{4+} valence of the compound, see inset of Fig. 3(a). The narrow line width is typical for local, weakly interacting $j = 1/2$ moments [12–21], while broader, dispersive features are observed in compounds with larger exchange interactions such as Sr_2IrO_4 and $Sr_3Ir_2O_7$ [22–26]. In agreement with previous RIXS data on K_2IrCl_6 measured with 35 meV resolution [29], we observe a two-peak structure of the spin-orbit exciton. The main peak at 0.63 eV features a weak shoulder that is about 0.05 eV higher in energy, see Fig. 4. The relative intensity of this shoulder increases with increasing temperature, see Fig. 3(a), in agreement with previous results for 10 and 300 K [29]. Similar two-peak structures were reported in L-edge RIXS on the sister compounds K_2IrBr_6 and $(NH_4)_2IrCl_6$, also in their cubic phases [29,30]. Furthermore, a splitting of the spin-orbit exciton in K_2IrCl_6 has been observed in Raman scattering [31] and in infrared absorption at room temperature [32].

In fact, such a splitting of the spin-orbit exciton is a common feature in RIXS studies on Ir^{4+} compounds, see, e.g., Refs. [12–26]. Typically, the splitting is attributed to a noncubic crystal field contribution Δ_{CF} that lifts the degeneracy of the $j = 3/2$ quartet. For a single site and assuming a tetragonal distortion, the physics is described by [11]

$$\mathcal{H}_{single} = \lambda \mathbf{S} \cdot \mathbf{L} + \Delta_{CF} L_z^2 \quad (1)$$

where L_z is the component of the angular moment $\mathbf{L}$ along the tetragonal axis. A finite $\Delta_{CF} \ll \lambda$ lifts the degeneracy of the $j = 3/2$ quartet, resulting in an experimental peak splitting

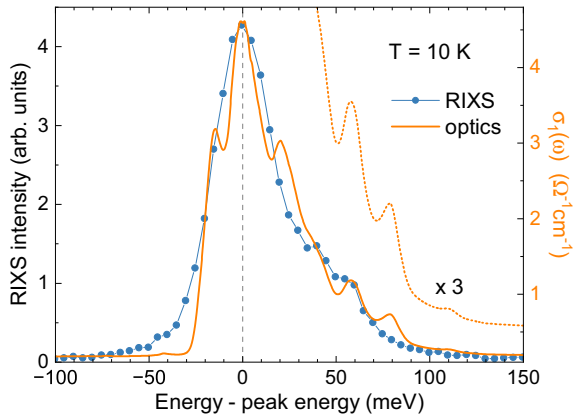

FIG. 4. Spin-orbit exciton at 10 K. The overall line shape is similar in RIXS (blue) and optics (orange, right axis). The optical conductivity shows a superposition of phonon-assisted excitations with different phonon energies, which effectively mimics the larger energy resolution of 25 meV in RIXS (see main text). For the comparison, both data sets have been shifted by the respective peak energy [633 meV for RIXS, 656 meV for $\sigma_1(\omega)$] to roughly compensate for the phonon shift. Dotted line: $\sigma_1(\omega)$ multiplied by 3 to emphasize the weak features at 0.735 and 0.766 eV, which are 0.08 and 0.11 eV above the main peak.

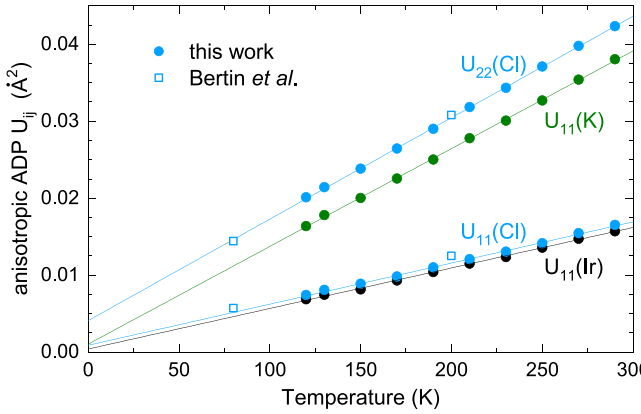

FIG. 5. Anisotropic atomic displacement parameters (ADP) U_{ij} as determined by single-crystal x-ray diffraction. Error bars are plotted but are smaller than the symbol size. Data at 80 and 200 K (open symbols) have been taken from Bertin *et al.* [27]. The lines are guides to the eye.

$\Delta_{\rm exp} = \frac{2}{3}\Delta_{\rm CF}$. Following this scenario, we empirically fit the RIXS spectra with a sum of two Voigt profiles. At 10 K, the fit yields peak energies of 0.635 and 0.676 eV, see Appendix. Solving Eq. (1), we find $\lambda = 434(1)$ meV and two possible values $\Delta_{\rm CF} = 62$ and -58 meV for elongation and compression of the octahedra, respectively.

However, a finite value of the noncubic crystal field splitting $\Delta_{\rm CF} \neq 0$ is in conflict with the globally cubic structure observed in x-ray and neutron diffraction experiments [27–29] as well as with the isotropic g factor found in an ESR study [33]. There are two scenarios to resolve this apparent discrepancy. (i) Cubic symmetry is broken locally in the initial state of the excitation process. (ii) A vibronic character of the Jahn-Teller active $j = 3/2$ excited states [5,35,36] yields sidebands while the cubic symmetry of the ground state is preserved.

In scenario (i), local deviations from cubic symmetry may be caused by either static defects or a strong magnetoelastic coupling that triggers distortions [16]. The latter can be reconciled with global cubic symmetry if the correlation length is small. Based on the short time scale of the RIXS process, also the thermal occupation of low-lying phonon modes effectively may break the cubic symmetry on the Ir site in the initial state [30]. In fact, x-ray studies reported comparably large atomic displacement parameters (ADPs) in the K_2PtCl_6-type antifluorite halides A_2MX_6 in general and also in K_2IrCl_6 [27,28]. Using a cubic crystal structure in the analysis of the x-ray data, such large ADPs in general may reflect local disorder or dynamical effects such as the thermal population of low-energy phonon modes. Based on a thorough analysis of the x-ray diffraction data, Bertin *et al.* [27] conclude that there is no indication for local disorder in K_2IrCl_6. Note that neighboring MX_6 or $IrCl_6$ octahedra are not connected in A_2MX_6 or K_2IrCl_6, see Fig. 1(a), i.e., they do not share a common ligand. This causes a rotational instability and low-energy librational modes [28,58–60]. For the halide ions, the largest ADPs indeed are found perpendicular to the Ir-Cl bonds [27,28], as expected for a predominantly rigid rotation of the octahedra in contrast to a local, noncubic distortion away from octahedral symmetry. To scrutinize this scenario of a dynamical origin for our samples, we studied the temperature dependence of the ADPs U_{ij} of the Ir, K, and Cl ions in the range from 120 to 290 K via single-crystal x-ray diffraction measurements, see Appendix. The results are plotted in Fig. 5 and agree very well with previous data reported for 80 and 200 K that were collected on samples from the same batch [27]. For the Cl ions, U_{11} and U_{22} refer to the displacement along and perpendicular to an Ir-Cl bond, respectively. We find $U_{22}(\rm Cl) \gg U_{11}(\rm Cl)$, in agreement with Refs. [27,28]. Using $\tan\varphi = \sqrt{U_{22}(\rm Cl)}/d$, we estimate the largest rotation angle $\varphi \approx 5^\circ$ at 300 K. The temperature dependence strongly supports a predominantly dynamical origin of the large U_{ij}. Above 120 K, we find a linear behavior for all U_{ij} that extrapolates to small values at low temperature, in agreement with data reported by Khan *et al.* [28]. The data do not provide any evidence for a static contribution of local distortions or defects. A more precise quantitative determination of a possible small static contribution present already at very low temperatures requires to consider zero point fluctuations [61] and a possible temperature dependence of the phonon energies. This is beyond the scope of our study. In comparison, the cubic double perovskite Ba_2CeIrO_6 exhibits a much smaller temperature dependence of the ADPs, with $U_{22}(O) = 0.022$ Å^2 at 100 K and 0.024 Å^2 at 300 K [16]. This suggests static disorder that may be explained by the presence of a few percent of Ce-Ir site disorder [16]. In K_2IrCl_6, the pronounced temperature dependence of the U_{ij} is in striking contrast to the much smaller temperature dependence of the peak splitting in RIXS. We conclude that the sizable atomic displacement parameters at elevated temperature have a dynamical origin. In particular, U_{22}(Cl) predominantly can be attributed to rigid rotations of the octahedra.

Thermal population of low-energy rotations of the octahedra preserves cubic symmetry on average. For spectroscopy,

however, it may break the cubic symmetry on the Ir site if the time scale of the electronic excitation is short enough. Nevertheless, only a small effect is expected for a rigid rotation of the octahedra. More precisely, Khan *et al.* [30] predict a dynamical rotation angle of about 5° in the cubic phase of the sister compound K_2IrBr_6 above 170 K, similar to the value that we find for K_2IrCl_6, as discussed above. This, however, is expected to cause a noncubic crystal-field splitting of less than 10 meV at high temperature [30], which is by far not large enough to explain the splitting observed in RIXS. In particular, a thermal population of low-energy octahedral rotations cannot explain the presence of high-energy sidebands already at 10 K.

A survey of many compounds of the AMX_6 antifluorite family reveals a clear correlation between the Goldschmidt tolerance factor t and the structural transition temperature T_s from the high-temperature cubic phase to a phase with lower symmetry [27]. The Goldschmidt tolerance factor t is based on the atomic radii and usually provides a criterion for rotational phase transition in perovskites. For the antifluorite halides, Bertin *et al.* [27] find a critical value of $t \approx 1$ below which a rotational phase transition occurs, where T_s increases linearly with t decreasing below 1. For K_2IrCl_6, the tolerance factor amounts to 1.0019 [27], in agreement with the observation of cubic symmetry down to at least 0.3 K [28,29].

Local distortions may also result from strong magnetoelastic coupling that has been proposed based on very similar results for the double perovskite Ba_2CeIrO_6 [16], another compound with $j = 1/2$ moments forming an fcc lattice. Also Ba_2CeIrO_6 shows global cubic symmetry in x-ray diffraction measurements while RIXS reveals a splitting of the spin-orbit exciton of about 0.1 eV [15,16], roughly a factor two larger than in K_2IrCl_6. Exchange couplings on the fcc lattice are highly frustrated, and this frustration may be lifted by small distortions [16]. Such distortions may escape detection in diffraction experiments if they are either very small or show a short correlation length. According to Iwahara and Furukawa [35], an interpretation of the two-peak line shape of the spin-orbit exciton of K_2IrCl_6 in terms of a static crystal-field splitting requires a displacement of the Cl ligands of $\delta r = 0.007$ Å. Such distortions would cause deviations from the cubic structure, but corresponding Bragg peaks have not been found [27–29]. Using a cubic structure in the analysis of diffraction data, deviations from cubic symmetry can also be detected via anomalously large atomic displacement parameters. However, effects as small as $(\delta r)^2 < 10^{-4}$ Å^2 cannot be detected in the ADPs. Altogether, the structural data do not provide any evidence for deviations from cubic symmetry. On the contrary, a thorough analysis of the x-ray diffraction data (see also Ref. [27]) and the temperature dependence of the ADPs rather support cubic symmetry. Small distortions nevertheless cannot be excluded.

Scenario (ii) explains the two-peak structure of the RIXS spectra in terms of a vibronic character of the spin-orbit exciton, as recently proposed for K_2IrCl_6 [35]. Vibronic excitations emerge from the coupling between electronic and vibrational excitations [48–50]. An electronic excitation such as the spin-orbit exciton may change the charge-density distribution such that the lattice is not in its corresponding ground state, causing a series of phonon sidebands of a given electronic excitation. A basic example is given by the vibrational satellite lines observed in photoemission on H_2 molecules [62]. Suddenly removing an electron changes the equilibrium distance and leaves the molecule in a vibrationally excited state, i.e., the molecule rings. In K_2IrCl_6, this vibronic scenario does not break cubic symmetry in the $j = 1/2$ ground state.

With the simple two-peak structure of the RIXS data, an unambiguous distinction between the two scenarios is challenging. To resolve the origin of the splitting in K_2IrCl_6, we study the spin-orbit exciton with optical spectroscopy, making use of the excellent energy resolution. We will show that a vibronic character is the key to understand the peculiar spectra of K_2IrCl_6 in RIXS and optics. The vibronic sidebands reflect the hybridization of spin-orbit exciton and vibrational states, i.e., spin orbital lattice entanglement.

IV. SPIN-ORBIT EXCITON IN OPTICAL DATA

A. Phonon-assisted character

The optical conductivity $\sigma_1(\omega)$ in the energy range of the spin-orbit exciton is plotted in Fig. 3(b). The spin-orbit exciton is an intra-t_{2g} excitation. In $\sigma_1(\omega)$, such on-site d-d excitations are parity forbidden due to the presence of inversion symmetry on the Ir site. Finite spectral weight arises in a phonon-assisted process via the simultaneous excitation of an odd-parity phonon [48–51], which explains the complex line shape. Such weakly dipole-active excitations can be studied very well in the transparency window above the phonons and below the Mott gap, as reported recently for K_2ReCl_6 and K_2OsCl_6 [52,53] as well as for the spin-orbit exciton in α-$RuCl_3$ [38]. In K_2IrCl_6 at 10 K, we observe the onset of excitations across the Mott gap around 1.7 eV, see inset of Fig. 3(b). At the peak of the spin-orbit exciton, $\sigma_1(\omega)$ reaches values of about 5 $(\Omega\text{cm})^{-1}$, which is roughly two orders of magnitude smaller than for the directly dipole-allowed intersite excitations $|d_i^5 d_j^5\rangle \rightarrow |d_i^4 d_j^6\rangle$ across the Mott gap, see Appendix.

At 10 K, the phonon-assisted character is evident from the shift of the peak energy in $\sigma_1(\omega)$ compared to RIXS and from the strong increase of the spectral weight with increasing temperature [52,63]. Despite the different excitation mechanisms, the overall line shape of the spin-orbit exciton is very similar in RIXS and $\sigma_1(\omega)$ at 10 K. This is highlighted in Fig. 4, where both data sets have been shifted by the peak energy to roughly compensate for the phonon shift. The RIXS data have been measured with an energy resolution of $\delta E =$ 25 meV and show a strong main peak and smaller intensity at higher energy. Qualitatively, the optical data show a very similar behavior but resolve an additional fine structure. The corresponding subbands are due to a superposition of phonon-assisted processes for different symmetry-breaking phonon modes with phonon energies in the range of roughly 10 to 40 meV, as discussed below. This superposition enhances the overall line width despite the much better energy resolution. The assignment of the subbands provides the key to understand the character of the weaker high-energy features. To this end, we need to have a close look at the peak assignment in the optical data.

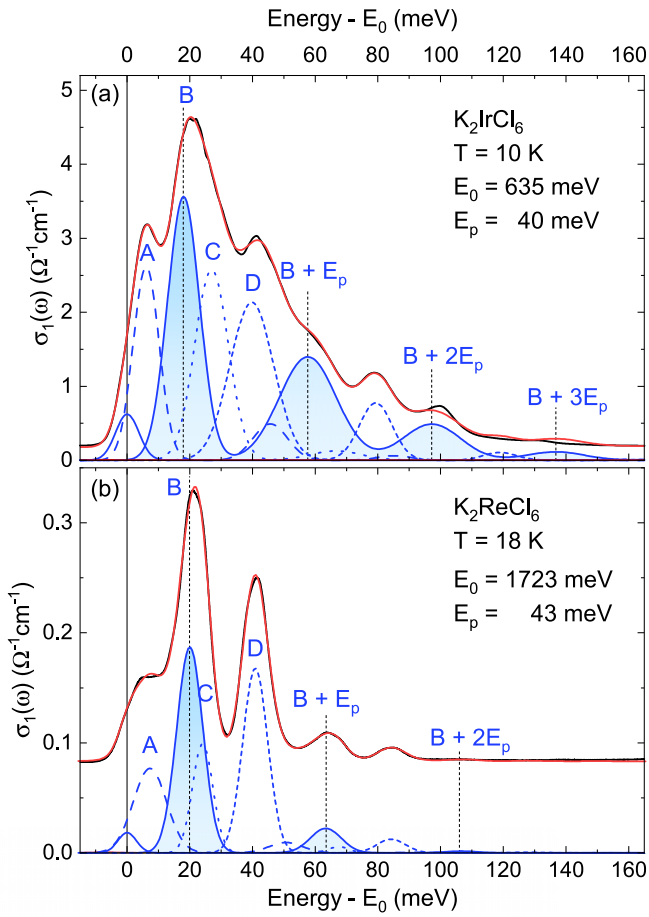

FIG. 6. Comparison of the line shape of $\sigma_1(\omega)$ for phonon-assisted intra-t_{2g} excitations in (a) K_2IrCl_6 and (b) its t_{2g}^3 sister compound K_2ReCl_6 [52]. The data (black) are shifted by the respective bare electronic energy E_0. The similar line shape underlines the common motif of four phonon-assisted excitations A–D, each dressed by a vibronic sideband progression (see main text). For peak B, this motif is emphasized by the blue shading. Note that A–D refer to processes involving odd-symmetry phonons that yield a finite spectral weight while E_p is the energy of an even mode, see Eq. (3) and Fig. 7. The weak mode at E_0 can be attributed to a magnetic dipole transition. The red line depicts the sum of the blue curves plus a small constant offset.

B. Assignment of phonon-assisted excitations

At 10 K, the dominant phonon-assisted peaks in $\sigma_1(\omega)$ occur at $E_0 + E_{odd}$, where $E_0 = 635$ meV is the energy of the bare electronic spin-orbit exciton while E_{odd} denotes the energy of a symmetry-breaking phonon mode. The cubic crystal structure of K_2IrCl_6 hosts four odd-symmetry optical phonon modes that have been observed at 10, 18, 23, and 41 meV in infrared spectroscopy and/or inelastic neutron scattering [32,64–66]. Given the quasimolecular crystal structure with separate $IrCl_6$ octahedra, the latter three of these modes can be viewed as the three odd-symmetry normal modes of a single $IrCl_6$ octahedron [48] while the fourth one is a lattice phonon mode. The main peaks in $\sigma_1(\omega)$ are well described by considering $E_{odd} = 6$, 18, 27, and 40 meV, see peaks A–D in Fig. 6(a). Taking into account that the symmetry-breaking modes do not have to be at the Γ point, the energies show good agreement with the values reported above, lending strong support to our peak assignment.

With increasing temperature, the spectral weight of a phonon-assisted process at $E_0 + E_{odd}$ increases with $1 + n(T)$, where $n(T)$ denotes the phonon occupation number of the odd-symmetry mode [48]. At finite temperatures, also phonon annihilation processes occurring at $E_0 - E_{odd}$ acquire spectral weight in $\sigma_1(\omega)$ that increases proportional to $n(T)$. The phonon-assisted character of the spin-orbit exciton in $\sigma_1(\omega)$ hence explains the different temperature dependence observed in RIXS and optics, in particular the strong overall increase of the spectral weight in $\sigma_1(\omega)$ with increasing temperature as well as the pronounced enhancement of absorption below E_0.

In the chloride, the energy E_{odd} of the symmetry-breaking phonons is limited to about 40 meV. The phonon-assisted character in $\sigma_1(\omega)$ hence explains the dominant spectral weight and the subbands in the range of roughly 0.64 to 0.68 eV. This does not yet reveal the nature of the weak features at higher energies, e.g., at 0.71, 0.74, and 0.77 eV, reaching energies as high as about $E_0 + 0.1$ eV. In general, a phonon-assisted character of the spin-orbit exciton is expected in $\sigma_1(\omega)$ as long as there is inversion symmetry on the Ir site. This phonon-assisted picture successfully has been used to describe the equivalent peaks of $IrCl_6$ impurities in different AMX_6-type host compounds such as cubic Cs_2ZrCl_6 or K_2SnCl_6 [67,68]. The data of these $IrCl_6$ impurities reveal the existence of vibronic sidebands. Remarkably, both the observed energies and the overall structure are very similar to our observations in single crystalline K_2IrCl_6.

V. VIBRONIC EXCITATIONS

A. Vibronic sidebands and the Franck-Condon principle

A vibronic character emerges from the coupling of electronic excitations to vibrational degrees of freedom. An on-site intra-t_{2g} excitation may give rise to a change of the charge distribution such that the lattice is not in its ground state anymore. This yields a series of phonon sidebands of the electronic excitation [48–50] and has been claimed to describe the RIXS data of K_2IrCl_6 [35].

In fact, vibronic sidebands of on-site intra-t_{2g} excitations are a common feature in the optical conductivity of the AMX_6 family, e.g., in the sister compounds K_2ReCl_6 and K_2OsCl_6 [52,53,69–72]. In RIXS measurements on the Os and Re halides, however, the energy resolution was not sufficient to resolve the vibronic character [52,53]. To put things into perspective, we consider the $5d^3$ compound K_2ReCl_6 that shows five different intra-t_{2g} excitations [52]. Optical data for one of them are depicted in Fig. 6(b). In $\sigma_1(\omega)$ of K_2ReCl_6, the subbands are very sharp and well resolved. The stronger peaks A–D reveal the subbands of the four odd phonon modes at $E_0 + E_{odd}$, demonstrating the phonon-assisted character [52]. On top, weak vibronic sidebands are resolved at $E_0 + E_{odd} + mE_p$, where mE_p with integer m denotes the energies of a phonon progression according to the Franck-Condon principle, see Fig. 7. For the data of K_2ReCl_6 in Fig. 6(b), the electronic excited state is a Γ_7 doublet [52]. An interpretation

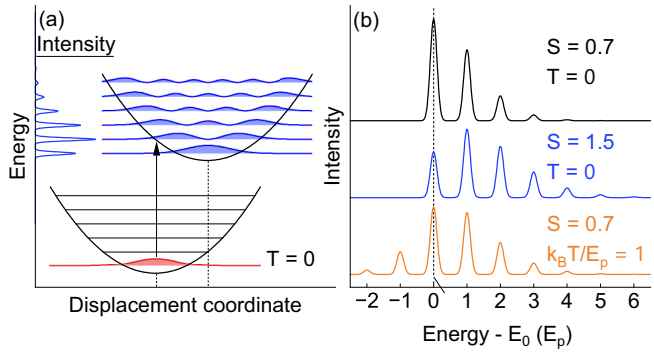

FIG. 7. Sketch of vibronic excitations in optical absorption according to the Franck-Condon principle. (a) Excitation from the ground state at $T = 0$ (red) to vibronic excited states (blue). The two parabolas depict the harmonic lattice potential with phonon excitations, where the shaded area gives the squared amplitude of the wavefunction. The parabola of the electronic excited state is shifted horizontally since a change of the charge distribution affects the equilibrium positions of the ions for finite electron-phonon coupling g. The arrow corresponds to a "vertical" transition according to the Franck-Condon principle, assuming a negligible timescale for electronic excitations. On the left (blue lines), the evenly spaced comb of peaks with splitting E_p illustrates the resulting excitation spectrum. (b) Examples of the Franck-Condon line shape for different values of the Huang-Rhys factor S, see Eq. (3). The orange line corresponds to a finite temperature $T = E_\mathrm{p}/k_\mathrm{B}$. For clarity, the curves are offset vertically.

of the high-energy sidebands in terms of crystal-field splitting is hence not applicable. These features unambiguously are of vibronic character. Remarkably, a very similar sideband structure has been observed for all five intra-t_{2g} excitations in K_2ReCl_6 [52]. This common motif also applies to the data of K_2IrCl_6 in Fig. 6(a).

The Franck-Condon principle offers a simplified, analytic, and intuitive description of the vibronic line shape. It assumes that the timescale of electronic excitations is negligible compared to phonon timescales. For an optical absorption process, this corresponds to an instantaneous, "vertical" transition from the electronic ground state to the excited state, see Fig. 7(a), where "vertical" implies no change on the horizontal axis that denotes a generalized displacement coordinate. For illustration and simplicity, we assume that there is only one odd-symmetry mode with energy E_odd that is relevant for the optical conductivity but not for RIXS. Furthermore, we assume that the electronic excited state is a Kramers doublet and that there is one dominant phonon mode with energy E_p that governs the progression of vibronic sidebands. Neglecting the entanglement between electronic and lattice degrees of freedom, the vibronic sidebands are shifted by mE_p in the Franck-Condon approximation, i.e., they yield an evenly spaced comb of peaks at $E_m = E_0 + E_\mathrm{odd} + mE_\mathrm{p}$ in $\sigma_1(\omega)$. At $T = 0$, the line shape for optical absorption is described by [48,73]

$$I(E) = I_0 \sum_{m=0}^{\infty} \frac{e^{-S}\, S^m}{m!}\, \delta(E_0 + E_\mathrm{odd} + mE_\mathrm{p} - E) \qquad (2)$$

with $\sigma_1(E) = I(E)E$, where I_0 is proportional to the squared dipole matrix element of the (phonon-assisted) electronic transition, $e^{-S}\, S^m/m!$ is the Franck-Condon factor, and S is the Huang-Rhys factor, which is equivalent to the average number of phonons that are present in the excited state. It is a measure of the electron-phonon coupling constant g and governs the line shape. A large value of S creates an envelope with a more Gaussian-like intensity distribution while a small S yields an asymmetric envelope, see Fig. 7(b). At finite temperatures, one has to consider the thermal occupation of the sideband phonon modes, $n_p = 1/[\exp(E_\mathrm{p}/k_\mathrm{B}T) - 1]$. The sum hence has to include negative values of m [48,73],

$$I(E) = I_0 \sum_{m=-\infty}^{\infty} \left(\frac{n_p + 1}{n_p}\right)^{m/2} J_m(2S\sqrt{n_p(n_p+1)}) \times e^{-S(2n_p+1)}\ \ \delta(E_0 + E_\mathrm{odd} + mE_\mathrm{p} - E), \qquad (3)$$

where J_m is the modified Bessel function of m^th order. For comparison with experiment, we replace the δ function in Eq. (3) with a Gaussian profile. This yields excellent agreement with $\sigma_1(\omega)$ of $5d^3$ K_2ReCl_6, see Fig. 6(b). The experimental spectrum can be described by a superposition of such Franck-Condon progressions for all four odd-symmetry phonon modes. In K_2ReCl_6, most of the spectral weight is in the peaks of order $m = 0$ with only a small contribution of $m = 1$ and basically negligible spectral weight for $m = 2$. This intensity distribution corresponds to a small Huang-Rhys factor $S = 0.14$. This reflects the spin-forbidden character of the excitation in K_2ReCl_6 that is observed at about $5J_H$, where J_H denotes Hund's coupling. The excitation roughly can be viewed as a flip of the spin of one electron in the t_{2g}^3 configuration, which causes only a small change of the charge distribution and corresponds to a small S. The same approach also yields an excellent description of $\sigma_1(\omega)$ of K_2IrCl_6, see Fig. 6(a). The blue shading highlights the Franck-Condon sidebands of peak B with a larger but still small value of $S \approx 0.7$. The larger S yields detectable spectral weight of the peaks of order $m = 2$ and even 3. Thereby, the vibronic model naturally explains the large number of peaks and the existence of weak features at energies as high as 0.74 and 0.77 eV, more than 0.1 eV above the bare electronic excitation energy $E_0 = 635$ meV.

Thus far we discussed the Franck-Condon approximation for an optical excitation. We claim that Eq. (3) can also be applied to vibronic sidebands of an electronic excitation studied in direct RIXS, which is supported by the overall agreement of the line shapes shown in Fig. 4. Note that the case is different for elementary phonons and multi-phonons. These are excited in an *indirect* RIXS process that can be approximated by using two Franck-Condon factors [74–77], see Sec. V D. For K_2IrCl_6, Eq. (3) provides an excellent empirical description of our RIXS spectra, see Fig. 8. At 10 K, the fit yields $S = 0.30$, $E_\mathrm{p} = 44$ meV, and the bare electronic energy $E_0 = 633$ meV. With an energy resolution of 25 meV, the latter agrees very well with $E_0 = 635$ meV found in $\sigma_1(\omega)$. In the next paragraph, we discuss E_p to collect evidence for the spin orbital lattice entangled character.

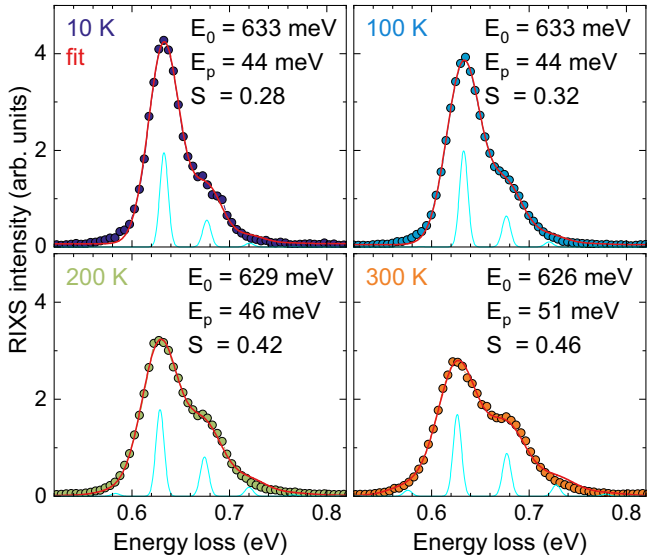

FIG. 8. Vibronic fits of the RIXS data at different temperatures using the Franck-Condon picture from Eq. (3). In each panel, we state the energy E_0 of the bare electronic excitation, the energy E_p of the phonon progression mode, and the Huang-Rhys factor S. The red lines depict the full fit. Cyan curves illustrate the phonon progression of sidebands for the same parameters with 10 meV width of the Gaussian profile and reduced total intensity.

B. Beyond the Franck-Condon approximation

The Franck-Condon principle is valuable for an intuitive explanation of the overall line shape. For a microscopic description of K_2IrCl_6, Iwahara and Furukawa [35] treated electron-phonon coupling g and spin-orbit coupling λ on the same footing. They find that the spin-orbit exciton with its vibronic sidebands is of spin orbital lattice entangled character. Strictly speaking, the simple picture of the simultaneous excitation of a spin-orbit exciton and one or several phonons, causing a comb of equidistant peaks, is only applicable for $g \to 0$, in which case the intensity of the sidebands vanishes. For finite g, the excitation spectrum is more complex. Iwahara and Furukawa [35] predict a larger number of peaks but many of them are small and hard to resolve experimentally. Furthermore, hybridization shifts the energies such that the sidebands are not equidistant anymore. In K_2IrCl_6, however, we can only determine two peak energies in RIXS, and the complex line shape of the phonon-assisted excitations in $\sigma_1(\omega)$ does not allow us to clearly identify deviations from a comb-like behavior. The hybridized character may also give rise to differences in line shape between RIXS and $\sigma_1(\omega)$, e.g., due to the presence of the symmetry-breaking phonon mode in the case of the optical data. However, we are lacking a theoretical prediction for such differences. From an experimental point of view, the hybridized character at this stage can be detected in the value of the peak splitting, which is captured by E_p in Eq. (3).

At 10 K, the fits yield $E_p = 40$ meV in $\sigma_1(\omega)$ and 44 meV in RIXS, see Figs. 6(a) and 8. In general, the even electronic excitations may couple to phonons of a_{1g}, e_g, and t_{2g} symmetry [78], where the latter usually is neglected. The elementary phonon modes of a_{1g} and e_g symmetry have been observed in Raman scattering at 44 and 37 meV, respectively [31]. In the Franck-Condon approximation, the experimental splitting thus appears to suggest a predominant coupling to the a_{1g} mode, the breathing mode of the $IrCl_6$ octahedron. This applies if, e.g., both the electronic ground state and the excited state show cubic symmetry, which is the case for ideal $j = 1/2$ and $3/2$ states. For the doublet excited state of K_2ReCl_6 addressed in Fig. 6(b), the phonon sidebands with $E_p = 43$ meV have been attributed to the a_{1g} mode [52,70]. However, the situation is different in K_2IrCl_6 due to the degeneracy of the excited $j = 3/2$ quartet that is lifted by coupling to the Jahn-Teller active e_g phonon mode [35]. In this case, the energy splitting between the lowest two strong RIXS peaks roughly is given by $E_p(1 + g^2/8)$. Note that g is dimensionless in the definition of Ref. [35]. With $E_p = 37$ meV for the e_g mode and $g = 1.2$, Iwahara and Furukawa find a splitting of 45 meV between the two strongest peaks in the calculated RIXS response, in excellent agreement with the experimental data at 10 K. The fact that the splitting depends on g reflects the dynamic Jahn-Teller effect, lifting the degeneracy of the $j = 3/2$ quartet. This is in particular relevant for the temperature dependence of the splitting, as discussed in the next paragraph. Strictly speaking, the splitting also depends on λ due to a finite admixture of $j = 1/2$ character via the pseudo-Jahn-Teller effect [35,79]. This, however, is small and can be neglected.

C. Temperature dependence

The convincing description of the temperature dependence of the RIXS data is a particular asset of the vibronic scenario. Using $g = 1.2$, Iwahara and Furukawa [35] showed that a vibronic model with spin orbital lattice entangled states describes the temperature dependence observed in RIXS. First, we address the qualitative behavior of the experimental data, see Figs. 3(a) and 8. This can be understood within the Franck-Condon picture, see Eq. (3) and the black and orange lines in Fig. 7(b). The thermal occupation of phonon modes gives rise to a redistribution of the intensity to high energies as well as to the range below the main peak, where the latter can be attributed to the emergence of a subband at $E_0 - E_p$.

As at 10 K, a quantitative analysis reveals fingerprints of the entangled character. With increasing temperature, the fit yields an increase of the peak splitting E_p and of S and a modest red shift of E_0, see Fig. 8. Remarkably, the behavior of all three observations is in line with an increase of the electron-phonon coupling constant g. An increase of g enhances S and, in a spin orbital lattice entangled scenario [35], reduces the energy E_0 of the main peak via the dynamic Jahn-Teller effect while increasing the splitting $E_p(1 + g^2/8)$ of the dominant RIXS peaks, as discussed above. In fact, the fit yields a splitting as large as 51 meV at 300 K. This is hard to reconcile with the phonon energies of the chloride in a Franck-Condon scenario but can be attributed to the g dependence of the splitting in a spin orbital lattice entangled picture.

A further contribution to the 1% reduction of E_0 may originate from thermal expansion of the lattice and a corresponding increase of the Ir-Cl distance. This modifies the cubic crystal field 10 Dq and thereby the effective value of λ. For the cubic

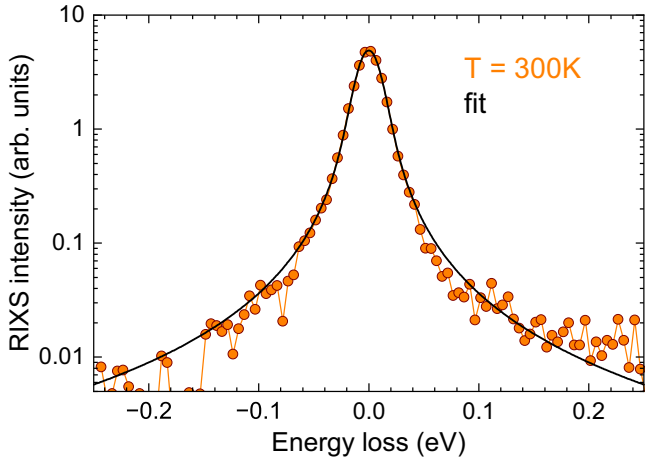

FIG. 9. RIXS data of K_2IrCl_6 around zero energy loss at 300 K. The data are plotted on a logarithmic scale to emphasize the tails of the elastic line that is fitted using a Voigt line shape with the instrumental resolution $\delta E = 25$ meV. The symmetric behavior around zero loss down to the noise level of about 0.01 provides no indication of low-energy excitations. In particular, the intensity of phonons is negligible in RIXS at the Ir L_3 edge.

phase of K_2IrBr_6, the peak splitting has been reported by Khan *et al.* [30] to increase from about 50 meV at 170 K to 70 meV at 300 K, while Reig-i-Plessis *et al.* find a smaller value of 47 meV at 300 K [29]. This discrepancy may originate from the line shape of the spin-orbit exciton in K_2IrBr_6 which rather shows a subtle shoulder instead of a clear splitting.

The temperature dependence of $\sigma_1(\omega)$ predominantly reflects the phonon-assisted character, which causes a pronounced increase of the spectral weight. The many subbands visible at 10 K are smeared out at elevated temperatures, see Fig. 3(b). Therefore we refrain from fitting $\sigma_1(\omega)$ at high temperature.

D. Phonons and phonon sidebands

The observation of vibronic "phonon" sidebands is particularly interesting given the fact that the intensity of elementary phonon excitations is negligible in L-edge RIXS on $5d^5$ Ir^{4+} $j = 1/2$ Mott insulators [42]. For K_2IrCl_6, this is highlighted in Fig. 9, which focuses on the RIXS response around zero loss. The data have been measured with a scattering angle 2θ close to 90°, which yields an elastic line of moderate strength. The symmetric behavior around zero loss is emphasized by a fit with a Voigt profile. The data are very well described by considering only the elastic line and do not provide any evidence for a sizable inelastic contribution below 0.1 eV. Even at 300 K, where the intensity of low-energy modes is enhanced by the Bose factor, the contribution of phonons is negligible.

In L-edge RIXS on Mott-insulating $5d^5$ iridates, spin and orbital excitations are boosted in a direct RIXS process [80]. The x-ray absorption step from the ground state to the intermediate state is followed by the x-ray emission step from the intermediate state to the final state. In general, phonons are excited with a much smaller cross section in *indirect* RIXS, i.e., via the dynamics in the *intermediate* state. In RIXS, a phonon is created if the lattice distorts in the intermediate state to screen the core hole [74–77,81]. A simplified description of phonon excitations can again be achieved in a Franck-Condon picture. However, with the coupling taking place in the intermediate state, one has to use *two* Franck-Condon factors, one for the absorption step, and the second one for x-ray emission [74–77]. For L-edge RIXS with an incident energy as large as 11.214 keV, the absence of any phonon signatures can be rationalized via the Ir $2p^5\ t_{2g}^6$ intermediate state, which is well screened and shows a short life time of only a few femtoseconds. In contrast, phonon contributions can be observed in RIXS on Ir oxides at the O K edge due to the very different intermediate state [40,74–76].

Previously, this phonon approach with two Franck-Condon factors has also been applied to vibronic sidebands of on-site d-d excitations studied in RIXS at the O K edge, e.g., in Li_2CuO_2 and α-Li_2IrO_3 [40,82], as well as at the Cu L edge in $Ca_2Y_2Cu_5O_{10}$ [43]. In our data of K_2IrCl_6, measured at the Ir L_3 edge, indirect RIXS processes are negligible. The spin-orbit exciton and its vibronic sidebands are resonantly enhanced in a direct RIXS process due to the electronic contribution to the wave function. Empirically, the data are described by Eq. (3), where the squared matrix element of the electronic transition in direct RIXS yields I_0. As in optical absorption, the electronic excitation leaves the system in a vibrationally excited state, see Fig. 7. In this sense, the coupling to the lattice occurs in the final state, in contrast to the case of elementary phonons discussed above.

VI. DOUBLE SPIN-ORBIT EXCITON

The excitation of double spin-orbit excitons in the optical conductivity around 1.3 eV provides a further example for a vibronic excitation in K_2IrCl_6, see Fig. 10(a). The feature is very weak, the integrated spectral weight being roughly a factor 30 smaller than for the single spin-orbit exciton, see inset of Fig. 3(b). Even such weak features can be determined accurately from the transmittance data measured on a sample with a thickness of 380 μm. At 10 K, the energy of the first peak $E_{2SO} = 1286$ meV $= 2 \times 643$ meV is very close to twice the energy $E_0 = 635$ meV for the single spin-orbit exciton. This peak at 1.3 eV can hence be assigned to the simultaneous excitation of two spin-orbit excitons on neighboring sites. Double and even triple spin-orbit excitons previously have been observed in $\sigma_1(\omega)$ of the $4d^5$ $j = 1/2$ compound α-$RuCl_3$ [38,39]. Similar overtones or double intra-t_{2g} excitations have also been reported in orbitally ordered YVO_3 as well as in K_2ReCl_6 and K_2OsCl_6 [52,53,71,83].

Figure 10(b) shows the spectral weight of the double spin-orbit exciton (blue) as a function of temperature, normalized to the value at 10 K. The data of $\sigma_1(\omega)$ have been integrated from 1.2 to 1.4 eV after subtraction of a constant background. The plot also shows the pronounced temperature dependence of the spectral weight of the single spin-orbit exciton (red), which reflects the phonon-assisted character. In comparison, the spectral weight of the double spin-orbit exciton is insensitive to temperature at least up to 200 K (full blue symbols). At still higher temperature, the double spin-orbit exciton drowns in the onset of excitations across the Mott gap that shifts to lower energies with increasing temperature,

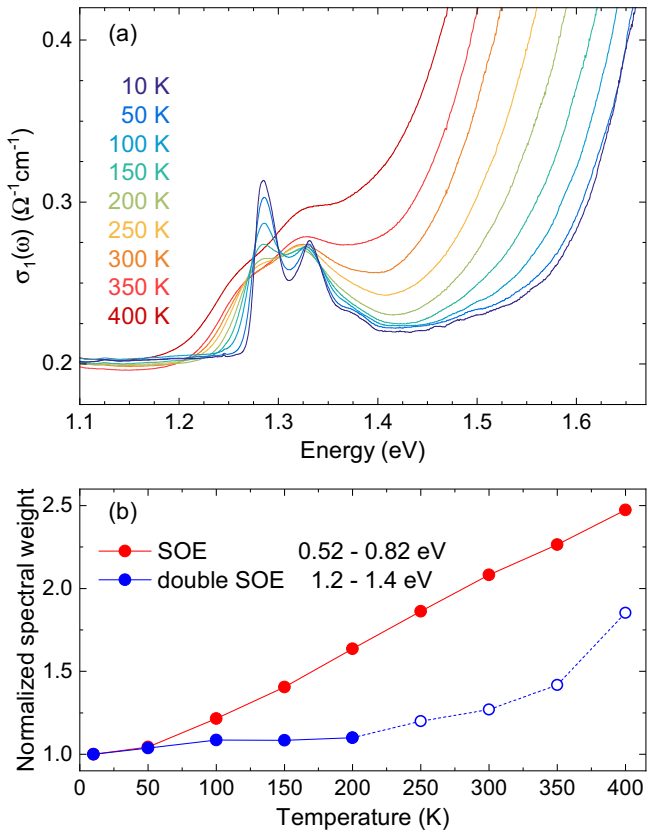

FIG. 10. (a) Double spin-orbit exciton around 1.3 eV with vibronic sidebands. Up to about 200 K, the three-peak structure of this very weak absorption band is located right below the onset of excitations across the Mott gap. (b) Normalized spectral weight of the single (red) and double (blue) spin-orbit excitons (SOE). The integration ranges are given in the plot. Before integration, a constant background has been subtracted from the data of $\sigma_1(\omega)$. The open symbols above 200 K indicate that the increase of spectral weight between 1.2 and 1.4 eV at high temperatures predominantly is caused by excitations across the Mott gap.

causing the increase of spectral weight in the considered energy range (open symbols). The almost temperature-independent spectral weight suggests that the double spin-orbit exciton is *not* phonon-assisted but rather directly infrared allowed, even though with a very small spectral weight. This agrees with results on K_2ReCl_6 and K_2OsCl_6 [52,53]. A finite dipole moment may arise if the total excited state breaks inversion symmetry on the bond. This is, e.g., the case for a spin-orbit exciton with $j_z = 3/2$ on one site but $j_z = 1/2$ on the neighboring site. At 10 K, the splitting between the main peak at $E_{2SO} = 1286$ meV and the first sideband amounts to 46 meV. The splitting between the second peak and the weak third peak is comparable but the large width prevents a more precise determination. The value of 46 meV is very similar to the vibronic splitting of the spin-orbit exciton, see Fig. 8, as well as to the vibronic splitting observed for the overtones in K_2ReCl_6 [52]. The line shape, the experimental peak splitting, and the analogy with the sister compound K_2ReCl_6 provide strong evidence for a vibronic character of the double spin-orbit exciton.

VII. DISCUSSION AND CONCLUSION

Spin-orbit entangled $j = 1/2$ moments are Kramers doublets and as such not Jahn-Teller active. In frustrated quantum magnets, magnetoelastic coupling nevertheless may give rise to distortions that break cubic symmetry and lift magnetic frustration in $j = 1/2$ compounds [16]. A possibly pronounced magnetoelastic coupling would play an essential role for the low-energy physics of $j = 1/2$ quantum magnets. We combined RIXS, optical spectroscopy, and single-crystal x-ray diffraction to study the possible role of magnetoelastic coupling in antifluorite-type K_2IrCl_6 with $j = 1/2$ moments on an fcc lattice with highly frustrated exchange couplings. The global cubic structure of K_2IrCl_6 is well established [27–29]. The sizable atomic displacement parameters reported for K_2IrCl_6 at elevated temperatures [27,28] exhibit a linear temperature dependence, underlining their dynamical origin based on rigid, low-energy rotations of the $IrCl_6$ octahedra. Even though the diffraction data do not provide any indication for deviations from cubic symmetry, the presence of local distortions cannot fully be excluded. Small distortions are a challenge for diffraction experiments and often are detected more easily in spectroscopy based on, e.g., a change of selection rules. The two-peak structure of the spin-orbit exciton observed in L-edge RIXS around 0.63 eV can be attributed to either a noncubic crystal-field splitting or to a vibronic character with phonon sidebands. Optical spectroscopy provides complementary information based on the excellent energy resolution and the different excitation process with different selection rules. We observe a multitude of phonon-assisted peaks in $\sigma_1(\omega)$ that reach as high as 0.74 and 0.77 eV. These features require an explanation in terms of vibronic sidebands, in agreement with previous results on $IrCl_6$ impurities in host crystals [67,68], with the vibronic character of the double spin-orbit exciton that we find around 1.3 eV, and with optical results on related intra-t_{2g} excitations in the sister compounds K_2ReCl_6 and K_2OsCl_6 [52,53]. Furthermore, the vibronic picture is able to describe the temperature dependence observed in RIXS [35]. The success of the vibronic scenario suggests that magnetoelastic coupling is not decisive for the stability of the $j = 1/2$ moments in K_2IrCl_6. Altogether, we conclude that K_2IrCl_6 hosts cubic $j = 1/2$ moments and spin orbital lattice entangled $j = 3/2$ excited states.

This spin orbital lattice entangled nature of the spin-orbit exciton is caused by electron-phonon coupling that yields a hybridization of the Jahn-Teller active $j = 3/2$ quartet with vibrational states [35]. The Franck-Condon approximation offers an analytic description of the vibronic line shape. It assumes a negligible timescale for electronic excitations, approximating the eigenstates as product states of electronic and vibrational states. Empirically, the Franck-Condon approach describes the data of RIXS and optics well and in an intuitive way. Equivalent to the analysis of optical data, a single Franck-Condon factor is appropriate to describe vibronic excitations studied in *direct* RIXS. This differs from the case of elementary phonons that contribute in an indirect RIXS process, and we have shown that this contribution is negligible in our L-edge RIXS data of K_2IrCl_6. This intuitively highlights the particular character of the vibronic "phonon" sidebands of the spin-orbit exciton, for which resonance enhancement in direct RIXS applies to the electronic part of the wave function.

A more detailed quantitative description of the experimental data reveals the limitations of the Franck-Condon scenario, in which the splitting is equal to the phonon energy. In particular, the large splitting of 44 meV observed at 10 K and even 51 meV at 300 K is hard to reconcile with an elementary phonon energy in K_2IrCl_6. In contrast, a theory describing the microscopic coupling of the spin-orbit entangled states to the e_g phonon mode with energy E_p yields $E_p(1 + g^2/8)$ for the splitting of the first two strong RIXS peaks [35]. We thus conclude that the large splitting and its temperature dependence are fingerprints of the spin orbital lattice entangled character beyond the Franck-Condon approximation.

Concerning L-edge RIXS, the well resolved vibronic sideband in K_2IrCl_6 stands out in transition-metal compounds in general as well as compared to other $5d^5$ iridates. The splittings larger than 0.1 eV observed in Ir^{4+} oxides [12,13,15–26] are caused by a noncubic crystal field. Vibronic sidebands of electronic excitations have been claimed in $Ca_2Y_2Cu_5O_{10}$ [43], K_2RuCl_6 [44], as well as in $5d^1$ compounds based on the asymmetric line shape of the excitation from $j = 3/2$ to $1/2$ [41,46], but individual peaks have not been resolved. Typically, the subbands of vibronic excitations are not resolved in solids, even in optical data. However, the vibronic features are particularly sharp in $\sigma_1(\omega)$ of K_2ReCl_6 [52] and still very well resolved in K_2IrCl_6, even in RIXS. This can be attributed to the quasimolecular crystal structure with well separated MCl_6 octahedra. The antifluorite-type A_2MX_6 compounds thus offer an ideal platform to further investigate the role of vibronic effects in RIXS. In this context, it may be interesting to reanalyse RIXS data of the related fluorides such as K_2IrF_6 [14]. They exhibit a sizable trigonal crystal-field splitting of the spin-orbit exciton with peaks at about 0.80 and 0.91 eV. However, a weak third peak at about 1 eV cannot be explained by the trigonal crystal field and may correspond to a vibronic sideband in the case of a noncubic crystal field.

Finally, we summarize the implications of our results for future research beyond K_2IrCl_6. The fact that ideal $j = 1/2$ moments can be realized despite magnetic frustration and finite magnetoelastic coupling is a promising result for the quest for quantum spin liquids that make use of the peculiar exchange interactions of $j = 1/2$ moments. Furthermore, our results highlight the relevance of vibronic coupling for the analysis of RIXS data, in particular for the interpretation of apparent peak splittings. For vibronic features, the data from RIXS and optical spectroscopy can be described using a common empirical approach with a single Franck-Condon factor. The combination of the two spectroscopies is particularly powerful for unraveling the character of an excitation and for such challenging tasks as revealing the spin orbital lattice entangled nature. Compounds with quasimolecular crystal structure are ideal for better understanding the experimental signatures of spin orbital lattice entangled states.

Note added. Recently, Wang *et al.* [84] reported inelastic neutron scattering data of the magnetic excitations of K_2IrCl_6. They discuss the existence of a nodal-line spin liquid and fluctuation-stabilized magnetic order arising from the competition of Heisenberg and Kitaev exchange with an energy scale of less than 1 meV. In agreement with our results, they employ cubic $j = 1/2$ moments and find that magnetoelastic coupling is negligible. Furthermore, they report the x-ray pair-distribution function at 300 K and find a single Ir-Cl distance with no evidence for structural distortions, again in agreement with our results.

TABLE I. Anisotropic atomic displacement parameters U_{ij}, derived from crystal structure determination by single crystal x-ray diffraction. The data were measured in the sequence from 290 to 120 K (I) and back to 290 K (II). Figure 5 shows the average of I and II. All U_{ij} are given in units of Å^2.

T (K)		U_{11}(Ir)	U_{11}(Cl)	U_{22}(Cl)	U_{11}(K)
290	I	0.01584(8)	0.0166(3)	0.0425(3)	0.0382(3)
	II	0.01557(7)	0.0164(2)	0.0422(2)	0.0379(2)
270	I	0.01466(7)	0.0153(2)	0.0397(2)	0.0353(2)
	II	0.01475(7)	0.0156(2)	0.0399(2)	0.0355(2)
250	I	0.01360(8)	0.0138(3)	0.0373(3)	0.0327(3)
	II	0.01354(7)	0.0145(2)	0.0369(2)	0.0327(2)
230	I	0.01219(6)	0.01285(18)	0.03407(17)	0.02996(17)
	II	0.01250(7)	0.0132(2)	0.0346(2)	0.0302(2)
210	I	0.01140(7)	0.0120(2)	0.0317(2)	0.0277(2)
	II	0.01157(7)	0.0121(2)	0.0320(2)	0.0279(2)
190	I	0.01035(6)	0.0110(2)	0.02898(19)	0.02500(19)
	II	0.01045(7)	0.0110(2)	0.0290(2)	0.0250(2)
170	I	0.00930(6)	0.00981(19)	0.02660(18)	0.02249(17)
	II	0.00931(7)	0.0098(2)	0.0263(2)	0.0226(2)
150	I	0.00836(6)	0.0090(2)	0.02420(18)	0.02019(18)
	II	0.00793(5)	0.00871(16)	0.02343(14)	0.01984(14)
130	I	0.00759(12)	0.0082(3)	0.0216(3)	0.0180(3)
	II	0.00729(6)	0.00797(19)	0.02123(17)	0.01761(16)
120	I	0.00686(6)	0.00739(19)	0.02010(17)	0.01635(16)

The data shown in the figures is available on Zenodo [85].

ACKNOWLEDGMENTS

We thank K. Hopfer and H. Schwab for experimental support and the European Synchrotron Radiation Facility for providing beam time at ID20 under proposal number HC-4491 and technical support. Furthermore, we acknowledge funding from the Deutsche Forschungsgemeinschaft (DFG, German Research Foundation) through Project No. 277146847–CRC 1238 (projects A02, B02, B03) as well as from the European Union Next Generation EU - PNRR - M4C2, investimento 1.1 - Fondo PRIN 2022 - Superlattices of relativistic oxides (ID 2022L28H97, CUP D53D23002260006).

APPENDIX

1. Crystal structure determination

The x-ray diffraction experiments for a crystal of K_2IrCl_6 with dimensions of 0.072 × 0.059 × 0.049 mm^3 were performed on a Bruker D8 VENTURE Kappa Duo PHOTONIII diffractometer with a IμS microfocus sealed tube (Mo K_α radiation, 0.71073 Å). Using an Oxford Cryostream Cooler800, we collected data between 290 and 120 K. The crystal structure was solved by direct methods (SHELXT) [86] and refined by full matrix least squares based on F^2 (SHELXL2019) [87]. Multiscan absorption correction was applied. The anisotropic atomic displacement parameters U_{ij} are given in Table I. The

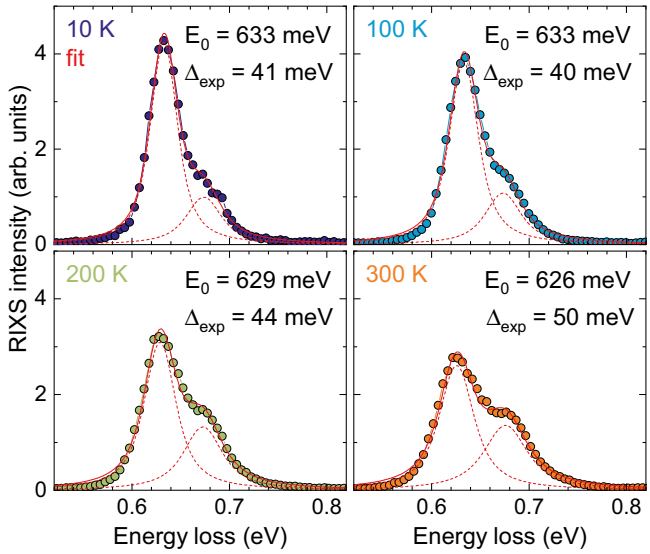

FIG. 11. Fits of the RIXS data using two Voigt profiles. The two features (dashed) are peaking at E_0 and $E_0 + \Delta_{exp}$. The solid red line depicts the sum.

data were obtained by first cooling down in steps from 290 to 120 K, while a second set of data points was measured upon heating back to 290 K.

The x-ray crystallographic data have been deposited at the Inorganic Crystal Structure Database via the joint CCDC/FIZ Karlsruhe deposition service, see Ref. [88] for more information.

2. Two-peak fit of RIXS

Phenomenologically, the apparent two-peak structure of the RIXS data can also be described by employing two oscillators with a Voigt line shape, see Fig. 11. The Voigt profile corresponds to a convolution of Gaussian and Lorentzian peaks. For the Gaussian part we use the instrumental width determined from the elastic line. These fits yield the energy E_0 of the dominant peak and the peak splitting Δ_{exp} of 40 to 50 meV. Compared to the vibronic fit shown in Fig. 8, we find the same result for E_0 while the peak splitting Δ_{exp} is slightly smaller than the phonon progression energy E_p. The agreement between the two-peak Voigt fits and the experimental data does not achieve the same quality as for the vibronic fits shown in Fig. 8. This applies in particular to the low-frequency side below 0.6 eV and reflects the extended tails of the Lorentzian contribution.

3. Optical conductivity above the Mott gap

We address the optical conductivity at higher energies to put the phonon-assisted features into context. Figure 12 shows $\sigma_1(\omega)$ above the Mott gap as determined by ellipsometry. Above about 4 eV, we observe charge-transfer excitations between Ir and Cl sites. In the energy range from 2 to 3.5 eV, we find Mott-Hubbard excitations across the Mott gap, i.e., *intersite* excitations $|d_i^5 d_j^5\rangle \rightarrow |d_i^4 d_j^6\rangle$ between the Ir sites i and j. Compared to *on-site d-d* excitations such as the spin-orbit exciton, the value of $\sigma_1(\omega)$ for these directly dipole-allowed excitations is about two orders of magnitude

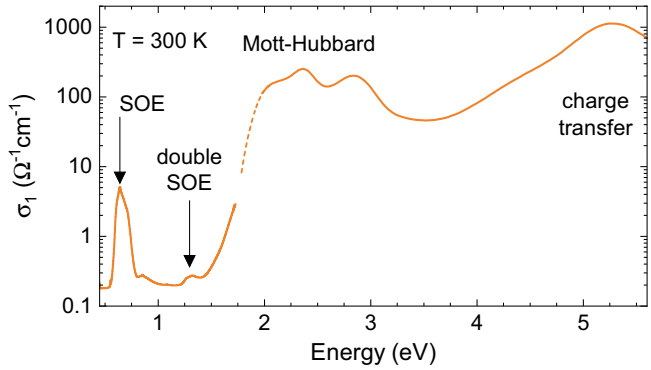

FIG. 12. Optical conductivity up to 5.6 eV at room temperature. Data above the Mott gap have been determined by ellipsometry measurements. Note the logarithmic scale. Above the Mott gap, $\sigma_1(\omega)$ is roughly two orders of magnitude larger than for the spin-orbit exciton. The dashed line depicts a fit that assumes a Tauc-Lorentz shape of the Mott gap.

larger. Accordingly, the strong intersite excitations cover the on-site crystal-field excitations from t_{2g} to e_g states. These are peaking in the energy range from 2.5 to 3.5 eV in RIXS on K_2IrCl_6 [29] but are not visible in the optical data. Considering the additional energy cost of the on-site Coulomb repulsion U for intersite excitations across the Mott gap, the two lowest peaks at about 2.4 and 2.9 eV have to be attributed to t_{2g} states. Their energies can be rationalized in terms of local multiplets. This approach is corroborated by the observation that the spectral weight of such intersite excitations in many transition-metal compounds reflects spin and orbital correlations between nearest neighbors [89–96]. In this picture, the lowest $|d_i^4 d_j^6\rangle$ excited states exhibit a $t_{2g}^6\ ^1A_1$ multiplet on site j while site i hosts a t_{2g}^4 multiplet with either $^3T_1$ or $^1T_2/^1E$ symmetry. In a t_{2g}-only picture, the corresponding excitation energies $E(t_{2g}^4) + E(t_{2g}^6) - 2E(t_{2g}^5)$ amount to $U - 3J_H$ and $U - J_H$ [97]. The energy difference of 2 J_H is reduced to about 1.5 J_H upon taking into account the interaction with e_g orbitals [53]. The observed energy difference of 0.5 eV thus agrees with the expectation $J_H \approx 0.3 - 0.4$ eV [53,98,99].

Finally, we want to point out the close relation to intersite excitations in d^1 compounds such as Mott insulating $YTiO_3$ [94]. There, the energy of the $|d_i^0 d_j^2\rangle$ excited states is governed by two-electron t_{2g}^2 multiplets that show the same symmetry as the two-hole t_{2g}^4 states discussed above for K_2IrCl_6. Remarkably, the lowest intersite excitation in $YTiO_3$, involving the $^3T_1$ multiplet, exhibits a two-peak structure that has been explained in terms of a Mott-Hubbard exciton [94] for which the energy is reduced by the Coulomb interaction of an electron-hole pair on nearest-neighbor sites as well as by magnetic and orbital correlations. The term Mott-Hubbard exciton is employed not only for truly bound excitons below the Mott gap but also for a nearly-bound resonance within the continuum, as observed in $YTiO_3$. Mott-Hubbard excitons have been discussed also for the $5d^5$ iridates Na_2IrO_3 and Sr_2IrO_4 [100,101]. In this light, one may speculate that the pronounced shoulder at 2 eV of the peak at 2.5 eV in $\sigma_1(\omega)$ of K_2IrCl_6 also reflects nearest-neighbor Coulomb interactions.

[1] W. Witczak-Krempa, G. Chen, Y. B. Kim, and L. Balents, Correlated quantum phenomena in the strong spin-orbit regime, Annu. Rev. Condens. Matter Phys. **5**, 57 (2014).

[2] J. G. Rau, E. Kin-Ho Lee, and H.-Y. Kee, Spin-orbit physics giving rise to novel phases in correlated systems: Iridates and related materials, Annu. Rev. Condens. Matter Phys. **7**, 195 (2016).

[3] R. Schaffer, E. Kin-Ho Lee, B.-J. Yang, and Y. B. Kim, Recent progress on correlated electron systems with strong spin-orbit coupling, Rep. Prog. Phys. **79**, 094504 (2016).

[4] H. Takagi, T. Takayama, G. Jackeli, G. Khaliullin, and S. E. Nagler, Concept and realization of Kitaev quantum spin liquids, Nat. Rev. Phys. **1**, 264 (2019).

[5] S. V. Streltsov and D. I. Khomskii, Jahn-Teller effect and spin-orbit coupling: Friends or foes? Phys. Rev. X **10**, 031043 (2020).

[6] T. Takayama, J. Chaloupka, A. Smerald, G. Khaliullin, and H. Takagi, Spin-orbit-entangled electronic phases in 4*d* and 5*d* transition-metal compounds, J. Phys. Soc. Jpn. **90**, 062001 (2021).

[7] D. I. Khomskii and S. V. Streltsov, Orbital effects in solids: Basics, recent progress, and opportunities, Chem. Rev. **121**, 2992 (2021).

[8] G. Jackeli and G. Khaliullin, Mott insulators in the strong spin-orbit coupling limit: From Heisenberg to a quantum compass and Kitaev models, Phys. Rev. Lett. **102**, 017205 (2009).

[9] S. H. Chun, J.-W. Kim, J. Kim, H. Zheng, C. C. Stoumpos, C. D. Malliakas, J. F. Mitchell, K. Mehlawat, Y. Singh, Y. Choi, T. Gog, A. Al-Zein, M. Moretti Sala, M. Krisch, J. Chaloupka, G. Jackeli, G. Khaliullin, and B. J. Kim, Direct evidence for dominant bond-directional interactions in a honeycomb lattice iridate Na_2IrO_3, Nat. Phys. **11**, 462 (2015).

[10] M. Magnaterra, K. Hopfer, Ch. J. Sahle, M. Moretti Sala, G. Monaco, J. Attig, C. Hickey, I.-M. Pietsch, F. Breitner, P. Gegenwart, M. H. Upton, J. Kim, S. Trebst, P. H. M. van Loosdrecht, J. van den Brink, and M. Grüninger, RIXS observation of bond-directional nearest-neighbor excitations in the Kitaev material Na_2IrO_3, arXiv:2301.08340.

[11] M. Moretti Sala, S. Boseggia, D. F. McMorrow, and G. Monaco, Resonant x-ray scattering and the $j_{\text{eff}} = 1/2$ electronic ground state in iridate perovskites, Phys. Rev. Lett. **112**, 026403 (2014).

[12] X. Liu, V. M. Katukuri, L. Hozoi, W.-G. Yin, M. P. M. Dean, M. H. Upton, J. Kim, D. Casa, A. Said, T. Gog, T. F. Qi, G. Cao, A. M. Tsvelik, J. van den Brink, and J. P. Hill, Testing the validity of the strong spin-orbit-coupling limit for octahedrally coordinated iridate compounds in a model system Sr_3CuIrO_6, Phys. Rev. Lett. **109**, 157401 (2012).

[13] H. Gretarsson, J. P. Clancy, X. Liu, J. P. Hill, E. Bozin, Y. Singh, S. Manni, P. Gegenwart, J. Kim, A. H. Said, D. Casa, T. Gog, M. H. Upton, H.-S. Kim, J. Yu, V. M. Katukuri, L. Hozoi, J. van den Brink, and Y.-J. Kim, Crystal-field splitting and correlation effect on the electronic structure of A_2IrO_3, Phys. Rev. Lett. **110**, 076402 (2013).

[14] M. Rossi, M. Retegan, C. Giacobbe, R. Fumagalli, A. Efimenko, T. Kulka, K. Wohlfeld, A. I. Gubanov, and M. Moretti Sala, Possibility to realize spin-orbit-induced correlated physics in iridium fluorides, Phys. Rev. B **95**, 235161 (2017).

[15] A. A. Aczel, J. P. Clancy, Q. Chen, H. D. Zhou, D. Reig-i-Plessis, G. J. MacDougall, J. P. C. Ruff, M. H. Upton, Z. Islam, T. J. Williams, S. Calder, and J.-Q. Yan, Revisiting the Kitaev material candidacy of Ir^{4+} double perovskite iridates, Phys. Rev. B **99**, 134417 (2019).

[16] A. Revelli, C. C. Loo, D. Kiese, P. Becker, T. Fröhlich, T. Lorenz, M. Moretti Sala, G. Monaco, F. L. Buessen, J. Attig, M. Hermanns, S. V. Streltsov, D. I. Khomskii, J. van den Brink, M. Braden, P. H. M. van Loosdrecht, S. Trebst, A. Paramekanti, and M. Grüninger, Spin-orbit entangled $j = 1/2$ moments in Ba_2CeIrO_6: A frustrated fcc quantum magnet, Phys. Rev. B **100**, 085139 (2019).

[17] A. Ruiz, N. P. Breznay, M. Li, I. Rousochatzakis, A. Allen, I. Zinda, V. Nagarajan, G. Lopez, Z. Islam, M. H. Upton, J. Kim, A. H. Said, X.-R. Huang, T. Gog, D. Casa, R. J. Birgeneau, J. D. Koralek, J. G. Analytis, N. B. Perkins, and A. Frano, Magnon-spinon dichotomy in the Kitaev hyperhoneycomb β-Li_2IrO_3, Phys. Rev. B **103**, 184404 (2021).

[18] A. de la Torre, B. Zager, F. Bahrami, M. DiScala, J. R. Chamorro, M. H. Upton, G. Fabbris, D. Haskel, D. Casa, T. M. McQueen, F. Tafti, and K. W. Plumb, Enhanced hybridization in the electronic ground state of the intercalated honeycomb iridate $Ag_3LiIr_2O_6$, Phys. Rev. B **104**, L100416 (2021).

[19] W. Jin, S. H. Chun, J. Kim, D. Casa, J. P. C. Ruff, C. J. Won, K. D. Lee, N. Hur, and Y.-J. Kim, Magnetic excitations in the double-perovskite iridates La_2MIrO_6 (M = Co, Ni, and Zn) mediated by 3*d*-5*d* hybridization, Phys. Rev. B **105**, 054419 (2022).

[20] M. Magnaterra, M. Moretti Sala, G. Monaco, P. Becker, M. Hermanns, P. Warzanowski, T. Lorenz, D. I. Khomskii, P. H. M. van Loosdrecht, J. van den Brink, and M. Grüninger, RIXS interferometry and the role of disorder in the quantum magnet $Ba_3Ti_{3-x}Ir_xO_9$, Phys. Rev. Res. **5**, 013167 (2023).

[21] A. de la Torre, B. Zager, F. Bahrami, M. H. Upton, J. Kim, G. Fabbris, G.-H. Lee, W. Yang, D. Haskel, F. Tafti, and K. W. Plumb, Momentum-independent magnetic excitation continuum in the honeycomb iridate $H_3LiIr_2O_6$, Nat. Commun. **14**, 5018 (2023).

[22] J. Kim, D. Casa, M. H. Upton, T. Gog, Y.-J. Kim, J. F. Mitchell, M. van Veenendaal, M. Daghofer, J. van den Brink, G. Khaliullin, and B. J. Kim, Magnetic excitation spectra of Sr_2IrO_4 probed by resonant inelastic x-ray scattering: Establishing links to cuprate superconductors, Phys. Rev. Lett. **108**, 177003 (2012).

[23] J. Kim, M. Daghofer, A. H. Said, T. Gog, J. van den Brink, G. Khaliullin, and B. J. Kim, Excitonic quasiparticles in a spin–orbit Mott insulator, Nat. Commun. **5**, 4453 (2014).

[24] J. Kim, A. H. Said, D. Casa, M. H. Upton, T. Gog, M. Daghofer, G. Jackeli, J. van den Brink, G. Khaliullin, and B. J. Kim, Large spin-wave energy gap in the bilayer iridate $Sr_3Ir_2O_7$: Evidence for enhanced dipolar interactions near the Mott metal-insulator transition, Phys. Rev. Lett. **109**, 157402 (2012).

[25] M. Moretti Sala, V. Schnells, S. Boseggia, L. Simonelli, A. Al-Zein, J. G. Vale, L. Paolasini, E. C. Hunter, R. S. Perry, D. Prabhakaran, A. T. Boothroyd, M. Krisch, G. Monaco, H. M. Rønnow, D. F. McMorrow, and F. Mila, Evidence of quantum dimer excitations in $Sr_3Ir_2O_7$, Phys. Rev. B **92**, 024405 (2015).

[26] X. Lu, P. Olalde-Velasco, Y. Huang, V. Bisogni, J. Pelliciari, S. Fatale, M. Dantz, J. G. Vale, E. C. Hunter, J. Chang, V. N.

Strocov, R. S. Perry, M. Grioni, D. F. McMorrow, H. M. Rønnow, and T. Schmitt, Dispersive magnetic and electronic excitations in iridate perovskites probed by oxygen K-edge resonant inelastic x-ray scattering, Phys. Rev. B **97**, 041102(R) (2018).

[27] A. Bertin, L. Kiefer, P. Becker, L. Bohatý, and M. Braden, Rotational phase transitions in antifluorite-type osmate and iridate compounds, J. Phys.: Condens. Matter **36**, 245402 (2024).

[28] N. Khan, D. Prishchenko, Y. Skourski, V. G. Mazurenko, and A. A. Tsirlin, Cubic symmetry and magnetic frustration on the fcc spin lattice in K_2IrCl_6, Phys. Rev. B **99**, 144425 (2019).

[29] D. Reig-i-Plessis, T. A. Johnson, K. Lu, Q. Chen, J. P. C. Ruff, M. H. Upton, T. J. Williams, S. Calder, H. D. Zhou, J. P. Clancy, A. A. Aczel, and G. J. MacDougall, Structural, electronic, and magnetic properties of nearly ideal $J_{\text{eff}} = 1/2$ iridium halides, Phys. Rev. Mater. **4**, 124407 (2020).

[30] N. Khan, D. Prishchenko, M. H. Upton, V. G. Mazurenko, and A. A. Tsirlin, Towards cubic symmetry for Ir^{4+}: Structure and magnetism of the antifluorite K_2IrBr_6, Phys. Rev. B **103**, 125158 (2021).

[31] S. Lee, B. H. Kim, M.-J. Seong, and K.-Y. Choi, Noncubic local distortions and spin-orbit excitons in K_2IrCl_6, Phys. Rev. B **105**, 184433 (2022).

[32] F. Meggle, M. Mikuta, M. Saule, V. Hermann, N. Khan, A. A. Tsirlin, and C. A. Kuntscher Optical signatures of the $J_{\text{eff}} = 1/2$ state in Ir^{4+} halides, Phys. Rev. B **107**, 235142 (2023).

[33] L. Bhaskaran, A. N. Ponomaryov, J. Wosnitza, N. Khan, A. A. Tsirlin, M. E. Zhitomirsky, and S. A. Zvyagin, Antiferromagnetic resonance in the cubic iridium hexahalides $(NH_4)_2IrCl_6$ and K_2IrCl_6, Phys. Rev. B **104**, 184404 (2021).

[34] P. Balla, Y. Iqbal, and K. Penc, Degenerate manifolds, helimagnets, and multi-Q chiral phases in the classical Heisenberg antiferromagnet on the face-centered-cubic lattice, Phys. Rev. Res. **2**, 043278 (2020).

[35] N. Iwahara and W. Furukawa, Vibronic effect on resonant inelastic x-ray scattering in cubic iridium hexahalides, Phys. Rev. B **108**, 075136 (2023).

[36] E. M. Plotnikova, M. Daghofer, J. van den Brink, and K. Wohlfeld, Jahn-Teller effect in systems with strong on-site spin-orbit coupling, Phys. Rev. Lett. **116**, 106401 (2016).

[37] M. Moretti Sala, K. Ohgushi, A. Al-Zein, Y. Hirata, G. Monaco, and M. Krisch, $CaIrO_3$: A spin-orbit Mott insulator beyond the $j_{\text{eff}} = 1/2$ ground state, Phys. Rev. Lett. **112**, 176402 (2014).

[38] P. Warzanowski, N. Borgwardt, K. Hopfer, J. Attig, T. C. Koethe, P. Becker, V. Tsurkan, A. Loidl, M. Hermanns, P. H. M. van Loosdrecht, and M. Grüninger, Multiple spin-orbit excitons and the electronic structure of α-$RuCl_3$, Phys. Rev. Res. **2**, 042007(R) (2020).

[39] J.-H. Lee, Y. Choi, S.-H. Do, B. H. Kim, M.-J. Seong, and K.-Y. Choi, Multiple spin-orbit excitons in α-$RuCl_3$ from bulk to atomically thin layers, npj Quantum Mater. **6**, 43 (2021).

[40] J. G. Vale, C. D. Dashwood, E. Paris, L. S. I. Veiga, M. Garcia-Fernandez, A. Nag, A. Walters, K.-J. Zhou, I.-M. Pietsch, A. Jesche, P. Gegenwart, R. Coldea, T. Schmitt, and D. F. McMorrow, High-resolution resonant inelastic x-ray scattering study of the electron-phonon coupling in honeycomb α-Li_2IrO_3, Phys. Rev. B **100**, 224303 (2019).

[41] S. Agrestini, F. Borgatti, P. Florio, J. Frassineti, D. Fiore Mosca, Q. Faure, B. Detlefs, C. J. Sahle, S. Francoual, J. Choi, M. Garcia-Fernandez, K.-J. Zhou, V. F. Mitrovic, P. M. Woodward, G. Ghiringhelli, C. Franchini, F. Boscherini, S. Sanna, and M. Moretti Sala, The origin of magnetism in a supposedly nonmagnetic osmium oxide, Phys. Rev. Lett. **133**, 066501 (2024).

[42] A. Revelli, M. Moretti Sala, G. Monaco, C. Hickey, P. Becker, F. Freund, A. Jesche, P. Gegenwart, T. Eschmann, F. L. Buessen, S. Trebst, P. H. M. van Loosdrecht, J. van den Brink, and M. Grüninger, Fingerprints of Kitaev physics in the magnetic excitations of honeycomb iridates, Phys. Rev. Res. **2**, 043094 (2020).

[43] J. J. Lee, B. Moritz, W. S. Lee, M. Yi, C. J. Jia, A. P. Sorini, K. Kudo, Y. Koike, K. J. Zhou, C. Monney, V. Strocov, L. Patthey, T. Schmitt, T. P. Devereaux, and Z. X. Shen, Charge-orbital-lattice coupling effects in the dd excitation profile of one-dimensional cuprates, Phys. Rev. B **89**, 041104(R) (2014).

[44] N. Iwahara and S. Shikano, Vibronic excitations in resonant inelastic x-ray scattering spectra of K_2RuCl_6, Phys. Rev. Res. **5**, 023051 (2023).

[45] H. Takahashi, H. Suzuki, J. Bertinshaw, S. Bette, C. Mühle, J. Nuss, R. Dinnebier, A. Yaresko, G. Khaliullin, H. Gretarsson, T. Takayama, H. Takagi, and B. Keimer, Nonmagnetic $J = 0$ state and spin-orbit excitations in K_2RuCl_6, Phys. Rev. Lett. **127**, 227201 (2021).

[46] F. I. Frontini, G. H. J. Johnstone, N. Iwahara, P. Bhattacharyya, N. A. Bogdanov, L. Hozoi, M. H. Upton, D. M. Casa, D. Hirai, and Y.-J. Kim, Spin-orbit-lattice entangled state in A_2MgReO_6 (A = Ca, Sr, Ba) revealed by resonant inelastic x-ray scattering, Phys. Rev. Lett. **133**, 036501 (2024).

[47] F. Hennies, A. Pietzsch, M. Berglund, A. Föhlisch, Th. Schmitt, V. Strocov, H. O. Karlsson, J. Andersson, and J.-E. Rubensson, Resonant inelastic scattering spectra of free molecules with vibrational resolution, Phys. Rev. Lett. **104**, 193002 (2010).

[48] B. Henderson and G. F. Imbusch, *Optical Spectroscopy of Inorganic Solids* (OUP, Oxford, 1989).

[49] B. N. Figgis and M. A. Hitchman, *Ligand Field Theory and its Applications* (Wiley-VCH, New York, 1999).

[50] C. F. Ballhausen, *Introduction to Ligand Field Theory* (McGraw-Hill, New York, 1962).

[51] R. Rückamp, E. Benckiser, M. W. Haverkort, H. Roth, T. Lorenz, A. Freimuth, L. Jongen, A. Möller, G. Meyer, P. Reutler, B. Büchner, A. Revcolevschi, S.-W. Cheong, C. Sekar, G. Krabbes, and M. Grüninger, Optical study of orbital excitations in transition-metal oxides, New J. Phys. **7**, 144 (2005).

[52] P. Warzanowski, M. Magnaterra, G. Schlicht, Q. Faure, Ch. J. Sahle, P. Becker, L. Bohatý, M. Moretti Sala, G. Monaco, M. Hermanns, P. H. M. van Loosdrecht, and M. Grüninger, Spin-orbit coupling in a half-filled t_{2g} shell: The case of $5d^3$ K_2ReCl_6, Phys. Rev. B **109**, 155149 (2024).

[53] P. Warzanowski, M. Magnaterra, P. Stein, G. Schlicht, Q. Faure, Ch. J. Sahle, T. Lorenz, P. Becker, L. Bohatý, M. Moretti Sala, G. Monaco, P. H. M. van Loosdrecht, and M. Grüninger, Electronic excitations in $5d^4 J = 0$ Os^{4+} halides studied by resonant inelastic x-ray scattering and optical spectroscopy, Phys. Rev. B **108**, 125120 (2023).

[54] A. H. Cooke, R. Lazenby, F. R. McKim, J. Owen, and W. P. Wolf, Exchange interactions in antiferromagnetic salts of

iridium II. Magnetic susceptibility measurements, Proc. R. Soc. London Ser. A **250**, 97 (1959).

[55] M. Moretti Sala, C. Henriquet, L. Simonelli, R. Verbeni, and G. Monaco, High energy-resolution set-up for Ir L_3 edge RIXS experiments, J. Electron Spectrosc. Relat. Phenom. **188**, 150 (2013).

[56] M. Moretti Sala, K. Martel, C. Henriquet, A. Al Zein, L. Simonelli, Ch. J. Sahle, H. Gonzalez, M.-C. Lagier, C. Ponchut, S. Huotari, R. Verbeni, M. Krisch, and G. Monaco, A high-energy-resolution resonant inelastic X-ray scattering spectrometer at ID20 of the European Synchrotron Radiation Facility, J. Synchrotron Rad. **25**, 580 (2018).

[57] R. M. A. Azzam and N. M. Bashara, *Ellipsometry and Polarized Light* (Elsevier, New York, 1987).

[58] J. W. Lynn, H. H. Patterson, G. Shirane, and R. G. Wheeler, Soft rotary mode and structural phase transition in K_2ReCl_6, Solid State Commun. **27**, 859 (1978).

[59] D. Mintz, R. L. Armstrong, B. M. Powell, and W. J. L. Buyers, Soft rotary mode in the antifluorite crystal K_2OsCl_6, Phys. Rev. B **19**, 448 (1979).

[60] G. P. O'Leary and R. G. Wheeler, Phase transitions and soft librational modes in cubic crystals, Phys. Rev. B **1**, 4409 (1970).

[61] P. Schweiss, W. Reichardt, M. Braden, G. Collin, G. Heger, H. Claus, and A. Erb, Static and dynamic displacements in $RBa_2Cu_3O_{7-\delta}$ (R =Y, Ho; $\delta = 0.05, 0.5$): A neutron-diffraction study on single crystals, Phys. Rev. B **49**, 1387 (1994).

[62] G. A. Sawatzky, Testing Fermi-liquid models, Nature (London) **342**, 480 (1989).

[63] M. A. Hitchman and P. J. Cassidy, Polarized crystal spectrum of bis(methylphenethylammonium) tetrachlorocuprate(II): Analysis of the energies, vibrational fine structure, and temperature dependence of the "d-d" transitions of the planar tetrachlorocuprate(2-) ion, Inorg. Chem. **18**, 1745 (1979).

[64] D. M. Adams and H. A. Gebbie, Absorption spectra of some inorganic complex halides by far infra-red interferometry, Spectrochim. Acta **19**, 925 (1963).

[65] G. L. Bottger and A. E. Salwin, The vibrational spectra of alkali salts of hexahaloiridates, Spectrochim. Acta A **28**, 925 (1972).

[66] S. F. Parker and J. B. Forsyth, K_2MCl_6 (M = Pt, Ir), location of the silent modes and forcefields, J. Chem. Soc. Faraday Trans. **94**, 1111 (1998).

[67] T. A. Keiderling, P. J. Stephens, S. B. Piepho, J. L. Slater, P. N. Schatz, Infrared absorption and magnetic circular dichroism of Cs_2ZrCl_6:Ir^{4+}, Chem. Phys. **11**, 343 (1975).

[68] R. K. Yoo and T. A. Keiderling, Intraconfigurational absorption spectroscopy of $IrCl_6^{2-}$ and $IrBr_6^{2-}$ in A_2MX_6-type host crystals, Chem. Phys. **108**, 317 (1986).

[69] L. Pross, K. Rössler, and H. J. Schenk, Optical studies on Hexahalorhenates - I Low temperature absorption spectra of $K_2[ReCl_6]$ single crystals, J. Inorg. Nucl. Chem. **36**, 317 (1974).

[70] R. K. Yoo, S. C. Lee, B. A. Kozikowski and T. A. Keiderling, Intraconfigurational absorption spectroscopy of $ReCl_6^{2-}$ in various A_2MCl_6 host crystals, Chem. Phys. **117**, 237 (1987).

[71] M. Bettinelli and C. D. Flint, Magnon sidebands and cooperative absorptions in K_2ReCl_6 and Cs_2ReCl_6, J. Phys. C: Solid State Phys. **21**, 5499 (1988).

[72] B. A. Kozikowski and T. A. Keiderling, Intraconfigurational absorption spectroscopy of osmium(4+) ion in dipotassium hexachlorostannate and dipotassium hexachloroosmate crystals, J. Phys. Chem. **87**, 4630 (1983).

[73] K. Huang and A. Rhys, Theory of light absorption and non-radiative transitions in F-centres, Proc. R. Soc. London A **204**, 406 (1950).

[74] L. J. P. Ament, M. van Veenendaal, and J. van den Brink, Determining the electron–phonon coupling strength from resonant inelastic x-ray scattering at transition metal L-edges, Europhys. Lett. **95**, 27008 (2011).

[75] A. Geondzhian and K. Gilmore, Generalization of the Franck-Condon model for phonon excitations by resonant inelastic x-ray scattering, Phys. Rev. B **101**, 214307 (2020).

[76] K. Gilmore, Quantifying vibronic coupling with resonant inelastic X-ray scattering, Phys. Chem. Chem. Phys. **25**, 217 (2022).

[77] L. Braicovich, M. Rossi, R. Fumagalli, Y. Peng, Y. Wang, R. Arpaia, D. Betto, G. M. De Luca, D. Di Castro, K. Kummer, M. Moretti Sala, M. Pagetti, G. Balestrino, N. B. Brookes, M. Salluzzo, S. Johnston, J. van den Brink, and G. Ghiringhelli, Determining the electron-phonon coupling in superconducting cuprates by resonant inelastic x-ray scattering: Methods and results on $Nd_{1+x}Ba_{2-x}Cu_3O_{7-\delta}$, Phys. Rev. Res. **2**, 023231 (2020).

[78] A. M. Black and C. D. Flint, Jahn-Teller effect in the $\Gamma_8(^2T_{2g}, t_{2g}^3)$ state of $ReBr_6^{2-}$, J. Chem. Soc., Faraday Trans. 2, **71**, 1871 (1975).

[79] H. Liu and G. Khaliullin, Pseudo-Jahn-Teller effect and magnetoelastic coupling in spin-orbit Mott insulators, Phys. Rev. Lett. **122**, 057203 (2019).

[80] L. J. P. Ament, M. van Veenendaal, T. P. Devereaux, J. P. Hill, and J. van den Brink, Resonant inelastic x-ray scattering studies of elementary excitations, Rev. Mod. Phys. **83**, 705 (2011).

[81] T. P. Devereaux, A. M. Shvaika, K. Wu, K. Wohlfeld, C. J. Jia, Y. Wang, B. Moritz, L. Chaix, W.-S. Lee, Z.-X. Shen, G. Ghiringhelli, and L. Braicovich, Directly characterizing the relative strength and momentum dependence of electron-phonon coupling using resonant inelastic x-ray scattering, Phys. Rev. X **6**, 041019 (2016).

[82] S. Johnston, C. Monney, V. Bisogni, K.-J. Zhou, R. Kraus, G. Behr, V. N. Strocov, J. Málek, S.-L. Drechsler, J. Geck, T. Schmitt, and J. van den Brink, Electron-lattice interactions strongly renormalize the charge-transfer energy in the spin-chain cuprate Li_2CuO_2, Nat. Commun. **7**, 10563 (2015).

[83] E. Benckiser, R. Rückamp, T. Möller, T. Taetz, A. Möller, A. A. Nugroho, T. T. M. Palstra, G. S. Uhrig, and M. Grüninger, Collective orbital excitations in orbitally ordered YVO_3 and $HoVO_3$, New J. Phys. **10**, 053027 (2008).

[84] Q. Wang, A. de la Torre, J. A. Rodriguez-Rivera, A. A. Podlesnyak, W. Tian, A. A. Aczel, M. Matsuda, P. J. Ryan, J.-W. Kim, J. G. Rau, and K. W. Plumb, Pulling order back from the brink of disorder: Observation of a nodal line spin liquid and fluctuation stabilized order in K_2IrCl_6, arXiv:2407.17559.

[85] P. Warzanowski, M. Magnaterra, Ch. J. Sahle, M. Moretti Sala, P. Becker, L. Bohatý, I. Císařová, G. Monaco, T. Lorenz, P. H. M. van Loosdrecht, J. van den Brink, and M. Grüninger, Data for "Spin orbital lattice entanglement in the ideal $j = \frac{1}{2}$ compound K_2IrCl_6" (2024), doi:10.5281/zenodo.13986892.

[86] G. M. Sheldrick, SHELXT–Integrated space-group and crystal-structure determination, Acta Cryst. A **71**, 3 (2015).

[87] G. M. Sheldrick, Crystal structure refinement with SHELXL, Acta Cryst. C **71**, 3 (2015).

[88] Joint CCDC/FIZ Karlsruhe deposition service, www.ccdc.cam.ac.uk/discover/news/2018-07-new-joint-services/ The crystallographic data deposition numbers are CCDC/CSD 2367387 to 2367405 and can be obtained free of charge from https://www.ccdc.cam.ac.uk/structures.

[89] G. Khaliullin, P. Horsch, and A. M. Oleś, Theory of optical spectral weights in Mott insulators with orbital degrees of freedom, Phys. Rev. B **70**, 195103 (2004).

[90] A. M. Oleś, G. Khaliullin, P. Horsch, and L. F. Feiner, Fingerprints of spin-orbital physics in cubic Mott insulators: Magnetic exchange interactions and optical spectral weights, Phys. Rev. B **72**, 214431 (2005).

[91] Z. Fang, N. Nagaosa, and K. Terakura, Anisotropic optical conductivities due to spin and orbital ordering in $LaVO_3$ and YVO_3: First-principles studies, Phys. Rev. B **67**, 035101 (2003).

[92] N. N. Kovaleva, A. V. Boris, C. Bernhard, A. Kulakov, A. Pimenov, A. M. Balbashov, G. Khaliullin, and B. Keimer, Spin-controlled Mott-Hubbard bands in $LaMnO_3$ probed by optical ellipsometry, Phys. Rev. Lett. **93**, 147204 (2004).

[93] J. S. Lee, M. W. Kim, and T. W. Noh, Optical excitations of transition-metal oxides under the orbital multiplicity effects, New J. Phys. **7**, 147 (2005).

[94] A. Gössling, R. Schmitz, H. Roth, M. W. Haverkort, T. Lorenz, J. A. Mydosh, E. Müller-Hartmann, and M. Grüninger, Mott-Hubbard exciton in the optical conductivity of $YTiO_3$ and $SmTiO_3$, Phys. Rev. B **78**, 075122 (2008).

[95] J. Reul, A. A. Nugroho, T. T. M. Palstra, and M. Grüninger, Probing orbital fluctuations in RVO_3 (R = Y, Gd, or Ce) by ellipsometry, Phys. Rev. B **86**, 125128 (2012).

[96] I. Vergara, M. Magnaterra, P. Warzanowski, J. Attig, S. Kunkemöller, D. I. Khomskii, M. Braden, M. Hermanns, and M. Grüninger, Spin-orbit coupling and crystal-field splitting in Ti-doped Ca_2RuO_4 studied by ellipsometry, Phys. Rev. B **106**, 085103 (2022).

[97] G. Zhang and E. Pavarini, Mott transition, spin-orbit effects, and magnetism in Ca_2RuO_4, Phys. Rev. B **95**, 075145 (2017).

[98] B. H. Kim, G. Khaliullin, and B. I. Min, Electronic excitations in the edge-shared relativistic Mott insulator: Na_2IrO_3, Phys. Rev. B **89**, 081109(R) (2014).

[99] S. M. Winter, A. A. Tsirlin, M. Daghofer, J. van den Brink, Y. Singh, P. Gegenwart, and R. Valentí, Models and materials for generalized Kitaev magnetism, J. Phys.: Condens. Matter **29**, 493002 (2017).

[100] Z. Alpichshev, F. Mahmood, G. Cao, and N. Gedik, Confinement-deconfinement transition as an indication of spin-liquid-type behavior in Na_2IrO_3, Phys. Rev. Lett. **114**, 017203 (2015).

[101] O. Mehio, X. Li, H. Ning, Z. Lenarčič, Y. Han, M. Buchhold, Z. Porter, N. J. Laurita, S. D. Wilson, and D. Hsieh, A Hubbard exciton fluid in a photo-doped antiferromagnetic Mott insulator, Nat. Phys. **19**, 1876 (2023).

8 Summary and outlook

Within this thesis, we have examined the electronic properties of 4*d* and 5*d* Mott insulators, which lie at the intersection of strong correlations and strong spin-orbit coupling. To investigate these materials, we have focused on the local electronic excitations. A central characteristic of our approach has been to combine methods that exhibit different sensitivities and selection rules. For α-$RuCl_3$, these have been optical spectroscopy and Raman scattering, and for the 5*d* antifluorites, we have employed optical spectroscopy and RIXS at the transition-metal L_3 edge.

(Multiple) spin-orbit excitons in α-$RuCl_3$

Regarding α-$RuCl_3$, we have answered the question about the origin of the main absorption features above the phonons and below the Mott gap. The comparison of the excitation features seen by Raman scattering and optical spectroscopy has allowed us to identify the spin-orbit exciton and the two higher-lying absorption bands at 0.53 eV and 0.75 eV as the double and triple spin-orbit excitons, respectively. Crucial for this interpretation has been the temperature dependence of the spectral weight, which can be attributed to the different phonon modes that break inversion symmetry on the single site for the single spin-orbit exciton and in between two sites for the double spin-orbit exciton. From the excitation energy and the splitting of the spin-orbit exciton, we have determined the spin-orbit coupling $\lambda_{\text{eff}} = 177\,\text{meV}$ and the trigonal splitting $\Delta_{\text{CF}} \approx 60\,\text{meV}$ in a t_{2g}-only model. This translates to a 98% $j = 1/2$ character of the ground state, similarly to the honeycomb iridates Na_2IrO_3 and α-Li_2IrO_3. Accounting for the e_g orbitals and a realistic value of $10Dq \approx 2.2\,\text{eV}$ [82, 246] yields a spin-orbit coupling $\lambda = 0.16\,\text{eV}$, which is in agreement with the range typically found for α-$RuCl_3$ of $\lambda \approx 0.13$ to $0.15\,\text{eV}$ [60, 83], but for which a precise experimental value had been missing.
The double spin-orbit exciton reflects the pairwise excitation from $j = 1/2$ to neighboring $j = 3/2$ states, and its comparatively large strength reflects the prominent role of the Kitaev interaction in this material. For our analysis, we compare the double spin-orbit exciton to a bi-magnon excitation, as seen, for instance, in the $S = 1/2$ cuprates. There, the exchange of two antiparallel spins on adjacent sites is equivalent to a double spin flip. In a Kitaev system, the exchange between neighboring $j = 1/2$ moments is suppressed, but hopping from $|j = 1/2, \pm 1/2\rangle_i$ to $|j = 3/2, \mp 3/2\rangle_j$ is allowed. Intriguingly, this is precisely the hopping path that promotes Kitaev interaction. Our two-site cluster calculation shows that the main weight of the double spin-orbit exciton emerges from the pairwise exchange that follows this hopping channel, hence the unusual strength of this absorption

feature. Our interpretation of the intersite nature of these excitations is further strengthened by the fact that the triple spin-orbit exciton is directly observable with optics, but not with Raman scattering. The process of exchanging three holes on three neighboring sites breaks inversion symmetry, turning this process infrared active. The comparatively large ratio of next-nearest-neighbor to nearest-neighbor hopping, $t'/t \approx 0.38$ [247], allows for a comparable spectral weight between the (phonon-assisted) double and (direct) triple excitation. Altogether, these results corroborate the realization of the $j = 1/2$ scenario in α-$RuCl_3$ and illustrate the exotic character of the Kitaev interaction imprinted on the electronic excitations.

The A_2MX_6 antifluorite halides

We have demonstrated for K_2ReCl_6, K_2OsCl_6, A_2OsBr_6 with $A = K, Rb$, and K_2IrCl_6 that the quasimolecular A_2MX_6 antifluorite halides are formidable model platforms to study the local effects of spin-orbit coupling for different $5d^N$ configurations. This is mainly a consequence of the isolated MX_6 octahedra and large nearest-neighbor distances, which reduce the bandwidths of the $5d$ states. This yields Mott gaps exceeding $\Delta_{gap} \geq 1.5\,eV$, which are unusually large values for $5d$ Mott insulators and which provide a wide transparency window for optical transmittance experiments. The reduced bandwidths also promote narrow lineshapes of the excitation features, which facilitate an accurate determination of the electronic parameters. An additional consequence of the isolated octahedra is the particularly clear observation of vibronic signatures, both for onsite excitations and intersite excitations. The observed vibronic sidebands are typically smeared in crystals with a more rigid and connected lattice structure, which allowed us to examine the effects of spin-orbital-lattice entanglement in these materials.
Combining optical spectroscopy and L-edge RIXS, our results provide a comprehensive picture of the excitations of the $5d$ electrons. With RIXS, we have recorded, for example, the resonance maps of K_2ReCl_6 and K_2OsCl_6 to assign the orbital character of the multiplet excitations. As such, we were able to distinguish intra-t_{2g} from t_{2g}-to-e_g excitations and identified analogously different charge-transfer processes at higher energies. Having established the character of the excitations, we have been able to utilize the superior energy resolution of optical transmittance measurements to further resolve the intra-t_{2g} excitations.
In the past, determining the electronic parameters for K_2ReCl_6 and K_2OsCl_6 has been difficult [143, 145, 211], especially because absorption experiments alone cannot resolve excitations into the e_g states above 2 eV, as these are buried by the much stronger and broader Mott-Hubbard excitations in the same energy range. It is therefore this combined approach of optics and RIXS that has allowed us to perform a very careful analysis of the local electronic structure.

Focusing on each system, we have established the Os^{4+} compounds K_2OsCl_6, K_2OsBr_6, and Rb_2OsCl_6 as clean $5d^4$ $J = 0$ systems that can serve very well as $5d^4$ reference

systems for future Os^{4+} RIXS studies. In particular, for K_2OsCl_6, we have observed all intra-t_{2g} multiplets with RIXS and demonstrated that the excitation $\Gamma_4(^3T_1) \rightarrow \Gamma_1(^1A_1)$ is only observable in the parallel polarization channel, which explains why the equivalent excitation has only been reported in certain L-edge RIXS studies on $5d^4$ systems [158–162]. The energies of the multiplets show that the local moments are best described in an intermediate-coupling regime, $\zeta/J_H \sim 1$, consistent with results reported for several $5d^4$ iridates [158–162].
Being able to resolve excitations involving e_g orbitals, we compared the results between two models: the often-employed t_{2g}-only scenario and a model accounting for the entire d shell. The main drawback of the t_{2g}-only model is the apparent degeneracy of certain intra-t_{2g} multiplets, e.g., for the ^1E and $^1T_2$ multiplets. However, these splittings are only resolved in optics. Thus, for the intra-t_{2g} RIXS energies, both models describe the intra-t_{2g} excitations equally well. A considerable difference appears in the simulated RIXS intensities for the excitation into the $J = 1$ and $J = 2$ states, which suggests a considerable sensitivity of the matrix elements to the admixture of e_g states. Concerning the values of the electronic parameters, we found $\zeta/J_H \approx 0.8$ and $\zeta^{eff}/J_H^{eff} \approx 1.5$ for K_2OsCl_6 with $10Dq = 3.3\,eV$. For K_2OsBr_6, with a lower crystal-field splitting of $10Dq = 2.9\,eV$, we find roughly the same values of $\zeta_{Br}/J_{H,Br} \approx 0.8$ and $\zeta_{Br}^{eff}/J_{H,Br}^{eff} \approx 1.3$. The values for these parameters are given in Tab. 8.1 alongside the parameters of the other compounds of this thesis. Regarding symmetry, we found a tiny splitting of $\Delta_{exp} \approx 4\,meV$ for the excitation to the $J = 1$ state in the tetragonal phase below $T = 45\,K$ for K_2OsCl_6. This reflects the almost ideal cubic conditions, especially for the chloride members K_2MCl_6 of this family.

The electron configuration $5d^3$ sets the stage to investigate the unusual role of spin-orbit coupling on the electronic properties. The two opposite scenarios of vanishing or dominant spin-orbit coupling yield very different ground states. The first results in the conventionally known $S = 3/2$ ground state with a quenched orbital moment, whereas the latter produces a Jahn-Teller-active $J = 3/2$ state [88], which is opposite to the usual trend that spin-orbit coupling suppresses Jahn-Teller distortions. The underlying mechanism is the competition between spin-orbit coupling and Hund's exchange, which favor stabilizing the electronic states in different bases. As such, ζ/J_H is a decisive parameter to characterize the ground state. Analyzing the multiplet energies of K_2ReCl_6, we found $\zeta/J_H \approx 0.6$, or analogously, $\zeta^{eff}/J_H^{eff} \approx 0.8$. Starting from LS coupling with $S = 3/2$, spin-orbit coupling adds orbital character mainly by admixing $^2T_2$ multiplets into the ground state. The expectation value of the L_z component is thus a useful gauge to estimate the strength of spin-orbit-induced effects. In the t_{2g}-only model, the expectation value scales to leading order as $\langle L_z \rangle \propto \left(\frac{\zeta^{eff}}{J_H^{eff}}\right)^2$. For $\zeta^{eff}/J_H^{eff} \approx 0.8$, our calculations show $\langle L_z \rangle \approx 0.027$, a very small value. Accordingly, we also found the ground state to exhibit 97% $^4A_2$ $S = 3/2$ character. Including the admixture of e_g states slightly reduces this weight to 93%. The effects of spin-orbit coupling on the local moments in K_2ReCl_6 are weak but not unnoticeable.
Albeit we did not find a sizeable Jahn-Teller effect, we still observed a subtle interplay

between spin-orbit coupling and lattice effects. The intra-t_{2g} features are very weak due to the parity selection rule and the spin selection rule, since all five multiplets show a spin-flip character. Three of these five intra-t_{2g} multiplets also exhibit narrow peaks, and the progression of the vibronic sidebands can be reconciled with a single, fully symmetric A_{1g} phonon mode. This implies a negligible coupling to the lattice. The other two multiplets, located at 0.95 and 1.9 eV, however, show broader lineshapes and a slightly different spectral weight distribution of the vibronic sidebands. This hints at a larger orbital character in these states and at stronger coupling to the lattice. A striking signature of the quasi-molecular character of this material is the well-resolvable observation of double intra-t_{2g} excitations. These can be found very close to the sum values of the individual single-site energies $E_{0,i,j} \approx E_{0,i} + E_{0,j}$ and show similarly narrow peak widths, reflecting negligible intersite interaction. Also for these excitations, we resolve a phonon sideband that can be identified with the A_{1g} mode.
Considering the structural phase transitions, we observe a common increase of the electronic excitation energies by roughly 3-4 meV, which we attribute to a lowering of the ground-state energy when cooling the sample from the cubic phase above 111 K across three structural transitions to the monoclinic phase below 76 K. A more unusual effect of spin-orbit coupling in this material manifests as a strong ferroelastic response driven by the reorientation of the domain structure [105]. An additional splitting in the multiplet features appears when cooling below the magnetic ordering temperature $T_N = 12$ K, which might tentatively be attributed to magnon sidebands [145]. Focusing on the role of spin-orbit coupling on the orbital structure in this work, we analyzed the excitation spectra mainly in the paramagnetic phase. Future experiments could shed light on the mixed vibronic and magnetic character of these excitations in the magnetically ordered phase.

The central question around $5d^5$ K_2IrCl_6 concerns the stability and robustness of the $j = 1/2$ state. Thus far, the $5d^5$ Mott insulators have repeatedly shown signatures of non-cubic distortions, putting into question whether ideal $j = 1/2$ moments can be realized [65]. In the antifluorite K_2IrCl_6, a splitting of the spin-orbit exciton of around 50 meV [107] has been reported, but the non-cubic scenario is challenged by high-resolution x-ray diffraction, magnetic susceptibility, and electron spin resonance spectroscopy, which support a cubic scenario with an isotropic g factor and a magnetic moment consistent with an ideal $j = 1/2$ state [103, 106, 108]. To investigate this discrepancy, Iwahara and Furukawa [137] studied the role of electron-phonon coupling and suggested a dynamic Jahn-Teller effect from coupling with E_g phonons as the origin of the splitting of the spin-orbit exciton. The central question addressed in chapter 7 was to experimentally analyze the vibronic scenario in K_2IrCl_6. From the RIXS data alone, a dynamic Jahn-Teller effect cannot be distinguished from a static distortion. It is the combination of RIXS and optical spectroscopy paired with single-crystal X-ray diffraction data that allowed us to tackle this problem.
The confirmation of the vibronic scenario followed two steps. First, we demonstrated the absence of a measurable splitting due to static distortions by comparing the line shapes of

the spin-orbit exciton in K_2IrCl_6 and the excitation into the Γ_7 ($^2T_2$) multiplet in K_2ReCl_6. The latter shows a multipeak structure with phonon sidebands originating from the A_{1g} phonon mode and is insensitive to non-cubic distortions. The lineshape shows a very similar multipeak structure with a common motif of phonon-assisted peaks and a vibronic sideband pattern without any additional features in K_2IrCl_6. We showed that we could describe the line shape in both cases using the same model of a progression of phonon sidebands following the Franck-Condon principle. The second step was to apply this model to the RIXS spectra, showing excellent agreement between data and calculation, corroborating the vibronic origin. The observation of a phonon sideband is conceptually different from the excitation of a "bare" phonon with RIXS. Typically, phonons in $5d$ compounds can only be observed via indirect RIXS at the ligand K edge due to the dynamics and the longer lifetime of the intermediate state. A phonon is created in RIXS if the core hole in the intermediate state is screened by a lattice distortion. This is also a vibronic process that can be understood from the same mechanism of the Franck-Condon principle. However, in this case, the indirect RIXS excitation process requires two Franck-Condon factors: one for the excitation into the intermediate state and one for the relaxation into the final state [147, 149, 206]. For the phonon sidebands observable with direct RIXS, this requires only one Franck-Condon factor.
Comparing the lineshape of the spin-orbit exciton at different temperatures, we found a strong sensitivity of the energy of the sideband progression and the Huang-Rhys parameter in the Franck-Condon model. This points to a scenario that goes beyond the Franck-Condon approximation with vanishing electron-phonon coupling, which implies coupling to the E_g phonons and, hence, a dynamic Jahn-Teller effect of the excited $j = 3/2$ state.
In summary, our results demonstrate the absence of a sizable static non-cubic distortion, and therefore, the realization of an ideal cubic $j = 1/2$ scenario in K_2IrCl_6. In addition, our results give the experimental evidence of spin-orbit-lattice entanglement in the electronic structure of K_2IrCl_6.

Taken together, our results on the A_2MX_6 antifluorite halides have proven them as a versatile model platform to explore the role of spin-orbit coupling for different $5d^N$ configurations. The quasimolecular character makes a combined approach of optical spectroscopy and direct L edge RIXS ideal to determine the relevant parameters and find distinct signatures of effects driven by spin-orbit coupling. Across the series, we find several things. First, a robust local $J = 0$ state for the $5d^4$ Os compounds that can serve as a clean reference system. Second, a tiny admixture of orbital moment from excited multiplets into the $S = 3/2$ ground state and a marginal coupling to the lattice for multiplets with a larger orbital contribution for $5d^3$ K_2ReCl_6. Third, the realization of an ideal cubic $j = 1/2$ state and the manifestation of spin-orbit-lattice entanglement in the form of a dynamic Jahn-Teller effect in $5d^5$ K_2IrCl_6. These findings underline the strength of the anifluorite halides as clean reference systems for future studies of correlated spin-orbit-entangled materials.

	ζ^{eff}	$J_{\text{H}}^{\text{eff}}$	ζ	J_{H}	$10Dq$	Δ_{CT}	Δ_{gap}
α-$RuCl_3$	0.18	–	0.16	–	2.2 [246]	5 [246]	1
K_2ReCl_6	0.28	0.34	0.29	0.46	3.3	5^R	2.7
K_2OsCl_6	0.41	0.28	0.34	0.43	3.3	4.6^R	2.2
K_2OsBr_6	0.39	0.30	0.33	0.42	2.9	4^R	1.8
K_2IrCl_6	0.42	0.2–0.3 [197]	–	–	–	5^E	1.7

Table 8.1 Summary of parameters of the single-site model as well as the charge-transfer energy (^{R}: determined from RIXS, ^{E}: determined from ellipsometry), and the onset of the Mott gap determined from the optical transmittance. All values are given in eV.

Outlook

Our results have established that the $5d$ antifluorite halides are suitable model systems to study the local physics of different $5d^N$ configurations. To complete this endeavor, the cases for $5d^1$ and $5d^2$ are still missing. In particular, these systems might stand out due to the multipolar character of the local moments. In the presence of intersite interactions and coupling to the lattice, $5d^1$ and $5d^2$ double perovskite systems can give rise to hidden-order phase transitions [90]. For the antifluorite halides, interactions play a minor role; however, it might prove interesting to study the role of spin-orbit-lattice entanglement for multipolar moments [138, 248]. For $5d^1$, RIXS at the Ta L_3 edge reveals a spin-orbit excitation around 0.4 eV on powder samples of K_2TaCl_6 and Rb_2TaCl_6 [112]. Given the experimental resolution of $\delta E \approx 0.09$ eV, the data do not reveal a putative splitting of the $j = 3/2$ quartet or any signature of vibronic effects. Here, a closer examination with optical spectroscopy and RIXS can offer a more detailed picture. Recently, W^{4+} $5d^2$ Rb_2WCl_6, Cs_2WCl_6, and the oxyhalide $Cs_2WO_xCl_{6-x}$ have been synthesized and characterized [115], but the multiplet structure of these compounds is widely unexplored. Up to now, however, larger experimental efforts on the Ta- and W-based antifluorite halides have been impeded by the air sensitivity of these samples [112, 249].

Bibliography

[1] P. W. Anderson, Science **177**, 393 (1972).

[2] Y. Tokura, M. Kawasaki, and N. Nagaosa, Nature Physics **13**, 1056 (2017).

[3] P. Wölfle, Reports on Progress in Physics **81**, 032501 (2018).

[4] N. W. Ashcroft and N. D. Mermin, *Solid state physics* (Brooks/Cole Thomson Learning, 2012).

[5] G. R. Stewart, Reviews of Modern Physics **56**, 755 (1984).

[6] A. K. Geim and K. S. Novoselov, Nature Materials **6**, 183 (2007).

[7] M. Z. Hasan and C. L. Kane, Reviews of Modern Physics **82**, 3045 (2010).

[8] C. Kim, A. Y. Matsuura, Z.-X. Shen, N. Motoyama, H. Eisaki, S. Uchida, T. Tohyama, and S. Maekawa, Physical Review Letters **77**, 4054 (1996).

[9] B. J. Kim, H. Koh, E. Rotenberg, S.-J. Oh, H. Eisaki, N. Motoyama, S. Uchida, T. Tohyama, S. Maekawa, Z.-X. Shen, and C. Kim, Nature Physics **2**, 397 (2006).

[10] H. L. Stormer, D. C. Tsui, and A. C. Gossard, Reviews of Modern Physics **71**, S298 (1999).

[11] J. K. Jain, Annual Review of Condensed Matter Physics **6**, 39 (2015).

[12] F. Bloch, Zeitschrift für Physik **52**, 555 (1929).

[13] N. F. Mott and R. Peierls, Proceedings of the Physical Society **49**, 72 (1937).

[14] N. F. Mott, Proceedings of the Physical Society. Section A **62**, 416 (1949).

[15] J. H. d. Boer and E. J. W. Verwey, Proceedings of the Physical Society **49**, 59 (1937).

[16] B. Brandow, Advances in Physics **26**, 651 (1977).

[17] M. Imada, A. Fujimori, and Y. Tokura, Reviews of Modern Physics **70**, 1039 (1998).

[18] E. Dagotto and Y. Tokura, MRS Bulletin **33**, 1037 (2008).

[19] D. Khomskii, *Transition metal compounds*, 1st ed. (Cambridge University Press, Cambridge, 2014) includes bibliographical references and index.

[20] Y. Tokura and N. Nagaosa, Science **288**, 462 (2000).

[21] C. Martins, M. Aichhorn, and S. Biermann, Journal of Physics: Condensed Matter **29**, 263001 (2017).

[22] D. Khomskii, Physics **2**, 20 (2009).

[23] T. Kimura, T. Goto, H. Shintani, K. Ishizaka, T. Arima, and Y. Tokura, Nature **426**, 55 (2003).

[24] M. Fiebig, T. Lottermoser, D. Meier, and M. Trassin, Nature Reviews Materials **1**, 1 (2016).

[25] S. Mühlbauer, B. Binz, F. Jonietz, C. Pfleiderer, A. Rosch, A. Neubauer, R. Georgii, and P. Böni, Science **323**, 915 (2009).

[26] S. Seki, X. Z. Yu, S. Ishiwata, and Y. Tokura, Science **336**, 198 (2012).

[27] T. Adams, A. Chacon, M. Wagner, A. Bauer, G. Brandl, B. Pedersen, H. Berger, P. Lemmens, and C. Pfleiderer, Physical Review Letters **108**, 237204 (2012).

[28] Y. Tokura and N. Kanazawa, Chemical Reviews **121**, 2857 (2020).

[29] B. J. Kim, H. Jin, S. J. Moon, J.-Y. Kim, B.-G. Park, C. S. Leem, J. Yu, T. W. Noh, C. Kim, S.-J. Oh, J.-H. Park, V. Durairaj, G. Cao, and E. Rotenberg, Phys. Rev. Lett. **101**, 076402 (2008).

[30] S. J. Moon, H. Jin, K. W. Kim, W. S. Choi, Y. S. Lee, J. Yu, G. Cao, A. Sumi, H. Funakubo, C. Bernhard, and T. W. Noh, Physical Review Letters **101**, 226402 (2008).

[31] R. Comin, G. Levy, B. Ludbrook, Z.-H. Zhu, C. N. Veenstra, J. A. Rosen, Y. Singh, P. Gegenwart, D. Stricker, J. N. Hancock, D. van der Marel, I. S. Elfimov, and A. Damascelli, Phys. Rev. Lett. **109**, 266406 (2012).

[32] W. Witczak-Krempa, G. Chen, Y. B. Kim, and L. Balents, Annual Review of Condensed Matter Physics **5**, 57 (2014).

[33] T. Takayama, J. Chaloupka, A. Smerald, G. Khaliullin, and H. Takagi, Journal of the Physical Society of Japan **90**, 062001 (2021).

[34] J. G. Rau, E. K.-H. Lee, and H.-Y. Kee, Annual Review of Condensed Matter Physics **7**, 195 (2016).

[35] J. Kim, D. Casa, M. H. Upton, T. Gog, Y.-J. Kim, J. F. Mitchell, M. van Veenendaal, M. Daghofer, J. van den Brink, G. Khaliullin, and B. J. Kim, Physical Review Letters **108**, 177003 (2012).

[36] R. Coldea, S. M. Hayden, G. Aeppli, T. G. Perring, C. D. Frost, T. E. Mason, S.-W. Cheong, and Z. Fisk, Physical Review Letters **86**, 5377 (2001).

[37] J. Bertinshaw, Y. Kim, G. Khaliullin, and B. Kim, Annual Review of Condensed Matter Physics **10**, 315 (2019).

[38] G. Jackeli and G. Khaliullin, Physical Review Letters **102**, 017205 (2009).

[39] I. Kimchi and A. Vishwanath, Physical Review B **89**, 014414 (2014).

[40] H. Takagi, T. Takayama, G. Jackeli, G. Khaliullin, and S. E. Nagler, Nature Reviews Physics **1**, 264 (2019).

[41] L. Savary and L. Balents, Reports on Progress in Physics **80**, 016502 (2016).

[42] C. Broholm, R. J. Cava, S. A. Kivelson, D. G. Nocera, M. R. Norman, and T. Senthil, Science **367**, 6475 (2020).

[43] A. Kitaev, Annals of Physics **321**, 2 (2006).

[44] J. Chaloupka, G. Jackeli, and G. Khaliullin, Physical Review Letters **105**, 027204 (2010).

[45] Y. Singh and P. Gegenwart, Physical Review B **82**, 064412 (2010).

[46] I. Kimchi and Y.-Z. You, Physical Review B **84**, 180407 (2011).

[47] Y. Singh, S. Manni, J. Reuther, T. Berlijn, R. Thomale, W. Ku, S. Trebst, and P. Gegenwart, Physical Review Letters **108**, 127203 (2012).

[48] F. Ye, S. Chi, H. Cao, B. C. Chakoumakos, J. A. Fernandez-Baca, R. Custelcean, T. F. Qi, O. B. Korneta, and G. Cao, Physical Review B **85**, 180403 (2012).

[49] H. Gretarsson, J. P. Clancy, Y. Singh, P. Gegenwart, J. P. Hill, J. Kim, M. H. Upton, A. H. Said, D. Casa, T. Gog, and Y.-J. Kim, Physical Review B **87**, 220407 (2013).

[50] S. Hwan Chun, J.-W. Kim, J. Kim, H. Zheng, C. Stoumpos, C. Malliakas, J. Mitchell, K. Mehlawat, Y. Singh, Y. Choi, T. Gog, A. Al-Zein, M. Sala, M. Krisch, J. Chaloupka, G. Jackeli, G. Khaliullin, and B. J. Kim, Nature Physics **11**, 462 (2015).

[51] E. K.-H. Lee and Y. B. Kim, Physical Review B **91**, 064407 (2015).

[52] I. Kimchi, R. Coldea, and A. Vishwanath, Physical Review B **91**, 245134 (2015).

[53] S. Williams, R. Johnson, F. Freund, S. Choi, A. Jesche, I. Kimchi, S. Manni, A. Bombardi, P. Manuel, P. Gegenwart, and R. Coldea, Physical Review B **93**, 195158 (2016).

[54] K. W. Plumb, J. P. Clancy, L. J. Sandilands, V. V. Shankar, Y. F. Hu, K. S. Burch, H.-Y. Kee, and Y.-J. Kim, Physical Review B **90**, 041112 (2014).

[55] R. D. Johnson, S. C. Williams, A. A. Haghighirad, J. Singleton, V. Zapf, P. Manuel, I. I. Mazin, Y. Li, H. O. Jeschke, R. Valentí, and R. Coldea, Physical Review B **92**, 235119 (2015).

[56] L. J. Sandilands, Y. Tian, K. W. Plumb, Y.-J. Kim, and K. S. Burch, Physical Review Letters **114**, 147201 (2015).

[57] M. Majumder, M. Schmidt, H. Rosner, A. A. Tsirlin, H. Yasuoka, and M. Baenitz, Physical Review B **91**, 180401 (2015).

[58] H.-S. Kim, V. S. V., A. Catuneanu, and H.-Y. Kee, Physical Review B **91**, 241110 (2015).

[59] H. B. Cao, A. Banerjee, J.-Q. Yan, C. A. Bridges, M. D. Lumsden, D. G. Mandrus, D. A. Tennant, B. C. Chakoumakos, and S. E. Nagler, Physical Review B **93**, 134423 (2016).

[60] A. Banerjee, C. A. Bridges, J.-Q. Yan, A. A. Aczel, L. Li, M. B. Stone, G. E. Granroth, M. D. Lumsden, Y. Yiu, J. Knolle, S. Bhattacharjee, D. L. Kovrizhin, R. Moessner, D. A. Tennant, D. G. Mandrus, and S. E. Nagler, Nature Materials **15**, 733 (2016).

[61] A. Banerjee, J. Yan, J. Knolle, C. A. Bridges, M. B. Stone, M. D. Lumsden, D. G. Mandrus, D. A. Tennant, R. Moessner, and S. E. Nagler, Science **356**, 1055 (2017).

[62] S.-H. Do, S.-Y. Park, J. Yoshitake, J. Nasu, Y. Motome, Y. Kwon, D. T. Adroja, D. J. Voneshen, K. Kim, T.-H. Jang, J.-H. Park, K.-Y. Choi, and S. Ji, Nature Physics **13**, 1079 (2017).

[63] S. Trebst and C. Hickey, Physics Reports **950**, 1 (2022).

[64] J. G. Rau, E. K.-H. Lee, and H.-Y. Kee, Physical Review Letters **112**, 077204 (2014).

[65] A. Revelli, C. C. Loo, D. Kiese, P. Becker, T. Fröhlich, T. Lorenz, M. Moretti Sala, G. Monaco, F. L. Buessen, J. Attig, M. Hermanns, S. V. Streltsov, D. I. Khomskii, J. van den Brink, M. Braden, P. H. M. van Loosdrecht, S. Trebst, A. Paramekanti, and M. Grüninger, Physical Review B **100**, 085139 (2019).

[66] M. Magnaterra, K. Hopfer, C. J. Sahle, M. M. Sala, G. Monaco, J. Attig, C. Hickey, I. M. Pietsch, F. Breitner, P. Gegenwart, M. H. Upton, J. Kim, S. Trebst, P. H. M. van Loosdrecht, J. van den Brink, and M. Grüninger, Rixs observation of bond-directional nearest-neighbor excitations in the kitaev material na_2iro_3 (2023).

[67] M. Braden, X. Wang, A. Bertin, P. Steffens, and Y. Su, Physical Review Letters **134**, 236702 (2025).

[68] Y. Kasahara, T. Ohnishi, Y. Mizukami, O. Tanaka, S. Ma, K. Sugii, N. Kurita, H. Tanaka, J. Nasu, Y. Motome, T. Shibauchi, and Y. Matsuda, Nature **559**, 227 (2018).

[69] T. Yokoi, S. Ma, Y. Kasahara, S. Kasahara, T. Shibauchi, N. Kurita, H. Tanaka, J. Nasu, Y. Motome, C. Hickey, S. Trebst, and Y. Matsuda, Science **373**, 568 (2021).

[70] Y. Vinkler-Aviv and A. Rosch, Physical Review X **8**, 031032 (2018).

[71] S.-H. Baek, S.-H. Do, K.-Y. Choi, Y. Kwon, A. Wolter, S. Nishimoto, J. van den Brink, and B. Büchner, Physical Review Letters **119**, 037201 (2017).

[72] A. Banerjee, P. Lampen-Kelley, J. Knolle, C. Balz, A. A. Aczel, B. Winn, Y. Liu, D. Pajerowski, J. Yan, C. A. Bridges, A. T. Savici, B. C. Chakoumakos, M. D. Lumsden, D. A. Tennant, R. Moessner, D. G. Mandrus, and S. E. Nagler, npj Quantum Materials **3**, 8 (2018).

[73] Y.-F. Jiang, T. P. Devereaux, and H.-C. Jiang, Physical Review B **100**, 165123 (2019).

[74] A. Ponomaryov, L. Zviagina, J. Wosnitza, P. Lampen-Kelley, A. Banerjee, J.-Q. Yan, C. Bridges, D. Mandrus, S. Nagler, and S. Zvyagin, Physical Review Letters **125**, 037202 (2020).

[75] S. Bachus, D. Kaib, Y. Tokiwa, A. Jesche, V. Tsurkan, A. Loidl, S. Winter, A. Tsirlin, R. Valentí, and P. Gegenwart, Physical Review Letters **125**, 097203 (2020).

[76] A. Sahasrabudhe, D. A. S. Kaib, S. Reschke, R. German, T. C. Koethe, J. Buhot, D. Kamenskyi, C. Hickey, P. Becker, V. Tsurkan, A. Loidl, S. H. Do, K. Y. Choi, M. Grüninger, S. M. Winter, Z. Wang, R. Valentí, and P. H. M. van Loosdrecht, Physical Review B **101**, 140410 (2020).

[77] P. Czajka, T. Gao, M. Hirschberger, P. Lampen-Kelley, A. Banerjee, J. Yan, D. G. Mandrus, S. E. Nagler, and N. P. Ong, Nature Physics **17**, 915 (2021).

[78] A. Sahasrabudhe, M. A. Prosnikov, T. C. Koethe, P. Stein, V. Tsurkan, A. Loidl, M. Grüninger, H. Hedayat, and P. H. M. van Loosdrecht, Physical Review Research **6**, l022005 (2024).

[79] G. L. Stamokostas and G. A. Fiete, Physical Review B **97**, 085150 (2018).

[80] S. Sugano, Y. Tanabe, and H. Kamimura, *Multiplets of Transition-Metal Ions in Crystals* (Academic Press, 1970).

[81] N. B. Perkins, Y. Sizyuk, and P. Wölfle, Physical Review B **89**, 035143 (2014).

[82] L. J. Sandilands, Y. Tian, A. A. Reijnders, H.-S. Kim, K. W. Plumb, Y.-J. Kim, H.-Y. Kee, and K. S. Burch, Physical Review B **93**, 075144 (2016).

[83] B. W. Lebert, S. Kim, V. Bisogni, I. Jarrige, A. M. Barbour, and Y.-J. Kim, Journal of Physics: Condensed Matter **32**, 144001 (2020).

[84] S. Reschke, F. Mayr, S. Widmann, H.-A. K. von Nidda, V. Tsurkan, M. V. Eremin, S.-H. Do, K.-Y. Choi, Z. Wang, and A. Loidl, Journal of Physics: Condensed Matter **30**, 475604 (2018).

[85] B. Henderson and G. F. Imbusch, *Optical Spectroscopy of Inorganic Solids* (Oxford University PressOxford, 2006).

[86] E. Benckiser, R. Rückamp, T. Möller, T. Taetz, A. Möller, A. A. Nugroho, T. T. M. Palstra, G. S. Uhrig, and M. Grüninger, New Journal of Physics **10**, 053027 (2008).

[87] G. Khaliullin, Physical Review Letters **111**, 197201 (2013).

[88] S. V. Streltsov and D. I. Khomskii, Physical Review X **10**, 031043 (2020).

[89] A. Paramekanti, D. D. Maharaj, and B. D. Gaulin, Physical Review B **101**, 054439 (2020).

[90] L. V. Pourovskii, D. Fiore Mosca, L. Celiberti, S. Khmelevskyi, A. Paramekanti, and C. Franchini, Nature Reviews Materials **10**, 674696 (2025).

[91] S. Vasala and M. Karppinen, Progress in Solid State Chemistry **43**, 1 (2015).

[92] R. L. Armstrong, Physics Reports **57**, 343 (1980).

[93] J. H. E. Griffiths, J. Owen, P. J. G., and M. F. Partridge, Proceedings of the Royal Society of London. Series A. Mathematical and Physical Sciences **250**, 84 (1959).

[94] V. Minkiewicz, G. Shirane, B. Frazer, R. Wheeler, and P. Dorain, Journal of Physics and Chemistry of Solids **29**, 881 (1968).

[95] H. U. Rahman, Physical Review B **3**, 729 (1971).

[96] J. W. Lynn, G. Shirane, and M. Blume, Physical Review Letters **37**, 154 (1976).

[97] G. P. O'Leary and R. G. Wheeler, Physical Review B **1**, 4409 (1970).

[98] J. Lynn, H. Patterson, G. Shirane, and R. Wheeler, Solid State Communications **27**, 859 (1978).

[99] R. L. Armstrong, D. Mintz, B. M. Powell, and W. J. L. Buyers, Physical Review B **17**, 1260 (1978).

[100] D. Mintz, R. L. Armstrong, B. M. Powell, and W. J. L. Buyers, Physical Review B **19**, 448 (1979).

[101] K. Rössler and J. Winter, Chemical Physics Letters **46**, 566 (1977).

[102] N. Khan, D. Prishchenko, M. H. Upton, V. G. Mazurenko, and A. A. Tsirlin, Physical Review B **103**, 125158 (2021).

[103] A. Bertin, L. Kiefer, P. Becker, L. Bohatý, and M. Braden, Journal of Physics: Condensed Matter **36**, 245402 (2024).

[104] M. Saura-Múzquiz, M. Avdeev, H. E. A. Brand, and B. J. Kennedy, Inorganic Chemistry **61**, 15961 (2022).

[105] A. Bertin, T. Dey, D. Brüning, D. Gorkov, K. Jenni, A. Krause, P. Becker, L. Bohatý, D. Khomskii, V. Pomjakushin, L. Keller, M. Braden, and T. Lorenz, Physical Review B **109**, 094409 (2024).

[106] N. Khan, D. Prishchenko, Y. Skourski, V. G. Mazurenko, and A. A. Tsirlin, Physical Review B **99**, 144425 (2019).

[107] D. Reig-i Plessis, T. A. Johnson, K. Lu, Q. Chen, J. P. C. Ruff, M. H. Upton, T. J. Williams, S. Calder, H. D. Zhou, J. P. Clancy, A. A. Aczel, and G. J. MacDougall, Physical Review Materials **4**, 124407 (2020).

[108] L. Bhaskaran, A. N. Ponomaryov, J. Wosnitza, N. Khan, A. A. Tsirlin, M. E. Zhitomirsky, and S. A. Zvyagin, Physical Review B **104**, 184404 (2021).

[109] S. Lee, B. H. Kim, M.-J. Seong, and K.-Y. Choi, Physical Review B **105**, 184433 (2022).

[110] Q. Wang, A. de la Torre, J. A. Rodriguez-Rivera, A. A. Podlesnyak, W. Tian, A. A. Aczel, M. Matsuda, P. J. Ryan, J.-W. Kim, J. G. Rau, and K. W. Plumb, Physical Review X **15**, 021021 (2025).

[111] P. Stein, T. C. Koethe, L. Bohatý, P. Becker, M. Grüninger, and P. H. M. van Loosdrecht, Physical Review B **107**, 214301 (2023).

[112] H. Ishikawa, T. Takayama, R. K. Kremer, J. Nuss, R. Dinnebier, K. Kitagawa, K. Ishii, and H. Takagi, Physical Review B **100**, 045142 (2019).

[113] H. Ishikawa, T. Yajima, A. Matsuo, and K. Kindo, Journal of Physics: Condensed Matter **33**, 125802 (2021).

[114] A. Mansouri Tehrani, J.-R. Soh, J. Pásztorová, M. E. Merkel, I. ivkovi, H. M. Rønnow, and N. A. Spaldin, Physical Review Research **5**, l012010 (2023).

[115] E. E. Morgan, G. T. Kent, A. Zohar, A. ODea, G. Wu, A. K. Cheetham, and R. Seshadri, Chemistry of Materials **35**, 7032 (2023).

[116] K. Pradhan, A. Paramekanti, and T. Saha-Dasgupta, Physical Review B **109**, 184416 (2024).

[117] Y. Li, R. Seshadri, S. D. Wilson, A. K. Cheetham, and R. Valentí, Physical Review Research **7**, l012083 (2025).

[118] G. Cao and P. Schlottmann, Reports on Progress in Physics **81**, 042502 (2018).

[119] N. Borgwardt, *Optics on materials with strong spin-orbit coupling: topological insulators* $Bi_{2-x}Sb_xTe_{3-y}Se_y$ *and the* $j = 1/2$ *compounds* Na_2IrO_3 *and* α-$RuCl_3$, Ph.D. thesis, University of Cologne (2019).

[120] A. Thompson, I. Lindau, D. Attwood, Y. Liu, E. Gullikson, P. Pianetta, H. Howell, A. Robinson, K.-J. Kim, J. Scofield, J. Kirz, J. Underwood, J. Kortright, G. Williams, and H. Winick, *X-ray data booklet*, Tech. Rep. (Center for X-Ray Optics and Advanced Light Source, Lawrence Berkely National Laboratory, University of California, 2009).

[121] A. M. Cook, S. Matern, C. Hickey, A. A. Aczel, and A. Paramekanti, Physical Review B **92**, 020417 (2015).

[122] A. P. Ramirez, Annual Review of Materials Science **24**, 453 (1994).

[123] P. Anderson, Materials Research Bulletin **8**, 153 (1973).

[124] G. Cao, A. Subedi, S. Calder, J.-Q. Yan, J. Yi, Z. Gai, L. Poudel, D. J. Singh, M. D. Lumsden, A. D. Christianson, B. C. Sales, and D. Mandrus, Physical Review B **87**, 155136 (2013).

[125] A. A. Aczel, A. M. Cook, T. J. Williams, S. Calder, A. D. Christianson, G.-X. Cao, D. Mandrus, Y.-B. Kim, and A. Paramekanti, Physical Review B **93**, 214426 (2016).

[126] X. Liu, V. M. Katukuri, L. Hozoi, W.-G. Yin, M. P. M. Dean, M. H. Upton, J. Kim, D. Casa, A. Said, T. Gog, T. F. Qi, G. Cao, A. M. Tsvelik, J. van den Brink, and J. P. Hill, Physical Review Letters **109**, 157401 (2012).

[127] J. Kim, A. H. Said, D. Casa, M. H. Upton, T. Gog, M. Daghofer, G. Jackeli, J. van den Brink, G. Khaliullin, and B. J. Kim, Physical Review Letters **109**, 157402 (2012).

[128] H. Gretarsson, J. P. Clancy, X. Liu, J. P. Hill, E. Bozin, Y. Singh, S. Manni, P. Gegenwart, J. Kim, A. H. Said, D. Casa, T. Gog, M. H. Upton, H.-S. Kim, J. Yu, V. M. Katukuri, L. Hozoi, J. van den Brink, and Y.-J. Kim, Physical Review Letters **110**, 076402 (2013).

[129] M. Rossi, M. Retegan, C. Giacobbe, R. Fumagalli, A. Efimenko, T. Kulka, K. Wohlfeld, A. I. Gubanov, and M. Moretti Sala, Physical Review B **95**, 235161 (2017).

[130] X. Lu, P. Olalde-Velasco, Y. Huang, V. Bisogni, J. Pelliciari, S. Fatale, M. Dantz, J. G. Vale, E. C. Hunter, J. Chang, V. N. Strocov, R. S. Perry, M. Grioni, D. F. McMorrow, H. M. Rønnow, and T. Schmitt, Physical Review B **97**, 041102 (2018).

[131] A. A. Aczel, J. P. Clancy, Q. Chen, H. D. Zhou, D. Reig-i Plessis, G. J. MacDougall, J. P. C. Ruff, M. H. Upton, Z. Islam, T. J. Williams, S. Calder, and J.-Q. Yan, Physical Review B **99**, 134417 (2019).

[132] A. Ruiz, N. P. Breznay, M. Li, I. Rousochatzakis, A. Allen, I. Zinda, V. Nagarajan, G. Lopez, Z. Islam, M. H. Upton, J. Kim, A. H. Said, X.-R. Huang, T. Gog, D. Casa, R. J. Birgeneau, J. D. Koralek, J. G. Analytis, N. B. Perkins, and A. Frano, Physical Review B **103**, 184404 (2021).

[133] A. de la Torre, B. Zager, F. Bahrami, M. DiScala, J. R. Chamorro, M. H. Upton, G. Fabbris, D. Haskel, D. Casa, T. M. McQueen, F. Tafti, and K. W. Plumb, Physical Review B **104**, l100416 (2021).

[134] W. Jin, S. H. Chun, J. Kim, D. Casa, J. P. C. Ruff, C. J. Won, K. D. Lee, N. Hur, and Y.-J. Kim, Physical Review B **105**, 054419 (2022).

[135] M. Magnaterra, M. Moretti Sala, G. Monaco, P. Becker, M. Hermanns, P. Warzanowski, T. Lorenz, D. I. Khomskii, P. H. M. van Loosdrecht, J. van den Brink, and M. Grüninger, Physical Review Research **5**, 013167 (2023).

[136] A. de la Torre, B. Zager, F. Bahrami, M. H. Upton, J. Kim, G. Fabbris, G.-H. Lee, W. Yang, D. Haskel, F. Tafti, and K. W. Plumb, Nature Communications **14**, 5018 (2023).

[137] N. Iwahara and W. Furukawa, Physical Review B **108**, 075136 (2023).

[138] N. Iwahara, Journal of the Physical Society of Japan **93**, 121003 (2024).

[139] T. Keiderling, P. Stephens, S. Piepho, J. Slater, and P. Schatz, Chemical Physics **11**, 343 (1975).

[140] C. D. Flint and A. G. Paulusz, Inorganic Chemistry **20**, 1768 (1981).

[141] R. K. Yoo and T. Keiderling, Chemical Physics **108**, 317 (1986).

[142] L. Pross, K. Rössler, and H. Schenk, Journal of Inorganic and Nuclear Chemistry **36**, 317 (1974).

[143] B. A. Kozikowski and T. A. Keiderling, The Journal of Physical Chemistry **87**, 4630 (1983).

[144] R. Yoo, S. Lee, B. Kozikowski, and T. Keiderling, Chemical Physics **117**, 237 (1987).

[145] M. Bettinelli and C. D. Flint, Journal of Physics C: Solid State Physics **21**, 5499 (1988).

[146] L. J. P. Ament, M. van Veenendaal, and J. van den Brink, Europhysics Letters **95**, 27008 (2011).

[147] A. Geondzhian and K. Gilmore, Physical Review B **101**, 214307 (2020).

[148] L. Braicovich, M. Rossi, R. Fumagalli, Y. Peng, Y. Wang, R. Arpaia, D. Betto, G. M. De Luca, D. Di Castro, K. Kummer, M. Moretti Sala, M. Pagetti, G. Balestrino, N. B. Brookes, M. Salluzzo, S. Johnston, J. van den Brink, and G. Ghiringhelli, Physical Review Research **2**, 023231 (2020).

[149] K. Gilmore, Physical Chemistry Chemical Physics **25**, 217 (2023).

[150] A. Jain, M. Krautloher, J. Porras, G. Ryu, D. Chen, D. Abernathy, J. Park, A. Ivanov, J. Chaloupka, G. Khaliullin, B. Keimer, and B. Kim, Nature Physics **13**, 633 (2017).

[151] S. Kunkemöller, D. Khomskii, P. Steffens, A. Piovano, A. Nugroho, and M. Braden, Physical Review Letters **115**, 247201 (2015).

[152] S. Kunkemöller, E. Komleva, S. V. Streltsov, S. Hoffmann, D. I. Khomskii, P. Steffens, Y. Sidis, K. Schmalzl, and M. Braden, Physical Review B **95**, 214408 (2017).

[153] H. Takahashi, H. Suzuki, J. Bertinshaw, S. Bette, C. Mühle, J. Nuss, R. Dinnebier, A. Yaresko, G. Khaliullin, H. Gretarsson, T. Takayama, H. Takagi, and B. Keimer, Physical Review Letters **127**, 227201 (2021).

[154] H. Wu, Z. Hu, T. Burnus, J. D. Denlinger, P. G. Khalifah, D. G. Mandrus, L.-Y. Jang, H. H. Hsieh, A. Tanaka, K. S. Liang, J. W. Allen, R. J. Cava, D. I. Khomskii, and L. H. Tjeng, Physical Review Letters **96**, 256402 (2006).

[155] I. Vergara, M. Magnaterra, P. Warzanowski, J. Attig, S. Kunkemöller, D. I. Khomskii, M. Braden, M. Hermanns, and M. Grüninger, Physical Review B **106**, 085103 (2022).

[156] Y. Zhang, L.-F. Lin, A. Moreo, and E. Dagotto, Physical Review B **106**, 155148 (2022).

[157] S. Bhowal and I. Dasgupta, Journal of Physics: Condensed Matter **33**, 453001 (2021).

[158] B. Yuan, J. P. Clancy, A. M. Cook, C. M. Thompson, J. Greedan, G. Cao, B. C. Jeon, T. W. Noh, M. H. Upton, D. Casa, T. Gog, A. Paramekanti, and Y.-J. Kim, Physical Review B **95**, 235114 (2017).

[159] A. Nag, S. Bhowal, A. Chakraborty, M. M. Sala, A. Efimenko, F. Bert, P. K. Biswas, A. D. Hillier, M. Itoh, S. D. Kaushik, V. Siruguri, C. Meneghini, I. Dasgupta, and S. Ray, Physical Review B **98**, 014431 (2018).

[160] M. Kusch, V. M. Katukuri, N. A. Bogdanov, B. Büchner, T. Dey, D. V. Efremov, J. E. Hamann-Borrero, B. H. Kim, M. Krisch, A. Maljuk, M. M. Sala, S. Wurmehl, G. Aslan-Cansever, M. Sturza, L. Hozoi, J. van den Brink, and J. Geck, Physical Review B **97**, 064421 (2018).

[161] A. Paramekanti, D. J. Singh, B. Yuan, D. Casa, A. Said, Y.-J. Kim, and A. D. Christianson, Physical Review B **97**, 235119 (2018).

[162] A. A. Aczel, Q. Chen, J. P. Clancy, C. dela Cruz, D. Reig-i Plessis, G. J. MacDougall, C. J. Pollock, M. H. Upton, T. J. Williams, N. LaManna, J. P. Carlo, J. Beare, G. M. Luke, and H. D. Zhou, Physical Review Materials **6**, 094409 (2022).

[163] G. Cao, T. Qi, L. Li, J. Terzic, S. Yuan, L. DeLong, G. Murthy, and R. Kaul, Physical Review Letters **112**, 056402 (2014).

[164] J. Terzic, H. Zheng, F. Ye, H. D. Zhao, P. Schlottmann, L. E. De Long, S. J. Yuan, and G. Cao, Physical Review B **96**, 064436 (2017).

[165] S. Fuchs, T. Dey, G. Aslan-Cansever, A. Maljuk, S. Wurmehl, B. Büchner, and V. Kataev, Physical Review Letters **120**, 237204 (2018).

[166] H. Gong, K. Kim, B. H. Kim, B. Kim, J. Kim, and B. Min, Journal of Magnetism and Magnetic Materials **454**, 66 (2018).

[167] M. A. Laguna-Marco, E. Arias-Egido, C. Piquer, V. Cuartero, L. Hernández-López, P. Kayser, J. A. Alonso, J. A. T. Barker, G. Fabbris, C. A. Escanhoela, and T. Irifune, Physical Review B **101**, 014449 (2020).

[168] Z. Y. Zhao, S. Calder, A. A. Aczel, M. A. McGuire, B. C. Sales, D. G. Mandrus, G. Chen, N. Trivedi, H. D. Zhou, and J.-Q. Yan, Physical Review B **93**, 134426 (2016).

[169] N. R. Davies, C. V. Topping, H. Jacobsen, A. J. Princep, F. K. K. Kirschner, M. C. Rahn, M. Bristow, J. G. Vale, I. da Silva, P. J. Baker, C. J. Sahle, Y.-F. Guo, D.-Y. Yan, Y.-G. Shi, S. J. Blundell, D. F. McMorrow, and A. T. Boothroyd, Physical Review B **99**, 174442 (2019).

[170] S. Calder, Z. Y. Zhao, M. H. Upton, and J.-Q. Yan, Physical Review B **109**, 054408 (2024).

[171] M. W. Haverkort, Journal of Physics: Conference Series **712**, 012001 (2016).

[172] Y. Du, Y. Hao, X. Hao, Y. Jia, K. Sun, and Y. Xu, Physical Chemistry Chemical Physics **27**, 20699 (2025).

[173] M. W. Haverkort, M. Zwierzycki, and O. K. Andersen, Physical Review B **85**, 165113 (2012).

[174] J. Kim, M. Daghofer, A. H. Said, T. Gog, J. van den Brink, G. Khaliullin, and B. J. Kim, Nature Communications **5**, 4453 (2014).

[175] C. J. Ballhausen, *Introduction to Ligand Field Theory* (New York: McGraw-Hill, 1962).

[176] J. S. Griffith, *The Theory of Transition-Metal Ions*, digitally printed version 2009 ed. (Cambridge University Press, 1961).

[177] E. U. Condon and G. Shortley, *The Theory of Atomic Spectra*, reprint d. ausg. 1935 ed. (Univ. Press, Cambridge, 1991).

[178] M. W. Haverkort, *Spin and orbital degrees of freedom in transition metal oxides and oxide thin films studied by soft x-ray absorption spectroscopy*, Ph.D. thesis, University of Cologne (2005), arXiv:cond-mat/0505214 [cond-mat.str-el] .

[179] K. Ishii, I. Jarrige, M. Yoshida, K. Ikeuchi, J. Mizuki, K. Ohashi, T. Takayama, J. Matsuno, and H. Takagi, Physical Review B **83**, 115121 (2011).

[180] M. Moretti Sala, M. Rossi, A. Al-Zein, S. Boseggia, E. C. Hunter, R. S. Perry, D. Prabhakaran, A. T. Boothroyd, N. B. Brookes, D. F. McMorrow, G. Monaco, and M. Krisch, Physical Review B **90**, 085126 (2014).

[181] M. Moretti Sala, K. Ohgushi, A. Al-Zein, Y. Hirata, G. Monaco, and M. Krisch, Physical Review Letters **112**, 176402 (2014).

[182] H. Gretarsson, H. Suzuki, H. Kim, K. Ueda, M. Krautloher, B. J. Kim, H. Yava, G. Khaliullin, and B. Keimer, Physical Review B **100**, 045123 (2019).

[183] S. Bhattacharjee, S.-S. Lee, and Y. B. Kim, New Journal of Physics **14**, 073015 (2012).

[184] G. Racah, Physical Review **62**, 438 (1942).

[185] R. E. Watson, Physical Review **118**, 1036 (1960).

[186] E. Pavarini and E. Koch, *Topology, entanglement, and strong correlations* (Forschungszentrum Jülich Zentralbibliothek, Verlag, Jülich, 2020).

[187] A. Georges, L. d. Medici, and J. Mravlje, Annual Review of Condensed Matter Physics **4**, 137 (2013).

[188] K. T. Moore and G. van der Laan, Reviews of Modern Physics **81**, 235 (2009).

[189] N. Iwahara and S. Shikano, Physical Review Research **5**, 023051 (2023).

[190] P. E. Hoggard, Zeitschrift für Naturforschung A **36**, 1276 (1981).

[191] J. Zaanen, G. A. Sawatzky, and J. W. Allen, Physical Review Letters **55**, 418 (1985).

[192] P. W. Anderson, Physical Review **79**, 350 (1950).

[193] J. B. Goodenough, *Magnetism And The Chemical Bond*, edited by F. A. Cotton (John Wiley And Sons, 1963).

[194] C. L. Cleveland and R. Medina A., American Journal of Physics **44**, 44 (1976).

[195] J. Kanamori, Journal of Physics and Chemistry of Solids **10**, 87 (1959).

[196] P. W. Anderson, Physical Review **115**, 2 (1959).

[197] S. M. Winter, A. A. Tsirlin, M. Daghofer, J. van den Brink, Y. Singh, P. Gegenwart, and R. Valentí, Journal of Physics: Condensed Matter **29**, 493002 (2017).

[198] J. D. Jackson, *Klassische Elektrodynamik* (DE GRUYTER, 2006).

[199] H. Kuzmany, *Solid-State Spectroscopy: An Introduction* (Springer Berlin Heidelberg, 2009).

[200] D. Franta, Journal of Applied Physics **127**, 223101 (2020).

[201] M. Dressel and G. Grüner, *Electrodynamics of solids* (Cambridge University Press, Cambridge, 2002).

[202] M. A. Hitchman and P. J. Cassidy, Inorganic Chemistry **18**, 1745 (1979).

[203] N. N. Kovaleva, A. V. Boris, C. Bernhard, A. Kulakov, A. Pimenov, A. M. Balbashov, G. Khaliullin, and B. Keimer, Physical Review Letters **93**, 147204 (2004).

[204] A. Gössling, M. W. Haverkort, M. Benomar, H. Wu, D. Senff, T. Möller, M. Braden, J. A. Mydosh, and M. Grüninger, Physical Review B **77**, 035109 (2008).

[205] J. Reul, A. A. Nugroho, T. T. M. Palstra, and M. Grüninger, Physical Review B **86**, 125128 (2012).

[206] L. J. P. Ament, M. van Veenendaal, T. P. Devereaux, J. P. Hill, and J. van den Brink, Reviews of Modern Physics **83**, 705 (2011).

[207] D. N. Basov, R. D. Averitt, D. van der Marel, M. Dressel, and K. Haule, Reviews of Modern Physics **83**, 471 (2011).

[208] J. Stöhr, *The Nature of X-Rays and Their Interactions with Matter* (Springer International Publishing, 2023).

[209] R. Rückamp, E. Benckiser, M. W. Haverkort, H. Roth, T. Lorenz, A. Freimuth, L. Jongen, A. Möller, G. Meyer, P. Reutler, B. Büchner, A. Revcolevschi, S.-W. Cheong, C. Sekar, G. Krabbes, and M. Grüninger, New Journal of Physics **7**, 144 (2005).

[210] E. Benckiser, *Optical Spectroscopy of Orbital and Magnetic Excitations in Vanadates and Cuprates*, Ph.D. thesis, University of Cologne (2007).

[211] R. Yoo, B. Kozikowski, S. Lee, and T. Keiderling, Chemical Physics **117**, 255 (1987).

[212] R. H. Lyddane, R. G. Sachs, and E. Teller, Physical Review **59**, 673 (1941).

[213] A. S. Barker, Physical Review **132**, 1474 (1963).

[214] A. B. Kuzmenko, Review of Scientific Instruments **76**, 083108 (2005).

[215] F. P. Mena, A. B. Kuzmenko, A. Hadipour, J. L. M. van Mechelen, D. van der Marel, and N. A. Babushkina, Physical Review B **72**, 134422 (2005).

[216] A. Akrap, M. Tran, A. Ubaldini, J. Teyssier, E. Giannini, D. van der Marel, P. Lerch, and C. C. Homes, Physical Review B **86**, 235207 (2012).

[217] J. Reul, L. Fels, N. Qureshi, K. Shportko, M. Braden, and M. Grüninger, Physical Review B **87**, 205142 (2013).

[218] G. K. Liu, X. Y. Chen, and J. Huang, Molecular Physics **101**, 1029 (2003).

[219] G. Liu, X. Chen, N. Edelstein, M. Reid, and J. Huang, Journal of Alloys and Compounds **374**, 240 (2004).

[220] G. E. Jellison and F. A. Modine, Applied Physics Letters **69**, 371 (1996).

[221] K.-E. Peiponen and E. M. Vartiainen, Physical Review B **44**, 8301 (1991).

[222] G. E. Jellison and F. A. Modine, Applied Physics Letters **69**, 2137 (1996).

[223] G. Grüner, Reviews of Modern Physics **60**, 1129 (1988).

[224] J. Bardeen, L. N. Cooper, and J. R. Schrieffer, Physical Review **108**, 1175 (1957).

[225] C. Franchini, M. Reticcioli, M. Setvin, and U. Diebold, Nature Reviews Materials **6**, 560 (2021).

[226] T. Azumi and K. Matsuzaki, Photochemistry and Photobiology **25**, 315 (1977).

[227] J. Franck and E. G. Dymond, Transactions of the Faraday Society **21**, 536 (1926).

[228] E. Condon, Physical Review **28**, 1182 (1926).

[229] E. U. Condon, Physical Review **32**, 858 (1928).

[230] M. Lax, The Journal of Chemical Physics **20**, 1752 (1952).

[231] W. E. Bron, Physical Review **140**, A2005 (1965).

[232] M. de Jong, L. Seijo, A. Meijerink, and F. T. Rabouw, Physical Chemistry Chemical Physics **17**, 16959 (2015).

[233] W. Herres and J. Gronholz, Comput. Appl. Lab. **2**, 216 (1984).

[234] R. Rückamp, *Orbital excitations of transition-metal oxides in optical spectroscopy*, Ph.D. thesis, Universität zu Köln (2006).

[235] A. Gössling, *Electronic structure of Titanates and layered Manganites probed by optical spectroscopy*, Ph.D. thesis, Universität zu Köln (2007).

[236] C. Hilgers, *The Electronic Structure of Spin Ladders and Spin Chains Studied by Ellipsometry*, Ph.D. thesis, University of Cologne (2009).

[237] J. Reul, *Eects of spin and orbital correlations on the optical spectral weights of transition-metal oxides*, Ph.D. thesis, University of Cologne (2013).

[238] W. Schülke, *Electron Dynamics by Inelastic X-ray Scattering.*, Oxford Series on Synchrotron Radiation Ser No. v.7 (Oxford University Press, Oxford, 2007) description based on publisher supplied metadata and other sources.

[239] F. M. F. de Groot, M. W. Haverkort, H. Elnaggar, A. Juhin, K.-J. Zhou, and P. Glatzel, Nature Reviews Methods Primers **4**, 45 (2024).

[240] M. Mitrano, S. Johnston, Y.-J. Kim, and M. Dean, Physical Review X **14**, 040501 (2024).

[241] W. He, Y. Shen, K. Wohlfeld, J. Sears, J. Li, J. Pelliciari, M. Walicki, S. Johnston, E. Baldini, V. Bisogni, M. Mitrano, and M. P. M. Dean, Nature Communications **15**, 3496 (2024).

[242] M. Moretti Sala, C. Henriquet, L. Simonelli, R. Verbeni, and G. Monaco, Journal of Electron Spectroscopy and Related Phenomena **188**, 150 (2013).

[243] M. Moretti Sala, K. Martel, C. Henriquet, A. Al Zein, L. Simonelli, C. J. Sahle, H. Gonzalez, M.-C. Lagier, C. Ponchut, S. Huotari, R. Verbeni, M. Krisch, and G. Monaco, Journal of Synchrotron Radiation **25**, 580 (2018).

[244] P. Willmott, *An Introduction to Synchrotron Radiation: Techniques and applications*, online-ausg. ed. (Wiley, Chichester, West Sussex, U.K, 2011).

[245] P. Warzanowski, M. Magnaterra, C. J. Sahle, M. Moretti Sala, P. Becker, L. Bohatý, I. Císařová, G. Monaco, T. Lorenz, P. H. M. van Loosdrecht, J. van den Brink, and M. Grüninger, Data for "Spin orbital lattice entanglement in the ideal $j = 1/2$ compound K_2IrCl_6" (2024).

[246] A. Koitzsch, C. Habenicht, E. Müller, M. Knupfer, B. Büchner, H. Kandpal, J. van den Brink, D. Nowak, A. Isaeva, and T. Doert, Physical Review Letters **117**, 126403 (2016).

[247] S. M. Winter, Y. Li, H. O. Jeschke, and R. Valentí, Physical Review B **93**, 214431 (2016).

[248] N. Iwahara and L. F. Chibotaru, Physical Review B **107**, l220404 (2023).

[249] E. E. Morgan, A. Brumberg, S. Panuganti, G. T. Kent, A. Zohar, A. A. Mikhailovsky, M. G. Kanatzidis, R. D. Schaller, M. L. Chabinyc, A. K. Cheetham, and R. Seshadri, Chemistry of Materials **36**, 7754 (2024).

Publications

The following is a list of publications to which I contributed during the period of my PhD. The publications marked with † are included as results in this thesis.

- M. Magnaterra, A. Sandberg, H. Schilling, P. Warzanowski, L. Pätzold, E. Bergamasco, Ch. J. Sahle, B. Detlefs, K. Ruotsalainen, M. Moretti Sala, G. Monaco, P. Becker, Q. Faure, G. S. Thakur, M. Songvilay, C. Felser, P. H. M. van Loosdrecht, J. van den Brink, M. Hermanns, and M. Grüninger, *Quasimolecular electronic structure of the trimer iridate* $Ba_4NbIr_3O_{12}$, Phys. Rev. B **111**, 085122 (2025).

- P. Warzanowski, M. Magnaterra, Ch. J. Sahle, M. Moretti Sala, P. Becker, L. Bohatý, I. Císařová, G. Monaco, T. Lorenz, P. H. M. van Loosdrecht, J. van den Brink, and M. Grüninger, *Spin orbital lattice entanglement in the ideal* $j = 1/2$ *compound* K_2IrCl_6, Phys. Rev. B **110**, 195120 (2024).†

- P. Warzanowski, M. Magnaterra, G. Schlicht, Q. Faure, Ch. J. Sahle, P. Becker, L. Bohatý, M. Moretti Sala, G. Monaco, M. Hermanns, P. H. M. van Loosdrecht, and M. Grüninger, *Spin-orbit coupling in a half-filled* t_{2g} *shell: The case of* $5d^3$ K_2ReCl_6, Phys. Rev. B **109**, 155149 (2024).†

- P. Warzanowski, M. Magnaterra, P. Stein, G. Schlicht, Q. Faure, Ch. J. Sahle, T. Lorenz, P. Becker, L. Bohatý, M. Moretti Sala, G. Monaco, P. H. M. van Loosdrecht, and M. Grüninger, *Electronic excitations in* $5d^4$ $J = 0$ Os^{4+} *halides studied by resonant inelastic x-ray scattering and optical spectroscopy*, Phys. Rev. B **108**, 125120 (2023).†

- M. Magnaterra, M. Moretti Sala, G. Monaco, P. Becker, M. Hermanns, P. Warzanowski, T. Lorenz, D. I. Khomskii, P. H. M. van Loosdrecht, J. van den Brink, and M. Grüninger, *RIXS interferometry and the role of disorder in the quantum magnet* $Ba_3Ti_{3-x}Ir_xO_9$, Phys. Rev. Research **5**, 013167 (2023).

- I. Vergara, M. Magnaterra, P. Warzanowski, J. Attig, S. Kunkemöller, D. I. Khomskii, M. Braden, M. Hermanns, and M. Grüninger, *Spin-orbit coupling and crystal-field splitting in Ti-doped* Ca_2RuO_4 *studied by ellipsometry*, Phys. Rev. B **106**, 085103 (2022).

- J. Zablocki, M. Schulz, G. Schnakenburg, L. Beverina, P. Warzanowski, A. Revelli, M. Grüninger, F. Balzer, K. Meerholz, A. Lützen, and M. Schiek, *Structure and Dielectric Properties of Anisotropic n-Alkyl Anilino Squaraine Thin Films*, J. Phys. Chem. C, **124**, 41, 22721 (2020).

- P. Warzanowski, N. Borgwardt, K. Hopfer, J. Attig, T. C. Koethe, P. Becker, V. Tsurkan, A. Loidl, M. Hermanns, P. H. M. van Loosdrecht, and M. Grüninger, *Multiple spin-orbit excitons and the electronic structure of α-$RuCl_3$*, Phys. Rev. Research **2**, 042007(R) (2020).[†]

- A. Revelli, M. Moretti Sala, G. Monaco, P. Becker, L. Bohatý, M. Hermanns, T. C. Koethe, T. Fröhlich, P. Warzanowski, T. Lorenz, S. V. Streltsov, P. H. M. van Loosdrecht, D. I. Khomskii, J. van den Brink, and M. Grüninger, *Resonant inelastic x-ray incarnation of Youngs double-slit experiment*, Sci. Adv. **5**: eaav402 (2019).